ATLAS CSC NOTE

ATL-PHYS-PUB-2007-xxx

Compiled on February 5, 2008

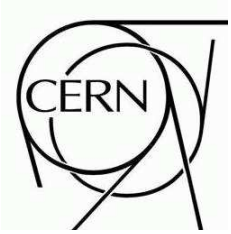

Diboson Physics Studies With the ATLAS Detector

Tom Barber[4], Richard Batley[4], Andrea Bocci[5], Electra Christidi[2], Tiesheng Dai[8], Al Goshaw[5], Liang Han[9], Chris Hays[7], Suen Hou[1], Yi Jiang[9], Bachas Konstantinos[2], Ashutosh Kotwal[5], Mark Kruse[5], Dan Levin[8], Xuefei Li[8], Zhijun Liang[1], Hong Ma[3], Chara Petridou[2], Dragan Popovic[6] Dusan Reljic[6], Dimos Sampsonidis[2], Ljiliana Simic[6], Nenad Vranjes[6], Song-Ming Wang[1], Pat Ward[4], Alan Wilson[8], Haijun Yang[8], Yi Yang[1], Pei Zhang[9], Zhengguo Zhao[8], Jiahang Zhong[1], Bing Zhou[8]

[1]*Academia Sinica, Taiwan*
[2]*Aristotle University of Thessaloniki, Greece*
[3]*Brookhaven National Laboratory, USA*
[4]*Cambridge University, UK*
[5]*Duke University, USA* [6]*Institute of Physics, Belgrade*
[7]*Oxford University, UK*
[8]*The University of Michigan, USA*
[9]*The University of Science and Technology of China*

Abstract

We present studies of the sensitivity of ATLAS to Standard Model (SM) diboson (W^+W^-, $W^\pm Z$, ZZ, $W^\pm\gamma$, and $Z\gamma$) production in pp collisions at $\sqrt{s} = 14$ TeV, through final states containing electrons, muons and photons Our studies use the ATLAS CSC (Computer-System-Commissioning) Monte Carlo datasets, which include trigger information and detector calibration and alignment corrections. We aim to establish the SM diboson detection sensitivities with the ATLAS experiment in early LHC physics runs (for 0.1 to 1 fb^{-1} integrated luminosities). We have included large fully simulated background events in our studies to understand the sources of background for diboson detection. We estimate the cross section measurement uncertainties (both statistical and systematic) as a function of integrated luminosity (from 0.1 to 30 fb^{-1}) and establish the ATLAS experiment sensitivities to anomalous triple gauge boson couplings. This note shows that the SM W^+W^-, $W^\pm Z$, $W^\pm\gamma$, $Z\gamma$ signals can be established with signal statistical sensitivity better than 5σ for the first 0.1 fb^{-1} integrated luminosity, and the ZZ signals can be established with 1.0 fb^{-1} integrated luminosity. The anomalous triple gauge boson coupling sensitivities can be significantly improved, even with 0.1 fb^{-1} data, over the results from Tevatron based on 1 fb^{-1} data.

Contents

1 Introduction

We present studies of diboson (W^+W^-, $W^\pm Z^0$, Z^0Z^0, $W^\pm\gamma$, $Z^0\gamma$) detection sensitivities with lepton and photon final states and corresponding triple gauge boson couplings (TGC) sensitivities as a function of integrated luminosity. Results are based on fully simulated ATLAS Monte Carlo data sets produced in the ATLAS Computing-System-Commissioning (CSC) program [1] from Fall 2006 - Summer 2007. This work augments previous diboson studies in two important ways. First, in order to understand deeply the sources of background to diboson signals, it includes about 30 million fully simulated background events from many SM processes. Second, the technique of *Boosted Decision Trees* [2, 3] is applied to some of the analyses to improve significantly the diboson detection sensitivities. This note documents the analysis methods and tools required for diboson physics studies.

Study of the diboson production at the LHC provides an important test of the high energy behavior of electroweak interactions. Vector boson self-couplings, uniquely fixed by Lorentz and gauge invariance, are a fundamental prediction of the Standard Model (SM), resulting from the non-Abelian nature of the $SU_L(2) \times U(1)$ gauge symmetric theory. Since these gauge boson self-couplings have not yet been measured with good precision it is possible that signals for physics beyond the SM could appear in this sector through discovery of anomalous TGC's.

LEP [4] and Tevatron [5]- [13] diboson studies have demonstrated the importance of precision determinations of the electroweak parameters as a tool to search indirectly for physics beyond the SM. The TGC's are currently studied at the Tevatron via production of W^+W^-, $W^\pm\gamma$, $Z^0\gamma$, $W^\pm Z^0$ and Z^0Z^0 in $p\bar{p}$ collisions at $\sqrt{s}$ =1.96 TeV. The W^+W^- process involves both $W^+W^-\gamma$ and $W^+W^-Z^0$ couplings, while $W^\pm\gamma$ and $W^\pm Z^0$ are concerned exclusively with the $W^+W^-\gamma$, and $W^+W^-Z^0$ couplings, respectively.

Anomalous couplings would lead to enhanced diboson cross sections, particularly at high boson transverse momentum and high diboson transverse mass. Experimental limits on non-SM TGC's can be obtained by comparing the shape of the measured transverse momentum or mass distribution (or transverse mass in final state involving W) with predictions, provided that the signal is not overwhelmed with background.

The study of diboson production is not only an effective probe for beyond-SM physics, but is also crucial for many important new physics searches at the LHC. For example, W^+W^- and Z^0Z^0 are major background sources for SM Higgs boson searches via the $H^0 \to Z^0Z^0$, Z^0Z^{*0}, W^+W^-, $W^\pm W^{*\mp}$ decay channels. Furthermore, if no light SM Higgs boson is found then electroweak symmetry breaking studies will require production rate measurements of energetic longitudinal gauge boson pairs. This is because the longitudinal components of $W^\pm$ and Z^0 are the Goldstone bosons of the symmetry breaking process. The new physics would appear as resonances or anomalous structures in the diboson spectra at high mass.

This note is structured as follows. In Section 2 the effective Lagrangian and TGC parameters are described. The generators used to produce the MC event samples for diboson studies are also described in section 2. In section 3 the current and expected Tevatron diboson physics, and analysis methods used to determine lepton identification efficiencies and to estimate backgrounds using data, are reviewed. The analyses of the five diboson final states are presented in Sections 4-8. A brief description of the analysis techniques, *Boosted Decision Trees* and binned maximum likelihood method, is provided in the appendices. Also included in the appendices are some alternative analyses.

2 Diboson production at LHC and effective Lagrangians

2.1 SM Diboson Production Cross Sections

The generic Standard Model tree-level Feynman diagrams for electroweak diboson production at hadron colliders are shown in Figure 1. The *s*-channel diagram contains the vector-boson self-interaction vertices which are discussed in this section.

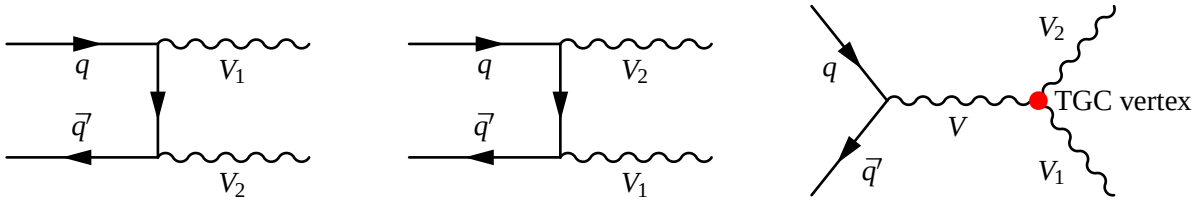

Figure 1: The generic Standard Model tree-level Feynman diagrams for diboson production at hadron colliders; $V, V_1, V_2 = \{W, Z, \gamma\}$. The *s*-channel diagram, on the right, contains the trilinear gauge boson vertex.

The diboson production cross sections at hadron colliders (Tevatron, LHC) predicted by the Standard Model are calculated at next-to-leading-order (NLO) [15], [16], [17]. For this CSC note we used the *MC@NLO* [18] Monte Carlo program to calculate the W^+W^-, $W^\pm Z^0$, Z^0Z^0 production cross sections (NLO). The parton-density-function (PDF) of $CTEQ6M$ [19] has been used. The leading-order (LO) cross section calculations are performed using the *PYTHIA* [20] program with the $CTEQ6L$ PDF. For $W^\pm\gamma$ and $Z^0\gamma$ productions, we have used the *BHO* [21] program to calculate both LO and NLO cross sections. The $CTEQ6M$ PDF is used in the calculations. The *BHO* LO calculations have been cross-checked with $PYTHIA$ calculations. They are consistent within a few percent. We list the calculated diboson production cross sections through $q\bar{q}'$ initial states in Table 1.

Table 1: The SM diboson production total cross sections at Tevatron and LHC hadron colliders. These values are calculated using $PYTHIA$ for LO cross sections, and using *MC@NLO* and *BHO*, for NLO cross sections. We quote 5% and 10% uncertainties for NLO and LO cross sections, respectively. Tevatron cross sections are quoted from the D0 and the CDF papers [5]. *The LO cross section for Z^0Z^0 from $PYTHIA$ has included $Z/\gamma*$ interference.

Diboson mode	Conditions	Tevatron $\sqrt{s} = 1.96$ TeV $\sigma(pb)$ NLO	LHC $\sqrt{s} = 14\ TeV$ $\sigma(pb)$ NLO	LHC $\sqrt{s} = 14\ TeV$ $\sigma(pb)$ LO
W^+W^-	W's on mass shell	12.4± 0.3	111.6±5.6	70.71±7.1
$W^\pm Z^0$	Z and W on mass shell, no $Z/\gamma*$	3.7 ± 0.3	47.8±3.3	27.12±2.7
Z^0Z^0	Z's on mass shell, no $Z/\gamma*$	1.43± 0.1	14.8±1.3	11.13±1.1*
$W^\pm\gamma$	$E_T^\gamma > 20$ GeV $\Delta R(\ell,\gamma) > 0.7$	19.3± 1.4	119.1±6.0	60.6± 6.1
$Z^0\gamma$	$E_T^\gamma > 20$ GeV, $\Delta R(\ell,\gamma) > 0.7$	4.74± 0.22	69.0±3.5	56.0±5.6

The diboson production rate at the LHC will be at least a factor of 100 higher than that at the Tevatron (ten times higher cross sections and ten times higher luminosity even at the initial LHC low luminosity of $\sim 2 \times 10^{33}$ cm^{-2}sec^{-1}). The higher event rate and the higher energy at the LHC will enable us to measure the vector-boson self-interaction couplings with much higher precision. The sensitivity to

anomalous TGC's, which allows the indirect search for new physics beyond the Standard Model, is expected to improve by orders of magnitude at the LHC over Tevatron and LEP.

2.2 Effective Lagrangian for charged TGC's

New physics may modify the self-interactions of vector bosons, in particular the triple gauge boson vertices. If the new physics occurs at an energy scale well above that being probed experimentally, it can be integrated out, and the result expressed as a set of anomalous (non-SM) interaction vertices. The most general effective Lagrangian, that conserves C and P separately, for charged triple gauge boson interactions is [24]:

$$L/g_{WWV} = ig_1^V(W^*_{\mu\nu}W^\mu V^\nu - W_{\mu\nu}W^{*\mu}V^\nu) + i\kappa^V W^*_\mu W_\nu V^{\mu\nu} + \frac{\lambda^V}{M_W^2}W^*_{\rho\mu}W^\mu_\nu V^{\nu\rho}$$

where V refers to the neutral vector-bosons, Z or γ; $X_{\mu\nu} \equiv \partial_\mu X_\nu - \partial_\nu X_\mu$ and the overall coupling constants g_{WWV} are given by $g_{WW\gamma} = -e$, $g_{WWZ} = -e\ cot\theta_W$, with e the positive electron charge and θ_W the weak mixing angle. The Standard Model triple gauge boson vertices are recovered by letting $g_1^V = \kappa^V = 1$ and $\lambda^V = 0$. The electromagnetic dipole and quadrupole moment of the W boson are proportional to the $WW\gamma$ coupling. They are given by:

$$\mu_W^{EM} = e(1+\kappa_\gamma+\lambda_\gamma)/2M_W, \quad Q_W^{EM} = -e(\kappa_\gamma-\lambda_\gamma)/M_W^2.$$

The weak dipole and quadrupole moment of the W boson are proportional to the WWZ coupling:

$$\mu_W^{weak} = e(g_1^Z+\kappa_Z+\lambda_Z)/2M_W, \quad Q_W^{weak} = -e(\kappa_Z-\lambda_Z)/M_W^2.$$

We can picture these as Z or γ fields radiated by the W boson.

Experimentally, we search for deviations from the Standard Model couplings; thus the anomalous coupling parameters are defined as

$$\Delta g_1^Z \equiv g_1^Z - 1, \quad \Delta\kappa_\gamma \equiv \kappa_\gamma - 1, \quad \Delta\kappa_Z \equiv \kappa_Z - 1, \quad \lambda_\gamma, \quad \text{and} \quad \lambda_Z.$$

Note that electromagnetic gauge invariance requires $g_1^\gamma = 1$ or $\Delta g_1^\gamma = 0$.

With non-SM coupling parameters, the amplitudes for gauge boson pair production grow with energy, eventually violating tree-level unitarity. The unitarity violation is avoided by introducing an effective cutoff scale, Λ. For charged anomalous TGC's we have used dipole form factors with a cutoff scale Λ. The the anomalous couplings take a form, for example,

$$\Delta\kappa(\hat{s}) = \frac{\Delta\kappa}{(1+\hat{s}/\Lambda^2)^2},$$

where $\sqrt{\hat{s}}$ is the invariant mass of the vector-boson pair and $\Delta\kappa$ is the coupling value in the low energy limit. Λ is physically interpreted as the mass scale where the new phenomenon which is responsible for the anomalous couplings would be directly observable.

Direct tests of the trilinear couplings are provided by e^+e^- and hadron colliders through production of gauge boson pairs. The signature for anomalous trilinear couplings is an excess of gauge boson pairs, particularly for large values of the invariant mass of the gauge boson pair and for large values of gauge boson transverse momentum, p_T .

Studies of three different diboson final states, W^+W^-, $W^\pm Z$, and $W^\pm\gamma$ will provide complementary sensitivities to the charged anomalous TGC's [21]. For example, the $\Delta\kappa_V$ terms in W^+W^- production grow like $\hat{s}$, whereas these terms increase only like $\sqrt{\hat{s}}$ in $W^\pm Z$ and $W^\pm\gamma$ production. One therefore

expects W^+W^- production to be considerably more sensitive than $W^\pm Z$ and $W^\pm\gamma$ production to $\Delta\kappa_V$. On the other hand, $W^\pm Z$ production is expected to be more sensitive than W^+W^- to Δg_1^Z, because terms in Δg_1^Z are proportional to $\hat{s}$ in $W^\pm Z$ production. The λ-type anomalous couplings have a strong $\hat{s}$ dependence in all three cases, thus the sensitivities will be greatly enhanced at high center-of-mass energy at LHC.

Our studies of the anomalous coupling parameters have followed two scenarios as described below.

- The anomalous couplings are uncorrelated. When setting limits on one coupling, the other couplings are set to their Standard Model values. When setting limits in two-dimensional space, two coupling parameters vary independently while the others are fixed at their Standard Model values.
- There are correlations between the anomalous coupling parameters. Different relations are obtained by invoking global symmetry arguments, or by fine tuning anomalous WWV couplings such that the most serious unitarity-violating contributions to the tree-level vector-boson scattering amplitudes are avoided [25]. We list below some assumptions used in our studies. We find limits in two-dimensions, so in the cases where there are three free parameters one is fixed to it's Standard Model value.
  - The so-called HISZ scenario [26] has two free parameters:
    $\Delta g_1^Z = \Delta\kappa_Z/(\cos^2\theta_W - \sin^2\theta_W), \quad \Delta\kappa_\gamma = 2\Delta\kappa_Z\ \cos^2\theta_W/(\cos^2\theta_W - \sin^2\theta_W), \quad \lambda_Z = \lambda_\gamma.$
  - Assuming, $\Delta\kappa_Z = \Delta\kappa_\gamma, \quad \lambda_Z = \lambda_\gamma.$
    leaving three free parameters.
  - The LEP assumption,
    $\Delta\kappa_\gamma = (\cos^2\theta_W/\sin^2\theta_W)(\Delta g_1^Z - \Delta\kappa_Z), \quad \lambda_Z = \lambda_\gamma.$
    leaving also three free parameters.

2.3 Effective Lagrangian for neutral TGC's

In the Standard Model, neutral boson pairs, ZZ and $Z\gamma$, are produced at hadron colliders through the t-channel diagrams shown in Figure 1. The ZZZ and $ZZ\gamma$ triple gauge boson couplings, and hence the contribution of the s-channel diagram, are zero at tree level. However, anomalous ZZZ or $ZZ\gamma$ couplings may contribute via the s-channel diagram. In this note we consider the effect of anomalous couplings on the production of pairs of on-shell Z bosons only. In this case, the most general form of the $Z^\alpha(q_1)Z^\beta(q_2)V^\mu(P)$ $(V = Z,\ \gamma)$ vertex function which respects Lorentz invariance and electromagnetic gauge invariance may be written as [27]

$$g_{ZZV}\Gamma^{\alpha\beta\mu}_{ZZV} = e\frac{P^2 - M_V^2}{M_Z^2}[\, i f_4^V(P^\alpha g^{\mu\beta} + P^\beta g^{\mu\alpha}) + i f_5^V \varepsilon^{\mu\alpha\beta\rho}(q_1 - q_2)_\rho\,]$$

where M_Z is the Z-boson mass and e is the positive electron charge; q_1, q_2 and P are the 4-momenta of the two on-shell Z bosons and the s-channel propagator respectively. The effective Lagrangian generating the g_{ZZV} vertex function is

$$L = -\frac{e}{M_Z^2}[f_4^V(\partial_\mu V^{\mu\beta})Z_\alpha(\partial^\alpha Z_\beta) + f_5^V(\partial^\sigma V_{\sigma\mu})\tilde{Z}^{\mu\beta}Z_\beta],$$

where $V_{\mu\nu} = \partial_\mu V_\nu - \partial_\nu V_\mu$ and $\tilde{Z}^{\mu\beta} = \frac{1}{2}\varepsilon_{\mu\nu\rho\sigma}Z^{\rho\sigma}$. The couplings f_i^V $(i = 4,\ 5)$ are dimensionless complex functions of $q_1^2,\ q_2^2$ and P^2 and, as indicated above, are zero at tree level in the Standard Model. All couplings are C odd; CP invariance forbids f_4^V, while parity conservation requires that f_5^V vanishes.

Because f_4^Z and f_4^γ are *CP*-odd, contributions to the helicity amplitudes proportional to these couplings will not interfere with the Standard Model terms, and hence ZZ production is not sensitive to the sign of these couplings. The *CP* conserving couplings f_5^V contribute to the Standard Model cross section at the one-loop level, but this contribution is $\mathcal{O}(10^{-4})$ [28].

As in the case of charged TGC's, the ZZ production cross section with non-SM couplings grows with the parton center-of-mass energy $\sqrt{\hat{s}}$. In order to avoid unphysical results that would violate unitarity, we use a generalized dipole form factor:

$$f_i^V(\hat{s}) = \frac{f_i^V}{(1+\hat{s}/\Lambda^2)^n} \quad (i = 4,\ 5)$$

where Λ is the form factor scale which is related to the scale of new physics which is generating the anomalous ZZV couplings. Theoretical arguments require that n should be greater than $3/2$ in order to satisfy unitarity. In our note, we have used $n = 3$ and $\Lambda = 2$ TeV to evaluate the ATLAS sensitivities to anomalous neutral TGC's from the ZZ diboson final state studies.

The signature of anomalous couplings in ZZ production is an increase in the cross section at high values of Z-boson transverse momentum. In our investigation of the ATLAS sensitivity to anomalous couplings, we have considered only the the case where one coupling in non-zero.

2.4 The Monte Carlo Event Generators

We have used two NLO Monte Carlo event generators, *MC@NLO* and *BHO*, for diboson physics analysis. The program of *MC@NLO* interfacing to *HERWIG/JIMMY* has been used to generate the W^+W^-, $W^\pm Z^0$, Z^0Z^0 events. Those events are fully simulated with the ATLAS detector responses, the electronic digitization's, and with final event reconstructions. The *BHO* MC program has been used to study the ATLAS detection sensitivity to anomalous triple gauge couplings. We present here a very brief description of these two programs.

- *MC@NLO* (version 3.1) [18]
  This generator incorporates NLO QCD matrix elements into the parton shower by interfacing to *HERWIG/Jimmy* [29] programs. Hard emission are treated as in NLO computations and soft/collinear emission is treated as in regular parton-shower MC. The matching between these two regions is smooth. (no double counting). W-mass width and spin-spin correlations are included in the generator. However, 'zero-width' approximations are used in $W^\pm Z^0$ and Z^0Z^0 calculations, and no $Z^0/\gamma*$ interference terms are included in the calculations. This program doesn't include anomalous triple gauge boson couplings.

- *BHO* (by Baur, Han and Ohnmenus) [21]
  This is a numerical parton level MC generator. The calculated W^+W^-, $W^\pm Z^0$ and Z^0Z^0 production rates are accurate to *NLO* and consistent with the *MC@LNO* calculations (total cross sections agree to $\sim$ 2-3%). The *BHO* MC program can calculate both LO and NLO cross sections for all five diboson final states (W^+W^-, $W^\pm Z^0$, Z^0Z^0, $W^\pm\gamma$, $Z^0\gamma$). However, it doesn't include parton-shower automatically. It generates n-body final states for Born and virtual contributions, and (n+1)-body final states for real emissions. It includes anomalous triple gauge boson coupling parameters, thus it is the vital program for anomalous coupling sensitivity studies.

For $W^\pm\gamma$, $Z^0\gamma$ and Z^0Z^0 events we have used the LO MC generator *PYTHIA* (version 6.4) [20] for full simulations. In contrast to the *MC@NLO* program, *PYTHIA* program has implemented the vector boson masses with Breit-Wigners, and included $Z/\gamma*$ interference terms. For normalization of the LO predictions of event production rates, a k-factor correction is used from NLO calculations. The k-factor is defined as the cross section ratio, $d\sigma(NLO)/d\sigma(LO)$.

For $gg \rightarrow W^+W^-$ events simulation we have used *gg2ww* MC generator (version 2.4) [23] interfacing to *HERWIG* and *JIMMY* programs for parton shower (hadronization) and pp collision underlying events.

2.5 Two approaches to study the anomalous couplings

To overcome the lack of anomalous couplings in the standard ATLAS MC generators, and to avoid full simulations of all the MC events with possible couplings, two approaches are used in our analysis to probe the anomalous TGC's:

- **Re-weighting the fully simulated events**
  - Generate and fully simulate the diboson events with SM couplings using the *MC@NLO* program. Event acceptances are determined by the fully simulated events.
  - Re-weight each fully simulated events. The weights are produced in anomalous coupling space according to parton level kinematics using the *BHO* program.
  - The theoretical 'expectations' (the vector boson P_T or diboson mass spectra), including those with non-SM coupling parameters are calculated by using fully simulated events, which pass the event selection criteria.
  - The SM 'mock data' are produced by MC experiments by simulating and selecting the diboson events.
  - Binned likelihood method is used to extract the sensitivities to the anomalous TGC's.
- **Fast simulation**
  - Generate and fully simulate the diboson events with SM couplings using the *MC@NLO* program.
  - Using Fast-Simulation (*ATLFAST* [30]) program to simulate the NLO MC events with anomalous couplings by *BHO* program.
  - Correcting the fast simulation (with *BHO*) by comparing with the full simulation (with *MC@NLO*) to determine the acceptance vs. the anomalous couplings.
  - Based on the 'mock data' with the SM couplings, to extract the sensitivities to the anomalous TGC's.

Detail techniques used to determine the 95% C.L. intervals for the anomalous couplings are given in the appendix of this note.

3 Review of Tevatron diboson measurements

In this section we present a brief review of measurements of diboson production at the Tevatron. The purpose is to establish the general status of the field, and to summarize those experimental issues relevant to the ATLAS diboson physics program.

3.1 Overview of measurements

The CDF and D0 experiments have recorded about 2 fb^{-1} of integrated $p\bar{p}$ luminosity as of August 2007. Recent measurements of most diboson channels are based upon about 1 fb^{-1} of data. A detailed review of these results is not appropriate here. What we have chosen to do is present representative measurements from the CDF or D0 experiments with statistics based upon 1.0 fb^{-1} integrated luminosity where available. The goal is to establish the general level of the statistics for Tevatron diboson signals, to characterize the dominant backgrounds encountered, and to establish the precision of the measurements.

Representative measurements in diboson channels are presented in Tables 2 to 6. These are limited to cases where the W/Z bosons are detected by e/μ decay modes. In addition to the measurement statistics, the backgrounds and their dominant sources are summarized. The cross sections quoted are as usual for a Standard Model interpretation of the decay phase space and branching ratios. As shown in the Tables, there is good agreement between the measured cross sections and theory predictions based upon NLO matrix element calculations.

For the WW and WZ channels the signals are at the level of tens of events, with a significant signal just starting to appear in the ZZ channel. The Wγ and Zγ channels are measured with photon E_T >7 GeV and $\Delta R(l\gamma) > 0.7$. With these cuts the statistics are on the order of a thousand events for each of the Wγ and Zγ channels with 1 fb^{-1} of data. The events of most interest are those without final state radiation. These can be selected by cuts on $M(l^+l^-\gamma) > 100$ GeV/c^2 and $M_T(l\nu\gamma) > 90$ GeV/c^2. With these selection the statistics in each of the Wγ and Zγ channels are on the order of a few hundred events.

The Tevatron diboson measurements have been used to improve on some of the anomalous gauge coupling limits made at LEP (hep-ex/0612034). By using measurements of $p\bar{p} \rightarrow W^{\pm}\gamma$ and $W^{\pm}$Z the WWγ and WWZ couplings can be separately studied. Deviations of the couplings from their SM values are usually parameterized with a dipole form factor to preserve tree-level unitarity at high energies. For example for the WWγ couplings: $\Delta\kappa_\gamma(\hat{s}) = \Delta\kappa_\gamma/(1+\hat{s}/\Lambda^2)^2$ and $\lambda_\gamma(\hat{s}) = \lambda_\gamma/(1+\hat{s}/\Lambda^2)^2$ where $\sqrt{\hat{s}}$ is the Wγ invariant mass and Λ sets the energy scale of new physics. For the limits on anomalous TGC's we use the convention of quoting 1D 95% confidence limits on one parameter with the others set to their Standard Model values.

The limits set from CDF and D0 measurements of the WWγ and WWZ TGC's are summarized in Table 7. The last two lines in the Table are limits obtained from the W^+W^- channel under the assumption that $\Delta\kappa_\gamma = \Delta\kappa_z$ and $\lambda_\gamma = \lambda_z$. Based upon the current data sets, the general picture is that the limits on $|\Delta\kappa|$ and $|\lambda|$ are on the order of 0.2. These limits will improve significantly by combing the constraints from the $W\gamma$, WZ and W^+W^- channels, and increasing the data sets using the 5 fb^{-1} expected at the Tevatron.

The current Tevatron studies of the Z Zγ and Z$\gamma\gamma$ couplings come from D0's measurements of Zγ production. Table 8 shows the limits for the CP conserving anomalous coupling parameters h_3 and h_4 using 1.0 fb^{-1} of data.

Tevatron diboson measurements in some channels are already limited by systematic uncertainties in lepton/photon identification efficiencies and backgrounds. We discuss below techniques used for these measurements at the Tevatron and their systematic limitations.

Table 2: $p\bar{p} \to W^+W^-$ (e e, $\mu\mu$, e μ)

Data = 95 events from CDF with 0.83 fb^{-1} Background = 38 $\pm$5 events distributed as (DY 30%, W+jets 30% other 40%) σ(data) = 13.6 $\pm$ 2.3 (stat) $\pm$ 1.6 (sys) $\pm$ 1.2 (lum) pb
Data = 25 events from D0 with 0.25 fb^{-1} Background = 8.1 $\pm$0.5 events distributed as (DY 30%, W+jets 50% other 20%) σ(data) = 13.8 $\pm$ 4.1 (stat) $\pm$ 1.1 (sys) $\pm$ 0.9 (lum) pb
σ(SM) = 12.4 $\pm$ 0.8 pb

Table 3: $p\bar{p} \to W^{\pm}Z$ ($l^{\pm}$ ν l^+ l^-)

Data = 25 events from CDF with 1.9 fb^{-1} Background = 5 $\pm$0.5 events distributed as (Z+jets/γ 50%, ZZ 30% other 20%) σ(data) = 4.3 $\pm$ 1.3 (stat) $\pm$ 0.2 (sys) $\pm$ 0.3 (lum) pb
Data = 13 events from D0 with 1.0 fb^{-1} Background = 4.5 $\pm$0.6 events distributed as (Z+jets/γ 60%, ZZ 20% other 20%) σ(data) = 2.7 + 1.7 - 1.3 pb
σ(SM) = 3.7 $\pm$ 0.3 pb

Table 4: $p\bar{p} \to Z\gamma$ (l^+ l^- γ)

Data = 968 events from D0 with 1.0 fb^{-1} Background = 117 $\pm$ 12 events (Z+jets 100%) σ(data) = 4.96 $\pm$ 0.30 (stat + sys) $\pm$ 0.30 (lum) pb σ(SM) = 4.7 $\pm$ 0.2 pb
Data = 72 events from CDF with 0.20 fb^{-1} Background = 4.9 $\pm$ 1.1 events (Z+jets 100%) σ(data) = 4.6 $\pm$ 0.60 (stat + sys) $\pm$ 0.30 (lum) pb σ(SM) = 4.5 $\pm$ 0.3 pb

Table 5: $p\bar{p} \rightarrow W\gamma$ ($l^{\pm}$ γ)

Data = 323 events from CDF with 0.20 fb^{-1}
Background = 114 $\pm$ 21 events (W+jets 100%)
σ(data) = 18.1 $\pm$ 3.1 (stat + sys) $\pm$ 1.2 (lum) pb
σ(SM) = 19.3 $\pm$ 1.4 pb
Data = 273 events from CDF with 0.16 fb^{-1}
Background = 132 $\pm$ 7 events (W+jets 100%)
σ(data) = 14.8 $\pm$ 1.9 (stat + sys) $\pm$ 1.0 (lum) pb
σ(SM) = 16.0 $\pm$ 0.4 pb

Table 6: $p\bar{p} \rightarrow ZZ$ (l^+ l^- l^+ l^-)

Data = 1 events from CDF with 1.5 fb^{-1}
Background = 0.03 events (100% Z+jets)
σ(data) = 0.75 $\pm$ 0.6 (stat + sys) $\pm$ .05 (lum) pb
Data = 1 events from D0 with 1.0 fb^{-1}
Background = 0.17 events (100% Z+jets)
σ(data) $<$ 4.3 pb
σ(SM) = 1.5 $\pm$ 0.2 pb

Table 7: Anomalous gauge coupling limits for WWγ and WWZ

Coupling	limits at 95% C.L.	Λ TeV	Data Source
WWγ from $W^{\pm}\gamma$	-0.88 $< \Delta\kappa_\gamma <$ 0.96	2 TeV	D0 with 0.16 fb^{-1}
	-0.20 $< \lambda_\gamma <$ 0.20		
WWZ from $W^{\pm}$Z	-0.12 $< \Delta\kappa_z <$ 0.29	2 TeV	D0 with 1.0 fb^{-1}
	-0.17 $< \lambda_z <$ 0.21		
	-0.82 $< \Delta\kappa_z <$ 1.27	2 TeV	CDF with 1.9 fb^{-1}
	-0.13 $< \lambda_z <$ 0.14		
WWZ = WWγ	-0.36 $< \Delta\kappa <$ 0.33	1.5 TeV	D0 with 0.25 fb^{-1}
from W^+W^-	-0.31 $< \lambda <$ 0.33		

Table 8: Anomalous gauge coupling limits for ZZγ and Z$\gamma\gamma$

Coupling	limits at 95% C.L.	Λ TeV	Data source
ZZγ	$\lvert h_3^\gamma \rvert <$ 0.085	1.2 TeV	D0 1.0 fb^{-1}
	$\lvert h_4^\gamma \rvert <$ 0.0054		
ZZZ	$\lvert h_3^Z \rvert <$ 0.082	1.2 TeV	
	$\lvert h_4^Z \rvert <$ 0.0054		

3.1.1 Measuring lepton and photon efficiencies from data

Electron and muon ID efficiencies at the transverse momenta (p_T) relevant for W and Z boson decay are measured reliably using leptons from Z boson decay. At the Tevatron, high-statistics samples of Z boson decays can typically be triggered and identified using only one of the two decay leptons. This leaves the second lepton unbiased from the point of view of trigger and offline identification. The rate at which the unbiased lepton passes the trigger and ID requirements provides a measurement of the respective efficiencies. The measurement can be performed as a function of p_T, though for $p_T > 60$ GeV it tends to be statistics-limited. Fortunately, the efficiencies at high p_T tend to be close to 100% and weakly p_T-dependent.

The lepton efficiency measurement may need to be corrected for the backgrounds present in the loosely-identified base sample of Z bosons. The background fraction can be measured using a similarly selected sample of like-sign leptons, and assuming that backgrounds due to mis-identified leptons are equally likely to produce pairs of like-sign and opposite-sign leptons. Another method used to measure mis-identification background in the Z boson sample is to constrain the mass distribution of the background using a background-dominated sample selected with the inverse of the lepton ID cuts. The mass distribution of the Z boson candidate sample is then fit with a sum of a simulated signal lineshape and the background shape. The background normalization is constrained by the sidebands of the Z boson mass peak.

Photon efficiency measurement is more difficult to perform, since pure high-statistics samples of photons are not as readily available as leptons. Various techniques have been employed. One method exploits the similarity between the electromagnetic calorimeter showers produced by electrons and photons. The electrons from Z boson decays are used to mimic high-p_T photons, and the photon ID cuts are emulated for electrons and their efficiency measured on the electron sample. The presence of the electron track is accounted for. To correct for any bias due to differences between electrons and photons, a detailed detector simulation has sometimes been employed. The simulation is validated and tuned using the electron efficiency measurements.

A second method for measuring photon ID efficiency has become available as the the statistics of the data have increased. The sample of $Z\gamma$ events has become sufficiently large that the final-state radiation (FSR) sub-sample (photon radiated off a decay lepton) provides a quasi-pure sample of unbiased photons for efficiency measurement. The FSR sample is selected kinematically by requiring that the $ll\gamma$ three-body invariant mass lies in the Z boson mass peak. Corrections for the mis-identified photon background can be made using the like-sign dilepton + photon sample, the anti-lepton + photon sample or the events in the mass sideband region.

Using these techniques, lepton and photon ID efficiencies have been measured with uncertainties of about 1%. Typically the lepton ID efficiencies are about 90% and photon ID efficiencies are about 80%.

3.1.2 Measuring backgrounds from data

As indicated in a previous section, the dominant backgrounds to be determined from the data are those due to W+jets and Z+jets events, where the jet(s) are misidentified as lepton(s) (in the case of WW, WZ and ZZ measurements in leptonic final states) or a jet is mis-identified as a photon (in the case of the $W\gamma$ and $Z\gamma$ measurements with the leptonic decay of the boson).

The technique used to determine these backgrounds is to weight the appropriate base sample containing jets by the mis-identification rate of a jet or jets. The boson + 1 jet and boson + 2 jets samples are selected from the data, using the signal selection cuts for the boson identification and requiring additional jets in the applicable kinematic and fiducial region.

Fake rates for leptons are determined from QCD jet samples. In order to avoid a trigger bias, the candidate jet is either required to have p_T sufficiently larger than the trigger threshold, or is required to

be a sub-leading jet (and therefore a non-trigger jet) in the event. The rate at which candidate jets also pass the lepton ID cuts is measured as a function of jet p_T and jet pseudo-rapidity. The jet-to-lepton fake rate tends to be about 10^{-3} in the central rapidity region and can increase to $\sim 10^{-2}$ in the forward rapidity region, depending on the selection cuts in the forward region.

The lepton fake rate can have a systematic uncertainty of a factor of $1.5-2$, since the fake rate can vary significantly due to quark vs gluon differences, and due to the semileptonic decays of heavy flavor and the variation of heavy flavor content. The dependence of the fake rate on the number of jets in the event and the p_T-ranking of the jet gives a measure of these systematic variations.

The measurement of the jet-to-photon fake rate follows the same procedure above, with an additional caveat. The candidate jet sample contains a significant contamination of prompt photons, which bias the fake rate to higher values. Therefore the prompt photon fraction of the candidate jet sample has to be measured from the data, and used to correct the observed jet-to-photon faking probability. The measurement of the prompt photon fraction is performed on a statistical basis using the differences in characteristics of fake and prompt photons. Most fake photons originate from hard fragmentation of jets to a leading π^0. At low p_T, the two photons from the π^0 are sufficiently separated in the electromagnetic calorimeter to have a discernably wider transverse shower profile compared to single prompt photons. Prompt photons also tend to be more isolated in energy. At higher p_T, the photons from π^0 decay merge and other means of statistical separation are employed. The calorimeter preshower detector is used to detect the photon conversion signal. Knowing the number of radiation lengths of passive material in front of the preshower, the conversion probability of single prompt photons and the $\pi^0 \to \gamma\gamma$ pair is calculated, the latter probability being higher. A variant of the second method employs the fact that prompt photons tend to have a deeper longitudinal shower profile in the electromagnetic calorimeter than the fake photons. These differences provides the ability to count the total number of prompt and fake photons. The measured prompt photon fraction increases from $\sim 20\%$ at low p_T to over 80% at high p_T, which makes the true fake rate more difficult to measure at high p_T. In the central rapidity region, where the full complement of photon ID cuts can be applied, the corrected photon fake rate varies between 10^{-4} and 10^{-3}, with a systematic uncertainty of order $\times 2$.

4 W^+W^- production and the $W^+W^-Z^0$ and $W^+W^-\gamma$ couplings

The measurement of the W^+W^- production cross section at the LHC will provide an important test of the Standard Model through the study of the charged triple gauge boson couplings, which are a consequence of the non-abelian structure of the gauge symmetry group, $SU(2)_L \times U(1)_Y$ of the SM [31]. The W^+W^- events produced through the SM process at the LHC are an irreducible background to the Higgs discovery principal signature proceeding through the W^+W^- final state. Understanding the SM W^+W^- production and ATLAS detection sensitivity to W-pair events is crucial to the Higgs search program at the LHC.

The dominant WW production mechanism at the LHC is shown in Figure 2 by the leading-order Feynman diagrams through the quark-antiquark initial state.

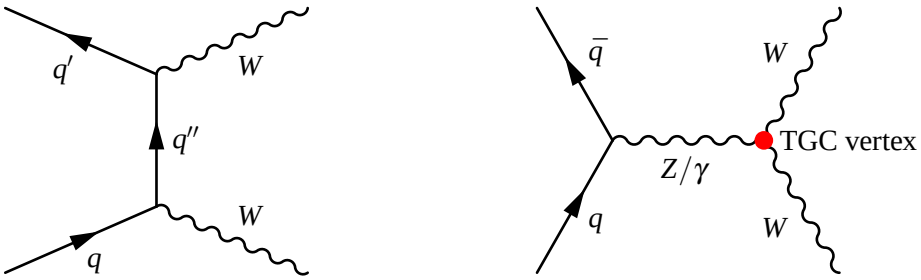

Figure 2: The Standard Model Tree-level Feynman diagrams for WW production through the $q\bar{q}$ initial state in hadron colliders. The s-channel diagram, on the right, contains the WWZ and $WW\gamma$ trilinear gauge boson coupling (TGC) vertex in which we are interested.

4.1 W^+W^- signal and background at the LHC

4.1.1 Production mechanism and cross sections

The $s-$channel diagram in Figure 2 gives us experimental access to the WWZ and $WW\gamma$ triple gauge boson couplings. Anomalous couplings could results in an enhanced rate of the W-pair production, mainly in the high p_T region of the vector boson or high mass region of the W-pair distributions.

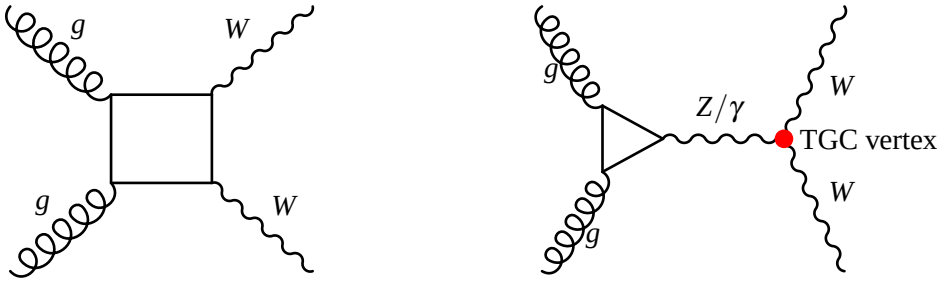

Figure 3: The Standard Model Feynman diagrams for WW production through gluon-gluon fusion in hadron colliders. Please note that the Z-exchange triangle diagrams cancel when summed over 'massless' up- and down-type contributions.

Another non-negligible production mechanism of the WW production at the LHC is gluon-gluon fusion. The Feynman diagrams are shown in Figure 3. This process contributes an additional $\sim 5\%$ event rate to the total WW production.

Theoretical calculations of the W^+W^- production cross section for the quark and the gluon scattering contributions to $pp \to W^+W^- \to e^+\nu e^-\nu$ are given in Table 9. We list the cross sections calculated

Table 9: Production cross section for the process of $pp \to WW \to e\nu e\nu$ at the LHC ($\sqrt{s} = 14$ TeV). *CTEQ6M* PDF and W decay branching ratio, $Br(W \to e\nu) = 0.108$ are used in the calculations.

Process	cross section (fb), LO	cross section (fb), NLO	MC program
$q\bar{q} \to WW \to e\nu e\nu$	841±42	1304±65	*MCFM* (v5.2)
$q\bar{q} \to WW \to e\nu e\nu$	–	1302±65	*MC@NLO* (v3.1)
$gg \to WW \to e\nu e\nu$	60±3	–	*gg2ww* (v2.4)

by using the *MC@LNO*(v3.1), *MCFM*(v5.2), and *gg2ww*(v2.4) generators, and the *CTEQ6M* parton-density-function set. A W leptonic decay branching ratio, $Br(W \to e\nu) = 0.108$ is also used. The NLO calculations agree well by using two different programs. We quote 5% uncertainties on the cross sections. The major contributions of the uncertainties come from the PDF and scaling values used in the calculations.

4.1.2 Experimental signals and major background

We focus our studies on the pure leptonic decay modes of the W-pair: $W^+W^- \to \ell^+\nu + \ell^-\nu$, $(\ell = e,\ \mu)$. The total branching ratio for two lepton flavors in final states is 4.32%. The experimental W^-W^- signature in this case is two high P_T leptons with opposite charge associated with large missing transverse energy, $\not\!\!E_T$, in final states. The other contributions to this final state are considered as the background for $W^+W^- \to \ell^+\ell^- + \not\!\!E_T$ detection. Major background contributions are from the following process:

- $t\bar{t} \to W^+bW^-b \to \ell^+\ell^- + X$, where the final states contain the basic W^+W^- signature plus an additional two b-jets. This background can be highly suppressed by rejecting events with large jet energies.
- $Z + jets$ and $W + jets$, where mis-identified leptons are the major sources of background.
- Drell-Yan ($Z/\gamma \to \ell^+\ell^-$ and $W^\pm \to \ell^\pm\nu$), where miss-measured missing-transverse-energy would fake the W^+W^- signature.
- $W\gamma$ and $Z\gamma$, where a γ mis-identified as an electron mimics the signal.
- WZ and ZZ, where mis-detected leptons fake missing E_T, thus mimicking the W^+W^- signal.

Many of the background processes listed above have much higher cross sections at the LHC than the W^+W^-. In order to establish the ATLAS detection sensitivity of the W^+W^- events, we have generally included large fully simulated MC background samples in our studies.

Studies of $W^+W^- \to \ell\tau + X$, $(\ell = e,\ \mu,\ \tau)$ are more complicated than pure electron or muon decay channels due to the short life-time and rich decay modes of the tau-leptons. In this note, we simply treat the W tau decay events as background.

4.2 Analysis methods and MC datasets

Two independent analyses were conducted by the Michigan and Belgrade groups. The former is based on the CBNT(Combined Ntuple) [1] datasets (listed in Table 10 and Table 12). The latter analysis is based the *AOD* (ATLAS-Object-Data) based HighPtView [1] ntuples (listed in Table 11). Basic performance of the ATLAS detector simulations, trigger simulations and reconstruction efficiencies are cross-checked in detail, and found to be consistent for both analyses. The event selection strategies and methods are complementary in the two analyses. The Belgrade group employed a straight cuts method while the

Table 10: Monte Carlo WW *signal* datasets used in the WW analysis. Cross sections are obtained from MC generators, *MC@NLO*, and *gg2ww*. We have used the decay branching ratio, $Br(W \to e\nu) = 0.108$. All the $q\bar{q}' \to WW$ datasets were produced with ATLAS software release 12.0.6.4. $gg \to WW$ event samples were produced using *gg2ww* interfacing to $Herwig/Jimmy$ program using ATLAS software version 12.0.6.5.

Process	cross section (fb)	Number of events	filter efficiency	dataset number
$q\bar{q}' \to WW \to e^+\nu e^-\nu$	1302	20,000	1.0	5921
$q\bar{q}' \to WW \to \mu^+\nu\mu^-\nu$	1302	20,000	1.0	5924
$q\bar{q}' \to WW \to e^\pm\nu\mu^\mp\nu$	2604	40,000	1.0	5925, 5922
$q\bar{q}' \to WW \to \tau^+\nu\tau^-\nu$	1302	20,000	1.0	5927
$q\bar{q}' \to WW \to e^\pm\nu\tau^\mp\nu$	2604	40,000	1.0	5928, 5923
$q\bar{q}' \to WW \to \mu^\pm\nu\tau^\mp\nu$	2604	40,000	1.0	5926, 5929
$gg \to WW \to e^+\nu e^-\nu$	60.0	20,000	0.96	2821
$gg \to WW \to \mu^+\nu\mu^-\nu$	60.0	20,000	0.96	2824
$gg \to WW \to e^\pm\nu\mu^\mp\nu$	120.0	20,000	0.96	2822, 2828

Michigan group used both straight cuts and $Boosted-Decision-Trees$ technique. In this note we provide a detailed description of the analysis with straight cuts by Belgrade group and the analysis with $Boosted-Decision-Trees$ by the Michigan group. For cross-check purposes, we also provide Michigan's analysis results using the straight-cuts method in the appendix.

Table 10 lists the ATLAS CSC program produced W^+W^- MC data-sets. The production through $q\bar{q}'$ is generated using the $MC@NLO(v3.1)$ program (interfaced to $HERWIG/JIMMY$ for hadronization and underlying events), and the $gg \to W^+W^-$ is generated using the $gg2WW(v2.4)$ program. Sub-processes, cross sections and number of events produced are given in the table. If a pre-filter is used, the filter-efficiency is also given. Final results of this CSC note have used CSC samples produced with software release version 12.0.6.4. The CSC *AOD* MC datasets used in W^+W^- event selections are listed in Table 11. It shows relevant information for the used process, ATLAS MC CSC dataset numbers, cross sections, generator filters (summary of cuts applied at the generator level), filters efficiencies, K-factor for LO cross section corrections, the number of analyzed events and the equivalent integrated luminosities in fb^{-1} . One should notice that the $W + jets$ and $Z + jets$ samples are not listed in Table 11 for the AOD based analysis, this is because no events from over 1.1 Million $Z/W + jets$ MC events have been selected into our final sample. Since the cross sections of the $W/Z + jets$ are very large, potentially, those events could contaminate the WW signature. Based on Tevatron experience and the WW analysis based on $CBNT$ datasets, which has used about 20 Million $Z/W + jets$ events, we estimate that the $W/Z + jets$ processes could contribute additional 10-15% background. We list in Table 12 the $CBNT$ MC background datasets used in the W^+W^- analysis. This table gives the physics final states from the pp-collisions; the CSC MC production dataset ID's; the total cross sections (for $\sqrt{s}$ = 14 TeV); the ratio, K, which is defined as σ_{NLO}/σ_{MC}; and the decay branching ratio for the corresponding MC final states. The last column gives the total simulated MC events in each process. All the processes in the list are forced W and Z leptonic delays.

4.3 Physics objects reconstruction and lepton ID efficiencies

The major physics objects used in $W^+W^- \to \ell^+\nu\ell^-\nu$ analysis are electrons, muons, missing E_T ($\not\!\!E_T$), and hadronic jets. We describe briefly the object reconstruction and identification process using the MC datasets produced by the ATLAS software programs, $ATHENA$ [1].

Table 11: The *AOD* Data-sets (v12.0.6.) used in W^+W^- analysis.

Dataset ID	Process	σ (pb)	Generator Cuts	Filter Eff.	K	Number of events	L fb^{-1}
5921	$WW \to ee$	1.30		1	1	19900	15.3
5924	$WW \to \mu\mu$	1.30		1	1	17250	13.3
5922/25	$WW \to e\mu$	2.60		1	1	39850	15.3
5923/28	$WW \to e\tau$	2.60		1	1	39750	15.3
5926/29	$WW \to \mu\tau$	2.60		1	1	40000	15.4
5927	$WW \to \tau\tau$	1.30		1	1	19950	15.3
5200	$t\bar{t}$	833	no all hadronic channels	0.54	1	567600	1.3
5144	$Z/\gamma^* \to ee$	1656	$M_{ee} > 60$ GeV $1e$ $p_T > 10$ GeV, $\|\eta\| < 2.7$	0.86	1.22	670000	0.47
5145	$Z/\gamma^* \to \mu\mu$	1656	$M_{\mu\mu} > 60$ GeV 1μ $p_T > 10$ GeV, $\|\eta\| < 2.7$	0.88	1.22	199850	0.14
5146	$Z/\gamma^* \to \tau\tau$	1656	$M_{\tau\tau} > 60$ GeV $1e$ or 1μ $p_T > 5$ GeV, $\|\eta\| < 2.7$	0.047	1.22	175500	2.2
5941	$W^+Z \to l\nu ll$	29.4	e or μ	0.015	1	49700	112.7
5971	$W^-Z \to l\nu ll$	18.4	e or μ	0.015	1	49750	180.2
5981	$ZZ \to ll\nu\nu$	0.33	2e, (2μ) $p_T > 5$GeV,$\|\eta\| < 2.7$	0.67	1.2	7950	36.0

4.3.1 Electron identification and selection efficiency

Electrons are reconstructed and identified with the *'egamma'* identification algorithm. An electron candidate must satisfy the quality criteria [1] and kinematic cuts. Quality criteria comprise calorimeter and track quality cuts, as well as spatial matching and an E/p (energy/momentum) cut. If an identification cut is not passed, then a bit is set in a 32-bit variable, called the **IsEM** flag (IsEM = 0 means that all cuts are passed, while IsEM&bitmask = 0 means that only certain parts of the identification criteria are passed [1]). Here we use IsEM &0×7FF= 0, meaning that all the cuts but the TRT are passed. The rapidity coverage for electron identification is $|\eta| < 2.5$. Also, the electrons in the two barrel/endcap transition regions $1.35 < |\eta| < 1.57$ are excluded.

It is also required that electrons are isolated. The requirement helps to discriminate the electrons from WW decays from electrons in processes having a large hadron activity (such as $t\bar{t}$). This is illustrated in Fig. 4 where the distributions of the E_T in a cone of $\Delta R = 0.45$ around the electron candidates are presented for WW, $t\bar{t}$ and Drell-Yan processes. An electron candidate is considered isolated if the transverse energy E_T deposited in a cone $\Delta R = \sqrt{\eta^2 + \phi^2}$ of radius 0.45 around the candidate is less than 8 GeV.

Figure 5 shows the identification efficiency for isolated electrons as a function of p_T (left plot) and η (right plot). This efficiency is calculated as a fraction of true electrons, within (p_T, η) acceptance, having a good match ($\Delta R < 0.02$) with reconstructed ones. There is a drop of the efficiency in low p_T region, and a slow decrease in high p_T region. The latter is stronger if the isolation criterion is tighter (i.e. $E_T < 5$ GeV for $\Delta R = 0.45$). The η dependence shows that electron efficiency is lower in endcap regions. The averaged reconstruction efficiency for such an electron, is (64.1 ± 0.3)% i.e. 68.6% before isolation.

Table 12: MC background samples for WW analysis. The first column indicates the physics final states from the pp-collisions. The second column gives the ATLAS MC production dataset IDs. The third collage gives the total cross section ($\sqrt{s}$ = 14 TeV). The fourth column gives the ratio, K which is defined as σ_{NLO}/σ_{MC}. If the MC cross section is given based on NLO calculations, the K equals 1, otherwise, it is the ratio of σ_{NLO}/σ_{LO}. All the processes in the list are forced W and Z leptonic delays. The fifth column gives the decay branching ratio for the corresponding MC final states. The last column gives the total simulated MC events in each process. $t\bar{t}$, $W^{\pm}Z$ and ZZ were produced with software release version 12.0.6.4, the rest samples were produced using version 11.0.42.

Process	dataset #	σ_{Total} (fb)	K	MC Br	N_{mc}
$W^+Z \to \ell^+\nu\ell^+\ell^-$	5941	0.2940E+05	1.0	0.0144	27000
$W^-Z \to \ell^-\nu\ell^+\ell^-$	5971	0.1840E+05	1.0	0.0144	17700
$t\bar{t} \to \ell + X$	5200	0.8330E+06	1.0	0.5550	688400
$ZZ \to \ell^+\ell^-\ell^+\ell^-$	5931	0.1480E+05	1.0	0.0045	36400
Drell-Yan$(\ell^+\ell^1)(30\text{ GeV} < M < 81\text{ GeV})$	4295	0.4220E+07	1.3	0.1010	599000
Drell-Yan$(\ell^+\ell^-)(81\text{ GeV} < M < 100\text{ GeV})$	4296	0.4610E+08	1.3	0.1010	499000
Drell-Yan$(\ell^+\ell^-)(M > 100\text{ GeV})$	4297	0.1750E+07	1.3	0.1010	493000
$W \to e\nu$	4281	0.1580E+09	1.3	0.1072	2494958
$W \to \mu\nu$	4280	0.1580E+09	1.3	0.1072	1998396
$W \to \tau\nu$	4282	0.1580E+09	1.3	0.1072	2493808
$W + JET\ (E_T^j : 10-20\text{ GeV})$	4285	0.4350E+08	1.3	0.3216	400000
$W + JET\ (E_T^j : 20-40\text{ GeV})$	4286	0.2680E+08	1.3	0.3216	303000
$W + JET\ (E_T^j : 40-80\text{ GeV})$	4287	0.1180E+08	1.3	0.3216	300000
$W + JET\ (E_T^j : 80-120\text{ GeV})$	4288	0.2160E+07	1.3	0.3216	299000
$W + JET\ (E_T^j > 120\ \text{GeV})$	4289	0.9080E+06	1.3	0.3216	296000
$Z(ee) + JET\ (E_T^j : 10-20\text{ GeV})$	4270	0.1360E+08	1.3	0.0336	597281
$Z(ee) + JET\ (E_T^j : 20-40\text{ GeV})$	4271	0.8670E+07	1.3	0.0336	398697
$Z(ee) + JET\ (E_T^j : 40-80\text{ GeV})$	4272	0.4120E+07	1.3	0.0336	397524
$Z(ee) + JET\ (E_T^j : 80-120\text{ GeV})$	4273	0.8270E+06	1.3	0.0336	397009
$Z(ee) + JET\ (E_T^j > 120\text{ GeV})$	4274	0.3830E+06	1.3	0.0336	198652
$Z(\mu\mu) + JET\ (E_T^j : 10-20\text{ GeV})$	4290	0.1360E+08	1.3	0.0336	597413
$Z(\mu\mu) + JET\ (E_T^j : 20-40\text{ GeV})$	4291	0.8670E+07	1.3	0.0336	396793
$Z(\mu\mu) + JET\ (E_T^j : 40-80\text{ GeV})$	4292	0.4120E+07	1.3	0.0336	776793
$Z(\mu\mu) + JET\ (E_T^j : 80-120\text{ GeV})$	4293	0.8270E+06	1.3	0.0336	396856
$Z(\mu\mu) + JET\ (E_T^j > 120\text{ GeV})$	4294	0.3830E+06	1.3	0.0336	194832
$Z(\tau\tau) + JET\ (E_T^j : 10-20\text{ GeV})$	4275	0.1360E+08	1.3	0.0336	598783
$Z(\tau\tau) + JET\ (E_T^j : 20-40\text{ GeV})$	4276	0.8670E+07	1.3	0.0336	399076
$Z(\tau\tau) + JET\ (E_T^j : 40-80\text{ GeV})$	4277	0.4120E+07	1.3	0.0336	398972
$Z(\tau\tau) + JET\ (E_T^j : 80-120\text{ GeV})$	4278	0.8270E+06	1.3	0.0336	396671
$Z(\tau\tau) + JET\ (E_T^j > 120\text{ GeV})$	4279	0.3830E+06	1.3	0.0336	199046
$W(\ell\nu)\gamma$	4195	0.1420E+07	2.5	0.2144	1996438
$W(\tau\nu)\gamma$	4198	0.1420E+07	2.5	0.1072	687999
$Z(\ell\ell)\gamma$	4190	0.8910E+06	1.3	0.0672	149742

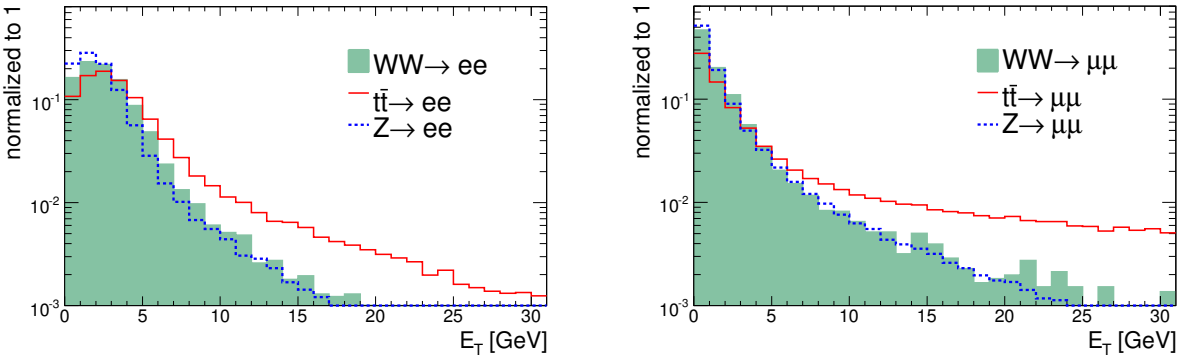

Figure 4: Transverse energy deposited in a cone $\Delta R = 0.45$ around the electrons (*left*) and muons (*right*).

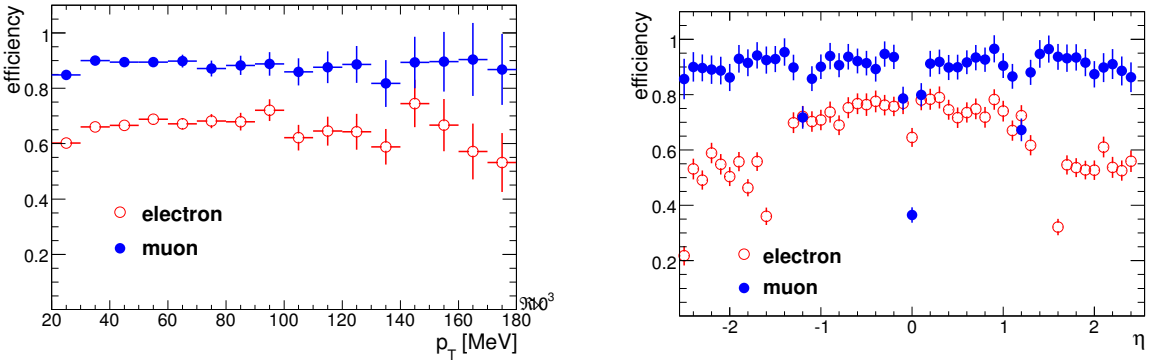

Figure 5: Electron and muon reconstruction efficiencies as a function of p_T (*left*) and η (*right*).

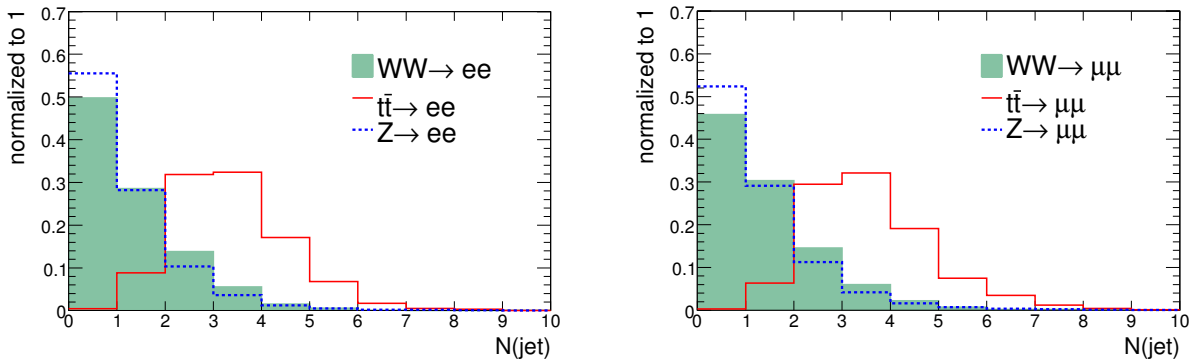

Figure 6: Jet multiplicity distribution in WW, $t\bar{t}$ and Z/γ leptonic decay processes. Jets are reconstructed with an 0.7 cone, $|\eta| < 3$, and $E_T > 20$ GeV.

4.3.2 Muon reconstruction and identification efficiency

Muons are identified and reconstructed with the **staco** algorithm [1]. **Staco** associates a track found in the Muon Spectrometer with the corresponding Inner Detector track, and takes proper corrections for energy loss in calorimeter. The combined muon detection rapidity coverage is $|\eta| < 2.5$. Minimum P_T of reconstructed muon track is 5 GeV. The muon is considered to be isolated if the transverse energy, in a cone $\Delta R < 0.45$, is less than 5 GeV. A tighter isolation criterion compared to the electron is used, since the E_T distribution in a cone $\Delta R = 0.45$ around the muon candidate is narrower than for electron candidate as illustrated in Fig.4. The muon reconstruction efficiencies as a function of p_T and η are shown in Fig. 5 (black circles). In contrast to electrons, no dependence on the muon p_T is observed. The cracks at $\eta = 0$ and the barrel-endcap transition region ($1.0 < |\eta| < 1.4$) are visible. The averaged reconstruction efficiency for such a muon, is (88.3 ± 0.2)% and 94.9 % before the isolation cut. Muons have a much higher reconstruction and identification efficiency than electrons.

4.3.3 Jets

The jets are reconstructed using the fixed-cone jet algorithm [1]. The cone size used in this analysis is 0.7. Additionally $E_T^{jet} > 20$ GeV and $|\eta| < 3$ is required. In ATLAS Athena software release 12.0.4 (and higher) the jet seed threshold on the transverse energy in a tower is set to $E_s = 1$ GeV, and the final energy cut on a jet is $E_t > 7$ GeV. With this cut the minimum measurable jet E_t should be 20 GeV [1]. In spite of this, we used $p_T^{jet} > 20$ GeV, since minimum measurable E_T is important for an efficient $t\bar{t}$ suppression when applying jet veto. The power of the jet-veto cut to remove $t\bar{t}$ events is illustrated in Fig. 6. This figure shows the multiplicity of jets with $E_T^{jet} > 20$, and $E_T^{jet} > 30$ GeV, for $WW, t\bar{t}$ and Z events with two reconstructed leptons.

4.3.4 Missing transverse energy

Missing transverse energy, $\not\!\!E_T$, is calculated from the energy deposited in all calorimeter cells and from muons ($\not\!\!E_T$_`EtMissRefFinal` [1]). A correction is applied for the energy lost in the cryostat. $\not\!\!E_T$ is also calculated from truth particles for comparison ($\not\!\!E_T$_`EtMissTruth`). Truth and reconstructed $\not\!\!E_T$ is compared shown in Fig. 7 for WW and Drell-Yan events in the ee and $\mu\mu$ channels. In events with real $\not\!\!E_T$ (such as WW or $t\bar{t}$) agreement between truth and reconstructed $\not\!\!E_T$ is fair while for the Drell-Yan

process a significant deviation from truth distribution appears in $\mu\mu$ channel where a large $\not\!\!E_T$ tail exists. The resolution of $\not\!\!E_T$, calculated as the difference between truth and reconstructed $\not\!\!E_T$ is shown in Fig. 8. For WW events, the $\not\!\!E_T$ resolution is about 6.5 GeV.

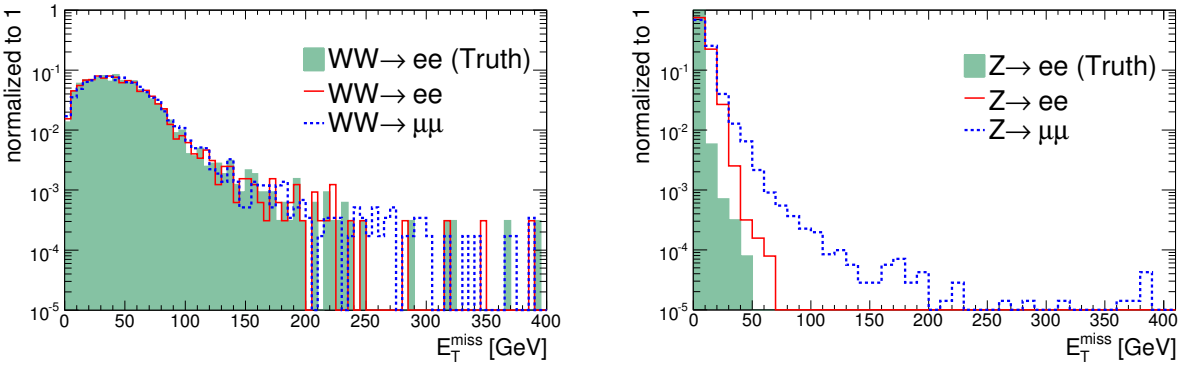

Figure 7: Comparison of truth and reconstructed E_T^{miss} in the ee and $\mu\mu$ channels for WW and Drell-Yan processes.

4.3.5 Trigger Selection and Efficiency

The ATLAS trigger consists of three levels of event selection: Level-1 (L1) Level-2 (L2) and event filter(EF). The L2 and EF together form the High-Level Trigger (HLT). According to the present physics trigger menu [1] the W^+W^- events are required to pass one of the following High-Level Trigger (HLT) paths: single isolated electron, e25i (L1_EM25 at L1), or single muon, mu20 (L1_MU20 or L1_MU40 at L1) trigger.

Table 13 shows the L1 and HLT trigger efficiencies for WW events with two opposite sign isolated leptons, with $p_T > 20$ GeV, $|\eta| < 2.5$. The overall trigger efficiency in events with two isolated leptons is $\sim 98\%$ in ee, $\sim 96\%$ in $\mu\mu$ and $\sim 97\%$ $e\mu$ channel. The L1 muon trigger has somewhat lower efficiency due to losses in the ATLAS feet region.

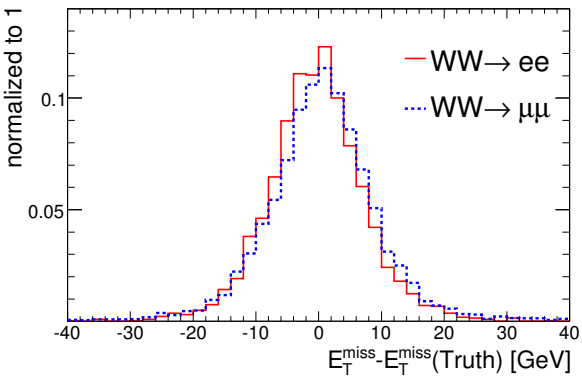

Figure 8: $\not\!\!E_T$ resolution for $WW \to ee$ and $WW \to \mu\mu$.

Table 13: L1 and HLT trigger efficiencies in (%) for $WW \to ee$, $WW \to \mu\mu$ and $WW \to e\mu$ events with two opposite sign isolated leptons ($p_T > 20$ GeV, $|\eta| < 2.5$)

	1e25i		1mu20		1e25i or 1mu20	
WW	L1	L1&HLT	L1	L1&HLT	L1	L1&HLT
ee	100	98.2	0	0	100	98.2
$\mu\mu$	13.5	0	98.4	95.9	98.5	95.9
$e\mu$	99.7	87.9	85.3	79.3	100	97.4

4.4 $W^+W^- \to \ell^+\nu\ell^-\nu$ analysis with straight cuts

Object reconstructed outputs (*AOD*) and HighPtView ntuple derived from AOD are used in this analysis. The *AOD* provides uniform access to the reconstructed particles (kinematics, identification variables etc.) while the *HighPtView* set of analysis tools removes overlaps and provides particle pre-selection. In the pre-selection, the electrons are inserted first, followed by muons and particle jets. Overlaps between the electron and particle jet are removed using ΔR=0.2.

4.4.1 Event Selection

The W^+W^- selection consists of two steps. In the first step, the basic kinematic selection cuts are applied. These cuts reject the events with topology clearly distinct from the signal topology and significantly suppress main background processes $t\bar{t}$ and Z/γ. In the second step, an additional event topology cut is applied and the signal to background ratio is further improved. Two options for this additional cut are considered and, together with the same basic kinematic cuts, labeled as Selection-A and Selection-B. The set of cuts for the Selection-A and Selection-B are presented in Table 14.

Table 14: Summary of the W^+W^- selection cuts. Two options (Selection-A and Selection-B) for the W^+W^- selection are considered.

	Selection-A	Selection-B
	Basic cuts	Basic cuts
Cut 1	Lepton cut: $p_T^l > 20$ GeV, $\|\eta\| < 2.5$	Lepton cut: $p_T^l > 20$ GeV, $\|\eta\| < 2.5$
Cut 2	Jet veto: $p_T^{jet} > 20$ GeV, $\|\eta\| < 3.$	Jet veto: $p_T^{jet} > 20$ GeV, $\|\eta\| < 3.$
Cut 3	$E_T^{miss} > 50$ GeV	$E_T^{miss} > 50$ GeV
Cut 4	M_Z veto: $\|M_Z - m(l^+l^-)\| > 15$ GeV	M_Z veto: $\|M_Z - m(l^+l^-)\| > 15$ GeV
	Additional cut	Additional cut
Cut 5	$\phi(l^+l^-) < 2$ rad	$\Phi(\mathbf{p}_T^{l^+l^-}, \mathbf{E}_T^{miss}) > 175^0$

Cut 1, or the lepton cut, requires two isolated leptons with opposite sign, $p_T^l > 20$ GeV, $|\eta| < 2.5$. This cut is consistent with the ATLAS trigger system and provides that all the isolated leptons originate from W bosons decay.

Cut 2 is a jet veto. It rejects events with any jet ($p_T^{jets} > 20$ GeV) in the rapidity region, $|\eta| < 3$. This cut is efficient in $t\bar{t}$ suppression (Fig. 6) since it contains one or two energetic b jets in addition to the W^+W^- signature.

Cut 3 requires $\not{E}_T > 50$ GeV. The large cut on $\not{E}_T$ is chosen to reduce potential background arising from the event pileup and the processes in which particles outside the detection rapidity range, contribute to the $\not{E}_T$. This cut particularly reduces the contributions from the Z/γ events (Fig. 9).

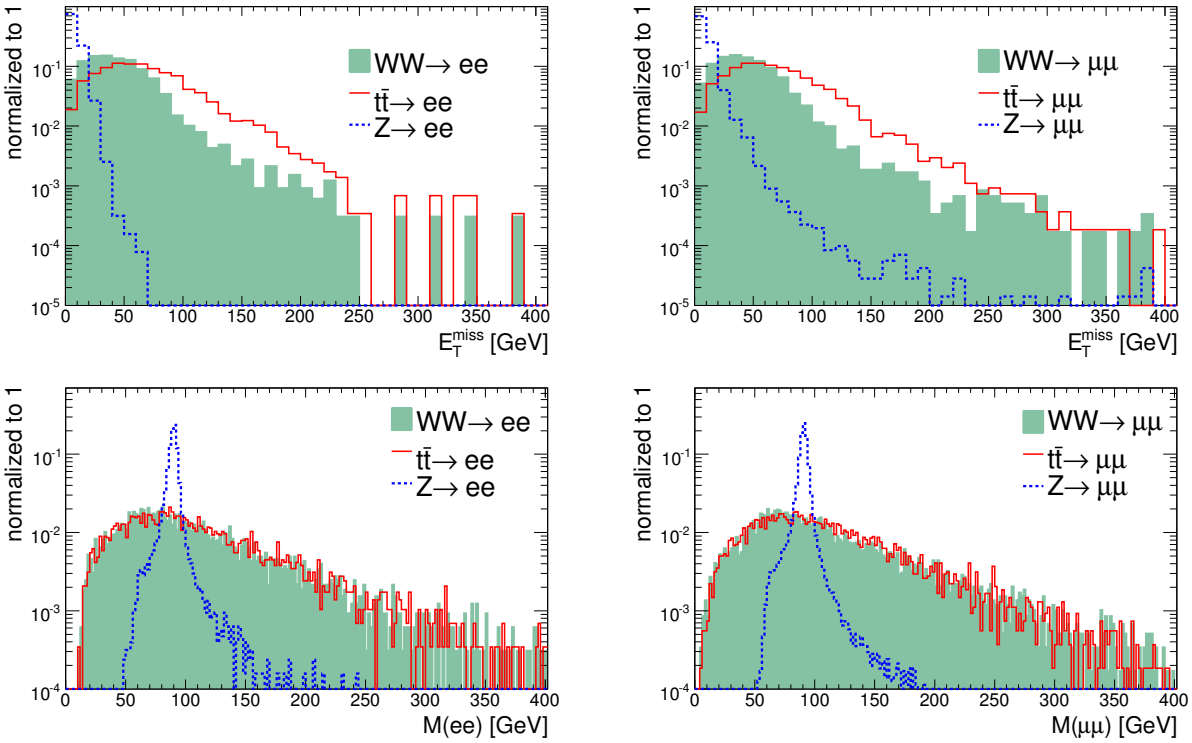

Figure 9: E_T^{miss}, and lepton invariant mass distributions for W^+W^-, $t\bar{t}$ and Z/γ (Triggered events with lepton cut.

Cut 4 is the M_Z veto and it rejects events in which $\ell^+\ell^-$ pair originates from a Z boson decay. This cut significantly reduces the contributions from the Z and the ZZ events (Fig. 9).

The effects of basic kinematic cuts on signal and main background processes are presented in Tables 15, 16 and 17 for ee, $\mu\mu$ and $e\mu$ channels, respectively. These Tables summarize the number of expected events after each selection cut, for an integrated luminosity of 1 fb^{-1}, and the relative efficiency with respect to the previous cut (in parenthesis). One can see that the cut efficiencies for ee, $\mu\mu$ and $e\mu$ channels are similar for signal and all backgrounds. An exception is the lepton cut due to difference in electron/muon reconstruction efficiencies. After the basic cuts, the signal is visible in ee and $e\mu$ channels with a signal to background ratio $S/B \approx 3-4$. However, these basic cuts are insufficient for the $\mu\mu$ channel, where the signal to background ratio is less than 0.4. This is due to a large E_T^{miss} tail in the Z/γ events. The signal to background ratio can be further improved by applying additional **Cut 5** Selection-A, $\phi_{\ell\ell} < 2$ rad, where $\phi_{\ell\ell}$ is the angle between transverse momenta of two leptons; or **Cut 5** Selection-B, $\Phi(\mathbf{p}_T^{\ell^+,\ell^-}, \mathbf{p}_T^{miss}) < 175^0$, where Φ is the angle between transverse momentum of the lepton pair, and the missing transverse momentum. Figure 10 shows the $\phi_{\ell\ell}$ and the Φ distributions for both ee and $\mu\mu$ channels. We see that both cuts are efficient in further suppression of Z/γ in $\mu\mu$ channel as well as $WW \to \tau\ell$ and $Z \to \tau\tau$ processes.

4.4.2 W^+W^- selection results based on straight cut analysis

Table 18 gives a summary of the signal efficiencies, the expected number of signal and background events for an integrated luminosity of 1 fb^{-1}, and signal to background ratios for Selection-A and Selection-B. The efficiencies comprise acceptance and trigger, reconstruction and selection efficiencies. The contribu-

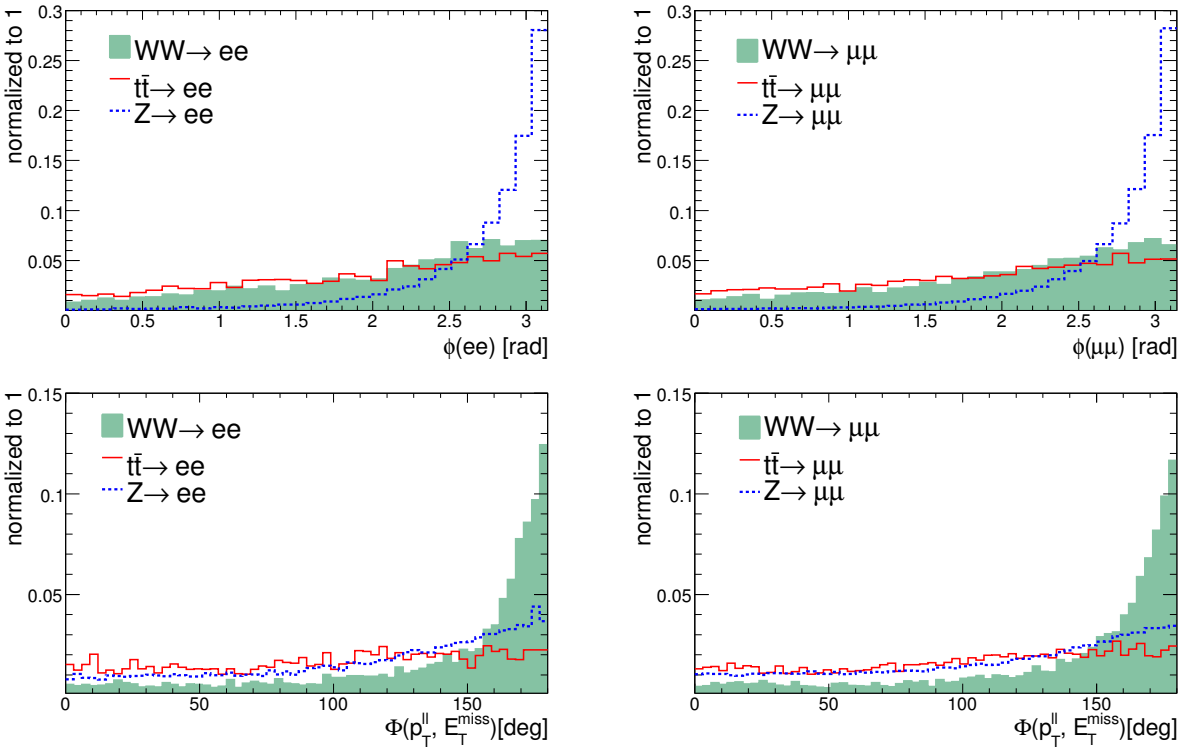

Figure 10: ϕ_{ll} and $\Phi(\mathbf{p}_T^{ll}, \mathbf{E}_T^{miss})$ distributions for W^+W^-, $t\bar{t}$ and Z/γ.

Table 15: Cut flow and expected number of events for L=1 fb^{-1} in the *ee* channel for signal and main background processes. The relative efficiency with respect to the previous cut is given in parentheses. The errors shown are statistical or 90% CL in the case of insufficient statistics.

	WW	tt	$Z \to ee$	$W^{\pm}Z$	ZZ	$WW \to l\tau$	$Z \to \tau\tau$
2 O.S. lep.	219.3 (16.9%)	2363.0 (0.5%)	340880 (19.7%)	74.4 (10.4%)	35.2 (13.3%)	27.6 (0.4%)	885.0 (0.9%)
Jet veto	107.0 (48.8%)	7.6 (0.3%)	186840 (54.8%)	24.1 (32.4%)	18.0 (51.1%)	10.3 (37.3%)	470.0 (53.1%)
$\not\!\!E_T$	32.0 (30.0%)	2.5 (32.9%)	< 199 -	7.8 (32.4%)	7.5 (41.7%)	3.0 (29.1%)	2.4 (0.5%)
M_Z veto	25.9 (80.9%)	2.5 (100%)	- -	0.6 (7.7%)	0.3 (4.8%)	2.1 (70%)	1.6 (67%)
$\phi_{ll} < 2$ rad Selection-A	17.8 (68.7%)	< 1.9 -	- -	0.3 (43%)	0.3 (86.1%)	0.9 (42.9%)	< 1.8 -
trigger	17.4±1.1 (97.8%)	- -	- -	0.3±0.1 (100%)	0.3±0.1 (100%)	0.8±0.3 (97%)	- -
$\Phi(\mathbf{p}_T^{ll}, \not\!\!\mathbf{p}_T)$ Selection-B	12.3 (47.5%)	< 1.9 -	- -	0.1 (14.3%)	0.2 (88.0%)	0.9 (43%)	1.6 (100%)
trigger	12.0±0.9 (97.6%)	- -	- -	0.1±0.01 (100%)	0.2±0.1 (100%)	0.9±0.3 (100%)	1.6±1.1 (100%)

Table 16: Cut flow and expected number of events for L=1 fb^{-1} in the $\mu\mu$ channel for signal and main background processes. The relative efficiency with respect to the previous cut is given in parentheses. The errors shown are statistical or 90% CL in the case of insufficient statistics.

	WW	$t\bar{t}$	$Z \to \mu\mu$	$W^{\pm}Z$	ZZ	$WW \to l\tau$	$Z \to \tau\tau$
2 O.S. lep.	451.1 (34.7%)	4456 (0.99%)	661234 (36.8%)	120.7 (16.8%)	72.5 (27.4%)	66.7 (1.0%)	1987 (2.1%)
Jet veto	203.6 (45.1%)	10.9 (0.2%)	350702 (53.0%)	39.0 (32.3%)	37.3 (51.5%)	29.9 (44.8%)	1000 (50.3%)
$\not\!\!E_T$	69.3 (34.0%)	5.9 (53.8%)	863.7 (0.2%)	13.9 (35.6%)	15.6 (41.9%)	7.0 (23.5%)	6.6 (0.6%)
M_Z veto	55.4 (80.0%)	5.1 (86%)	197.9 (23.0%)	2.5 (18.0%)	1.6 (10.5%)	5.2 (74.1%)	5.0 (75.0%)
$\phi_{ll} < 2$ rad Selection-A	39.0 (70.3%)	4.2 (83.3%)	< 20.7 -	1.7 (68%)	1.4 (88.8%)	2.9 (55.0%)	0.8 (83.3%)
trigger	36.4±2.2 (93.3%)	4.2±1.9 (100%)	- -	1.6±0.1 (94.5%)	1.3±0.3 (95.6%)	2.8±0.6 (95.5%)	0.8±0.8 (100%)
$\Phi(\mathbf{p}_T^{ll}, \not\!\!\mathbf{p}_T)$ Selection-B	26.9 (48.6%)	0.8 (17%)	< 20.7 -	1.2 (48%)	1.1 (71.4%)	1.8 (35.0%)	< 1.8 -
trigger	25.5±1.8 (94.8%)	0.8±0.8 (100%)	- -	1.1±0.1 (93.5%)	1.1±0.1 (95.0%)	1.8±0.5 (100%)	- -

tion of $gg \to WW$ events is shown in separate columns and yields 4-7% depending whether Selection-A or Selection-B is applied. With a relatively simple set of selection cuts we can extract 2% of the total number of produced WW events in electron/muon channels, which amounts to 104 events for an integrated luminosity of 1 fb^{-1}. The total background is estimated to be 19, although it has still large uncertainty from limited statistics of MC samples. After all the cuts a significant contribution originates from $WW \to \tau\ell$ in the remaining background.

The resulting (signal plus background) $p_T(l)$ and $p_T(ll)$ distributions, for an integrated luminosity of 1 fb^{-1}, are shown in Figure 11 and Figure 12. The contributions of various backgrounds are shown as shaded histograms. Although the overall signal efficiency is higher after Selection-A, this selection strongly reduces high p_T region of leptons and lepton pairs and therefore strongly reduces sensitivity for TGCs measurements.

The p_T distribution of the leptons obtained after selection "B" is used to estimate limits on anomalous WWZ and $WW\gamma$ couplings. The method used to obtain limits when only one parameter of the WWZ and $WW\gamma$ couplings is varied is described in more detail in Appendix E. Table 72 summarizes the 95% C.L. limits obtained when only one parameter of the WWZ and $WW\gamma$ couplings is varied. From the Table 72 we can see that with increasing integrated luminosity from 1 to 30 fb^{-1} limits will be improved and precise investigation of TGC will be possible with the first 10fb^{-1} of LHC data.

4.5 W^+W^- analysis using Boosted-Decision-Trees technique

In order to optimize diboson detection efficiencies, we used an advanced data analysis technique, *Boosted Decision Trees(BDT)*, to select events in multi-variable space. Details of this technique can be found in the references [3]. A brief description of the *BDT* method is provided as an appendix to this note. In the

Table 17: Cut flow and expected number of events for L=1 fb^{-1} in the $e\mu$ channel for signal and main background processes. The relative efficiency with respect to the previous cut is given in parenthesis. The errors shown are statistical or 90% CL in the case of insufficient statistics.

	WW	$t\bar{t}$	$W^{\pm}Z$	$WW \to l\tau$	$Z \to \tau\tau$
2 O.S. lep.	620.9 (23.9%)	6507.1 (1.4%)	36.8 (5.1%)	90.3 (0.2%)	2544 (2.7%)
Jet veto	291.8 (47.0%)	11.8 (0.2%)	9.2 (25.0%)	42.7 (47.3%)	1428 (56.1%)
$\not\!\!E_T$	93.5 (32.0%)	7.5 (63.9%)	3.6 (39.1%)	12.4 (29.0%)	4.1 (0.3%)
M_Z veto	74.4 (79.5%)	5.9 (78%)	2.8 (77.7%)	9.7 (78.2%)	1.6 (40%)
$\phi_{ll} < 2$ rad Selection-A	51.9 (69.8%)	< 1.9 -	1.6 (57.4%)	4.9 (55.0%)	0.8 (50%)
trigger	50.6±1.8 (97.5%)	- -	1.6±0.1 (96.1%)	4.8±0.9 (95.5%)	0.8±0.8 (100%)
$\Phi(\mathbf{p}_T^{ll}, \not\!\!\mathbf{p}_T)$ Selection-B	35.9 (48.3%)	1.7 (28%)	0.8 (28.3%)	5.0 (51.5%)	< 1.8 -
trigger	35.3±1.5 (98.3%)	1.7±1.2 (100%)	0.7±0.1 (94.5%)	5.0±0.3 (95.0%)	- -

Table 18: Yield of the WW selection for an integrated luminosity of 1fb $^{-1}$. The errors shown are statistical only

Selection-A						
	efficiency		N_{WW}		$N_{totalbkg.}$	S/B
	$gg \to WW$	$q\bar{q} \to WW$	$gg \to WW$	$q\bar{q} \to WW$		
ee	2.1%	1.33%	1.25±0.05	17.4 ± 1.1	1.4 ±0.3	13.3±3.0
$\mu\mu$	4.1%	2.80%	2.43±0.08	36.4 ± 2.2	10.7 ± 2.1	3.6± 0.8
$e\mu$	2.8%	1.94%	3.33±0.13	50.6± 1.8	7.2 ± 1.2	7.5 ± 1.3
ll	3.0%	2.00%	7.00±0.16	104.4±2.4	19.3±2.4	5.8 ± 0.8
Selection-B						
	efficiency		N_{WW}		$N_{totalbkg.}$	S/B
	$gg \to WW$	$q\bar{q} \to WW$	$gg \to WW$	$q\bar{q} \to WW$		
ee	0.94%	0.92%	0.6±0.04	12.0 ± 0.9	2.8± 1.2	4.5 ± 1.9
$\mu\mu$	2.1%	1.96%	1.1±0.03	25.5 ± 1.8	4.8±1.0	5.5 ±1.2
$e\mu$	1.3%	1.36%	1.54± 0.09	35.3 ± 1.5	7.4± 1.3	5.0 ± 0.9
ll	1.4%	1.40%	3.24±0.10	72.8 ±2.5	15.0 ± 2.0	5.1 ± 0.8

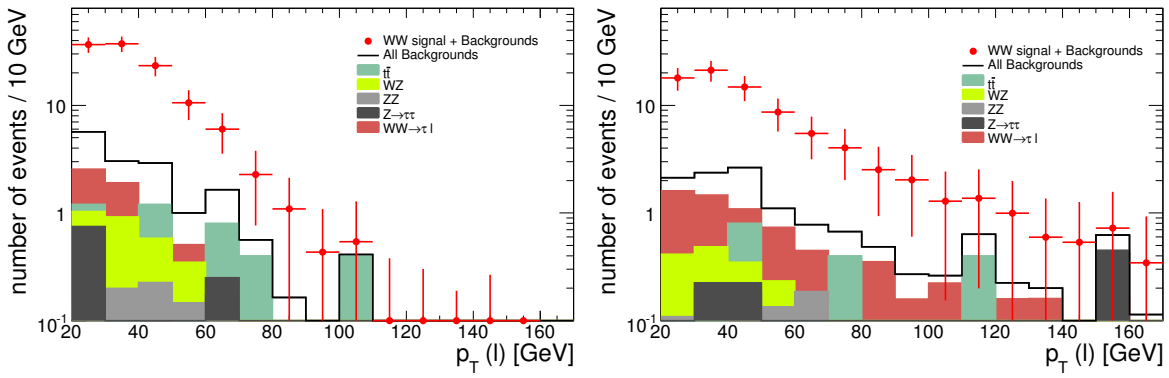

Figure 11: Transverse momentum distributions of leptons after applying kinematic cuts from Selection-A (left) and Selection-B (right).The distributions are shown for sum of signal and various backgrounds, and for separated backgrounds for L=1 fb^{-1}.

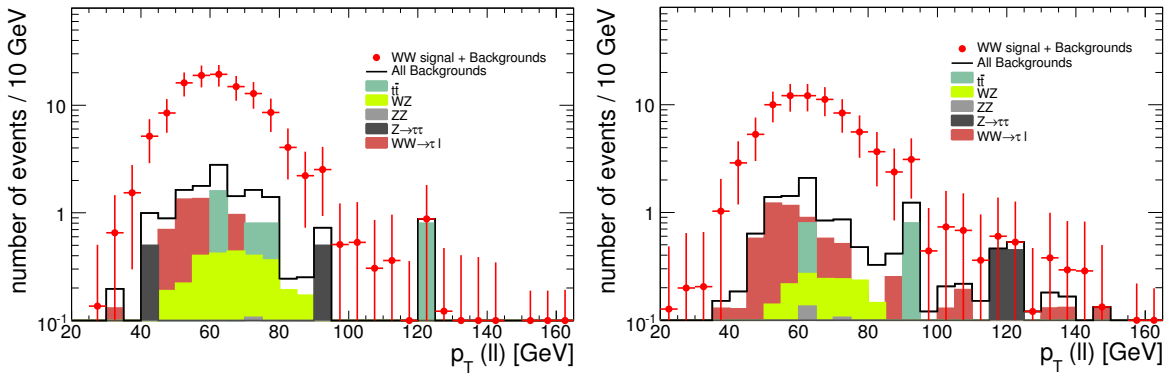

Figure 12: Transverse momentum distributions of lepton pairs after applying kinematic cuts from Selection-A (left) and Selection-B (right). The distributions are shown for sum of signal and various backgrounds, and for separated backgrounds for L=1 fb^{-1}.

W^+W^- analysis, we have used a one thousand decision trees program, wherein tree has 20 *nodes* that are used to separate signal from background based on the input variables. The input data for the *BDT* analysis must first pass the following event pre-selection criteria:

- Two, opposite charged, high p_T leptons (e^+e^-, $e^\pm\mu^\mp$, or $\mu^+\mu^-$). The transverse momentum threshold for each lepton is 10 GeV.
- $\not\!\!E_T > 15$ GeV.

The pre-selected MC samples are divided into two equal parts, sample A and B, where sample A is used for BDT training and B to test performance, or vice versa. The results quoted in our analysis are based on the test sample performance.

4.5.1 Input variables for *BDT* training

We list below the variables for $W^\pm W^\mp \to e^\pm\nu\mu^\mp\nu$ analysis. The variables used for $W^+W^- \to \ell^+\nu\ell^-\nu$, $(\ell = e,\ \mu)$ analysis are similar. A total 15 variables, listed below, are carefully selected for the *BDT* training and testing. The distributions of these variables are shown in Figure 13. The normalizations of the distributions are arbitrary.

- $P_t(\mu)$ – the muon transverse momentum.
- Sum P_t in cone=0.4(μ) – muon isolation variable, the sum of track p_T around the muon track in a cone, $\Delta R = \sqrt{\Delta\phi^2 + \Delta\eta^2} < 0.4$.
- E(e)/P(e) – the ratio of the electron energy measured in EM calorimetry and the momentum measured in inner tracker.
- scalar sum E_t(l)+Jets – sum of the total visible transverse energies from the leptons and the jets in an event.
- Total recoil E_t – total recoil transverse energy in an event.
- Vector sum E_t(l)+$\not\!\!E_T$ – is the vector-sum of the hadronic energy calculated from lepton and Missing E_T from a formula: $|\sum_i(\vec{E}_T(lepton)_i) + \vec{M}issingE_T|$.
- $\not\!\!E_T/\sqrt{(Vector-sum(l,Jets))}$ – is the missing E_T over square-root of the total visible transverse energy.
- NJets($E_t > 30$ GeV) – is number of jet (with jet E_T greater than 30 GeV).
- $\Delta\phi(e,\mu)$ – is the dilepton ϕ angle difference.
- $P_t(e+\mu)$ – is the dilepton system transverse momentum.
- Inv. mass(e,μ) – is the invariant mass of the di-lepton in final state.
- Trans. mass(WW) – is the transverse mass of the W-pair based on lepton and missing E_T variables.
- $\Delta\phi(e\mu, \not\!\!E_T)$ – is the minimum $\Delta\phi$ between the missing E_T and the leptons.
- $\Delta Z(e,\mu)$ – is the vertex Z difference between two final state leptons
- $\Delta A(e,\mu)$ – is the vertex impact parameter difference between two final state leptons

The MC samples for signal and background for the BDT training are listed in Table 19, which lists the MC processes, the event *weight* in the *BDT* training, the pre-selection efficiencies, the number of events passing the pre-selection, and the expected number of pre-selected events corresponding to 1 fb^{-1} integrated luminosity.

Table 19: List of the MC samples for W^+W^- BDT analysis and their rate of selection by the $W^\pm W^\mp \to e^\pm \nu \mu^\mp \nu$ pre-cuts. $N_{precut,MC}$ is the number of events selected from the MC dataset and $N_{precut,1/fb}$ is the equivalent number selected for an integrated luminosity of 1 fb^{-1} . The initial training *weights* for different events are given in the second column of the table. The weight is the scale factor between number of events in the pre-selected dataset to the expected number of events in 1 fb^{-1} of data, so $N_{MC} \times \text{Weight} = N_{1/fb}$.

MC Process	Weight	Eff$_{precut}$	$N_{precut,MC}$	$N_{precut,1/fb}$
$W^+W^- \to e^+\nu\mu^-\nu$	0.0289	0.388	18233	527.0
$W^+W^- \to \mu^+\nu e^-\nu$	0.0283	0.392	18813	532.9
$W^+Z \to \ell^+\nu\ell^+\ell^-$	0.0196	0.178	4815	94.3
$W^-Z \to \ell^-\nu\ell^+\ell^-$	0.0171	0.200	3537	60.4
$t\bar{t} \to \ell + X$	0.6119	0.0332	22849	13981.7
$ZZ \to \ell^+\ell^-\ell^+\ell^-$	0.0023	0.147	5341	12.5
Drell-Yan$(\ell^+\ell^-)(30\text{ GeV} < M < 81\text{ GeV})$	0.9250	0.000267	160	148.0
Drell-Yan$(\ell^+\ell^-)(81\text{ GeV} < M < 100\text{ GeV})$	12.1301	0.00129	649	7872.4
Drell-Yan$(\ell^+\ell^-)(M > 100\text{ GeV})$	0.4661	0.00232	1145	533.7
$W \to e\nu$	8.8254	0.000110	274	2418.1
$W \to \mu\nu$	11.0183	0.000152	304	3349.6
$W \to \tau\nu$	8.8294	0.0000212	53	468.0
$W + JET\ (E_T^j : 10-20\text{ GeV})$	45.4662	0.000085	34	1545.9
$W + JET\ (E_T^j : 20-40\text{ GeV})$	36.9787	0.000238	72	2662.5
$W + JET\ (E_T^j : 40-80\text{ GeV})$	16.4445	0.00041	123	2022.7
$W + JET\ (E_T^j : 80-120\text{ GeV})$	3.0202	0.000378	113	341.3
$W + JET\ (E_T^j > 120\text{ GeV})$	1.2825	0.000287	85	109.0
$Z(ee) + JET\ (E_T^j : 10-20\text{ GeV})$	0.9946	0.000206	123	122.3
$Z(ee) + JET\ (E_T^j : 20-40\text{ GeV})$	0.9499	0.000554	221	209.9
$Z(ee) + JET\ (E_T^j : 40-80\text{ GeV})$	0.4527	0.00118	468	211.9
$Z(ee) + JET\ (E_T^j : 80-120\text{ GeV})$	0.0910	0.00103	408	37.1
$Z(ee) + JET\ (E_T^j > 120\text{ GeV})$	0.0842	0.000790	157	13.2
$Z(\mu\mu) + JET\ (E_T^j : 10-20\text{ GeV})$	0.9944	0.000822	491	488.2
$Z(\mu\mu) + JET\ (E_T^j : 20-40\text{ GeV})$	0.9544	0.00123	489	466.7
$Z(\mu\mu) + JET\ (E_T^j : 40-80\text{ GeV})$	0.2317	0.00176	1365	316.2
$Z(\mu\mu) + JET\ (E_T^j : 80-120\text{ GeV})$	0.0910	0.00205	813	74.0
$Z(\mu\mu) + JET\ (E_T^j > 120\text{ GeV})$	0.0859	0.00327	638	54.8
$Z(\tau\tau) + JET\ (E_T^j : 10-20\text{ GeV})$	0.9921	0.00314	1883	1868.1
$Z(\tau\tau) + JET\ (E_T^j : 20-40\text{ GeV})$	0.9490	0.00423	1688	1601.8
$Z(\tau\tau) + JET\ (E_T^j : 40-80\text{ GeV})$	0.4511	0.00623	2487	1121.8
$Z(\tau\tau) + JET\ (E_T^j : 80-120\text{ GeV})$	0.0911	0.00903	3582	326.2
$Z(\tau\tau) + JET\ (E_T^j > 120\text{ GeV})$	0.0840	0.0150	2984	250.8
$W(\ell\nu)\gamma$	0.1525	0.000231	462	70.5
$W(\tau\nu)\gamma$	0.2213	0.0000436	30	6.6
$Z(\ell\ell)\gamma$	0.5998	0.000347	52	31.2

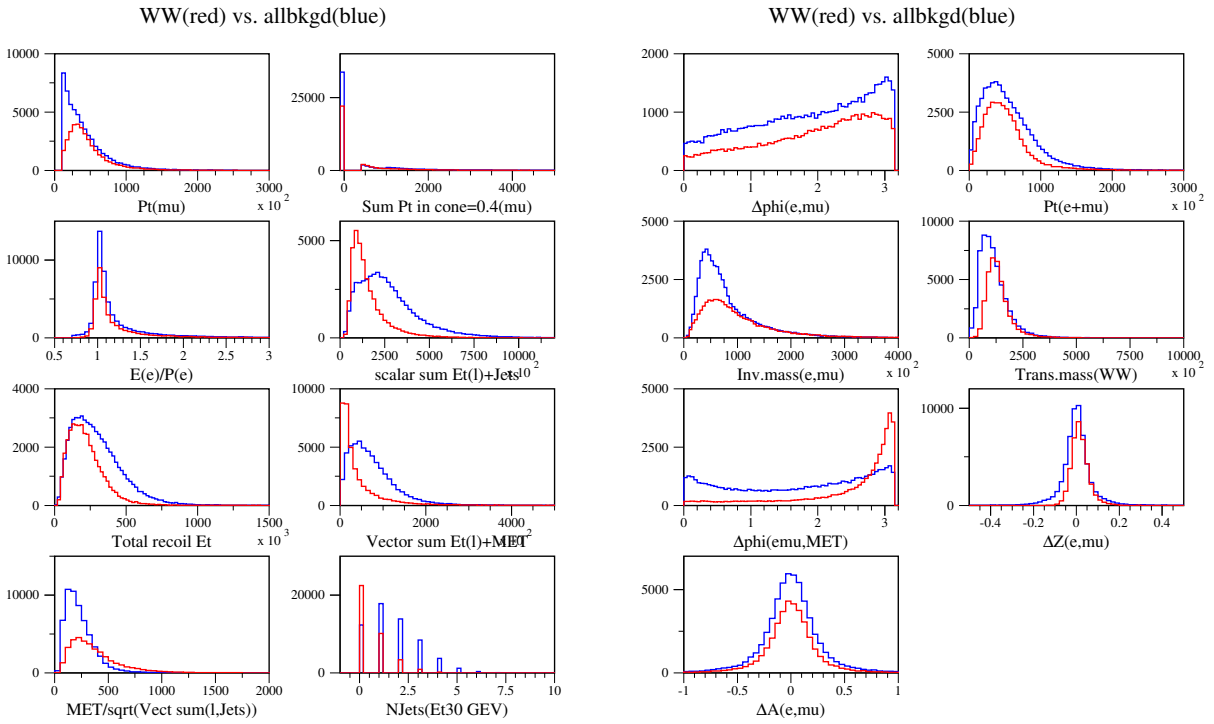

Figure 13: Distributions of the BDT training input variables for $W^{\pm}W^{\mp} \to e^{\pm}\nu\mu^{\mp}\nu$ analysis. Red histograms are for W^+W^- signal, and the blue are for all the background.

4.5.2 The outputs of the *BDT* analysis

The *BDT*-output for each event is a sum of the **scores** over all the decision-trees. If an event is classified as a **signal** in a tree, the score from that tree for this event is +1; otherwise, -1. Thus, a high score means the event is most likely signal, and a low score, most likely background. The *BDT* output spectra for signal and background from the statistically independent testing samples are shown in Figure 14. The red histogram (in the positive score side) is the W^+W^- events *BDT* output distribution, and the blue histogram (in the negative score side) is the overall background *BDT* output distribution.

We use the *BDT* output as our 'discriminator' to separate signal from background by applying a cut on the BDT-output spectrum. Table 20 presents the detection sensitivities for $WW \to e^{\pm}\nu\mu^{\mp}\nu$ with various *BDT* output cuts. For a total integrated luminosity of 1 fb^{-1} , we list the selected number of signal events (N_{WW}), the background ($N_{bkg.}$) events, the corresponding signal efficiency (Eff$_{WW}$), and signal to background ratio (N_{WW}/N_{bkg}). In the last row are the expected numbers of signal and background events for 1 fb^{-1} using straight cuts analysis. Detailed selection criteria for this straight cuts analysis are given in appendix. events that are available in the *CBNT*s than the analysis presented in section of 'Results based on straight cut analysis'.

The overall *BDT* selection efficiency is about 15% for a *BDT* cut greater than 200. The signal to background ratio is 5.2. With the straight cuts analysis, the overall signal selection efficiency is 6.5% with a signal to background ratio of 2.

The *BDT* has also been applied to $gg \to W^+W^- \to \ell^+\nu\ell^-\nu$ events. The overall selection efficiency is less than 5%. Thus, the total contribution to the W^+W^- events from the gluon-gluon fusion process is expected to be less than 2%.

Background contributions from different SM processes for $e^{\pm}\mu^{\mp} + \not{E}_T$ signature are listed in Ta-

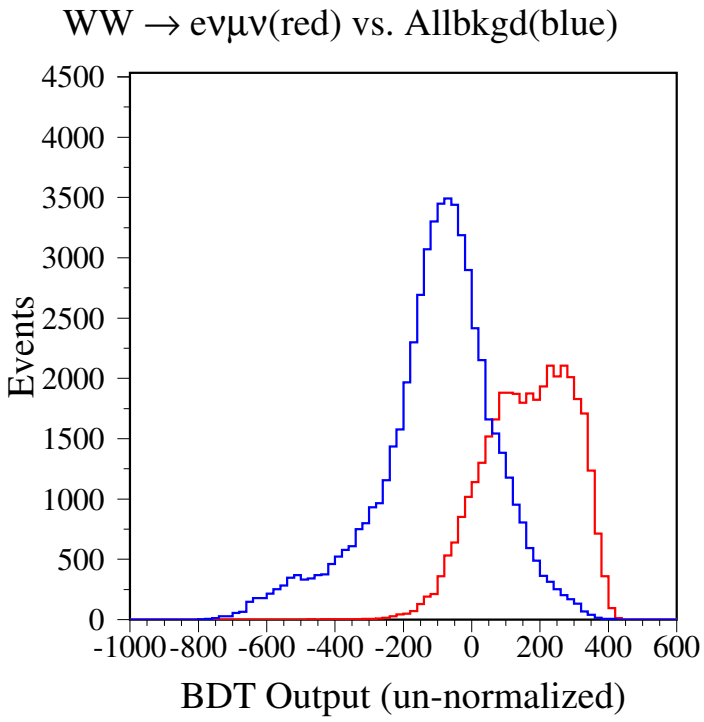

Figure 14: Distributions of the *BDT*-output spectra. Red histogram is for WW signal events, and the blue, is for all the background.

Table 20: $WW \to e\mu + \not\!\!E_T$ detection sensitivities in terms of accepted signal and background events for 1 fb^{-1} luminosity. Results from the BDT analysis applied with different BDT cuts are compared to that with the straight cut analysis. The BDT and straight-cut efficiencies are relative to the pre-cut output. Thus, the overall WW detection efficiency based on straight-cut analysis is 6.5% (0.385×0.168), and for BDT based analysis is about 15% for a BDT cut at 200. The contribution from tau decays of a W is not included in these results. See Table 21 for the contributions from tau final states as well as a breakdown of the background for a BDT cut at 200.

Cut	$\text{Eff}_{WW}(\%)$	$N_{WW\to e\nu\mu\nu}$	$N_{bkg.}$	$N_{WW}/N_{bkg.}$
Pre-cuts	38.5	1059.9	42884	0.025
BDT $\geq$ 200	**39.6**	**419.9± 3.5**	**80.8± 6.0**	**5.2**
BDT $\geq$ 220	34.9	370.3± 3.3	50.0± 4.4	7.4
BDT $\geq$ 250	27.4	290.3± 2.9	25.4± 2.9	11.5
BDT $\geq$ 270	22.3	236.5± 2.6	19.0± 2.5	12.4
BDT $\geq$ 290	17.3	183.7± 2.3	10.6± 1.7	17.3
BDT $\geq$ 300	14.8	156.5± 2.1	8.3± 1.5	18.7
Straight cuts	16.8	178.0	88.8	2.0

Table 21: Major background contributions for $WW \to e\nu\mu\nu$ with BDT cut ≥ 200. The number of events are normalized to 1 fb^{-1} integrated luminosity.

Type	MC Process	$N_{selected}$	Bkg. %
Signal	$WW \to e\nu\mu\nu$	**420.0**	-
W's decay to tau's	$WW \to e\nu\tau\nu$	6.6	-
	$WW \to \mu\nu\tau\nu$	9.0	-
	$WW \to \tau\nu\tau\nu$	0.4	-
Background	**Total**	**80.8**	100.0%
	$t\bar{t}$	36.7	45.4%
	$W^+Z \to \ell\nu\ell\ell$	12.1	15.0%
	$W^-Z \to \ell\nu\ell\ell$	9.26	11.5%
	$Z(\mu\mu)+JET$	4.58	5.7%
	$Z(\tau\tau)+JET$	10.95	13.6%
	Drell-Yan $\to \ell\ell$	5.12	6.3%
	$W\gamma \to \ell\nu$	1.75	2.2%
	$ZZ \to \ell\ell\ell\ell$	0.34	0.4%

ble 21. Major background comes from $t\bar{t}$ and other diboson final states. The contributions from tau decays of the $WW \to \ell\tau + X \to e\mu + X$ ($\ell = e,\ \mu,\ \tau$) processes are also given in this table.

We show in Figure 15 the distributions of the transverse mass of the W-pair ($M_T(WW)$) before and after the BDT-output cut (left plot), and the *BDT* selection efficiency as a function of the $M_T(WW)$. The selection efficiency drop in the high end of the $M_T(WW)$ spectrum is due to the effective rejection of the events with jets in final states.

Using the same pre-selection criteria and similar input variables for the *BDT* training, we also performed *BDT* analysis on W^+W^- decays to $e^+\nu e^-\nu$ and to $\mu^+\nu\mu^-\nu$ final states. Table 22 shows the *BDT* analysis results for $WW \to \mu^+\nu\mu^-\nu$ event selection. The numbers of events are normalized to 1 fb^{-1} integrated luminosity. Pre-selection efficiencies and the signal to background ratios for different selection cuts are given in this table.

Table 23 shows background contributions from different SM processes when applying the BDT cut at 290. It is clear that the $t\bar{t}$ is the major background. In this table are also the contributions from the tau final states from the W^+W^- events for a BDT cut at 290.

Table 24 shows the *BDT* analysis results for $WW \to e^+\nu e^-\nu$ event selection. The number of events are normalized to 1 fb^{-1} integrated luminosity. Table 25 shows the breakdown of the background contributions from different SM processes. The BDT cut is applied at 240. Similar to other channels above, the major background again is from the $t\bar{t}$ events.

4.5.3 Estimate the uncertainties for cross section measurements

The uncertainties of the *WW* production cross section measurement include both statistic and systematic errors. Based on our current studies, we expect that systematic errors would dominate when integrated luminosity reaches 10 fb^{-1} . In principle, all the systematic uncertainties should be determined with data or Monte Carlo simulations by changing the selection cuts or simulation parameters. For this note, we plan mainly to use the Tevatron experiment quoted systematic uncertainties. We list the systematic errors below.

- 6.5% luminosity uncertainty (based on Tevatron Run II initial luminosity uncertainty quoted in

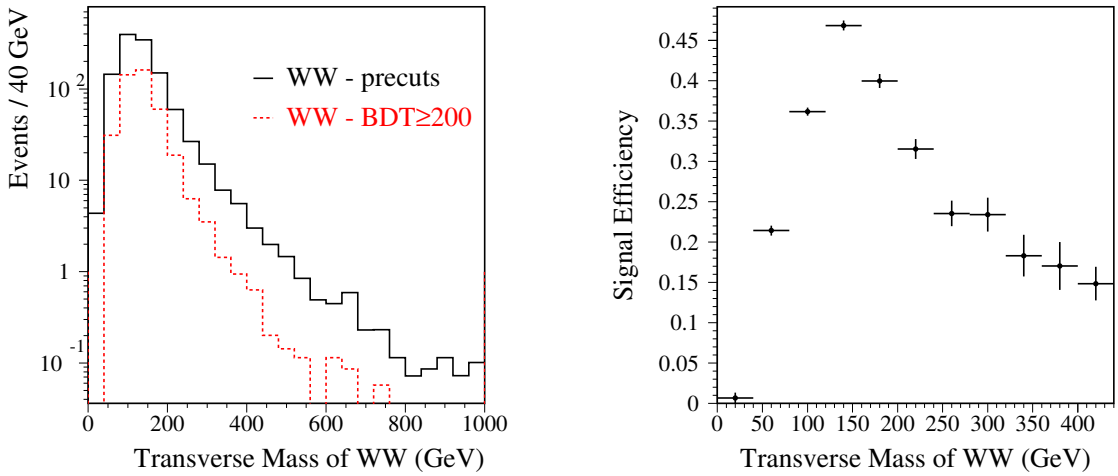

Figure 15: The left plot: the distributions of the transverse mass of the W-pair ($M_T(WW)$) before and after the BDT-output cut (> 200); The right plot: the *BDT* selection efficiency as a function of the $M_T(WW)$. The last bin is the sum of all the overflow bin.

Table 22: Results for $WW \to \mu\nu\mu\nu$ with different BDT cuts assuming 1 fb^{-1} integrated luminosity. The BDT efficiencies are relative to the pre-cut output. Thus, the overall efficiency for the signal in this channel is about 6.6% when applying a BDT cut at 290. The contribution from tau decays of a W is not included in these results. See Table 23 for the contributions from tau final states as well as a breakdown of the background for a BDT cut at 290.

Cut	Eff$_{WW}$(%)	$N_{WW\to\mu\nu\mu\nu}$	$N_{bkg.}$	$N_{WW}/N_{bkg.}$
Pre-cuts	42.7	581.1	145791.6	0.004
BDT $\geq$ 200	39.1	226.9$\pm$ 2.5	293.7$\pm$ 12.5	0.8
BDT $\geq$ 220	33.1	192.1$\pm$ 2.3	174.2$\pm$ 9.6	1.1
BDT $\geq$ 250	25.1	145.9$\pm$ 2.0	68.8$\pm$ 5.7	2.1
BDT $\geq$ 270	20.0	116.3$\pm$ 1.8	40.7$\pm$ 4.4	2.9
BDT $\geq$ 290	**15.5**	**90.3$\pm$ 1.6**	**20.2$\pm$ 2.8**	**4.5**
BDT $\geq$ 300	13.6	78.9$\pm$ 1.5	15.9$\pm$ 2.4	5.0

Table 23: Event selection for $WW \to \mu\nu\mu\nu$ process with BDT cut ≥ 290. Numbers of events for each process listed in table are normalized to 1 fb^{-1} .

Type	MC Process	$N_{selected}$	Bkg. %
Signal	$WW \to \mu\nu\mu\nu$	**90.3**	-
W's decay to tau's	$WW \to \mu\nu\tau\nu$	15.7	-
	$WW \to \tau\nu\tau\nu$	0.6	-
Background	**Total**	**20.2**	100.0%
	$t\bar{t}$	10.8	53.5%
	$W^+Z \to \ell\nu\ell\ell$	4.2	20.8%
	$W^-Z \to \ell\nu\ell\ell$	2.7	13.4%
	$ZZ \to \ell\ell\ell\ell$	0.8	4.0%
	Drell-Yan $\to \ell\ell$	0.6	3.0%
	$Z(\mu\mu) + JET$	0.9	4.5%
	$Z\gamma \to \ell\ell$	0.2	1.0%

Table 24: Event selection for $WW \to e\nu e\nu$ process with variant BDT cuts. Numbers of events for each process listed in table are nomalized to 1 fb^{-1} . The BDT efficiencies are relative to the pre-cut output. Thus, the overall efficiency for the signal in this channel is about 4% when applying a BDT cut at 250. The contributions from tau decays of W's are not included in these results. See Table 25 for the contributions from tau final states as well as a breakdown of the background for a BDT cut at 240.

Cuts	Eff$_{WW}$(%)	$N_{WW\to e\nu e\nu}$	$N_{bkgd.}$	$N_{WW}/N_{bkgd.}$
Pre-cuts	28.0	380.8	37612.0	0.01
BDT ≥ 200	25.8	98.1$\pm$ 1.8	49.4$\pm$ 5.2	2.0
BDT ≥ 220	20.5	78.0$\pm$ 1.6	24.7$\pm$ 3.6	3.2
BDT ≥ 240	15.9	60.5$\pm$ 1.4	13.4$\pm$ 2.8	4.5
BDT ≥ 250	13.9	52.8$\pm$ 1.3	7.7$\pm$ 2.1	6.8
BDT ≥ 260	11.8	45.0$\pm$ 1.2	4.1$\pm$ 1.4	10.9
BDT ≥ 270	10.1	38.5$\pm$ 1.1	1.8$\pm$ 0.7	21.5
BDT ≥ 290	6.6	25.0$\pm$ 0.9	1.0$\pm$ 0.7	24.6

Table 25: Major background contributions for $WW \to e\nu e\nu$ with BDT cut ≥ 240.

Type	MC Process	$N_{selected}$	Bkgd. %
Signal	$WW \to e\nu e\nu$	**60.5**	-
Decay to tau	$WW \to e\nu\tau\nu$	7.6	-
	$WW \to \tau\nu\tau\nu$	0.4	-
Background	**Total**	**13.4**	100.0%
	$t\bar{t}$	10.84	80.6%
	Drell-Yan $\to \ell\ell$	1.5	11.2%
	$W^+Z \to \ell\nu\ell\ell$	0.55	4.1%
	$W^-Z \to \ell\nu\ell\ell$	0.41	3.1%
	others	0.15	1.1%

physics paper.)

- 3% PDF errors.
- 5% scaling uncertainty (for NLO calculations)
- 3% uncertainty on lepton identification acceptance (both for electrons and for muons)
- 15% background estimate uncertainties mainly due to limited MC data sample statistics. (Our current background statistical uncertainties range from 12% to 18%. Tevatron experiments have used data to estimate the background: typical uncertainties for diboson physics analysis are around 10% for 1 fb^{-1} data.)
- 5% uncertainty due to energy scale uncertainties (considering initially 10% on hadronic energy and 3% on lepton energy, which could contribute to uncertainties in cross section measurements ranging from 3% to 7% based on Tevatron and our studies).

We have used Log-likelihood method to 'fit' the W^+W^- production cross sections for different integrated luminosities. The MC experiments were run 100 times to determine the measurement uncertainties. The procedure is briefly described below.

- Use the binned Log-likelihood function based on BDT output spectra for signal and background :

$$-2\,Ln\,L \;=\; -2\,Ln\prod P_i(N_{obs};\; N_S(\sigma)+N_B),\;\; i=1,N_{bin}$$

  where $P(n;\lambda)=\lambda^n e^{-\lambda}/n!$ is the Poisson distribution function, λ is the mean value of the expected signal plus background events, n is the 'observed' number of events. Please note that the expected number of signal N_S is a function of the WW production cross section (σ).

- The 'observed' events are randomly selected from MC samples (based on Poisson distributions) with additional 9.2% systematic errors add to the 'data' selection. By varying the cross section the maximum likelihood function value is found. The corresponding cross section value represents the 'measured' cross section.
- Run the MC experiment 100 times with different 'observed-data' to fit the W^+W^- production cross sections. The standard deviation (RMS) of 100 fitted cross section distributions is taken as the measurement error.

The MC experiment *BDT* output spectra are shown in Figure 16 for $W^\pm W^\mp \to e^\pm \nu \mu^\mp \nu$ detection. The left plot shows 'data' for 0.1 fb^{-1} integrated luminosity (dots) compared to MC expected 'signal' (red histogram) and 'background' (blue histogram). The right plot shows the same for 1 fb^{-1} integrated luminosity.

To understand the optimal cut on the *BDT* spectra for cross section measurement, the cuts on the *BDT* spectra were varied and the cross section measurement was performed. Figure 17 (left plot) shows the cross section measurement error as a function of the BDT cut for different integrated luminosities. The optimal *BDT* cut is around 200. The right plot of the Figure 17 shows the relative errors as a function of integrated luminosity (with *BDT* spectrum cut at 200). Here the systematic error starts to dominate after 5 fb^{-1} integrated luminosity.

Following the same procedure as described above, the same studies were conducted for $W^+W^- \to \mu^+\nu\mu^-\nu$ detection. Figure 18 shows MC experimental *BDT* spectra for $\mu^+\mu^- + \not\!\!E_T$ final state. Figure 19 shows cross section uncertainty studies related to the *BDT* cuts and to the integrated luminosities.

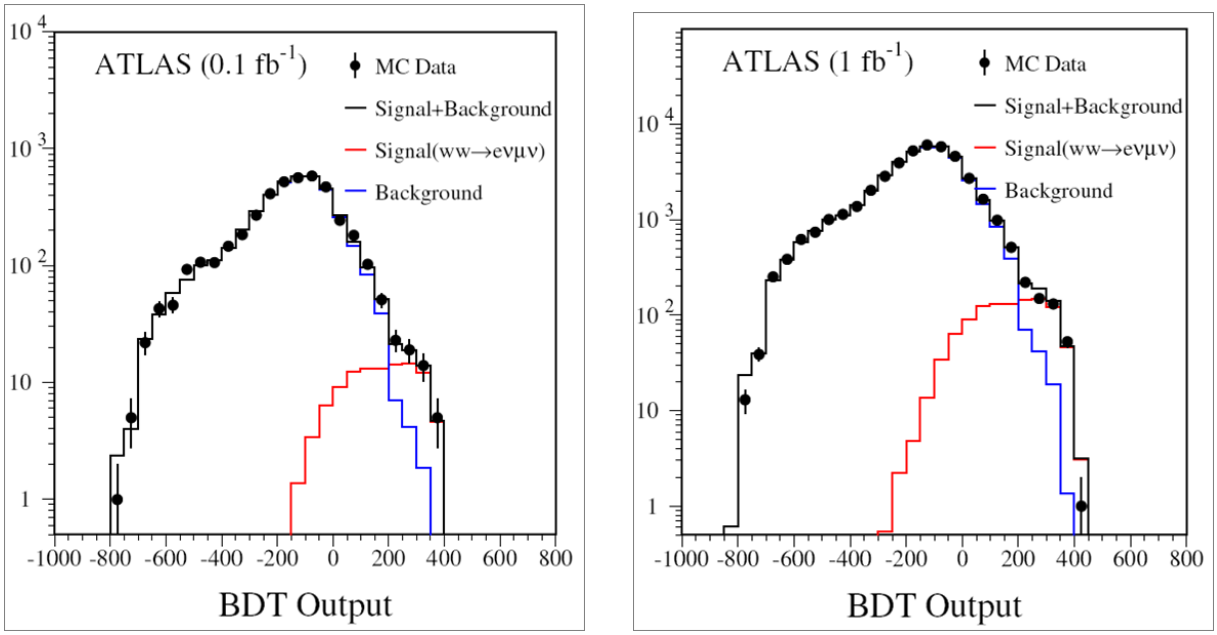

Figure 16: MC experiment *BDT* output spectra for $W^{\pm}W^{\mp} \rightarrow e^{\pm}\nu\mu^{\mp}\nu$ detection. The left plot shows 'data' for 0.1 fb^{-1} integrated luminosity (dots) compared to MC expected 'signal' (red histogram) and 'background' (blue histogram). The right plot shows the same for 1 fb^{-1} integrated luminosity.

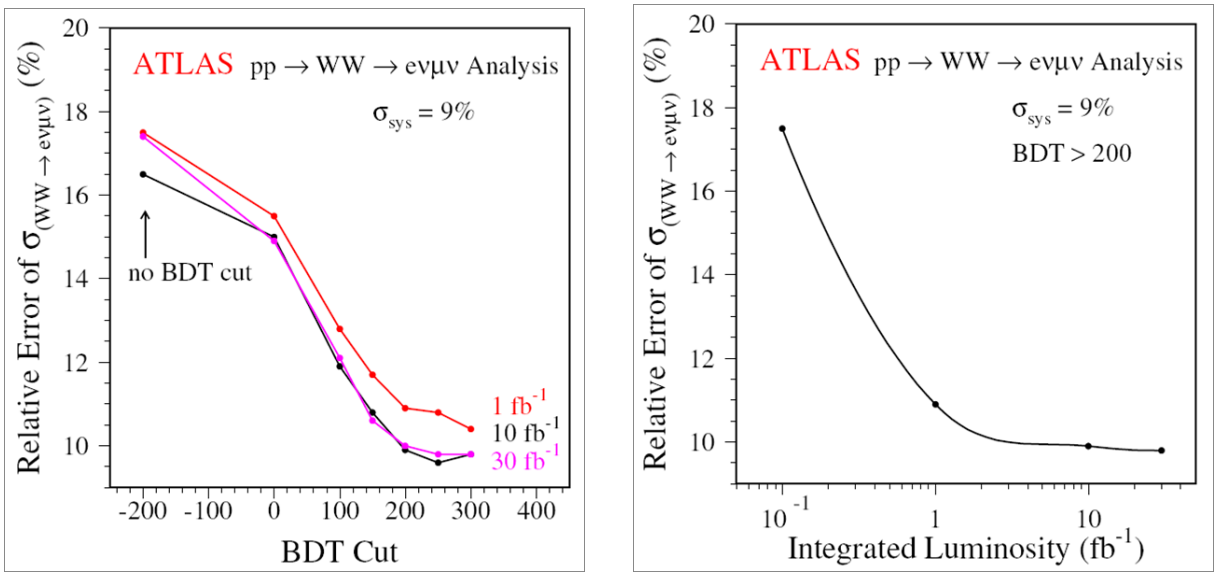

Figure 17: Left plot: the relative errors for cross section measurement as a function of the BDT cut. The optimal BDT spectrum cut should be around 200. Right plot: the relative errors as a function of integrated luminosity (with BDT spectrum cut at 200). From this plot, we see that systematic error starts to dominate after 5 fb^{-1} integrated luminosity.

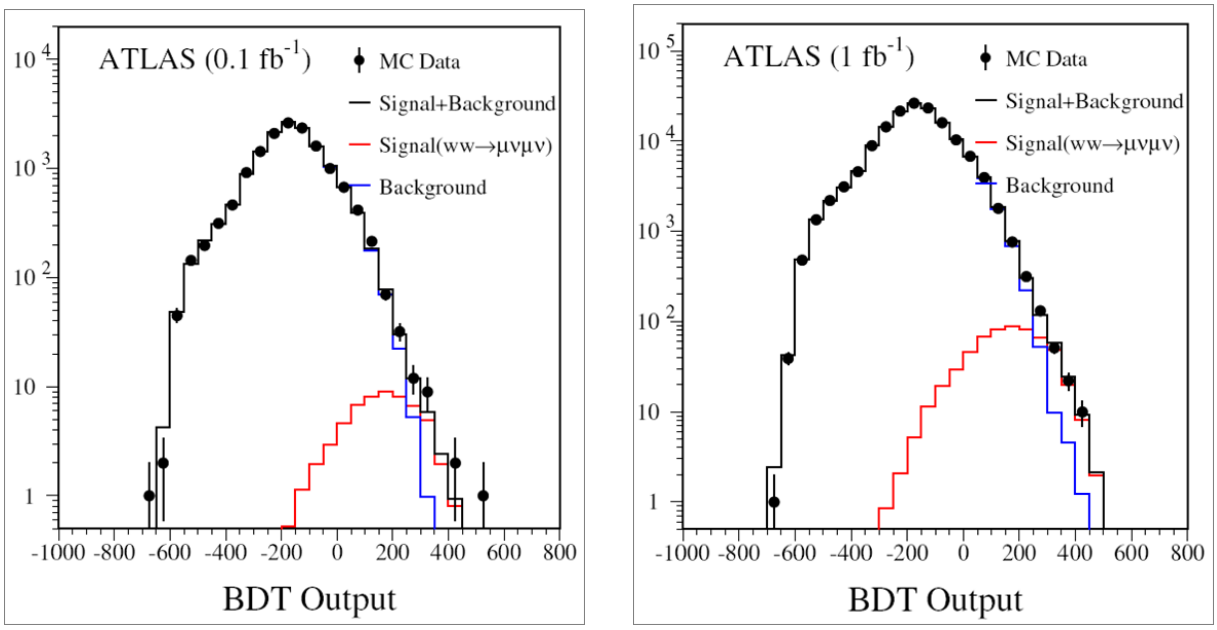

Figure 18: MC experiment *BDT* output spectra for $W^+W^- \to \mu^+\nu\mu^-\nu$ detection. The left plot shows 'data' for 0.1 fb^{-1} integrated luminosity (dots) compared to MC expected 'signal' (red histogram) and 'background' (blue histogram). The right plot shows the same for 1 fb^{-1} integrated luminosity.

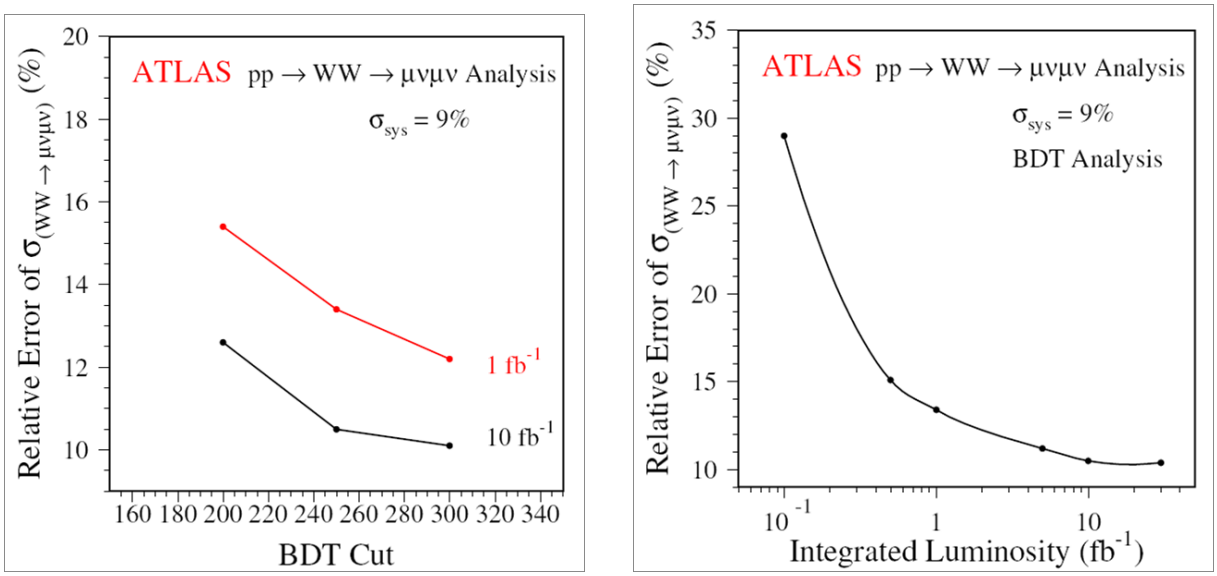

Figure 19: Left plot: the relative errors for cross section measurement as a function of the *BDT* cut. The optimal *BDT* spectrum cut should be around 240. Right plot: the relative errors as a function of integrated luminosity (with the *BDT* spectrum cut at 240). From this plot, we see that systematic error starts to dominate after 10 fb^{-1} integrated luminosity.

4.6 Sensitivity to charged anomalous couplings

Studies of W^+W^- production allow measurement of both the WWZ and the $WW\gamma$ couplings. At present, theory and experiments (at LEP) are in agreement to within 3-10% [4]. From our study, we expect that LHC could improve the sensitivity significantly with the first 10 - 30 fb^{-1} integrated luminosities. In this section we describe the **re-weighting** method and the results from this method for anomalous TGCs. Another study whose results are included in an appendix, has used fast simulation method.

4.6.1 Re-weighting and fitting method

To study the the anomalous couplings, the W-pair transverse mass ($M_T(WW)$) spectrum is fitted. The method used to determine the anomalous coupling sensitivity intervals is described below.

- Generate the $W^+W^- \to \ell^+\nu\ell^-\nu$ events in a coupling parameter space (*grid*). Each point of the grid corresponds to a pair of coupling parameters. Monte Carlo events are produced with the *BHO* NLO generator [21], which has the capability to produce events with non-SM values of the WWZ and $WW\gamma$ couplings. 5 million events per grid-point with pre-filter cut ($p_T^\ell > 20$ GeV, $|\eta^\ell| < 2.7$) were generated. The *BHO* generator has been cross-checked to be consistent with the *MC@LNO* generator using the SM couplings. The output of the *BHO* MC program in each *grid* point is a set of distributions of the differential cross sections of $d\sigma/dp_T(V)$ and $d\sigma/dM_T(VV)$.

- Each fully simulated event is *re-weighted* at generator level based on $p_T(V)$ and $M_T(VV)$ distributions. The *weight* is determined by differential cross section ratio,

  $$\text{weight} = d\sigma(\text{non-SM})/d\sigma(\text{SM}).$$

  Examples can be found in Figure 20, which shows (left plot) the transverse mass distributions of the W-pair for the SM couplings compared to anomalous couplings, and (right plot) the corresponding differential cross section ratio, which will be used to re-weight the events.

- Event selection using the *BDT* algorithm. For $WW \to e\nu\mu\nu$ process, the *BDT* output is cut at greater than 210, resulting in $\nu_s = 393.6$ and $\nu_b = 69.4$. An MC 'observation' is simulated by pulling selected signal events with Poisson fluctuations from an independent subset of the sample corresponding to a desired integrated luminosity. The background 'observation' is simulated by using the total background M_T or p_T distributions with Poisson bin-by-bin fluctuations. Following this procedure the 'observation': $n = n_s + n_b$ is made for in each bin for likelihood function calculations. For example, Figure 21 and 22 show the MC experiment WW transverse mass distributions for 0.1 and 1 fb^{-1} integrated luminosities. The 'cross' shown in the plots are 'observations', the expected background, and signal+background with SM prediction superimposed with anomalous coupling predictions are shown as histograms in the plots. The last bin of the plots are the 'overflow'-bin.

- Finally, the Log-likelihood is fit in anomalous coupling space with the quadratic functions. Figure 23 shows the one dimensional anomalous coupling parameter fits with 1 fb^{-1} MC data. The same fitting procedure is followed for 0.1, 1.0, 10.0 and 30.0 fb^{-1} MC data. For one-dimensional fitting,only one parameter is varied; the remaining parameters are fixed to SM values.

4.6.2 Charged anomalous TGC sensitivity in W^+W^- analysis

One dimensional anomalous coupling sensitivity intervals at 95% CL are given Table 26. The cutoff $\Lambda = 2TeV$ is used in our calculations. For two-dimensional AC limits from the W^+W^- production the following scenarios relating the anomalous coupling parameters have been investigated:

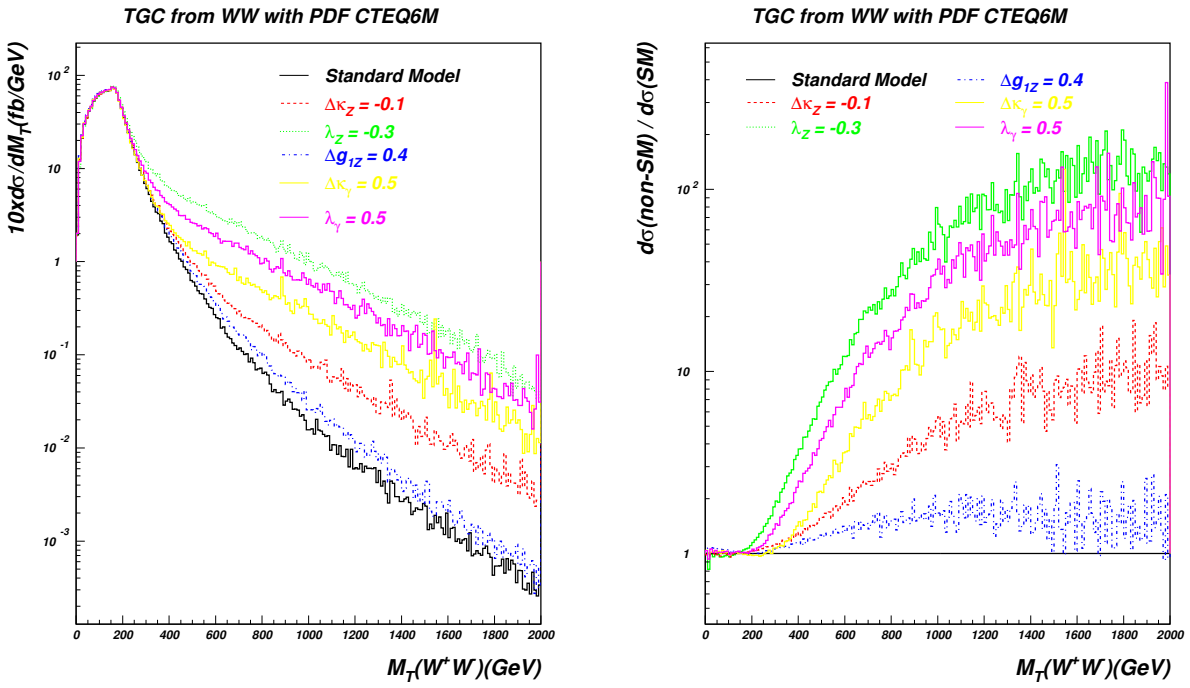

Figure 20: Left: WW transverse mass, M_T, distributions. Events are generated with the SM coupling (black) and anomalous couplings (color); Right: the corresponding differential cross section ratio, $d\sigma(non-SM)/d\sigma(SM)$.

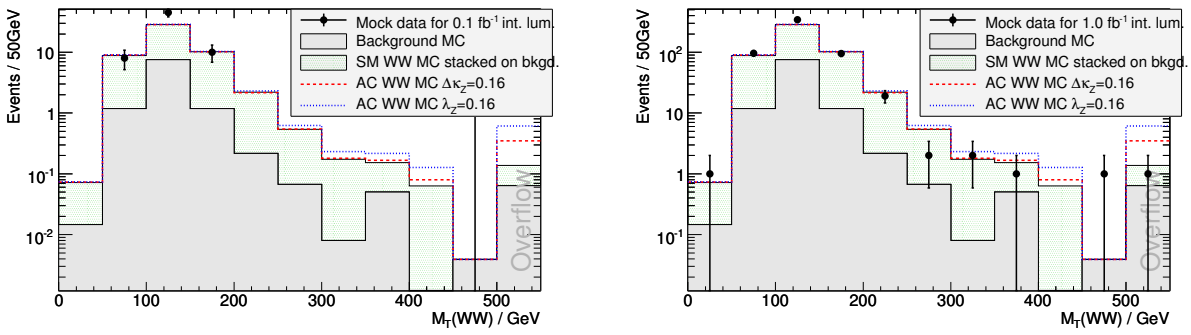

Figure 21: the MC experiment WW transverse mass distributions for 0.1 (left) and 1 fb^{-1} (right) integrated luminosities. The last bins in the plots are 'overflow'-bins.

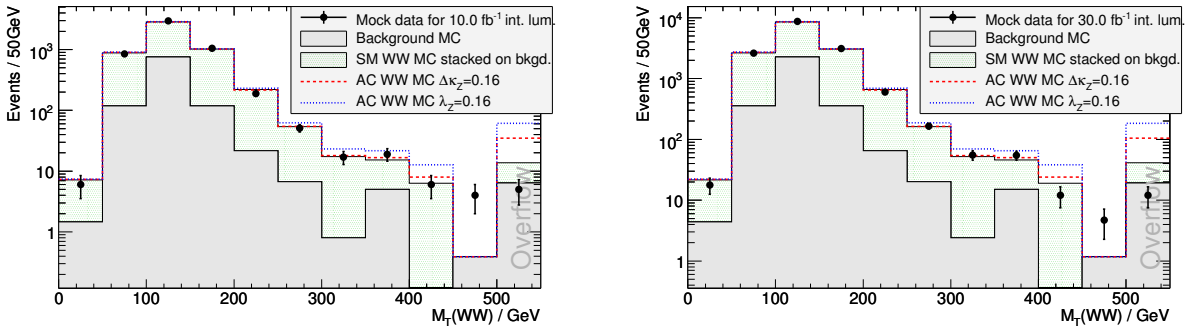

Figure 22: The MC experiment WW transverse mass distributions for 10 (left) and 30 fb^{-1} (right) integrated luminosities. The last bins in the plots are 'overflow'-bins.

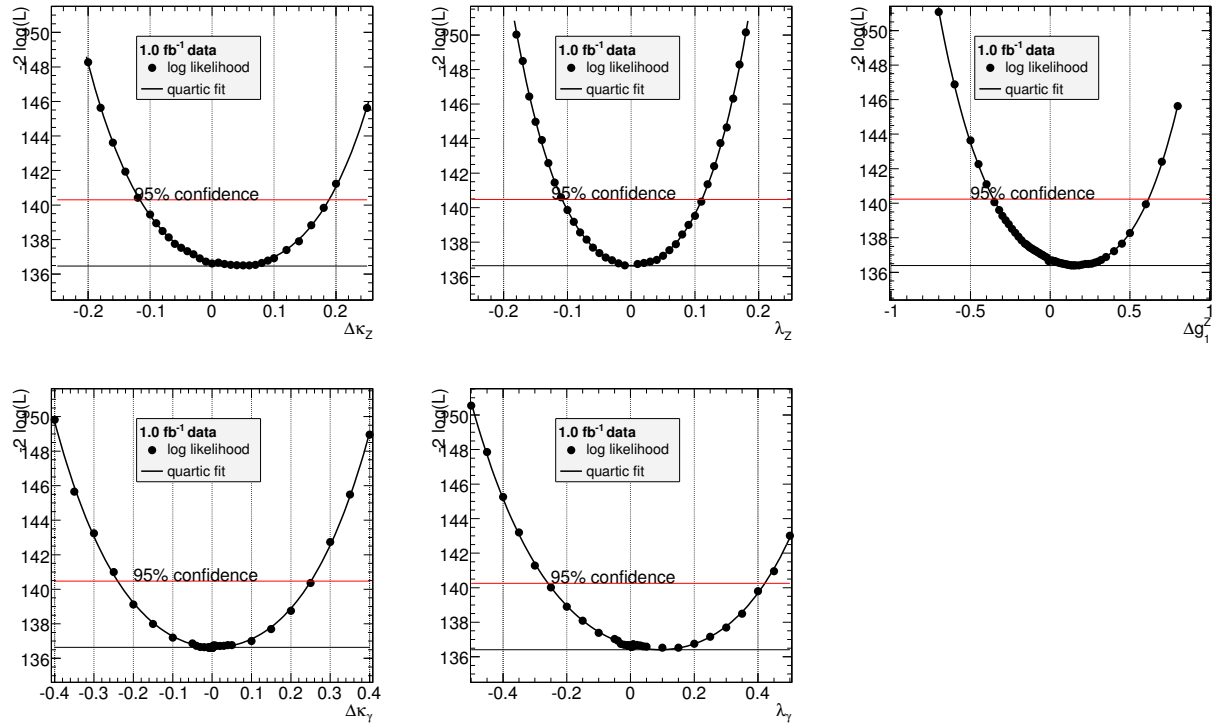

Figure 23: Anomalous coupling parameters Likelihood fitting for 1 fb^{-1} MC data.

Table 26: One-dimensional 95% C.L. interval of the anomalous coupling sensitivities from the WW final state analysis for 0.1, 1.0, 10.0 and 30.0 integrated luminosities.

Int. Lum. (fb^{-1})	$\Delta\kappa_Z$ 95% conf.	λ_Z 95% conf.	Δg_1^Z 95% conf.	$\Delta\kappa_\gamma$ 95% conf.	λ_γ 95% conf.
0.1	[-0.242, 0.356]	[-0.206, 0.225]	[-0.741, 1.177]	[-0.476, 0.512]	[-0.564, 0.775]
1.0	[-0.117, 0.187]	[-0.108, 0.111]	[-0.355, 0.616]	[-0.240, 0.251]	[-0.259, 0.421]
10.0	[-0.035, 0.072]	[-0.040, 0.038]	[-0.149, 0.309]	[-0.088, 0.089]	[-0.074, 0.165]
30.0	[-0.026, 0.048]	[-0.028, 0.027]	[-0.149, 0.251]	[-0.056, 0.054]	[-0.052, 0.100]

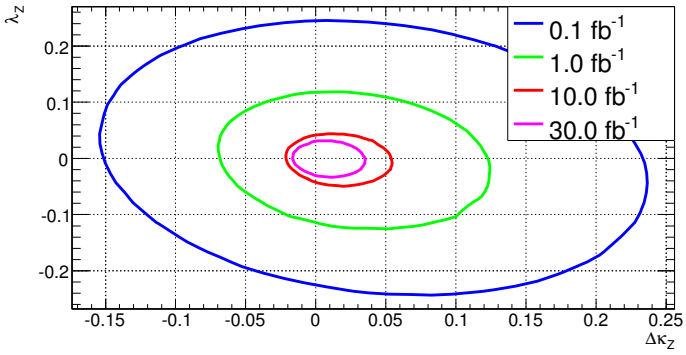

Figure 24: Two-dimensional anomalous coupling parameters fitting for 0.1 - 30 fb^{-1} MC data based on the HISZ assumption to relate the coupling parameters.

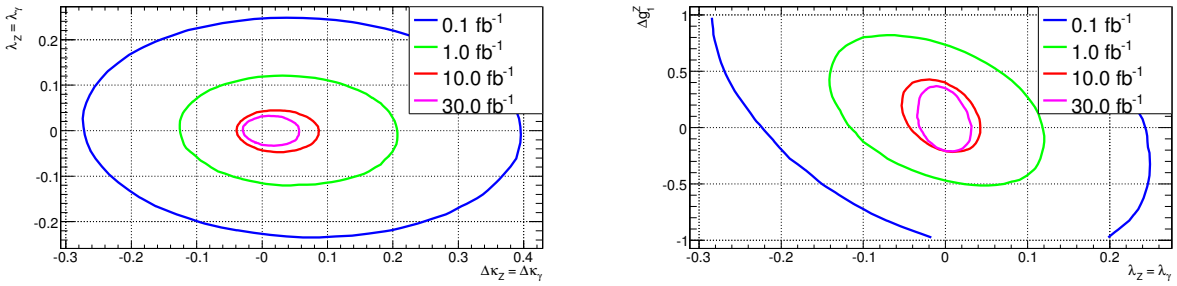

Figure 25: Two-dimensional anomalous coupling parameters fitting for 0.1 - 30 fb^{-1} MC data. For these fit, we have assumed $Z = \gamma$ in parameter space: $\Delta\kappa_Z = \Delta\kappa_\gamma$, $\lambda_Z = \lambda_\gamma$.

- The simplest HISZ scenario [26] with only two free parameters.

$$\Delta g_1^Z = \Delta\kappa_Z\,(C-S), \quad \Delta_\gamma = 2\Delta\kappa_Z C/(C-S), \quad \lambda_Z = \lambda_\gamma.$$

  where $C = cos^2\theta_W$, $S = sin^2\theta_W$. Figure 24 shows the two-dimensional anomalous coupling parameter fit using the HISZ assumption.

- Assume Z and γ parameters are the same. This has three free parameters.

$$\Delta\kappa_Z = \Delta\kappa_\gamma, \quad \lambda_Z = \lambda_\gamma.$$

  Figure 25 shows the two-dimensional Anomalous coupling parameter fit based on this assumption.

There are other assumptions related to WWZ and $WW\gamma$ anomalous couplings used in LEP and in Tevatron studies, such as

- the "LEP assumption". This has three free parameters.

$$\Delta\kappa_\gamma = (C/S)(\Delta g_1^Z - \Delta\kappa_Z), \quad \lambda_Z = \lambda_\gamma \quad \text{where} \quad C = cos^2\theta_W, \quad S = sin^2\theta_W,$$

- No constrains on the anomalous coupling parameters.

4.7 Summary of W^+W^- production studies

In this section a study of ATLAS W^+W^- detection sensitivity based on 30 million fully simulated Monte Carlo events has been presented. A straight cut analysis predicts that for the first 100 pb^{-1} integrated luminosity ATLAS experiment could detect $\sim$11 dilepton plus large missing E_T events as W^+W^- event candidates. The W^+W^- signal purity should be better than 80%. Using the Boosted Decision Trees we expect to detect ~ 72 $\ell^+\ell^- + \not\!\!E_T$ events with signal purity better than 85%.

Using the maximum likelihood method and one-dimensional fittings, we could set the 95% confidence limits on the anomalous coupling parameters as the following:

$$-0.026 < \Delta\kappa_Z < 0.048, \quad -0.028 < \Delta\lambda_Z < 0.027, \quad -0.149 < \Delta g_1^Z < 0.251,$$

$$-0.056 < \Delta\kappa_\gamma < 0.054, \quad -0.052 < \Delta\lambda_\gamma < 0.100$$

with 30 fb^{-1} integrated luminosity. Notice that from the W^+W^- diboson production one can obtain better $\Delta\kappa$-type parameter limits compared to that from the WZ and $W\gamma$ production studies. However, better λ-type parameters can be obtained from WZ and $W\gamma$ diboson final state studies.

5 $W^{\pm}Z^0$ production and the $W^+W^-Z^0$ coupling

5.1 $W^{\pm}Z^0$ signal and background at LHC

5.1.1 Production mechanism and cross section

The $W^{\pm}Z^0$ production at hadron colliders is exclusively the result of the $W^+W^-Z^0$ trilinear gauge boson couplings. The SM tree-level Feynman diagrams are shown in Figure 26.

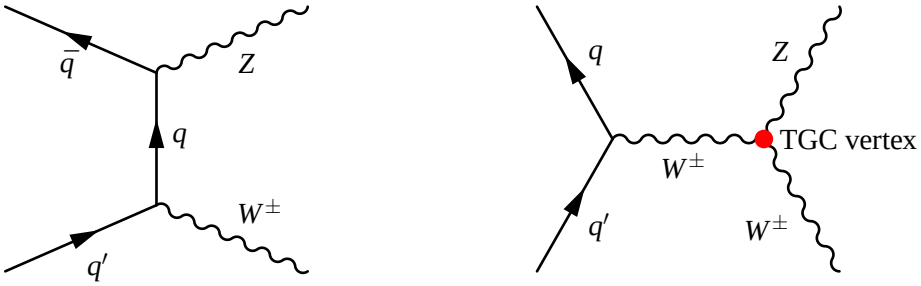

Figure 26: The SM Tree-level Feynman diagrams for $W^{\pm}Z^0$ production in hadron colliders. The $s-$channel diagram, on the right, contains the $W^+W^-Z^0$ trilinear gauge boson vertex of interest.

The $W^+W^-Z^0$ gauge coupling, on which the production cross section $\sigma(pp \to W^{\pm}Z^0)$ depends, is predicted by the SM to be $-e\cot\theta_W$, where e is the positron charge and θ_W is the weak mixing angle. The SM predicts the total W^+Z^0 production cross section to be 29.4 pb and the W^-Z^0 production cross section to be 18.4 pb [15], [16]. The difference between $\sigma(W^+Z^0)$ and $\sigma(W^-Z^0)$ is due to the parton density function (PDF) difference between the quarks that can pair to produce positively and negatively charged states at the proton-proton LHC. Compared to the Tevatron $W^{\pm}Z^0$ production cross section, $3.68 \pm 0.25 pb$ at $\sqrt{s}$=1.96 TeV, the $W^{\pm}Z^0$ production cross section at the LHC with $\sqrt{s}$ = 14 TeV will be more than 10 times higher. Thus, ATLAS should have much better sensitivity to the anomalous couplings compared to the Tevatron experiments.

Table 27: Monte Carlo $W^{\pm}Z^0$ *signal* datasets used in the $W^{\pm}Z^0$ analysis. The leptonic decay channels include two lepton flavors: electrons and muons. The cross sections are scaled by 3.5% based on cross sections calculated by *MC@NLO*. This is accounts for additional trilepton events due to $Z^0/\gamma*$ interference within the Z^0-mass window: $M_{Z^0} \pm 15\ GeV$.

Process	$\sigma_t \times Br$ (fb)	Number of events	dataset number
$W^+Z \to \ell^+\nu\ell^+\ell^-$	441.7	50,000	5941
$W^-Z \to \ell^-\nu\ell^+\ell^-$	276.4	50,000	5971

5.1.2 Experimental signals and background

This analysis focuses on the pure leptonic decay channels of the $W^{\pm}Z^0$ events,

$$W^{\pm}Z^0 \to e^{\pm}\nu e^+e^-, \quad \mu^{\pm}\nu e^+e^-, \quad e^{\pm}\nu\mu^+\mu^-, \quad \mu^{\pm}\nu\mu^+\mu^-.$$

These channels, although with only a total 1.5% branching ratio, have the cleanest experimental signature. Experimentally, we are looking for events with three high p_T (transverse momentum) leptons plus

missing transverse energies ($\not\!\!E_T$) due to final state neutrinos. The analysis method therefore requires high lepton identification efficiencies, and high rejection power of fake leptons and $\not\!\!E_T$ from other SM processes.

Major background for $W^{\pm}Z^0 \to \ell^{\pm}\nu\ell^+\ell^-$ signal come from the following processes:

- $Z^0Z^0 \to \ell^+\ell^-\ell^+\ell^-$ with one lepton undetected;
- $Z^0 + jets \to \ell^+\ell^- + X$ with a jet faking a lepton;
- $t\bar{t} \to W^+W^-b\bar{b} \to \ell + \ell + \ell + X$;
- $Z^0 + \gamma \to \ell^+\ell^- + X$ with a photon fake an electron.

Monte Carlo samples for signal and background used in $W^{\pm}Z^0$ analysis are listed in Table 28. The diboson and $t\bar{t}$ events were generated using *MC@LNO* generator (v3.1). The parton-shower and underlying events are simulated with the *HERWIG* and *Jimmy* programs. Detector simulation, digitization and reconstructions are done with ATLAS software release 12.0.6.4. No pre-filter has been applied to MC generated events for simulations. Other background ($Z^0 + X$) events are generated with *PYTHIA* program. The detector simulations, digitizations and reconstructions for those background events are done with software release 11.0.42.

5.2 Analysis

In following sections, we will first describe the physics objects (electron, muon, $\not\!\!E_T$ and jets) identification and lepton selection efficiencies. Following that we will show in detail the $W^{\pm}Z^0$ event selection criteria, based on pre-selection and final selections:

- Pre-selection with relatively loose cuts.
- Further selection with
  - Tightened straight cuts.
  - The Boosted Decision Trees (*BDT*) technique.

Finally, based on the expected signal and background from the $W^{\pm}Z^0$ event selection, we determine the $W^{\pm}Z^0$ cross section measurement uncertainties, and extract the ATLAS experiment sensitivities to the $W^+W^-Z^0$ anomalous couplings as a function of integrated luminosities.

5.3 $W^{\pm}Z \to \ell^{\pm}\nu\ell^+\ell^-$ analysis

5.3.1 Lepton identification efficiency determined by tag-probe method.

The major physics objects used in $W^{\pm}Z^0$ analysis are electrons, muons, $\not\!\!E_T$, and hadronic jets. We use the same methods of object reconstructions and identifications as described in the W^+W^- analysis section except that the lepton isolation cuts are applied during the event selection process. In this section we present the muon identification efficiencies using a **tag-probe** method which has been used at Tevatron data analysis (see Section 3.1.1).

The fully reconstructed final states from Z^0 decay offer distinct advantages. In particular, muon identification efficiencies can be determined with a *'tag and probe'* method using $Z^0 \to \mu^+\mu^-$ events. In this method one of the muons, passing tightened selection cuts, is used as a *tag* while the other muon is used as a *probe* to determine the selection efficiencies. Figure 27 shows the muon detection efficiency as a function of muon p_T and as a function of muon η. For comparison we also show the

muon reconstruction efficiencies obtained from the MC *truth* information where a muon is considered reconstructed if its track is matched to the *truth* track within an η - ϕ cone of $\Delta R = 0.01$. We see that muon identification efficiencies determined by both methods agree very well. A similar technique may also be used to determine electron identification efficiency.

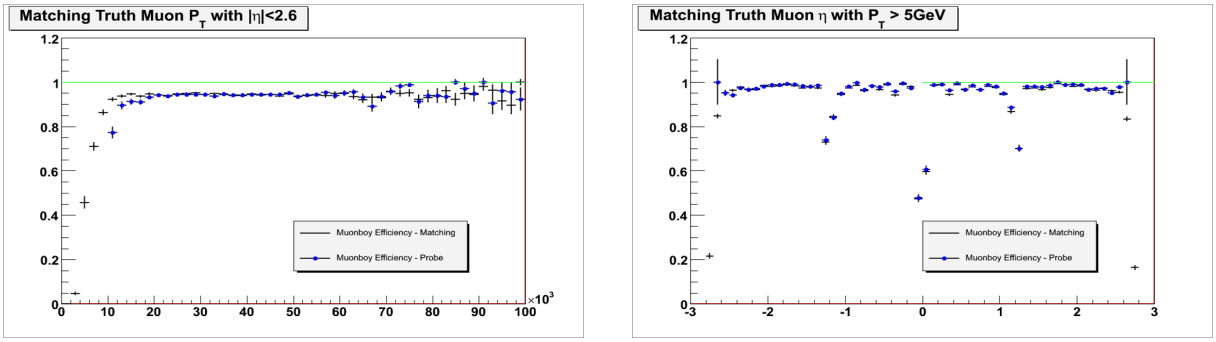

Figure 27: (a) left: the muon reconstruction efficiency as a function of muon p_T, (b) right: the muon reconstruction efficiency as a function of rapidity η.

5.3.2 Pre-selection of the $W^{\pm}Z^0$ events

The pre-selection of the $W^{\pm}Z^0$ events is done by identifying three leptons and $\not\!\!E_T$ in an event with characteristics consistent with Z boson dilepton decays and W boson leptonic decays. The pre-selection criteria are:

- Select at least three leptons from electrons and muons as in the W^+W^- Section excluding the isolation cuts. All leptons have transverse momentum $p_T > 6$ GeV, while at least one has $p_T >$ 25 GeV.
- Missing $E_T > 15$ GeV.
- Identify a Z^0-boson by invariant mass matching:
  The best invariant mass from e^+e^- or from $\mu^+\mu^-$ pairs must be within (91.18 ± 20) GeV.
- Identify a W-boson:
  The third lepton (not associated to the Z^0) must have $p_T > 15$ GeV, and the transverse mass, (M_T) determined by the third lepton and the $\not\!\!E_T$ falls in the range 10 GeV to 400 GeV.

The overall pre-selection efficiency for W^+Z^0 events is 25.8%, and for W^-Z^0 events is 29.3%. The difference of the acceptance for $W^{\pm}Z^0$ and for W^-Z^0 is due the leptons decay from W^+ and W^- have different η distributions. Table 28 summarizes the signal and background pre-selection results, while the figures below show distributions of signal superimposed with background after the pre-selection.

The overall trigger efficiency for $W^{\pm}Z^0$ events with trileptons in final state is 98.86% which is determined by combining the single lepton and dilepton triggers.

- Figure 28 shows (a) the lepton p_T distributions associated with the Z^0 decay final state, and (b) lepton p_T distributions selected from $W^{\pm}$ decays.
- Figure 29 shows (a) the missing transverse energy distributions, (b) $\Delta\phi$ between the missing E_T and the third lepton associated with $W^{\pm}$ decays.

Table 28: MC data samples used in $W^{\pm}Z^0$ analysis. The first column lists the physics process. The total cross sections, the k-factors, branching ratios for the generated MC events, the total produced and preselected number of MC events, and normalized number of events for 1fb^{-1} after pre-selection and the initial weights for BDT training are given.

MC process	$\sigma(fb)$	K	Br	N_{mc}	N_{precut}	N/fb	Weight
$W^+Z^0 \to \ell^+\nu\ell^+\ell^-$	0.2940×10^5	1.0	0.0144	26550	6848	136.4	0.0199
$W^-Z^0 \to \ell^-\nu\ell^+\ell^-$	0.1840×10^5	1.0	0.0144	17450	5118	88.7	0.0173
$ZZ \to \ell^+\ell^-\ell^+\ell^-$	0.1486×10^5	1.0	0.0045	35700	8597	20.4	0.0024
$t\bar{t} \to \ell + X$ $(McAtNlo, Jimmy)$	0.8330×10^6	1.0	0.5400	604750	1071	746.0	0.6966
$Z(\ell\ell)\gamma$	0.8910×10^6	1.5	0.0672	999742	111	10.0	0.0898
$\gamma\gamma$ $(Pythia)$	0.7100×10^5	1.0	1.0000	45300	0	0.0	1.5673
Drell-Yan$(\ell^+\ell^-)(30\ \mathrm{GeV} < M < 81\ \mathrm{GeV})$	0.4220×10^7	1.3	0.1010	1000000	16	8.9	0.5541
Drell-Yan$(\ell^+\ell^-)(81\ \mathrm{GeV} < M < 100\ \mathrm{GeV})$	0.4610×10^8	1.3	0.1010	3284999	406	748.1	1.8426
Drell-Yan$(\ell^+\ell^-)(M > 100\ \mathrm{GeV})$	0.1750×10^7	1.3	0.1010	971000	271	64.1	0.2366
$Z \to \mu^+\mu^-(Jimmy, M = 150GeV)$	0.1750×10^7	1.0	0.0336	43000	33	36.1	1.0940
$Z(\mu\mu) + JET$ $(Pythia)$	0.8270×10^6	1.0	0.0336	35000	20	12.7	0.6351
$Z \to e^+e^-(Pythia, p_t > 100GeV)$	0.8270×10^6	1.0	0.0336	46000	11	5.3	0.4833
$Z \to \mu^+\mu^-(Pythia, p_t > 100GeV)$	0.8270×10^6	1.0	0.0336	33000	42	28.3	0.6736
$Z \to \tau^+\tau^-(Pythia, p_t > 100GeV)$	0.8270×10^6	1.0	0.0003	32000	41	0.3	0.0069
$Z(ee) + JET$ $(E_T^j : 10-20\ \mathrm{GeV})$	0.1360×10^8	1.3	0.0336	597281	0	0.0	0.9946
$Z(ee) + JET$ $(E_T^j : 20-40\ \mathrm{GeV})$	0.8670×10^7	1.3	0.0336	398697	0	0.0	0.9499
$Z(ee) + JET$ $(E_T^j : 40-80\ \mathrm{GeV})$	0.4120×10^7	1.3	0.0336	397524	0	0.0	0.4527
$Z(ee) + JET$ $(E_T^j : 80-120\ \mathrm{GeV})$	0.8270×10^6	1.3	0.0336	397009	0	0.0	0.0910
$Z(ee) + JET$ $(E_T^j > 120\ \mathrm{GeV})$	0.3830×10^6	1.3	0.0336	198652	0	0.0	0.0842
$Z(\mu\mu) + JET$ $(E_T^j : 10-20\ \mathrm{GeV})$	0.1360×10^8	1.3	0.0336	2996413	492	97.5	0.1983
$Z(\mu\mu) + JET$ $(E_T^j : 20-40\ \mathrm{GeV})$	0.8670×10^7	1.3	0.0336	1995792	789	149.7	0.1898
$Z(\mu\mu) + JET$ $(E_T^j : 40-80\ \mathrm{GeV})$	0.4120×10^7	1.3	0.0336	1189793	1516	229.3	0.1513
$Z(\mu\mu) + JET$ $(E_T^j : 80-120\ \mathrm{GeV})$	0.8270×10^6	1.3	0.0336	397856	1105	100.3	0.0908
$Z(\mu\mu) + JET$ $(E_T^j > 120\ \mathrm{GeV})$	0.3830×10^6	1.3	0.0336	199832	1133	94.9	0.0837
$Z(\tau\tau) + JET$ $(E_T^j : 10-20\ \mathrm{GeV})$	0.1360×10^8	1.3	0.0336	598783	0	0.0	0.9921
$Z(\tau\tau) + JET$ $(E_T^j : 20-40\ \mathrm{GeV})$	0.8670×10^7	1.3	0.0336	399076	0	0.0	0.9490
$Z(\tau\tau) + JET$ $(E_T^j : 40-80\ \mathrm{GeV})$	0.4120×10^7	1.3	0.0336	398972	0	0.0	0.4511
$Z(\tau\tau) + JET$ $(E_T^j : 80-120\ \mathrm{GeV})$	0.8270×10^6	1.3	0.0336	396671	0	0.0	0.0911
$Z(\tau\tau) + JET$ $(E_T^j > 120\ \mathrm{GeV})$	0.3830×10^6	1.3	0.0336	199046	0	0.0	0.0840
$W^+W^- \to e^+\nu e^-\nu$	0.1116×10^6	1.0	0.0120	41950	9	0.3	0.0324
$W^+W^- \to e^+\nu\mu^-\nu$	0.1116×10^6	1.0	0.0120	45900	22	0.7	0.0296
$W^+W^- \to e^+\nu\tau^-\nu$	0.1116×10^6	1.0	0.0120	71000	7	0.1	0.0191
$W^+W^- \to \mu^+\nu e^-\nu$	0.1116×10^6	1.0	0.0120	47000	18	0.5	0.0289
$W^+W^- \to \mu^+\nu\mu^-\nu$	0.1116×10^6	1.0	0.0120	48950	30	0.8	0.0278
$W^+W^- \to \mu^+\nu\tau^-\nu$	0.1116×10^6	1.0	0.0120	44000	8	0.2	0.0309
$W^+W^- \to \tau^+\nu e^-\nu$	0.1116×10^6	1.0	0.0120	47700	2	0.1	0.0285
$W^+W^- \to \tau^+\nu\mu^-\nu$	0.1116×10^6	1.0	0.0120	45800	8	0.2	0.0297
$W^+W^- \to \tau^+\nu\tau^-\nu$	0.1116×10^6	1.0	0.0120	34850	0	0.0	0.0390

- Figure 30 shows (a) the dilepton invariant mass distributions associated with the Z^0 decay final state, and (b) the transverse mass distributions associated with $W \to \ell\nu$ process.
- Figure 31 shows (a) the p_T distributions of the $W^{\pm}Z^0$ system, and (b) the transverse mass distributions of the $W^{\pm}Z^0$ system.
- Figure 32 shows (a) the ϕ distributions of the $W^{\pm}Z^0$, and (b) the $\Delta\phi$ between the Z^0 and the $W^{\pm}$.
- Figure 33 shows the E_T^{had} (V_T) distributions, and (b) shows the scalar sum of all the particles' E_T (H_T) distribution.

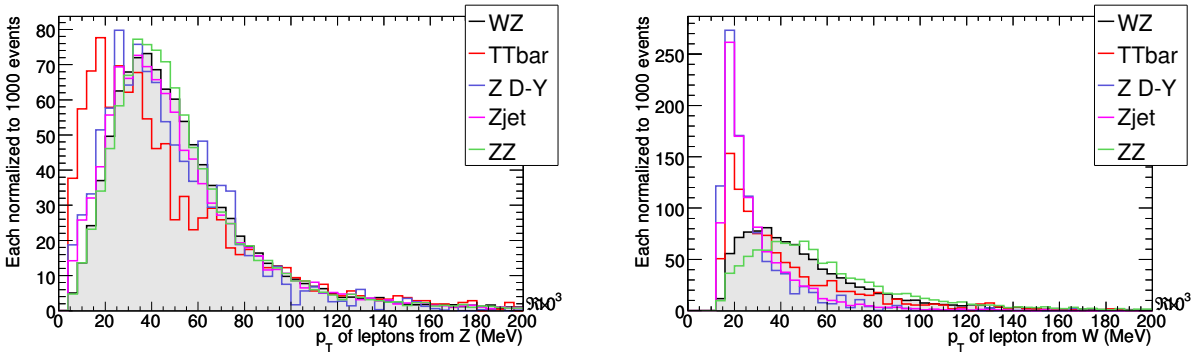

Figure 28: (a) left: the lepton p_T distributions associated with the Z-boson decays, (b) right: the lepton p_T distributions associated with the W-boson decays. Events are with pre-selection cuts without normalization.

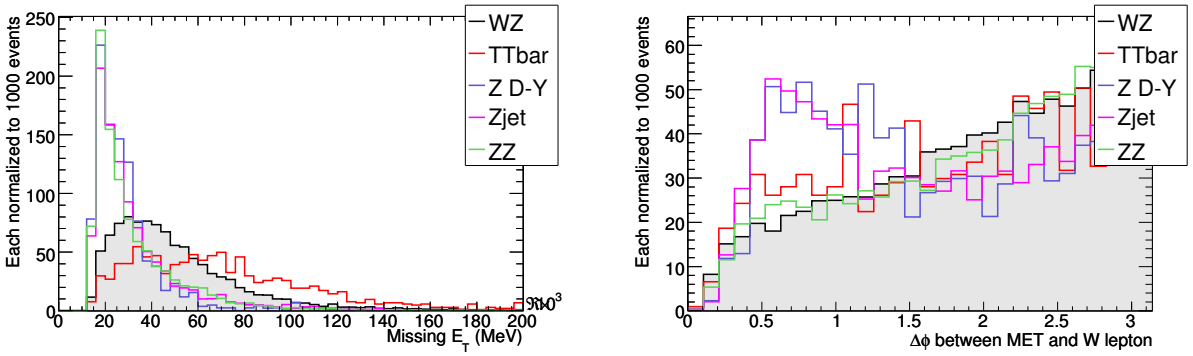

Figure 29: (a) left: Missing transverse energy ($\not\!\!E_T$) distributions, (b) right: $\Delta\phi$ between the third lepton and $\not\!\!E_T$. Events are with pre-selection cuts without normalization.

5.3.3 Final selection with tightened straight cuts

Based on pre-selected events, we further apply tightened cuts to event samples to optimize the detection sensitivity as gauged by the signal to background ratio. Our final cuts are listed below:

- Missing transverse energy: $\not\!\!E_T > 25$ GeV.

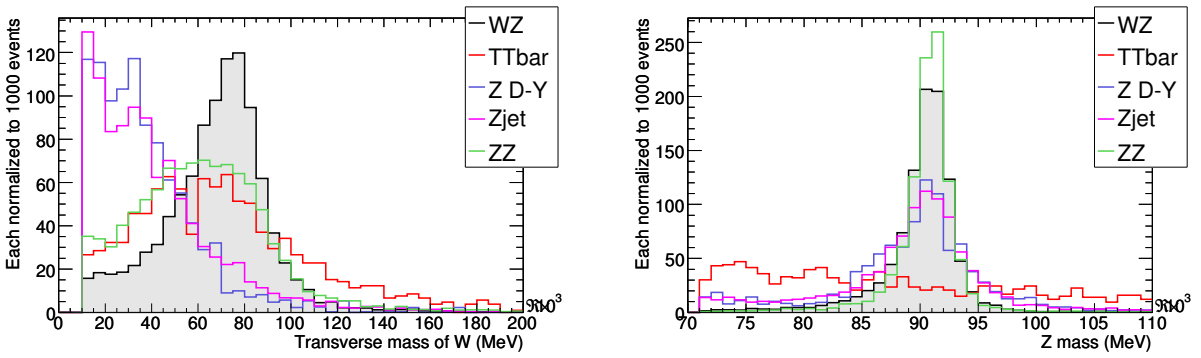

Figure 30: (a) left: the transverse mass distributions selected as the W-boson. (b) right: the dilepton invariant mass distributions selected as the Z-boson, Events are with pre-selection cuts without normalization.

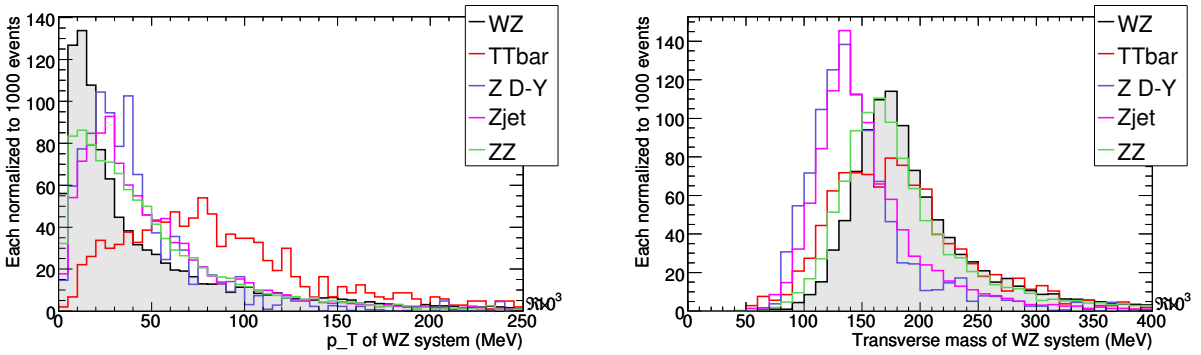

Figure 31: (a) left: the p_T distributions of the $W^{\pm}Z^0$ system, and (b) right: the transverse mass distributions of the $W^{\pm}Z^0$ system. Events are with pre-selection cuts without normalization.

- $E_T^{had} < 120$ GeV, where E_T^{had} is the vector-sum of the lepton $\vec{p}_T$ and MET.
  $E_T^{had} = (E_x^{had} \times E_x^{had} + E_y^{had} \times E_y^{had})^{\frac{1}{2}}$,
  where $E_x^{\rm had} = \sum(p_x(\ell) + \not\!\!E_{T_x})$; $E_y^{\rm had} = \sum(p_y(\ell) + \not\!\!E_{T_y})$.
- Total scalar sum of jet transverse energy < 200 GeV.
- Any pair of leptons must satisfy $\Delta R = \sqrt{(\Delta\eta^2 + \Delta\phi^2)} > 0.2$
- The sum of the additional p_T and the number of tracks found in a cone with $\Delta R = 0.4(0.5)$ around muons(electrons) must be less than 8 GeV and 4 respectively; no jet with $E_T > 10$ GeV can lie in the cone.
- The electron isolation energy fraction, $f = [E_T(\Delta R = 0.4) - E_T(\Delta R = 0.2)]/E_T^{\ell} < 10\%$.

The Z-boson is identified by requesting:

- Two leptons with $p_T^{\ell} > 10$ GeV have opposite charge sign and the same flavor.
- Dilepton invariant mass best matches to the mass of Z, and within the Z-mass window of $|M_Z - M_{\mu\mu}| < 12$ GeV, and $|M_Z - M_{ee}| < 9$ GeV.

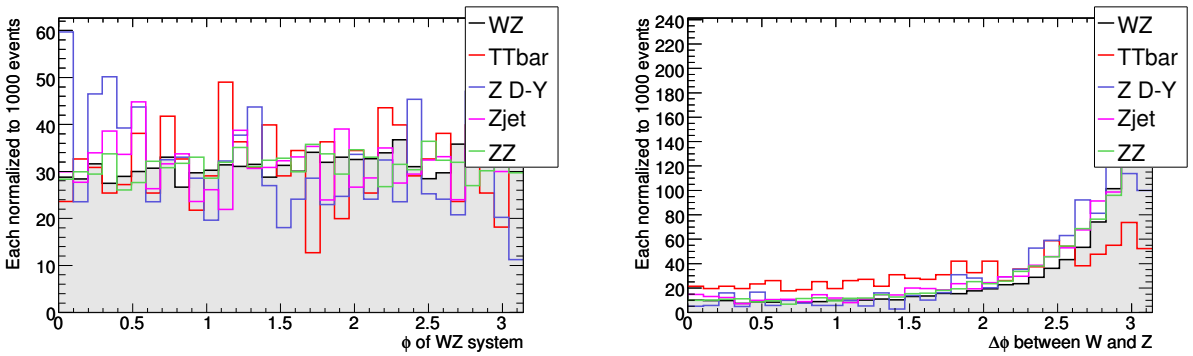

Figure 32: (a) left: the ϕ distributions of the $W^{\pm}Z^0$, and (b) right: the $\Delta\phi$ between the Z^0 and the $W^{\pm}$. Events are with pre-selection cuts without normalization.

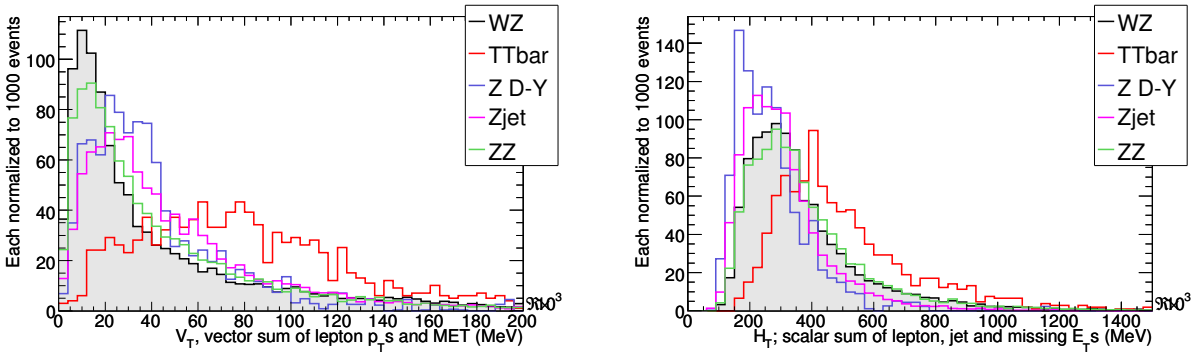

Figure 33: (a) left: the E_T^{had} (V_T) distributions, and (b) right: shows the scalar sum of all the particles' E_T (H_T) distribution. Events are with pre-selection cuts without normalization.

The $W^{\pm}$ is identified by applying following cuts:

- $p_T > 20,\ 25$ GeV for muon and electron, respectively.
- The transverse mass determined by the third lepton (not from Z^0 decay) and the $\not\!\!E_T$ must be within the W-mass window:
  40 GeV $< M_T <$ 120 GeV.
- The difference of the vertex position, represented by Z_0 and d_0, of the third lepton and the lepton pair from Z^0-decay must satisfy $\Delta Z_0 < 0.7$ *mm*, and $\Delta d_0 < 0.1$ *mm*.

The $W^{\pm}Z^0$ events are finally selected after following cuts are applied:

- $\Delta\phi$ between $W^{\pm}$ and Z^0 must be > 0.5 rad.
- The transverse mass of $W^{\pm}Z^0$, $M_T(W^{\pm}Z^0) > 70$ GeV.
- Maximum number of jets with $E_T^{jet} > 30$ GeV should not exceed 1.

The total and selected numbers of the signal and the background events for each trilepton final state are listed in Table 29. The overall signal acceptance is 8.7% and 7.1% for W^-Z^0 and W^+Z^0, respectively.

Table 29: Total and selected numbers of $W^{\pm}Z^0$ signal and background events by applying the straight cuts. The last column contains the acceptances for the signal and background.

Process	N_{MC}	$N_{eee\nu}$	$N_{ee\mu\nu}$	$N_{\mu\mu e\nu}$	$N_{\mu\mu\mu\nu}$	N_{sum}	N_{sum}/N_{MC}
ZW^-	147750	1562	2633	3571	5093	12859	8.70×10^{-2}
ZW^+	133674	1159	2134	2599	3600	9492	7.10×10^{-2}
ZZ	49250	64	550	99	1269	1982	4.02×10^{-2}
W^+W^-	525000	0	0	0	1	1	1.90×10^{-6}
$Z+jet$	1.08×10^7	0	0	9	6	15	1.39×10^{-6}
$Z+\gamma$	1.10×10^6	1	0	1	0	2	1.82×10^{-6}
DY	1.80×10^7	1	0	0	1	2	1.11×10^{-7}

Table 30: Number of expected $W^{\pm}Z^0$ signal (N_s) and background (N_b) for 1 fb^{-1} data with straight cut analysis.

Process	$N_{eee\nu}$	$N_{ee\mu\nu}$	$N_{\mu\mu e\nu}$	$N_{\mu\mu\mu\nu}$	N_{sum}
ZW^-	2.82	4.75	6.44	9.19	23.19
ZW^+	3.69	6.80	8.28	11.47	30.24
ZZ	0.0865	0.7438	0.1339	1.7160	2.68
W^+W^-	0	0	0	0.0228	0.0228
$Z+jet$	0	0	1.5451	0.9198	2.46
$Z+\gamma$	0.0898	0	0.0898	0	0.18
DY	1.3436	0	1.3436	0	2.69
Sum of signals (N_S)	6.51	11.55	14.72	20.65	53.43
Sum of backgrounds (N_B)	1.52	0.74	1.77	3.98	8.03
N_S/N_B	4.28	15.52	8.32	5.19	6.66

For 1 fb^{-1} integrated luminosity of data, we expect to observe 53 $W^{\pm}Z^0$ signal events and 8 background events, giving a signal to background ratio of about 6.7, as shown in Table 30.

The dominant background contributions are from ZZ, Z+Jet and Drell-Yan (DY) processes, while $Z+\gamma$ and WW contribute a small fraction of the total background events, as listed in Table 31.

Figure 34 shows dilepton invariant mass distributions, signal superimposed with background (left) and the Z-boson p_T distributions (right). Events are normalized to 1 fb^{-1} integrated luminosity.

Figure 35 shows the $W^{\pm}Z^0$ transverse mass distributions, signal superimposed with background (left) and the $W^{\pm}Z^0$ p_T distributions (right). Events are normalized to 1 fb^{-1} integrated luminosity.

5.3.4 Final selection based on the boosted decision tree technique

The Boosted-Decision-Trees (BDT) is a relatively new method used in high energy physics data analysis [2,3]. This technique has been applied to improve the discrimination power for signal and background separations. Detailed BDT parameters and the boosting algorithm used in this analysis are found in an appendix of this note. The following 22 variables are used in the BDT-based analysis for $W^{\pm}Z^0$ event selection.

- Transverse momentum of negative-charged lepton from Z^0 decay

Table 31: Relative background contribution to $W^{\pm}Z^0$ signal candidates from the straight cuts.

Process	DY	ZZ	Z+Jet	Zγ	WW
Relative contribution (%)	33.5	33.4	30.6	2.2	0.3

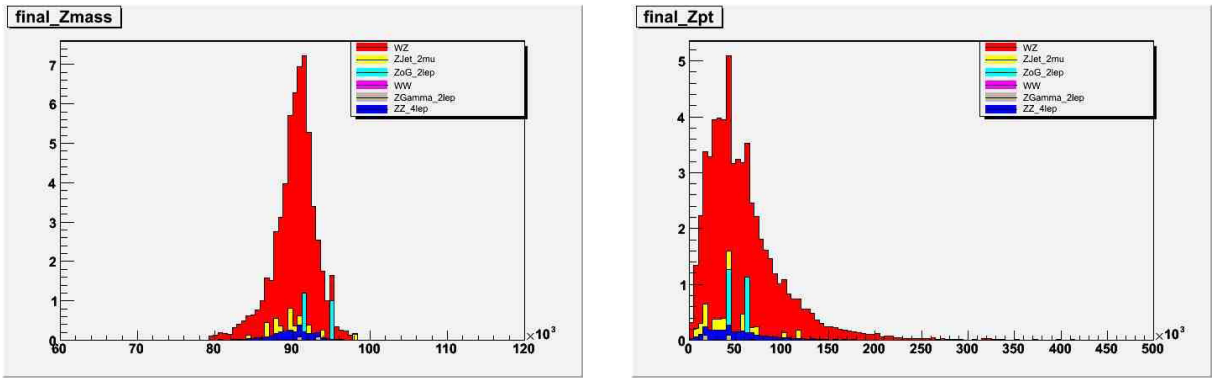

Figure 34: (a) left: Final selected dilepton invariant mass distributions. (b) right: $p_T(Z)$ distributions with final selection. Number of events are normalized to 1 fb^{-1}.

- Transverse momentum of positive-charged lepton from Z^0 decay
- Transverse momentum of charged lepton from $W^{\pm}$ decay
- Number of isolated tracks in a $\Delta R < 0.4$ cone around negative-charged lepton from Z^0 decay, $\Delta R = \sqrt{(\phi - \phi_\ell)^2 + (\eta - \eta_\ell)^2}$
- Number of isolated tracks in a $\Delta R < 0.4$ cone around positive-charged lepton from Z^0 decay
- Momentum of isolated tracks in a $\Delta R < 0.4$ cone around charged lepton from $W^{\pm}$ decay
- Number of isolated tracks in a $\Delta R < 0.4$ cone around charged lepton from $W^{\pm}$ decay
- Energy of isolated jets in a $\Delta R < 0.4$ cone around charged lepton from $W^{\pm}$ decay
- Fraction of energy = E($\Delta R < 0.4$)-E($\Delta R < 0.2$) / Transverse Momentum of charged lepton from $W^{\pm}$ decay
- Difference of $A0$ between positive charged lepton from Z^0 decay and lepton from $W^{\pm}$ decay
- Difference of ΔR between positive-charged lepton from Z^0 decay and lepton from $W^{\pm}$ decay
- Difference of $A0$ between negative-charged lepton from Z^0 decay and lepton from $W^{\pm}$ decay
- Difference of ΔR between negative-charged lepton from Z^0 decay and lepton from $W^{\pm}$ decay
- Missing Transverse Energy ($\not\!\!E_T$)
- p_T of the $W^{\pm}Z^0$ system

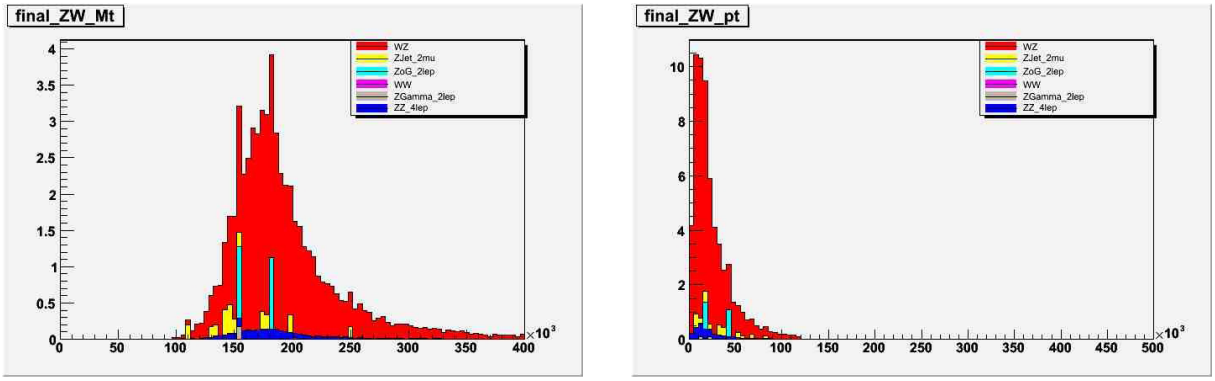

Figure 35: After the final tightened cuts, (a) left: the transverse mass of the $W^{\pm}Z^0$ system. (b) right: the transverse mass distributions of the $W^{\pm}Z^0$. both signal and background are normalized to 1 fb^{-1}.

- Invariant mass of two leptons from Z^0 decay
- Transverse mass of $W^{\pm}$
- Scalar sum of momentum from Jets, leptons and $\not\!\!E_T$
- Vector sum of momentum from Jets, leptons and $\not\!\!E_T$
- Vector sum of momentum from leptons and $\not\!\!E_T$
- $\not\!\!E_T$ / $\sqrt{}$(scalar sum of momentum of jets and leptons)
- The total recoil transverse energy

As shown in Table 28, about 12000 pre-selected signal events and 18000 pre-selected background events were used in the BDT-based analysis. 50% of signal and background events are used for the **training**, and another 50% of statistically independent events are used for the BDT **test** sample sets. The BDT output spectra from the testing sample are used as the 'discriminator' to separate the signals from the background as shown in Figure 36. In the spectra both signal and background events are normalized to an integrated luminosity of 1 fb^{-1}. Application of a cut at different values on the BDT output, determines the signal to background ratios in final selected event sample. For example, a cut at $BDT > 200$, gives a signal to background ratio of 10 as shown in Table 32, which lists the selection results with various BDT cuts: the selected number of signal (N_{ZW}) and number of background (N_{BKGD}) events, the corresponding signal efficiency (Eff$_{ZW}$) and the signal to background ratio (N_{ZW}/N_{Bkgd}). The listed number of events are normalized to a total integrated luminosity of 1 fb^{-1}. For comparison the results using the straight cuts analysis is also indicated.

We have used the binomial error formula to calculate the statistical uncertainties for signal and background events selection,

$$\sigma_{stat} = \sqrt{N_{\text{total}} \times \text{efficiency} \times (1 - \text{efficiency})},$$

where N_{total} is the total number of events for a certain process used in the analysis, and the $efficiency$ is the overall efficiency for the corresponding channel. Based on this expression the total background uncertainties listed in the table are calculated as

$$\sigma_{stat}^{all} = \sqrt{\sum_i w_i \times \sigma_i^2}$$

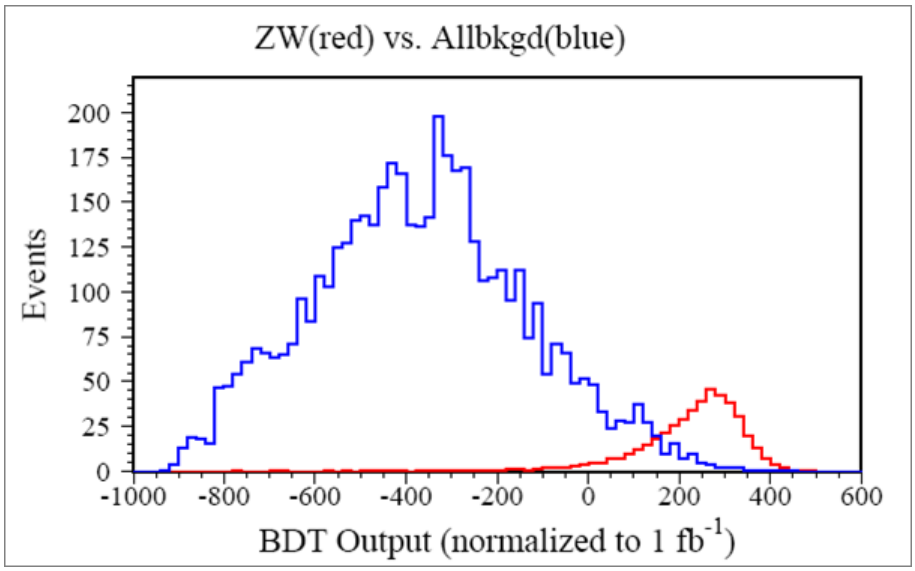

Figure 36: The *BDT* output distributions for signal (red histogram) and background (blue histogram). Events are normalized to an integrated luminosity of 1 fb^{-1}. A cut on the BDT output > 200, yields a signal to background ratio of about 10.

where w_i is the *weight* determined by the ratio of $\frac{N_i^{exp}}{N_i^{total}}$ passed the selection cuts. The N_i^{exp} denotes the expected MC events for the i^{th} process assuming 1 fb^{-1} luminosity. Table 32 indicates that the statistical errors on the signal are $\sim$ 1%, but the background errors are 15-20% due to the limited number of MC events available for this study.

After applying the BDT cuts, the breakdown of the events from four different decay channels, $ZW \rightarrow eee\nu$, $ee\mu\nu$, $\mu\mu e\nu$, $\mu\mu\mu\nu$, are listed in Table 33.

Compared to the straight cuts analysis technique, the BDT works significantly better. The signal to background ratio of the $W^{\pm}Z^0$ analysis could be improved from about 6.7 (from the straight cuts) to 10 $\sim$ 24 depending on the BDT cut value while the signal efficiency will be more than doubled.

The major background events for $W^{\pm}Z^0$ analysis come from $Z^0Z^0 \rightarrow 4\ell$, $t\bar{t}$ and $DY \rightarrow \ell^+\ell^-$ with mass around the Z^0-peak. There are some spikes in the background distributions due to relatively low statistics in some of the background channels which results in a relatively large uncertainty in the background estimation.

Figure 37 shows the distribution of the transverse mass of the $W^{\pm}Z^0$ and the corresponding efficiency, and Figure 38 shows the transverse momentum of the Z^0 from $W^{\pm}Z^0$ and the corresponding efficency. These plots indicate that the event selection with the *BDT* analysis preserves high signal efficiencies in high $P_T(Z^0)$ and high $M_T(W^{\pm}Z^0)$ regions. Thus, the selected events would have high sensitivity to the anomalous TGC couplings.

5.4 Results

5.4.1 Summary of $W^{\pm}Z^0$ detection sensitivity for 1 fb^{-1} integrated luminosity

Using the straight cut analysis, a total of 61 trilepton events with 53 $W^{\pm}Z^0$ signal events and 10 background events will be observed. With the *BDT* used to select events a total of 169 trilepton events with a signal to background ratio close to 10 cane observed. Based on this study, we are confident that even with the first 0.1 fb^{-1} integrated luminosity we should be able to establish the $W^{\pm}Z^0$ production signal at

Table 32: Results of the $W^{\pm}Z^{0}$ event selection by using various BDT cuts. Expected numbers of signal and background events are given for 1 fb^{-1}. For comparison purpose, the results from the straight cuts analysis are listed also. The quoted errors are statistical only.

Cut	Eff_{ZW}(%)	N_{ZW}	N_{BKGD}	N_{ZW}/N_{BKGD}
BDT $\geq$ 200	65.1	152.6 ± 1.7	16.1 ± 2.5	9.5
BDT $\geq$ 210	62.2	145.7 ± 1.7	14.6 ± 2.4	10.0
BDT $\geq$ 220	59.0	138.3 ± 1.6	12.6 ± 2.3	11.0
BDT $\geq$ 230	55.5	130.1 ± 1.6	10.7 ± 2.2	12.1
BDT $\geq$ 240	51.8	121.4 ± 1.5	7.7 ± 1.1	15.7
BDT $\geq$ 250	47.7	111.9 ± 1.5	6.6 ± 1.1	17.0
BDT $\geq$ 260	43.5	102.0 ± 1.4	5.5 ± 1.0	18.5
BDT $\geq$ 270	38.7	90.6 ± 1.3	4.1 ± 0.8	22.1
BDT $\geq$ 280	33.7	79.0 ± 1.2	3.5 ± 0.7	22.6
BDT $\geq$ 290	29.4	68.8 ± 1.1	3.0 ± 0.7	23.1
BDT $\geq$ 300	24.8	58.0 ± 1.0	2.4 ± 0.7	24.1
Straight cuts	22.8	53.4	8.0	6.7

Table 33: Breakdown of selected $ZW \rightarrow eee\nu$, ,$ee\mu\nu$, $\mu\mu e\nu$, $\mu\mu\mu\nu$ events after the BDT cuts. Results from straight cut analysis are given also. The number of events are normalized to 1 fb^{-1}.

Cut	$eee\nu$ N_{ZW}/N_{BG}	$ee\mu\nu$ N_{ZW}/N_{BG}	$\mu\mu e\nu$ N_{ZW}/N_{BG}	$\mu\mu\mu\nu$ N_{ZW}/N_{BG}	All 4 Channels N_{ZW}/N_{BG}
BDT $\geq$ 200	31.7/ 4.0	34.9/ 2.7	39.5/ 3.9	46.6/ 5.5	152.6/ 16.1
BDT $\geq$ 210	30.5/ 3.9	33.2/ 2.5	37.9/ 3.5	44.1/ 4.7	145.7/ 14.6
BDT $\geq$ 220	29.4/ 3.1	31.6/ 2.3	36.0/ 3.0	41.2/ 4.2	138.3/ 12.6
BDT $\geq$ 230	28.1/ 3.0	29.7/ 2.1	34.3/ 1.9	37.9/ 3.7	130.1/ 10.7
BDT $\geq$ 240	26.7/ 0.6	27.8/ 1.9	32.8/ 1.8	34.2/ 3.3	121.4/ 7.7
BDT $\geq$ 250	25.2/ 0.5	25.4/ 1.7	30.6/ 1.5	30.6/ 2.9	111.9/ 6.6
BDT $\geq$ 260	23.7/ 0.2	23.3/ 1.5	28.3/ 1.2	26.7/ 2.6	102.0/ 5.5
BDT $\geq$ 270	21.8/ 0.2	20.6/ 1.3	25.7/ 1.1	22.5/ 1.5	90.6/ 4.1
BDT $\geq$ 280	19.9/ 0.2	17.5/ 1.1	23.0/ 1.0	18.6/ 1.2	79.0/ 3.5
BDT $\geq$ 290	18.2/ 0.2	14.8/ 0.8	20.6/ 1.0	15.2/ 1.0	68.8/ 3.0
BDT $\geq$ 300	16.4/ 0.1	11.6/ 0.7	18.1/ 1.0	11.9/ 0.7	58.0/ 2.4
Straight cuts	6.51/ 1.52	11.55/ 0.74	14.72/ 1.77	20.65/ 3.98	53.43/ 8.0

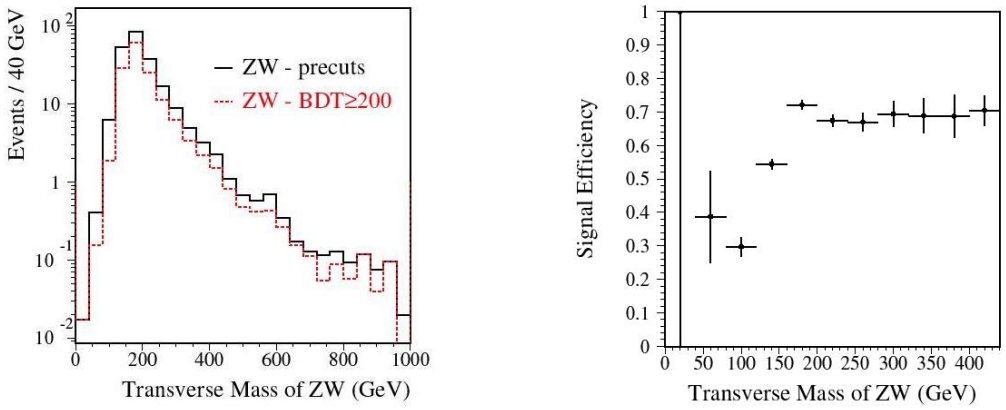

Figure 37: Distribution of transverse mass of $W^{\pm}Z^0$ before and after the *BDT* selection (left); Selection efficency ($BDT > 200$) as a function of the transverse mass of $W^{\pm}Z^0$ (right).

the LHC with a detection sensitivity greater than 5σ, which is defined as $S/\sqrt{B}$ or by Poisson statistics analysis.

Based on more than 30 million fully simulated background events from many SM processes the major backgrounds for the $W^{\pm}Z^0$ signal are seen to derive from following processes:

- $pp \to Z^0Z^0 \to \ell^+\ell^-\ell^+\ell^-$ with one lepton undetected. (47.8%)
- $pp \to Z^0 + jet \to \ell^+\ell^- + X$ with jet fake a lepton. (15.5%)
- $pp \to t\bar{t} \to W^+W^-b\bar{b}$. (17.4%)
- $pp \to Z^0/\gamma \to \ell^+\ell^- + X$. (12.4%)

The average statistical error for the background estimate using all the Monte Carlo samples listed in the $W^{\pm}Z^0$ analysis for this note is about 13%. In some channels, such as the $Drell-Yan$ process near the Z^0-peak, the background estimate has larger uncertainty since it is limited by the MC sample statistics.

5.4.2 Cross-section measurement uncertainty studies

The major systematic errors affecting diboson studies are catalogued in the W^+W^- analysis section. For the $W^{\pm}Z^0$ analysis several additional studies of the uncertainties have been conducted:

- Jet energy scale and lepton energy scale uncertainties.
  The *BDT* has been trained with MC events simulated with the 'standard' detector energy resolutions and energy scale. For independent test samples, 10% and 3% are added to the jet and lepton energy resolutions respectively and the reconstructed energy related quantities are 'smeared' to obtain the uncertainties of the diboson detection sensitivity (signal-to-background ratio). In this study the signal efficiencies are fixed and changes to the background acceptance are gauged. The results are summarized in Table 34. As an example, for BDT signal selection efficiency of 60%, the change of the signal-to-background ratio is 3.4%.

- *BDT* training stabilities with different event weighting and different test samples.
  As described in a previous section, each event is given an initial weight for *BDT* training. This weight of an MC process is defined as the ratio of number of expected events for a given integrated

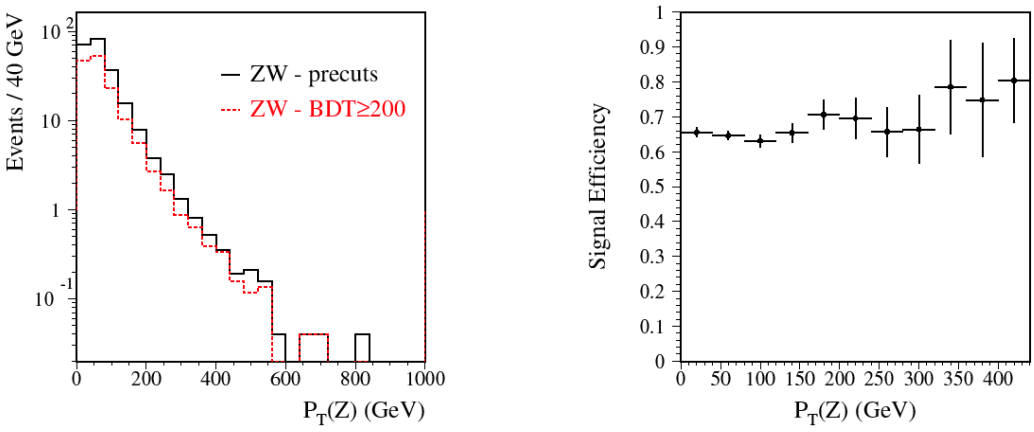

Figure 38: Transverse momentum distribution of the Z^0 from $W^{\pm}Z^0$ before and after the *BDT* cut (left); *BDT* selection efficiency as a function of transverse momentum of the Z^0 (right).

Table 34: Change of background acceptance in test of *BDT* ($W^{\pm}Z^0$ vs. Z^0Z^0) performed by smearing jet energy E_{jet} and Missing E_T, $\not\!\!E_T$ by additional 10% resolution, and the lepton energy E_T^{ℓ} by additional 3%.

Signal Efficiency	Background Eff. No additional smearing	Background Eff. 10% for E_{jet} & $\not\!\!E_T$	Background Eff. 10% for E_{jet}& $\not\!\!E_T$, 3% for E_T^{ℓ}
40%	3.96%	4.19% (+5.7%)	4.23%(+6.7%)
50%	8.59%	8.91% (+3.7%)	9.00%(+4.8%)
60%	14.55%	14.87% (+2.2%)	15.08%(+3.7%)
70%	22.27%	22.70% (+2.0%)	23.02%(+3.4%)

luminosity (1 fb^{-1}) and number of generated MC events (N_{exp}/N_{gen}). A test in which the weight of training events has been varied by 20% has been performed. The resultant change of the signal to background ratio is less than 6%

A 'software release' test has also been performed: The *BDT* was trained with the MC samples produced using software release v11.0.42 and the results obtained by test samples from both release v11.0.42 and by v12.0.6.4 were compared. These test results for the signal are shown in Figure 39. By varying the *BDT* cuts from 200 to 300, the change in the signal efficiencies range from 0.2% to 0.8%.

- Uncertainty test using *Bootstrap* sampling method.
  A study the optimal *BDT* training and test procedure: A *Bootstrap* test method is used to perform the *BDT* analysis by selecting events for training and test randomly. At each point for which a given fraction of events are selected for training the test is repeated 50 times. For a fixed signal efficiency, the mean background acceptance and the uncertainties (RMS) are determined. Figure 40 shows the test results. The left plot shows the background acceptance for each given signal efficiency as a function of the event percentage for training. The right plot shows the related errors of the background acceptance as a function of the event percentage for training. From this plot,

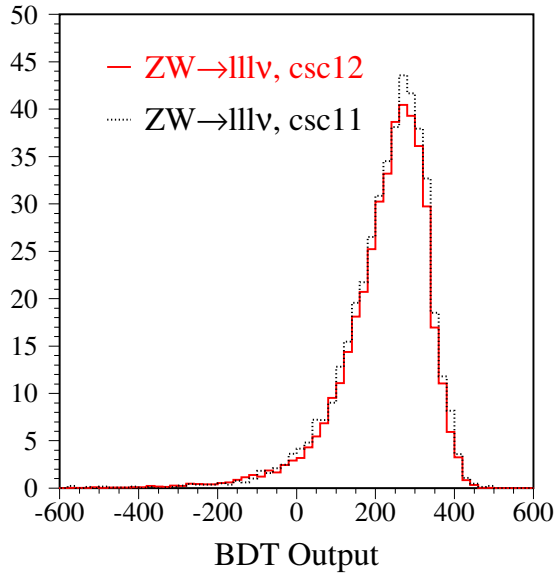

Figure 39: The *BDT* output spectra comparison: *BDT* training used CSC11 MC sample, and *BDT* test used both CSC11 and CSC12 samples. The output spectrum shows the stability of the *BDT* analysis technique.

for signal efficiency around 50-70% (the range we select events using the *BDT* cut), the relative errors of the background acceptance are around 13-18% when using 50-60% events for training. In the *BDT* analysis 50% of the events are always allocated for training and 50% for tests. The background uncertainties are consistent with the calculated statistical errors based on total events and selected events. We conclude that the *BDT* training uncertainties are small compared to large statistical uncertainties due to limited background statistics.

Also performed are MC 'experiments' where the *BDT* spectra are used to fit the $W^{\pm}Z^0$ production cross section and to extract the $W^+W^-Z^0$ triple gauge boson couplings. Figure 41 shows the expected observation for $0.1 fb^{-1}$ and $1.0 fb^{-1}$ integrated luminosity. In those plots the points are simulated MC data based on expected total number of events with Poisson statistics fluctuations, the red histograms are expected contribution from $W^{\pm}Z^0$ signal, and the blue histograms are the overall background contributions.

To minimize the cross section measurement uncertainties, the cross section fitting 'experiments' have been performed with different cuts on the *BDT* output spectrum. The MC experiments were done 100 times with randomly selected events corresponding to the integrated luminosities. The standard deviation (RMS) of the fitted cross sections are considered as the measurement uncertainties. Figure 42 shows the cross section fitting errors as a function of the *BDT* cut (the left plot) and the cross section fitting errors as a function of integrated luminosity (the right plot). We observe that the proper cut on the *BDT* output value could be set as $BDT > 200$, and the cross section measurement uncertainty would be totally dominated by the systematic errors with data corresponding to an integrated luminosity of 10 fb^{-1}.

5.5 Studies of the sensitivity to anomalous $W^+W^-Z^0$ couplings

The $W^{\pm}Z^0$ diboson production involves exclusively the $W^+W^-Z^0$ coupling, which is different from the W^+W^- diboson final state that contains both $W^+W^-Z^0$ and $W^+W^-\gamma$ couplings. To avoid producing an impractically large number of fully simulated events in non-SM anomalous coupling parameter space, a

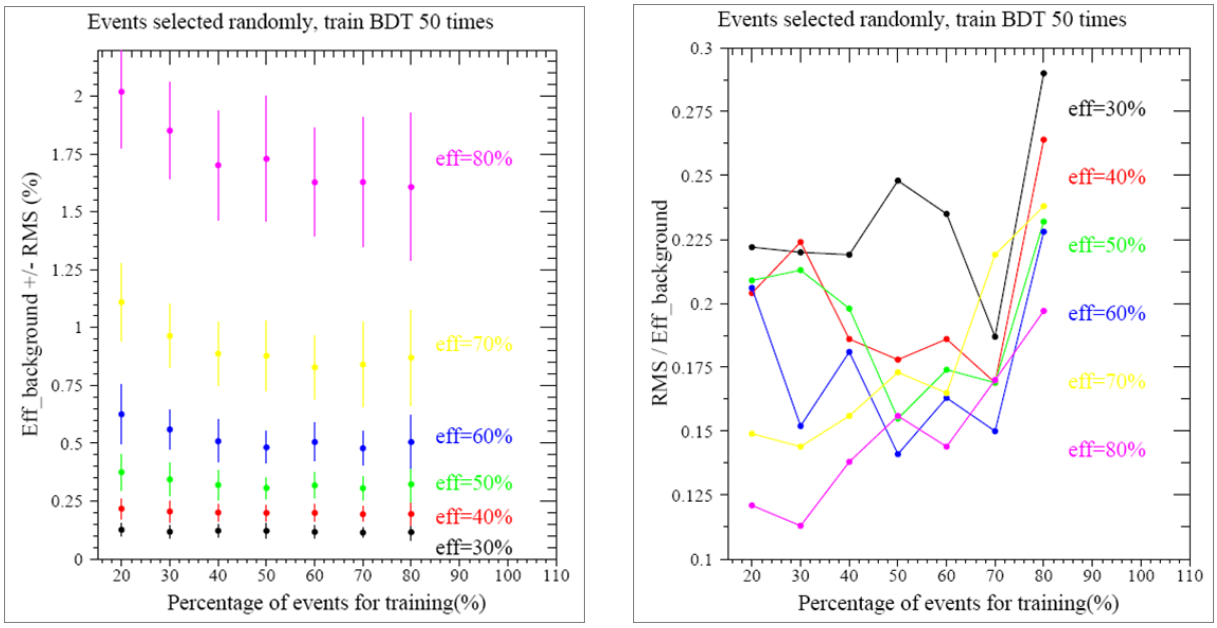

Figure 40: Left figure: Background acceptance as a function of percentage of events used for *BDT* training for given signal efficiencies. Each point presented in the plot is averaged from 50 times randomly selected events samples for test. The error bar is the standard deviation (RMS) of the mean value. Right: Relative errors as a function of the percentage of the training samples.

re-weighting method was invoked to study the ATLAS detector sensitivities to the $W^+W^-Z^0$ anomalous coupling parameters. A brief description of this method is presented in Section 2.5 of this note. The detailed procedure has been described in the W^+W^- analysis section. To extract the 95% C.L. sensitivity intervals of the anomalous parameters, $\Delta\kappa_Z, \Delta g_1^Z$, and λ_Z, from the $W^\pm Z^0$ diboson final state, both $M_T(W^\pm Z^0)$ (the transverse mass of $W^\pm Z^0$) and $P_T(Z^0)$ (the transverse momentum of Z) spectra were used to fit the anomalous couplings.

5.5.1 The procedure to study the anomalous couplings

For anomalous TGC studies we rely on the BHO [21] MC program to produce the events in non-SM coupling space, and use the kinematics of these events to re-weight the fully simulated events produced by MC@NLO program. Figure 43 shows an example of the BHO MC program generated $p_T(Z)$ distributions for different $W^+W^-Z^0$ couplings ($\Delta\kappa_Z$) and the differential cross section ratio, $d\sigma(non-SM)/d\sigma(SM)$. These ratios are used to reweight fully simulated SM $W^\pm Z^0$ events (from *MC@NLO* generator).

The expected number of events for signal and for background are determined from *BDT* based analysis. A *BDT* cut > 200 is used, resulting in 153 signal events and 16 background events for 1 fb^{-1} integrated luminosity.

An *'observation'* ($n = n_s + n_b$) is simulated by randomly pulling selected signal events from an independent subset of the sample. To determine the background, the total background p_T and M_T distributions and the "observations" are fluctuated by Poisson statistics.

Figure 44 shows the expected signal+background of the SM, superimposed with the MC experiment 'observations' (points with error bars), and the non-SM (anomalous couplings) predicted signal+background histograms.

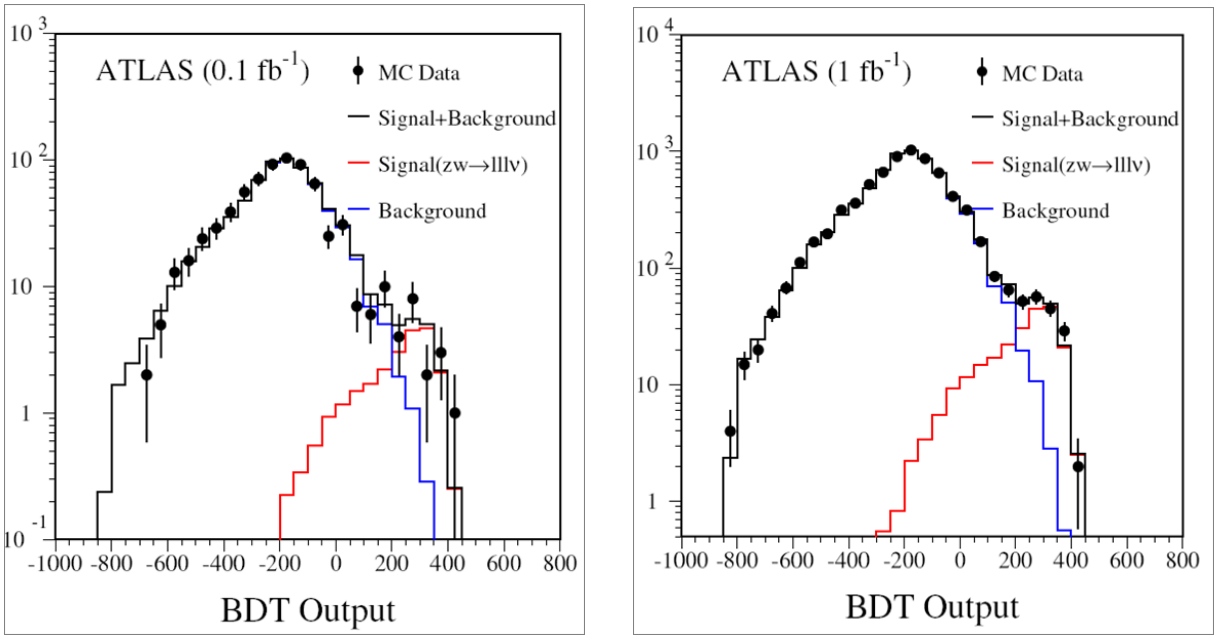

Figure 41: The Boosted-Decision-Tree output spectra for signal and background. Events are normalized to an integrated luminosity of 0.1 fb^{-1} (left) and 1.0 fb^{-1} (right). The points in plots are MC simulated data based on total expected mean value of signal plus background, and fluctuated with Poisson statistics.

Binned maximum likelihood calculations are performed to find the 95% C.L. intervals of the anomalous couplings. Figure 45 shows the 1-dimensional anomalous coupling limit fits based on the transverse mass $M_T(W^{\pm}Z^0)$ spectra for 0.1 fb^{-1} MC data.

5.5.2 One-dimensional 95% C.L. intervals

The summary of 1-dimensional 95% C.L. anomalous coupling parameter intervals based on the $M_T(W^{\pm}Z^0)$ spectra fitting is given in Table 35. Results corresponding to 0.1, 1.0, 10.0 and 30.0 fb^{-1} integrated luminosities for cutoff, $\Lambda = 2$ *TeV* and $\Lambda = 3$ *TeV* are listed. Even for 0.1 fb^{-1} integrated luminosity, the ATLAS sensitivity to $W^+W^-Z^0$ anomalous couplings could be at least 5 times better (tight) compared to Tevatron experiment limits based on 1 fb^{-1} $p\bar{p}$ collision data.

For comparison purposes, the summary of 1-dimensional 95% C.L. anomalous coupling parameter intervals based on the $p_T(Z)$ spectra fitting is given in Table 36. Results corresponding to 0.1, 1.0, 10.0 and 30.0 fb^{-1} integrated luminosities for cutoff, $\Lambda = 2$ *TeV* and $\Lambda = 3$ *TeV* are listed. From this table the results from the $p_T(Z)$ spectra fitting are seen to be less sensitive than those from the $M_T(W^{\pm}Z^0)$ fitting. This could be explained that the $M_T(WZ)$ spectra contain both bosons' kinematic information, while $p_T(Z)$ spectra only contain the Z-boson kinematic information.

To understand the systematic error effects on the TGC sensitivity, three different systematic error assumptions were considered:

- No systematic errors: $\sigma_S = 0$, and $\sigma_B = 0$.
- Assume 7.2% (5% + 6.5% Lumi.) for signal, and 12% (10% + 6.5% lumi.) for background.
- 9.2% uncertainty for signal, and 18.3% uncertainty for background. These values are based on the diboson working group's *systematic error assumption proposal*, indicated in the WW analysis section.

Table 35: Summary of one-dimensional anomalous coupling parameter 95% CL sensitivities using the $M_T(W^{\pm}Z^0)$ fitting for $\Lambda = 2$ *TeV* and $\Lambda = 3$ *TeV* for integrated luminosities of 0.1, 1.0, 10.0 and 30.0 fb^{-1}.

Int. Lumi (fb^{-1})	Cutoff Λ (TeV)	$\Delta\kappa_Z$	λ_Z	Δg_1^Z
0.1	2.0	[-0.440, 0.609]	[-0.062, 0.056]	[-0.063, 0.119]
1.0	2.0	[-0.203, 0.339]	[-0.028, 0.024]	[-0.021, 0.054]
10.0	2.0	[-0.095, 0.222]	[-0.015, 0.013]	[-0.011, 0.034]
30.0	2.0	[-0.080, 0.169]	[-0.012, 0.008]	[-0.005, 0.023]
0.1	3.0	[-0.399, 0.547]	[-0.050, 0.046]	[-0.054, 0.094]
1.0	3.0	[-0.178, 0.281]	[-0.020, 0.018]	[-0.017, 0.038]
10.0	3.0	[-0.135, 0.201]	[-0.015, 0.013]	[-0.013, 0.018]
30.0	3.0	[-0.069, 0.131]	[-0.008, 0.005]	[-0.003, 0.016]

Table 36: Summary of one-dimensional anomalous coupling parameter 95% CL sensitivities using the $p_T(Z)$ fit for $\Lambda = 2$ *TeV* and $\Lambda = 3$ *TeV* for integrated luminosities of 0.1, 1.0, 10.0 and 30.0 fb^{-1}. Note that the results from the $p_T(Z)$ fit are less sensitive than those from the $M_T(WZ)$ fit.

Int. Lumi (fb^{-1})	Cutoff Λ (TeV)	$\Delta\kappa_Z$	λ_Z	Δg_1^Z
0.1	2.0	[-0.950, 1.140]	[-0.204, 0.194]	[-0.228, 0.325]
1.0	2.0	[-0.574, 0.692]	[-0.093, 0.083]	[-0.106, 0.158]
10.0	2.0	[-0.228, 0.302]	[-0.033, 0.027]	[-0.022, 0.070]
30.0	2.0	[-0.164, 0.212]	[-0.026, 0.018]	[-0.009, 0.055]
0.1	3.0	[-0.910, 1.090]	[-0.177, 0.169]	[-0.206, 0.285]
1.0	3.0	[-0.539, 0.643]	[-0.077, 0.069]	[-0.090, 0.125]
10.0	3.0	[-0.206, 0.267]	[-0.024, 0.022]	[-0.018, 0.052]
30.0	3.0	[-0.148, 0.192]	[-0.021, 0.015]	[-0.008, 0.043]

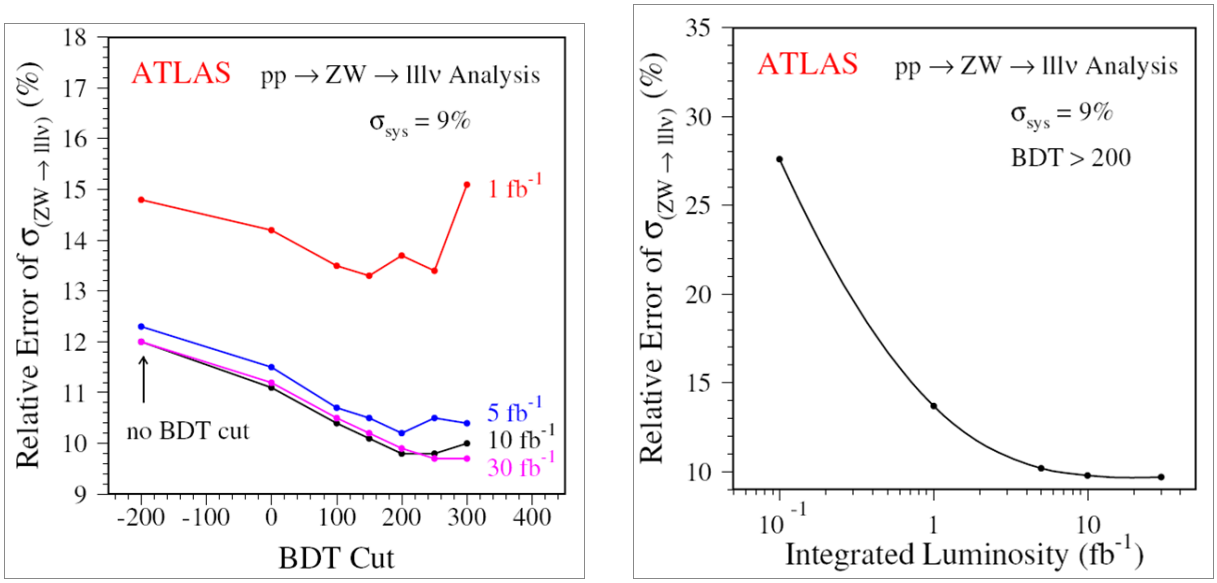

Figure 42: The relative errors of the cross section fitting as a function of the *BDT* cut (the left plot) and the cross section fitting errors as a function of integrated luminosity (the right plot).

The 95% CL 1-dimensional WWZ anomalous coupling limits based on the $p_T(Z)$ fit, and using $\Lambda = 2TeV$ for different systematic error assumptions are listed in Table 37. From this table it is seen that only when reaching 30 fb^{-1} integrated luminosity do the systematic errors become significant enough to effect the TGC sensitivities.

5.5.3 Two-dimensional 95% C.L. contours

The studies on the WWZ anomalous couplings in 2-dimensional space are also based on the $p_T(Z)$ fits for different luminosities (0.1, 1.0, 10.0 and 30.0 fb^{-1}) and for two cutoff values, $\Lambda = 2$ *TeV* and 3 *TeV*. The AC limit contours are not very sensitive to these cutoff values.

Figure 46 shows the 2-dimensional 95% C.L. contours of the anomalous coupling limits based on the $p_T(Z)$ fit for $\Lambda = 2$ *TeV*:

- The left-top plot shows the contour in λ_Z and $\Delta\kappa_Z = \Delta g_1^Z$ space;
- The right-top plot shows the contour in $\Delta\kappa_Z$ and Δg_1^Z space with ($\lambda_Z = 0$);
- The left-bottom plot shows the contour in λ_Z and $\Delta\kappa_Z$ space with ($\Delta g_1^Z = 0$);
- The right-bottom plot shows the contour in Δg_1^Z and λ_Z space with ($\Delta\kappa_Z = 0$).

The different systematic error effects on the 2-dimensional TGC sensitivity contour are shown in Figure 47: the left plot shows the 95% CL TGC limit contour without including the systematic errors in parameter space of λ_Z vs. $\Delta\kappa_Z = \Delta g_1^Z$; the right plot shows the 95% CL TGC limit contour with the systematic errors ($\sigma_S = 9.2\%$, $\sigma_B = 18.3\%$) in parameter space of λ_Z vs. $\Delta\kappa_Z = \Delta g_1^Z$. Again, we see that the systematic errors become significant when integrated luminosity reaches 30 fb^{-1}.

5.6 Summary of the TGC studies in $W^{\pm}Z^0$ analysis

Using the fully simulated ATLAS $W^{\pm}Z^0$ events with tri-lepton plus $\not\!\!E_T$ final states ($eee\nu$, $ee\mu\nu$, $\mu\mu e\nu$, and $\mu\mu\mu\nu$) we have studied the ATLAS detector sensitivities to the anomalous $W^+W^-Z^0$ trilinear gauge

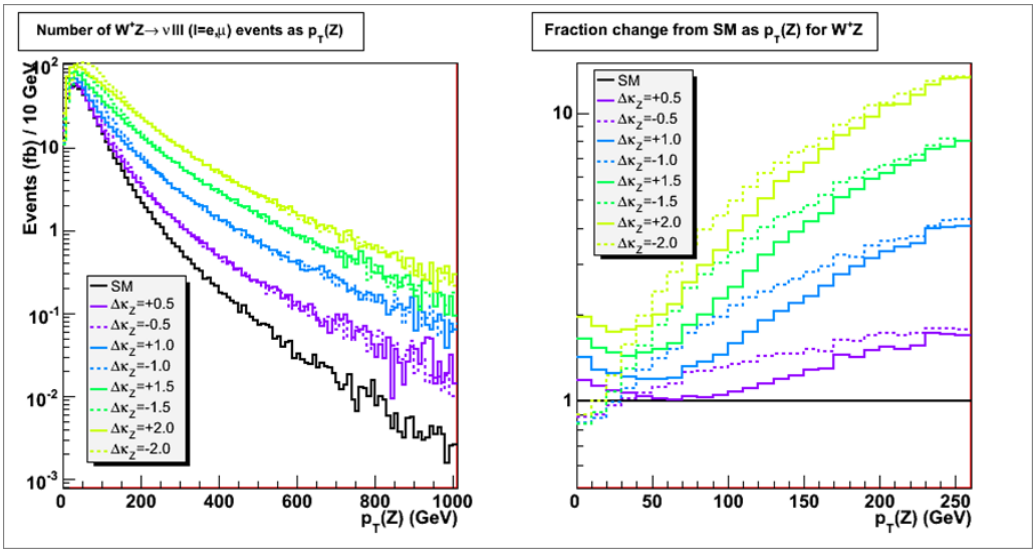

Figure 43: Left plot, The $p_T(Z)$ distributions for different $W^+W^-Z^0$ couplings ($\Delta\kappa_Z$) and right plot, the differential cross section ratio, $d\sigma(non-SM)/d\sigma(SM)$.

boson couplings: λ_Z, $\Delta\kappa_Z$, and Δg_1^Z. The largest available MC background samples ($\sim$ 30 million) have been included and both Z-boson transverse momentum $p_T(Z)$ and the WZ diboson $M_T(WZ)$ kinematic information has been used to determine the WZ anomalous coupling sensitivity. Our results indicate that ATLAS WWZ TGC sensitivity should greatly improve the Tevatron and LEP limits with the first 30 fb^{-1} integrated luminosity:

$$-0.069 < \Delta\kappa_Z < 0.131, \quad -0.008 < \lambda_Z < 0.005, \quad -0.003 < \Delta g_1^Z < 0.016.$$

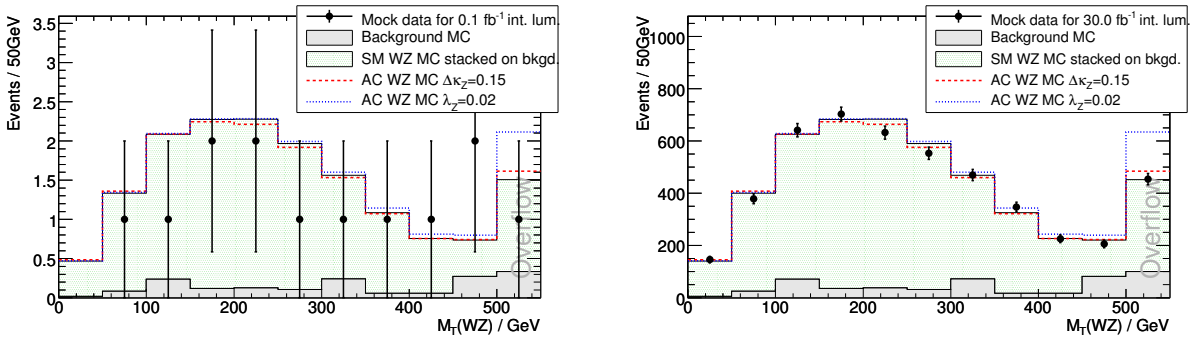

Figure 44: The expected signal+background of the SM, superimposed with the MC experiment "observations" (points with error bars showing statistical uncertainty), and the non-SM (anomalous couplings) predicted signal+background histograms (red and blue dashed lines). the left plot is for 0.1 fb^{-1} and the right plot is for 30 fb^{-1}.

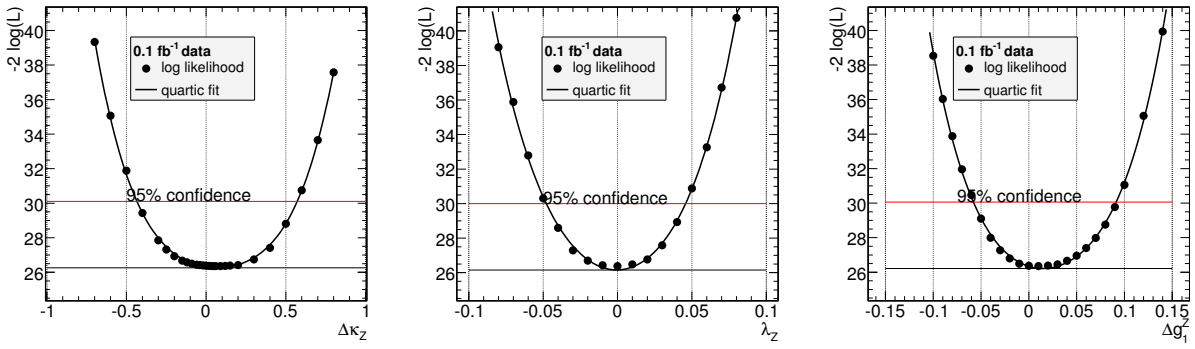

Figure 45: One-dimensional anomalous coupling limit fits based on the $M_T(W^{\pm}Z^0)$ spectra for 0.1 fb^{-1} data. When varying one anomalous coupling parameter for fitting, the other parameters are fixed to SM values.

Table 37: Comparison of one-dimensional anomalous coupling parameter 95% CL sensitivities for different systematic errors. Results obtained in this table are using the $p_T(Z)$ fit for $\Lambda = 2\ TeV$ and $\Lambda = 3\ TeV$ for integrated luminosities of 0.1, 1.0, 10.0 and 30.0 fb^{-1}.

Systematic errors	Int. Lumi (fb^{-1})	Cutoff Λ (TeV)	$\Delta\kappa_Z$	λ_Z	Δg_1^Z
$\sigma_S = 0$	0.1	2.0	[-0.942, 1.130]	[-0.203, 0.193]	[-0.227, 0.324]
$\sigma_B = 0$	1.0	2.0	[-0.561, 0.664]	[-0.093, 0.082]	[-0.106, 0.154]
	10.0	2.0	[-0.233, 0.231]	[-0.033, 0.024]	[-0.025, 0.061]
	30.0	2.0	[-0.128, 0.136]	[-0.024, 0.013]	[-0.009, 0.047]
$\sigma_S = 7.2\%$	0.1	3.0	[-0.950, 1.140]	[-0.204, 0.194]	[-0.228, 0.325]
$\sigma_B = 12.0\%$	1.0	3.0	[-0.574, 0.692]	[-0.093, 0.083]	[-0.106, 0.158]
	10.0	2.0	[-0.228, 0.302]	[-0.033, 0.027]	[-0.022, 0.070]
	30.0	2.0	[-0.164, 0.212]	[-0.026, 0.018]	[-0.009, 0.055]
$\sigma_S = 9.2\%$	0.1	3.0	[-0.956, 1.150]	[-0.204, 0.194]	[-0.229, 0.326]
$\sigma_B = 18.3\%$	1.0	3.0	[-0.583, 0.706]	[-0.094, 0.084]	[-0.106, 0.159]
	10.0	2.0	[-0.241, 0.316]	[-0.033, 0.028]	[-0.024, 0.071]
	30.0	2.0	[-0.184, 0.228]	[-0.028, 0.020]	[-0.011, 0.056]

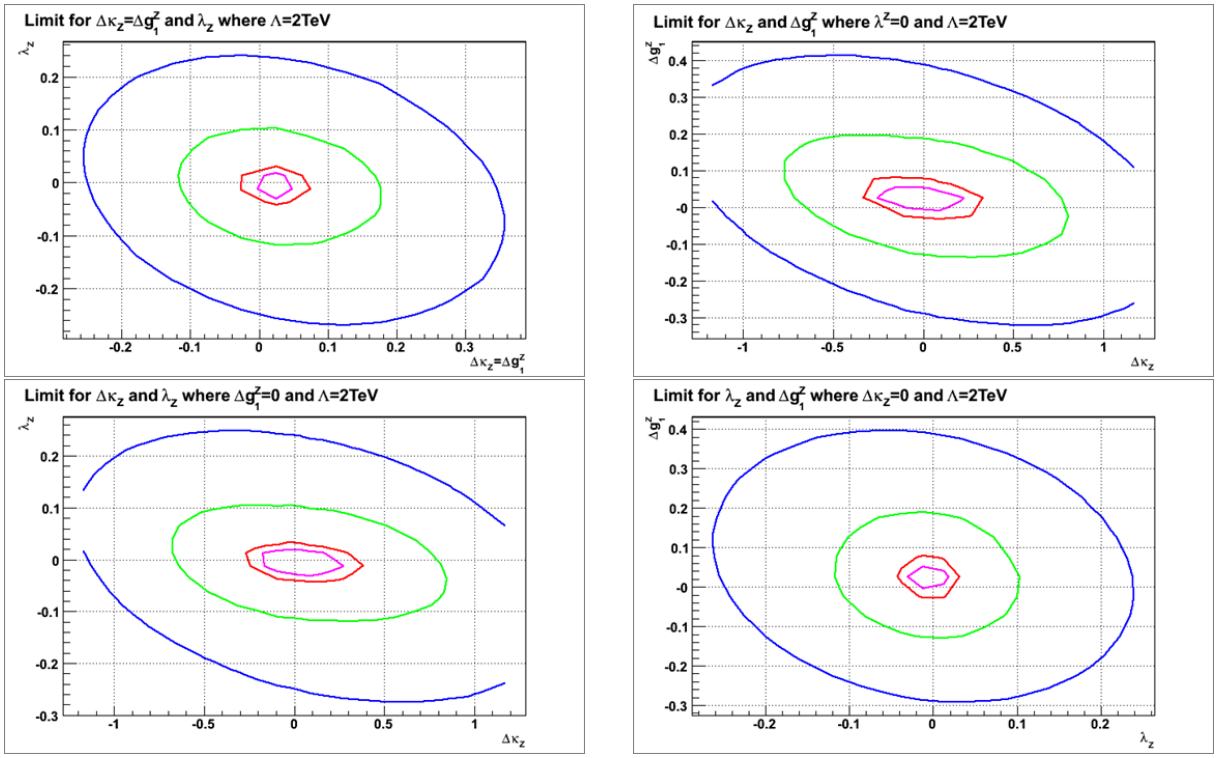

Figure 46: Two-dimensional 95% C.L. contour of the WWZ AC limits based on $p_T(Z)$ fit for $\Lambda = 2\ TeV$. The left-top plot shows the contour in λ_Z and $\Delta\kappa_Z = \Delta g_1^Z$ space; the right-top plot shows the contour in $\Delta\kappa_Z$ and Δg_1^Z space with ($\lambda_Z = 0$); the left-bottom plot shows the contour in λ_Z and $\Delta\kappa_Z$ space with ($\Delta g_1^Z = 0$); the right-bottom plot shows the contour in Δg_1^Z and λ_Z space with ($\Delta\kappa_Z = 0$). The AC limit contours from outer to inner corresponding integrated luminosities of 0.1, 1.0, 10.0 and 30.0 fb^{-1}, respectively.

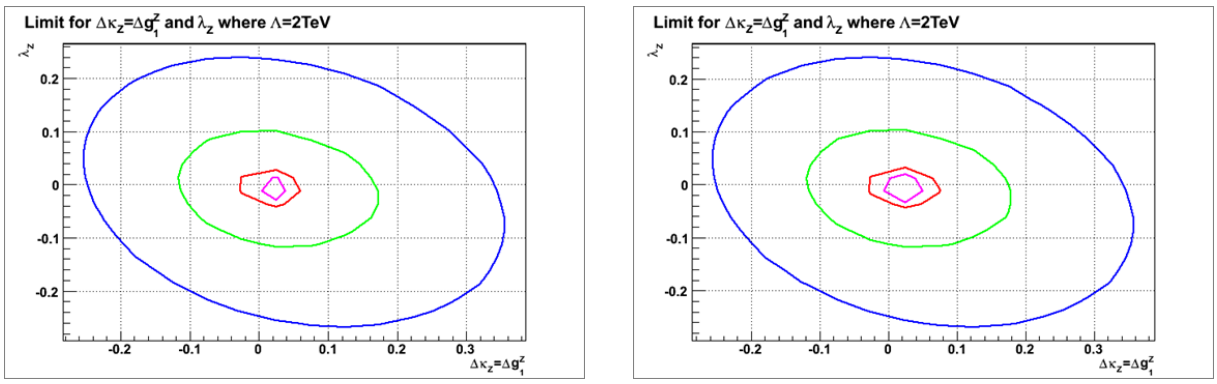

Figure 47: The left plot: 95% C.L. WWZ TGC limit contour without including the systematic errors in parameter space of λ_Z vs. $\Delta\kappa_Z = \Delta g_1^Z$; The right plot: the 95% C.L. WWZ TGC limit contour with the systematic errors ($\sigma_S = 9.2\%$, $\sigma_B = 18.3\%$) in parameter space of λ_Z vs. $\Delta\kappa_Z = \Delta g_1^Z$. The AC limit contours from outer to inner corresponding integrated luminosities of 0.1, 1.0, 10.0 and 30.0 fb^{-1}, respectively. We should notice that the systematic errors become significant when integrated luminosity reaching 30 fb^{-1}.

6 $W^{\pm}\gamma$ production and the $WW\gamma$ couplings

6.1 $W^{\pm}\gamma$ production mechanism

The leading order (Born) Feynman diagrams for $W^{\pm}\gamma$ production are show in Fig. 48. The left diagram is the W production with the initial state photon radiation (ISR). The middle diagram is the W production with a photon radiating from the W. This diagram contains the $WW\gamma$ vertex of interest. The right diagram is the W production with leptonic decays with a photon radiating from the final state lepton (FSR). The $\ell^{\pm}\nu\gamma$ events from FSR process are considered as the background of the $W^{\pm}\gamma$ diboson signals.

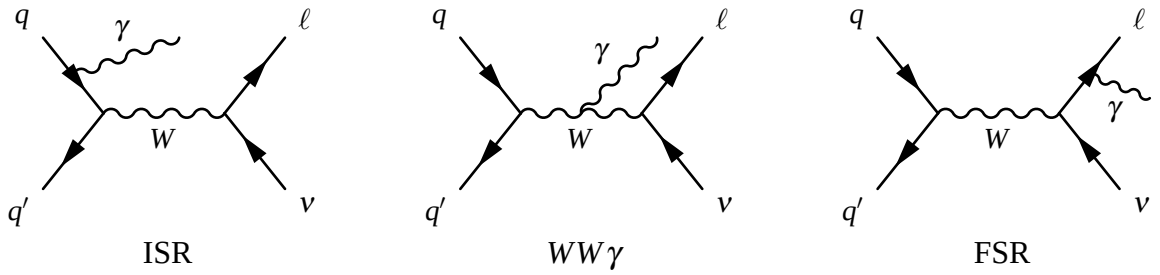

Figure 48: Feynman diagrams for $W\gamma$ production. The W production with the ISR (initial state sadiation) and the W radiating a photon with the $WW\gamma$ vertex (left and middle diagrams) are considered as our signal. The right diagram is the W production with a photon radiating from the final state lepton (FSR), which is considered as the $W^{\pm}\gamma$ background.

The $W^{\pm}\gamma$ production cross section is highly depending on the transverse energy cut on the photon, and on the separation of photon and final state lepton, $\Delta R(\ell,\gamma)$. We show the $W^{\pm}\gamma$ production cross sections in Table 38. We list the LO calculations done by *PYTHIA* program using *CETQ6L* PDF with different photon $E_T(\gamma)$ cuts. We also list the calculations done by BHO program for both LO and NLO cross sections. For $E_T(\gamma) > 25$ GeV, both programs give basically the same LO cross sections. The k-factors which are defined the cross section ratio: $d\sigma(NLO)/d\sigma(LO)$ are given in the table as well.

The $E_T(\gamma)$ distributions of Pythia and BosoMC (BHO) LO calculation (Fig. 49) are consistent. The NLO calculation gives a higher $E_T(\gamma)$ tail. and the increase to LO is approximately linear.

Table 38: Production cross sections of $W^{\pm}\gamma$ events for a single lepton decay flavor of $W^{\pm} \to l^{\pm}\nu$. The k-factor is derived for BHO $\sigma(NLO)/\sigma(Born)$. The $E_T^*(\gamma)$ is the photon energy in CM frame.

PYTHIA	$W^+\gamma$	$W^-\gamma$	$W^+\gamma$	$W^-\gamma$
(condition)	$E_T^*(\gamma) > 10$ GeV		$E_T(\gamma) > 25$ GeV	
$\sigma(Born)$ (pb)	10.22	6.82	2.56	1.71
BHO	$W^+\gamma$	$W^-\gamma$	$W^+\gamma$	$W^-\gamma$
(condition)	$E_T(\gamma) > 10$ GeV		$E_T(\gamma) > 25$ GeV	
$\sigma(Born)$ (pb)	11.66	8.15	2.56	1.72
$\sigma(NLO)$ (pb)	19.26	13.63	5.25	3.75
k-factor	1.65	1.67	2.05	2.18

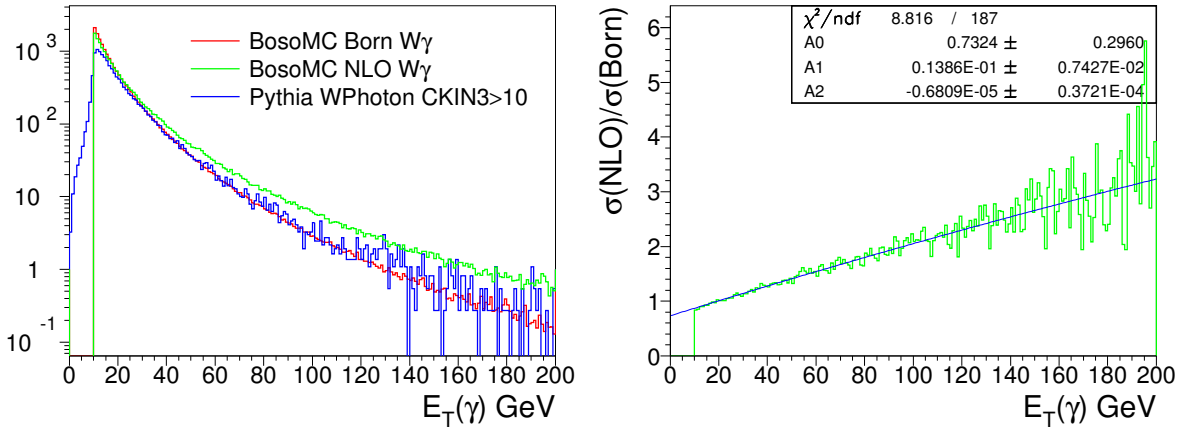

Figure 49: $E_T(\gamma)$ distributions of $W^{\pm}\gamma$ events of Pythia and BosoMC calculations (right). Pythia distribution is normalized to BosoMC for $E_T(\gamma) > 25$ GeV, where both programs give consistent production cross section. For comparison of the $E_T(\gamma)$ slopes, the BosoMC NLO distribution is normalized to the LO statistics, and the ratio as a function of $E_T(\gamma)$ is plot (right).

6.2 Experimental signal and background

We focus our studies on pure W leptonic decay final states.

$$pp \to W^{\pm}\gamma \to \ell^{\pm}\nu\gamma \quad (\ell = a,\ \mu).$$

The experimental signature is the final states with one high P_T lepton, one high P_T photon and large transverse missing energy $\not{E}_T$. Major background contribute to such final states are events from the processes:

- $q\bar{q}' \to W^{\pm} \to \ell^{\pm}\nu \quad (\ell \to \ell\gamma)$, where photon come from lepton final state radiation.
- $W/Z + jets$ or event underlying remnants, with meson faking a photon, or quark final state radiates a photon.

Photon isolation cut can effectively reject these background.

Production of $W^{\pm}\gamma$ events in leptonic decay channels are investigated with the ATLAS CSC datasets produced by atlas-software version 12.0.6. The datasets used (Table 39) are of Pythia leading order simulations for the Standard Model leading order production of inclusive $W^{\pm}$ production of proton-proton collisions at $\sqrt{s} = 14$ TeV. Previous studies of the prospect of $W^{\pm}\gamma$ measurement were conducted with the ATLAS fast simulations reported in [34, 35].

The Pythia $W^{\pm}\gamma$ datasets (CSC dataset 5909 and 5910) include the ISR and the $WW\gamma$ vertex diagrams. The $WW\gamma$ vertex introduces a destructive interference of *'zero amplitude'* at $\cos\theta_{\bar{q},\gamma} = \pm 1/3$ for $W^{\pm}$ production, where $\theta_{\bar{q},\gamma}$ is the photon scattering angle to the incoming anti-quarks.

The Pythia simulation of $W^{\pm}$ inclusive events (CSC datasets 5104, 5105) includes channels of ISR photons from colliding quarks and FSR photons from $W^{\pm}$ decay leptons. It does not include the $WW\gamma$ triple gauge coupling (TGC) term. The inclusive $W^{\pm}$ production cross section is 17440 pb^{-1} with 0.83% of the events containing an ISR photon.

Table 39: Datasets used for the studies of $W^{\pm}\gamma$ production. Listed are the dataset name, ATLAS software version, number of events generated and the corresponding integrated luminosity for pp collisions at $\sqrt{s} = 14$ TeV.

CSC dataset ID	process	cuts	version	Events	pb^{-1}
5909_TW	$W \to \mu\nu)\gamma$	$E_T^*(\gamma) > 10GeV$	12.06.04	64k	-
5910_TW	$W \to \ell\nu)\gamma$	$E_T^*(\gamma) > 25GeV$	12.06.01	6.6k	-
5105	$W \to \mu\nu$	-	12.06.01	270k	23
5105_TW	$W \to \mu\nu$	-	12.06.02	121k	10
5104	$W \to e\nu$	-	12.06.01	460k	42
5104_TW	$W \to \mu\nu$	-	12.06.02	392k	36

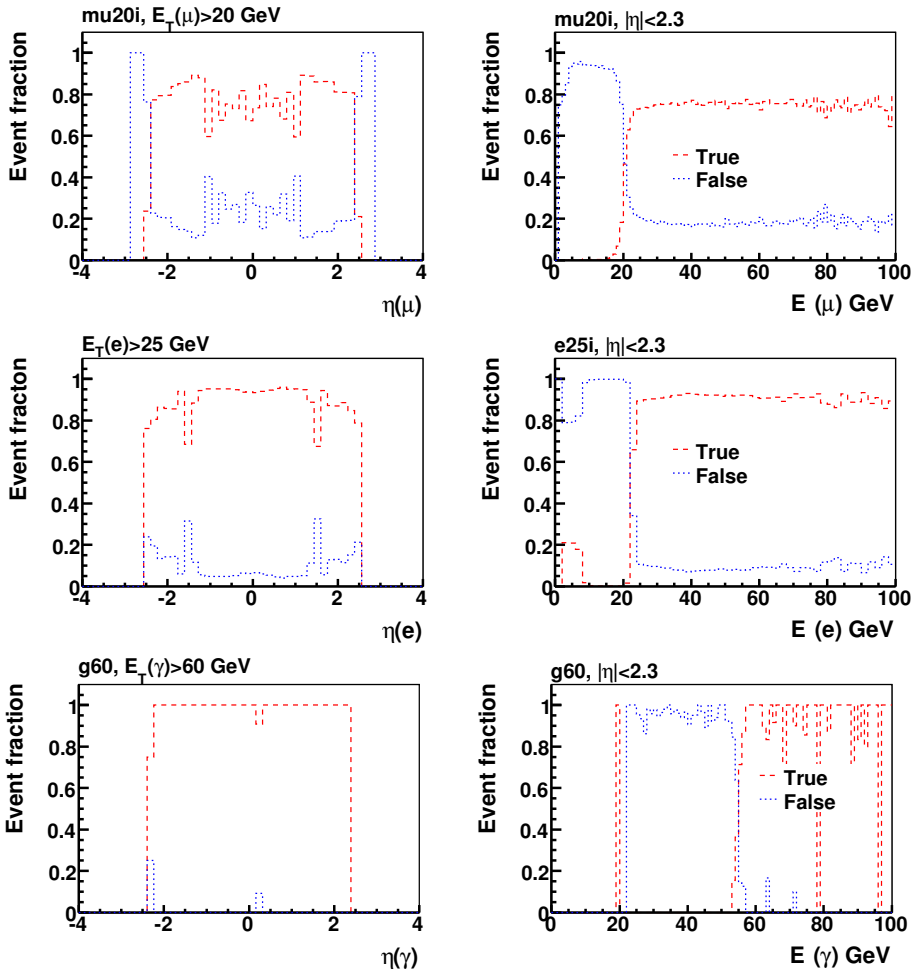

Figure 50: Trigger efficiencies of mu20i, e25i and g60 estimated with $W^{\pm}$ decay leptons and ISR photons. The reference are the muons, electrons, and photons of muon_boy and IsEM 0x7FF reconstruction that match with MCtruth.

6.3 Selection of $W^{\pm}\gamma \rightarrow l^{\pm}\gamma$ events

The $W^{\pm}$ bosons are selected for leptonic decay channels of $W^{\pm} \rightarrow l^{\pm}\nu$. An electron is an IsEM object of category 0x7FF that matches with an inner detector particle track. A photon is an IsEM 0x7FF object without a matching track. A muon is a muon_boy object. The $W^{\pm}$ decay leptons are tagged by the MCtruth for particle four momentum and decay records. The $W^{\pm}\gamma$ candidates are inclusive $e^{\pm}\gamma$ or $\mu^{\pm}\gamma$ events having only one electron or muon observed and the absence of the oppositely charged lepton of the same type. The photon is the most energetic IsEM photon.

Trigger efficiencies were investigated for the Event-Filter (EF) words of mu20i (isolate muon of $p_T > 20$ GeV), e25i (isolate electron of $p_T > 25$ GeV), and g60 (photon of $E_T(\gamma) > 60$ GeV). The references are the reconstructed muons, electrons, and photons that match with the MCtruth tags of generated particles. The single particle trigger efficiencies are best evaluated with the $W^{\pm}\gamma$ datasets for having only one energetic lepton of $W^{\pm}$ decay, and a ISR photon of $E_T(\gamma) > 25$ GeV. The distributions shown in Fig. 50 are the event fractions of reconstructed particles with EF words "True" or "False". The mu20i trigger efficiency for a single muon of $p_T > 25$ GeV is 75 %. The e25i trigger has a uniform spectra in η and $p_T(e)$ and the efficiency reaches 90 %. The photon g60 trigger has imposed a very high energy threshold of $E_T(\gamma) > 60$ GeV. The efficiency is 100 % in the full ECAL coverage of $|\eta| < 2.3$. The tests were also conducted for Z events with both decay leptons reconstructed in the detector fiducial volume. The trigger efficiencies are close 100 %, as the two leptons provide redundancy in firing the trigger words.

By MCtruth records we tag an "ISR event" with the photon generated from ISR and $WW\gamma$ diagrams, and a "FSR event" with the photon emitted from the $W^{\pm}$ decay lepton. The FSR photons are distinguishable by the event topology for having close opening angles to the $W^{\pm}$ decay leptons. The distributions of $W^{\pm}\gamma$ events are shown in Fig. 51. The event missing transverse energy ($\not\!\!E_T$) is used to represent the undetected neutrino of $W^{\pm}$ decay. The transverse masses of the observables, $m_T(l^{\pm}, \not\!\!E_T)$ and $m_T(l^{\pm}, \not\!\!E_T, \gamma)$, also wear signatures for photon types. The $m_T(W,\gamma)$ variable in use is given by

$$\begin{array}{ll} E_T(W) = E_T(\not\!\!E_T) + E_T(\ell) & E_T(W,\gamma) = E_T(\gamma) + E_T(\not\!\!E_T) + E_T(\ell) \\ p_i(W) = E_i(\not\!\!E_T) + p_i(\ell) & p_i(W,\gamma) = p_i(\gamma) + E_i(\not\!\!E_T) + p_i(\ell) \\ m_T(W) = (E_T(W)^2 - p_x(W)^2 - p_y(W)^2)^{1/2} & m_T(W,\gamma) = (E_T(W,\gamma)^2 - p_x(W,\gamma)^2 - p_y(W,\gamma)^2)^{1/2} \end{array} \quad (1)$$

Background to $W^{\pm}\gamma$ is dominated by the inclusive $W^{\pm}$ events with a fake photon. Contamination from inclusive Z events is also considerable. In Fig. 51 we also show Z events with one lepton escaping detection and a photon of any type reconstructed.

6.4 $W^{\pm}\gamma$ analysis using Boosted Decision Trees

Selection of inclusive $W^{\pm}$ and $W^{\pm}\gamma$ events were estimated with the CSC Pythia datasets for inclusive $W^{\pm}$ production and WPhoton10 for signal photons of ISR and $WW\gamma$ diagrams. Background of FSR and fake photons were estimated with the inclusive $W^{\pm}$ datasets. The number of events to be observed for an integrated luminosity of 1 fb^{-1} are listed in Table 40.

The candidate $W^{\pm}\gamma$ events consist of one energetic electron or muon plus a photon. It is easily contaminated by events of other physics processes. With data of atlas-software version 11, we had studied $t\bar{t}$ background and found that background jet based physics processes can be easily discriminated by the event missing E_T and jet multiplicities. The only irreducible background is the $Z\gamma$ events with one of the Z decay lepton escaping detection or mis-identified. The $e\gamma$ events are contaminated by the $Z \rightarrow ee$ events, with one of the electron mis-identified as a photon, and the event rate is five times to the $W^{\pm}\gamma$ with an ISR or $WW\gamma$ photon. Luckily this background can be discriminated by the invariant mass of $m(e\gamma)$ that consists with $m(Z)$.

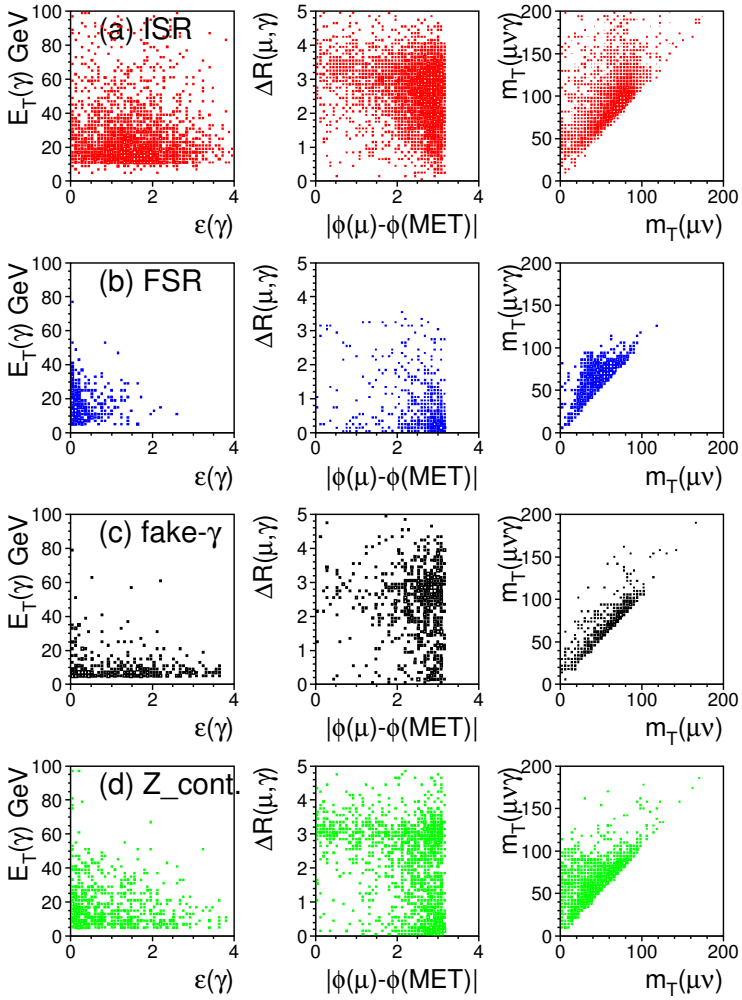

Figure 51: Distributions of $W^{\pm}(\mu^{\pm}\nu)\gamma$ event variables, with a photon of ISR, FSR, fake background, and of inclusive Z contamination.

Table 40: Number of $W^{\pm}$ and $W^{\pm}\gamma$ events for an integrated luminosity of 1 fb^{-1}. Photons are tagged for signal photon of ISR and $WW\gamma$ vertex, and background of FSR and fake photon. Contamination of inclusive Z events is also listed. The ISR signal to noise ratios are 0.95 and 0.98 for electron and muon channels, respectively.

Pythia	W inclusive ($\sigma(W \to e\nu) = 17440$ pb^{-1})				Z inclusive	WPhoton10
Detectable	$e^{\pm}$	+ISR_γ	+FSR_γ	+fake_γ	$Z(ee)\gamma$	$e^{\pm}$+Signal γ
$E_T(\gamma) > 10$ GeV	6.7 M	5760	11440	7890	32480	1710
BDT cut ($\varepsilon = 67$ %)	–	–	242	791	101	1145
NLO scaled	background (k=1.3)				1474	(k=1.66) 1901

Pythia	W inclusive ($\sigma(W \to \mu\nu) = 17440$ pb^{-1})				Z inclusive	WPhoton10
Detectable	$\mu^{\pm}$	+ISR_γ	+FSR_γ	+fake_γ	$Z(\mu\mu)\gamma$	$\mu^{\pm}$+Signal γ
$E_T(\gamma) > 10$ GeV	11.1 M	9100	28410	10250	3950	2680
BDT cut ($\varepsilon = 67$ %)	–	–	413	961	409	1793
NLO scaled	background (k=1.3)				2318	(k=1.66) 2976

The Boosted Decision Tree method is conducted for $W^{\pm}\gamma$ events with three trainings to separate 1) FSR photon from the rest, 2) signal photons (of ISR and $WW\gamma$ diagrams) from fake photon, and 3) signal photons from the contamination of Z inclusive events. The 19 variables used in the decision trees are illustrated in Fig. 52, for events of $W^{\pm}(e^{\pm}\nu)$ plus an ISR photon and $Z(ee)$ contamination. Almost every variable shows distinguishable feature for decision tree training. The test scores are plotted in Fig. 53 for the three trainings. The cuts chosen for ISR selection corresponds to a selection efficiency of 65 % for the WPhoton10 dataset with Signal (of WPhoton10) to Noise (of W inclusive) ratio of 0.95 (0.98) for electron (muon) final state, respectively. The number of events selected with the BDT cuts are listed in Table 40.

The Boost Decision Tree discriminates signal photons (ISR and WWγ) effectively from FSR and fake photon in the high $E_T(\gamma)$ region. Illustrated in Fig. 54 are the selection efficiencies as functions of $E_T(\gamma)$ and $m_T(W^{\pm},\gamma)$ transverse mass. One sees fast climbing curves to high $E_T(\gamma)$ ($m_T(W^{\pm},\gamma)$ regions that is sensitive to discovery of new phenomenon beyond Standard Model predictions. The photon $E_T(\gamma)$ distributions of $W^{\pm}\gamma$ candidates selected before and after the decision tree cuts are show

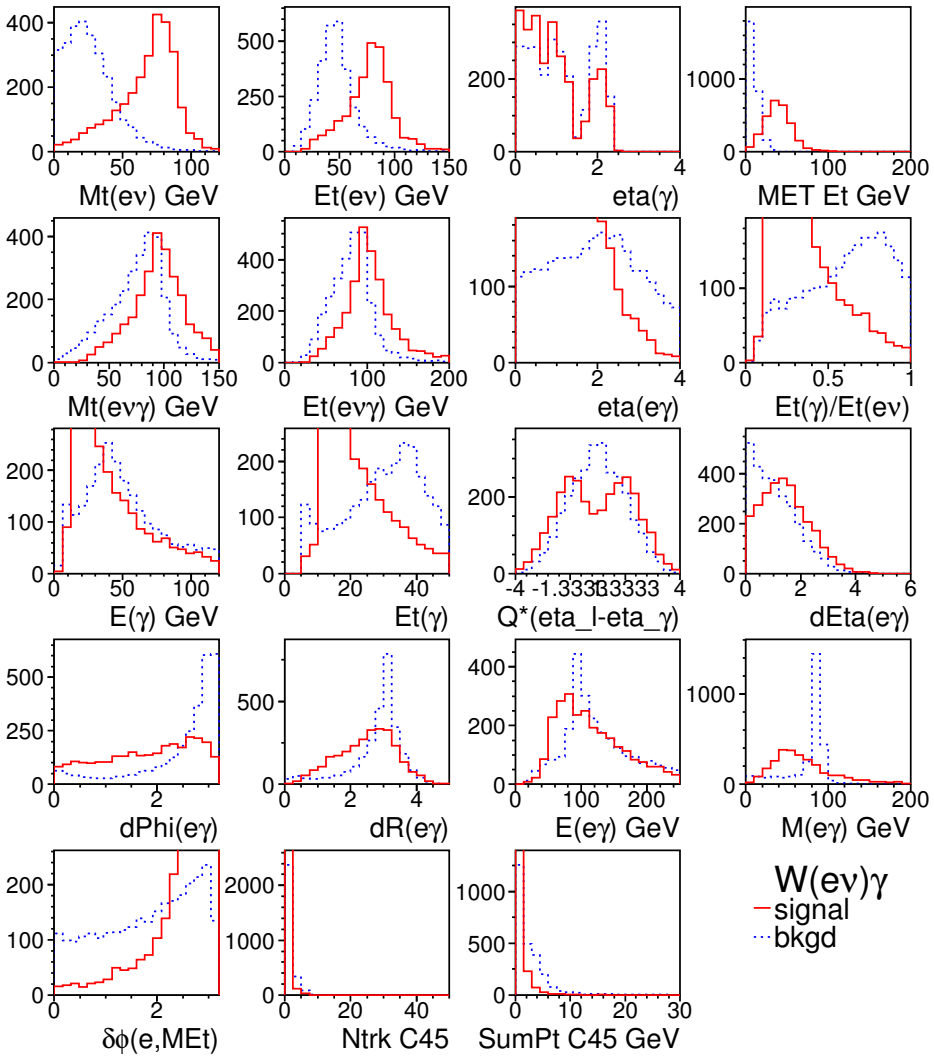

Figure 52: Distributions of event variables used in Boosted decision tree for $W^{\pm}(e^{\pm}\nu)\gamma$ with signal of ISR photons and background of inclusive $Z(ee)$ contamination.

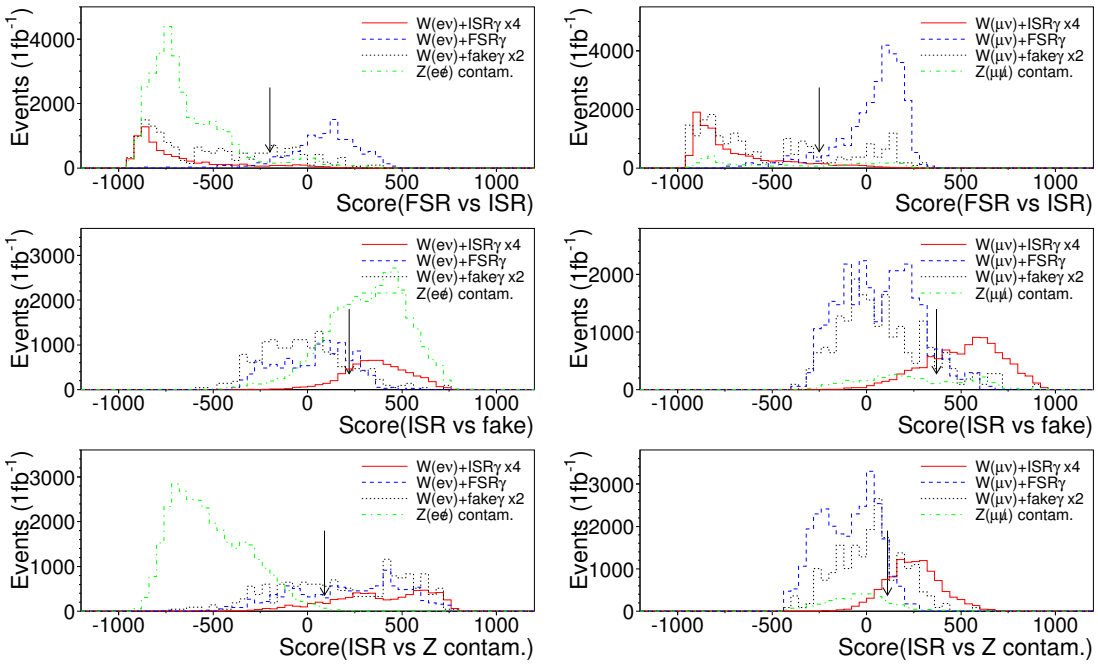

Figure 53: Test scores of the three trainings for $W^{\pm}\gamma$ events of four photon types of FSR, ISR, fake background and inclusive Z contamination). The training and tests are separated for $W^{\pm}$ decays to electron (left) and muon (right) final states. The arrows indicate cuts chosen to optimized selection of ISR photon.

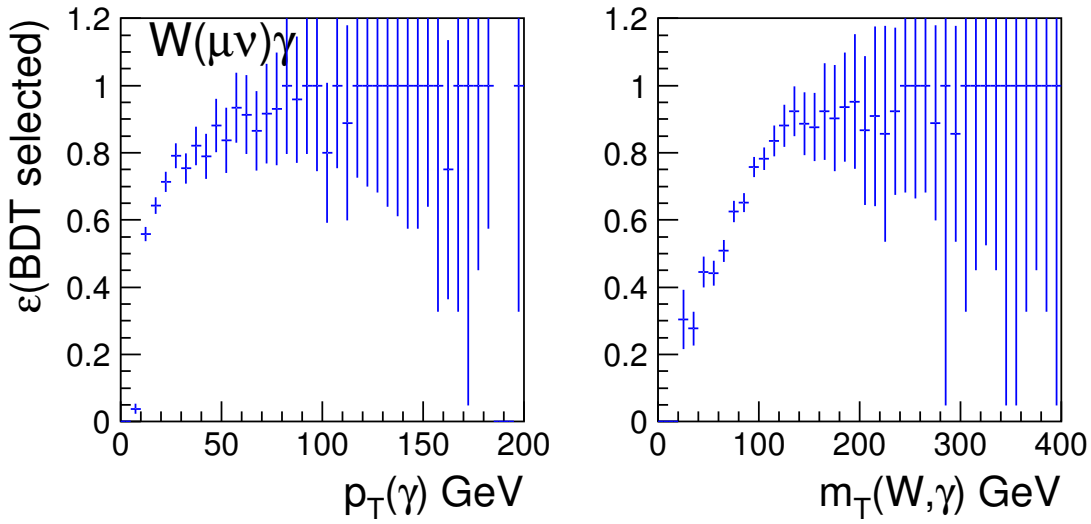

Figure 54: BDT selection efficiencies as a function of the $E_T(\gamma)$ and the transverse mass of $m_T(W^{\pm},\gamma)$.

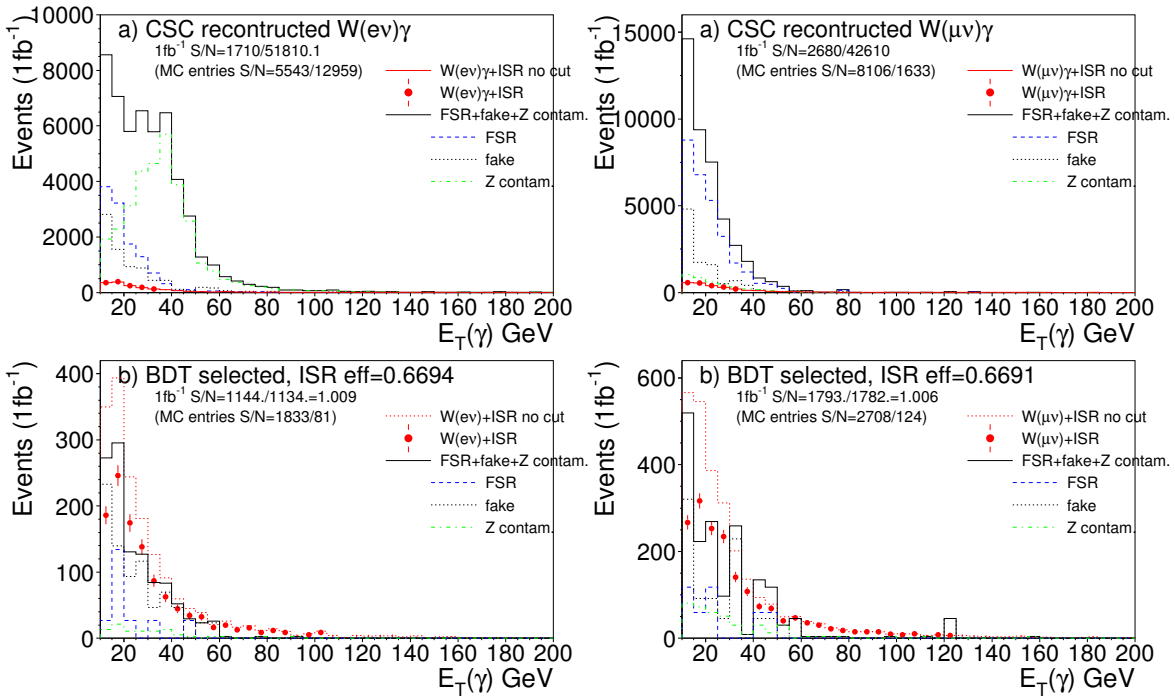

Figure 55: $E_T(\gamma)$ distributions of reconstructed $W^{\pm}\gamma$ events (upper row) and after decision tress cuts (lower row), for $W^{\pm}$ decays into electron (left) and muon pairs (right). The distributions are normalized (by about a factor two to ISR and a factor 14 to background) to the 1 fb^{-1} expectation.

in Fig. 55, for both the $e^{\pm}\gamma$ and $\mu^{\pm}\gamma$ channels. The background of fake photons are distributed mostly in low $E_T(\gamma)$ region. Fake photons originate from meson of underlying and jet secondaries. The $\mu^{\pm}\gamma$ channel has little inclusive Z contamination. The $e^{\pm}\gamma$ channel is contaminated by the $Z \to e^+e^-$ events with one electron mis-identified as a photon distributed in $E_T(\gamma) \sim 40$ GeV. The decision tree selection is effective in suppressing fake photons and Z background. The $E_T(\gamma)$ spectra of ISR photons also shows the dominance over background in $E_T(\gamma) \sim 20$ GeV region (similar to the $Z\gamma$ case). The distributions are normalized to 1 fb^{-1} expectation. The event statistics using WPhoton10 dataset for signal photons is sufficient, however, the background events of inclusive W dataset are very limited, showing large fluctuation that does not represent the 1 fb^{-1} statistics.

The $W^{\pm}\gamma$ events of WPhoton10 simulation has included the $WW\gamma$ coupling that has a destructive radiation zero amplitude at $\cos\theta^{*}_{\bar{q},\gamma} = \pm 1/3$ (for $W^{\pm}$) for the ISR scattering angle to the colliding anti-quark. The distribution of $(\eta(l^{\pm}) - \eta(\gamma))$ is suppressed near zero, and is asymmetric for having more $W^{+}\gamma$ events in the forward $+\eta$ region and more $W^{-}\gamma$ events in $-\eta$ region. Plotted in Fig.56 are the Radiation Zero spectra multiplied by $W^{\pm}$ charge, $Q_W \cdot (\eta(l^{\pm}) - \eta(\gamma))$, for ISR, FSR and background of fake photons and Z contamination. The distributions of FSR and fake photons are approximately uniform in η. Given the large statistics of $W^{\pm}\gamma$ events to be observed for 1 fb^{-1} of data, the Radiation Zero amplitude phenomenon can be observed quantitatively.

With the boosted decision tree method we gain the flexibility for not having to impose selection cuts on individual event variables. The final selection is on the decision tree test scores is effective and have preserved the kinematic range for variables like $E_T(\gamma)$ for physics study. By the topological distributions of ISR and FSR photons, we will be able to differentiate their contributions and may be used to probe physics contents beyond the Standard Model.

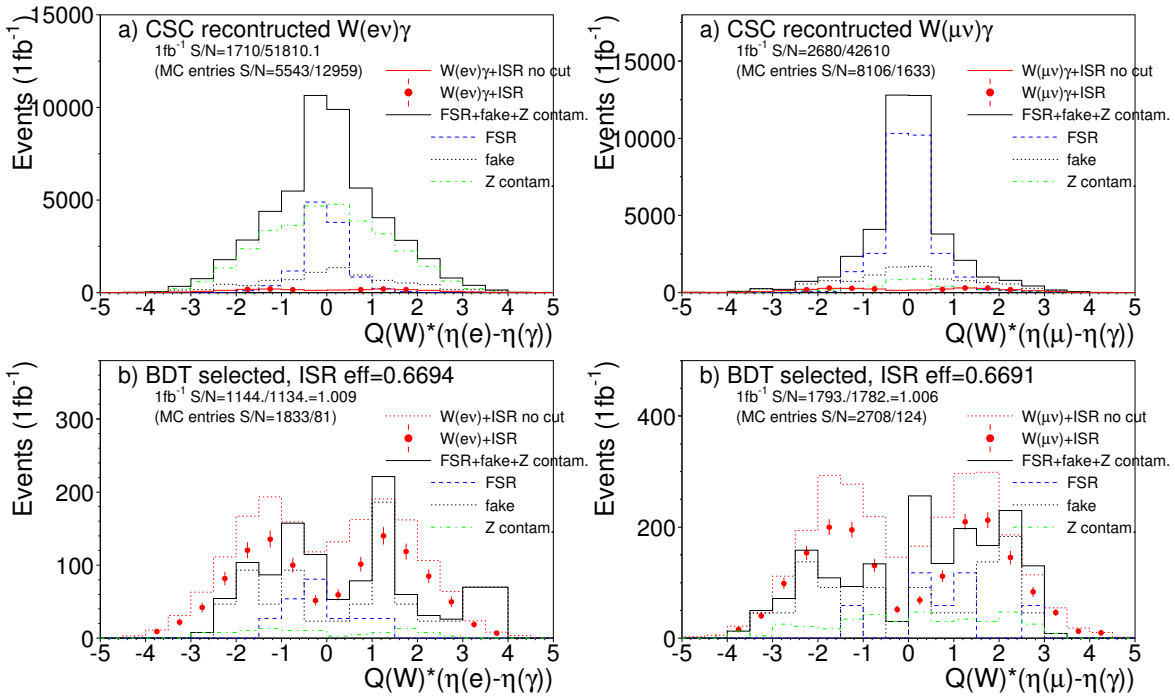

Figure 56: Distributions of $Q_W \cdot (\eta(l) - \eta(\gamma))$ for reconstructed $W^{\pm}\gamma$ candidates (upper row) and after decision tree cuts (lower row), for $W^{\pm}$ decays in electron (left) and muon (right) channels. The distributions are normalized (by about a factor two to ISR and a factor 14 to background) to the 1 fb^{-1} expectation.

6.5 $WW\gamma$ coupling

6.5.1 $WW\gamma$ coupling parameters

Measurement of $W^{\pm}\gamma$ production provides a direct investigation of the triple gauge boson couplings of $WW\gamma$ interaction (Fig.48) with the effective Lagrangian given by

$$\begin{aligned} i\mathscr{L}^{WW\gamma}/g_{WW\gamma} &= A^{\mu}(W^{-}_{\mu\nu}W^{+\nu} - W^{+}_{\mu\nu}W^{-\nu}) \\ &\quad +(1+\Delta\kappa_{\gamma})W^{+}_{\mu}W^{-}_{\nu}F^{\mu\nu} + \frac{\lambda_{\gamma}}{M_W^2}F^{\mu\nu}W^{+\rho}_{\nu}W^{-}_{\rho\mu}. \end{aligned} \quad (2)$$

The Standard Model describes the $WW\gamma$ coupling with the two parameters, $\Delta\kappa_{\gamma}$ and λ_{γ}, equal zero. The signature of anomalous TGC coupling, indicating new physics at much higher energy scale, will be observed with higher event rate of W and photons produced in high transverse momentum regions.

Dependence of anomalous $WW\gamma$ coupling is evaluated with the BosoMC program [34]. The distributions shown in Fig. 57 are examples of transverse momenta and transverse mass of observables with a set of non-zero $\Delta\kappa_{\gamma}$ and λ_{γ} values. The $E_T(\gamma)$ distribution has outstanding sensitivity to $\Delta\kappa_{\gamma}$ and λ_{γ}. It is used for binned log likelihood calculations to evaluate the confidence limits of anomalous coupling amplitudes.

The CSC datasets are of Pythia simulation of the Standard Model leading order calculation with $\Delta\kappa_{\gamma} = 0$ and $\lambda_{\gamma} = 0$. We first compare the $E_T(\gamma)$ and $m_T(W^{\pm},\gamma)$ distributions of selected $W^{\pm}\gamma$ events, shown in Fig. 58, with those of Monte Carlo generators. The event selection efficiency increases with

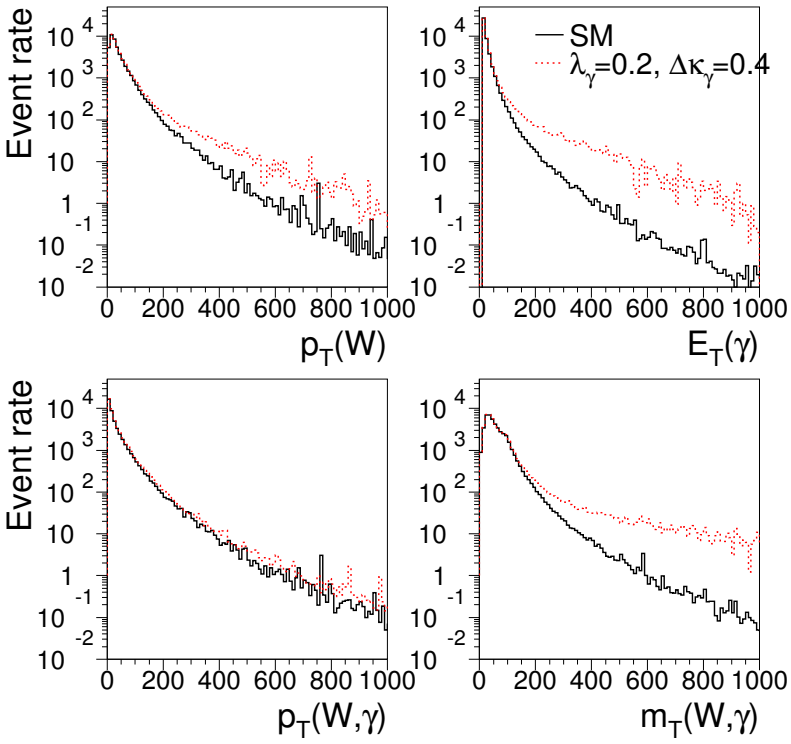

Figure 57: Distributions of transverse momenta and transverse masses of $W\gamma$ final state particles of BosoMC calculations with $\lambda_\gamma = 0.2$ and $\Delta\kappa_\gamma = 0.4$.

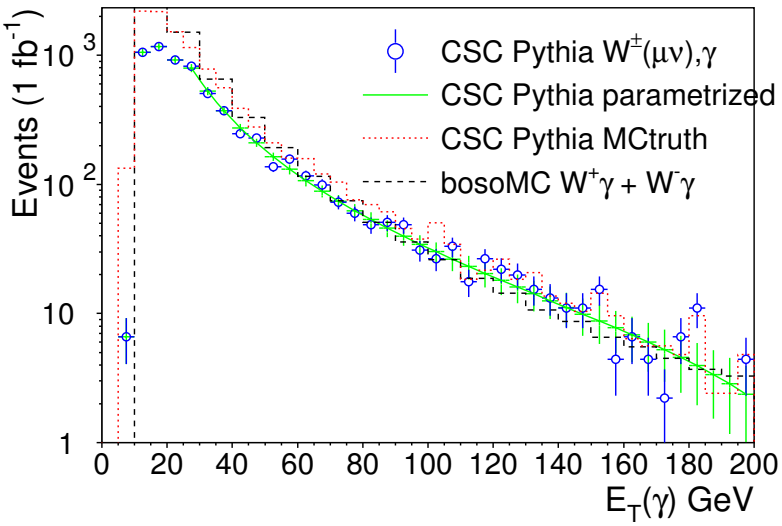

Figure 58: Distributions of $E_T(\gamma)$ $W\gamma$ events (points) in comparison with the MCtruth of CSC data and LO Standard Model distributions of BosoMC calculations.

$E_T(\gamma)$ and reaches a uniform plateau at $E_T(\gamma)$ around 80 GeV (Fig. 54). In high $E_T(\gamma)$ region the distribution (Fig. 58.a) is consistent with the Pythia MCtruth and the BosoMC LO calculation. The CSC datasets have not included anomalous coupling in the simulations. The agreement with Pythia and BosoMC distributions gives us the the confidence to reweigh the CSC data distributions according to the BosoMC calculations for dependence on the $\Delta\kappa_\gamma$ and λ_γ parameters.

6.5.2 Confidence limits for anomalous $WW\gamma$ coupling

The BosoMC has imposed a form factor on the coupling parameters for conservation of unitary at arbitrary energy scale. The two $WW\gamma$ coupling parameters are expressed by

$$\Delta\kappa_\gamma = \Delta\kappa_{\gamma 0}/(1+\frac{m^2_{W\gamma}}{\Lambda^2_{FF}})^n, \qquad \lambda_\gamma = \lambda_{\gamma 0}/(1+\frac{m^2_{W\gamma}}{\Lambda^2_{FF}})^n, \tag{3}$$

with $n = 2$, $\Lambda = 2$ TeV applied in this practice. The production of $W\gamma$ events increases with $\Delta\kappa_\gamma$ and λ_γ. It is demonstrated by the two dimensional contour plot in Fig. 59 for the integrated cross section of events with photon $E_T(\gamma)$ larger than 50 GeV.

The selected $W^\pm\gamma$ events are limited by the data statistics for presenting the integrated luminosity of 1 fb^{-1} or higher. In order to better present the expected $E_T(\gamma)$ distributions we did parameterization for the "background-subtracted" distributions of leading order expectation, and the confidence intervals of anomalous coupling parameters were calculated by binned likelihood estimation to these curves. The background in higher $E_T(\gamma)$ region drops faster than the signal. It indicates that the uncertainty in background scaling is not significant as the likelihood depends mostly on the shape of distribution in high $E_T(\gamma)$ region.

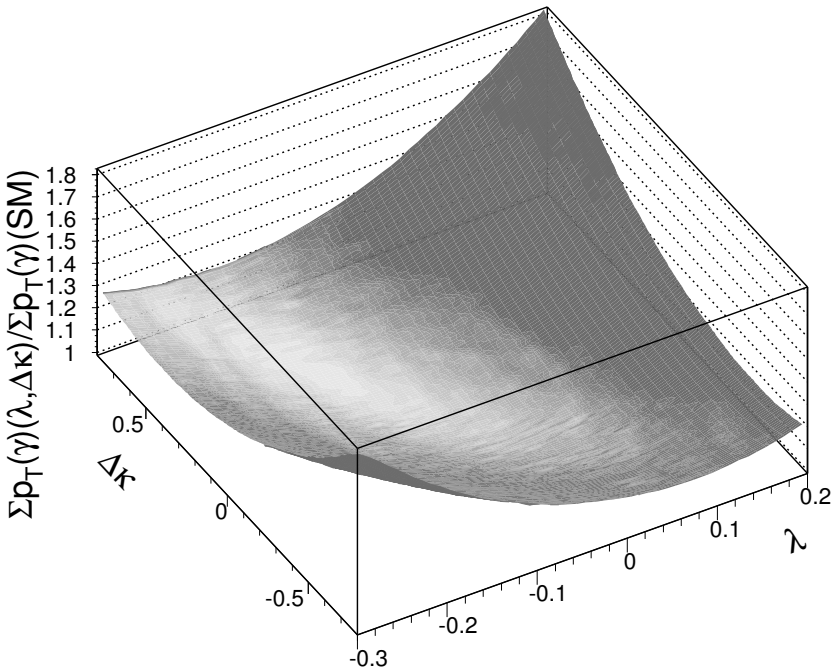

Figure 59: Dependence on the anomalous $\Delta\kappa_\gamma$ and λ_γ parameters is illustrated by the ratio of production cross section to the Standard Model for $W\gamma$ of with $E_T(\gamma) > 50$ GeV.

Although the CSC data is simulated for Standard Model leading order expectation. With the NLO calculations of BosoMC, we may study the NLO sensitivity to anomalous TGC parameters by scaling the Standard Model observables accordingly. The $E_T(\gamma)$ spectra of selected events were first scaled to NLO expectation according to the linear increase of $\sigma(NLO)/\sigma(Born)$ in $E_T(\gamma)$ (Fig. 49), and the expected number of events normalized by the k-factor in Table 38. The dependence on the anomalous coupling parameters were evaluated and scaled by the weight distributions of BosoMC calculation of

$$R(E_T;\lambda_\gamma,\Delta\kappa_\gamma) = \sigma(E_T;\lambda_\gamma,\Delta\kappa_\gamma)/\sigma(E_T;0,0). \quad (4)$$

The confidence intervals of $\Delta\kappa_\gamma$ and λ_γ are estimated by binned log likelihood functions on the histogram of

$$-\log L(y_{tot},\lambda_\gamma,\Delta\kappa_\gamma) = y_{tot} - \sum_i n_i \log y_i(y_{tot},\lambda_\gamma,\Delta\kappa_\gamma) \quad (5)$$

where y_i is the hypothesis for the i-th bin with measurable of n_i events. From the reference distributions of CSC data we scale the histograms to the integrated luminosity expected, and the histograms employed for confidence interval calculations are prepared with

1. the Mock data histograms (n_i): are the scaled reference distributions with the number of events of each bin smeared by a random Poisson distribution.

2. the Test hypotheses of λ_γ and $\Delta\kappa_\gamma$ (y_i): are the reference distributions multiplied by $R(E_T;\lambda_\gamma,\Delta\kappa_\gamma)$. Monte Carlo of BosoMC were conducted for a carpet scan in steps of 0.01 for both λ_γ and $\Delta\kappa_\gamma$. The $R(E_T;\lambda_\gamma,\Delta\kappa_\gamma)$ in Eq. 5 is return by interpolation of the BosoMC distributions.

The confidence intervals are calculated for $W^\pm\gamma$ events of electron and muon decays channels separately. Shown in Fig. 60 are an example applied to the $E_T(\gamma)$ of $W^\pm(\mu^\pm\nu)\gamma$ distribution normalized to 1 fb^{-1}. The signal expectations of LO and NLO are shown by the dashed and dotted line in Fig. 60.a. The binned log likelihood functions for signal expectation and mock data are plotted in Fig. 60.c and d for the two anomalous coupling parameters λ_γ and $\Delta\kappa\gamma$. The 95 % confidence countor is plotted in Fig. 60.b and the intervals obtained are listed in Table 41. These values are competitive to the LEP combined result of $-0.089 < \lambda_\gamma < 0.20$ and $-0.13 < \Delta\kappa_\gamma < 0.13$ [36].

The theoretical understanding by the LO calculations of Pythia and BosoMC is consistent well within 5 %. The dominant systematic certainty may be attributed by the parton density functions that is not yet investigated. Also note that the $E_T(\gamma)$ slope of NLO differs from LO. With the sensitivity estimated on anomalous coupling parameters, we would be able to distinguish NLO expectation from LO by as little as 1 fb^{-1} of data.

Table 41: 95% confidence intervals for the anomalous $WW\gamma$ coupling parameters obtained with the $E_T(\gamma)$ of NLO expectations.

	$W(e\nu)+ISR\gamma$			$W(\mu\nu)+ISR\gamma$		
	1 fb^{-1}	10 fb^{-1}	30 fb^{-1}	1 fb^{-1}	10 fb^{-1}	30 fb^{-1}
λ_γ	[-0.12, 0.07]	[-0.07, 0.03]	[-0.05,0.02]	[-0.09, 0.05]	[-0.05, 0.02]	[-0.03,0.01]
$\Delta\kappa_\gamma$	[-0.53, 0.30]	[-0.34, 0.12]	[-0.28,0.08]	[-0.46, 0.23]	[-0.30, 0.09]	[-0.13,0.06]

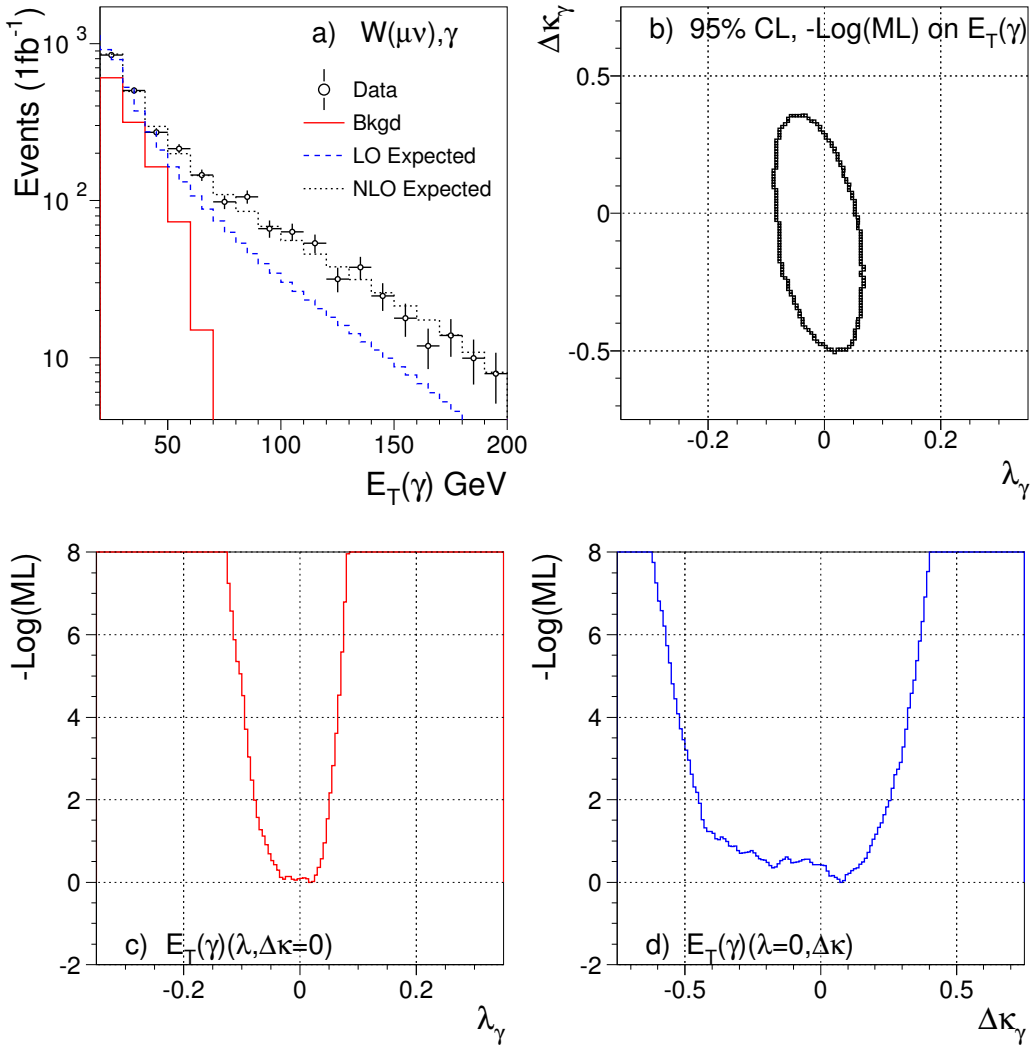

Figure 60: The Log likelihood was calculated for the $E_T(\gamma)$ distribution of NLO expectation of 1 fb^{-1} of data in a). The 95 % confidence contour is plotted in b), and the log likelihood functions of λ_γ and $\Delta\kappa_\gamma$ are plotted in c) and d), respectively.

7 Study of $Z^0\gamma$ production

7.1 $Z^0\gamma$ production mechanism

The Standard Model leading order Feynman diagrams for $Z^0\gamma$ production are shown in Fig. 61. The initial state photon radiation (ISR) in s-channel $Z^0/\gamma*$ production (left diagram) is considered as our signal, and the final state radiation (FSR) $Z/\gamma*$ process is considered as the $Z^0\gamma$ signal background. The $Z\gamma V$ vertex is forbidden at the tree-level in Standard Model. The anomalous $Z\gamma V$ couplings could be investigated.

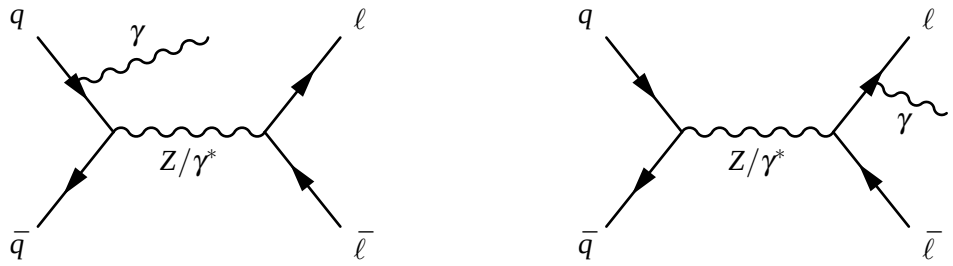

Figure 61: Born diagrams of the $Z^0\gamma$ production in hadron collider.

The Pythia calculated LO cross sections for Z^0 plus an ISR photon are compared to the *BHO* program [21]. The production cross sections are listed in Table 42. The CSC ZPhoton10 dataset (5189) of process number MSUB(19)=1 is generated with a cutoff of CKIN(3)=10 GeV for the transverse momentum of $2 \to 2$ hard scattering of the $q\bar{q} \to Z^0$ production. The ZPhoton10 cross section is lower than the cross section of $E_T(\gamma) > 10$ GeV, due to the round off of events which failed CKIN(3)$>$ 10 GeV. Thus we compare cross sections at a higher threshold of $E_T(\gamma) > 25$ GeV, with the Pythia value derived by the event fraction in ZPhoton10 dataset. The Next Leading Order (NLO) contribution is evaluated with the BHO. The BHO calculations has excluded Z^0,Jet events that contributes to inclusive $Z^0\gamma$ production with final state of $Zq\gamma$. The k-factor of the NLO cross sections to the LO calculations are also given.

7.2 $Z^0\gamma$ Monte Carlo datasets

Production of $Z^0\gamma$ events in leptonic decay channels were investigated with the ATLAS CSC datasets of full detector simulation and the reconstruction of atlas-software version 12.0.6. The datasets in use

Table 42: Production cross sections of Z and an ISR photon with single lepton flavor of $Z \to \ell\ell$ decay. The k-factor is derived by the BHO $\sigma(NLO)/\sigma(Born)$.

Pythia ZPhoton10	CKIN(3)$>$ 10 GeV	$E_T(\gamma) > 25$ GeV
σ(LO) (pb)	5.28	1.39
BHO	$E_T(\gamma) > 10$ GeV	$E_T(\gamma) > 25$ GeV
σ(Born) (pb)	4.65	1.30
σ(NLO) (pb)	5.44	1.70
k-factor	1.17	1.30

(listed in Table 43) are of Pythia generator [20] simulations for the Standard Model leading order (LO) production of inclusive Z^0 events at the proton-proton collisions of $\sqrt{s} = 14$ TeV. Previous studies of the prospect of $Z^0\gamma$ measurement were investigated with the ATLAS fast simulation reported in [33].

The Pythia simulation of inclusive Z^0 boson production (CSC dataset 5144, 5145) has included initial state radiation (ISR) of photons irradiated from the colliding quarks, and final state photon radiation (FSR) from the Z^0 decay leptons. The production cross section is 1675 pb^{-1}, with 0.83 % of the events containing an ISR photon with a $E_T(\gamma)$ threshold of about 5 GeV.

Table 43: Datasets in use for the study of $Z^0\gamma$ production. Dataset name, version, number of events generated, and the corresponding integrated luminosity are listed.

CSC dataset ID	dataset name	version	Events	pb^{-1}
5899_TW	Zphoton10($ee, \mu\mu$)	12.06.04	66k	-
5900	Zphoton25($ee, \mu\mu$)	12.06.01	6.6k	-
5900_TW	Zphoton25($ee, \mu\mu$)	12.06.01	31.2k	-
5145	PythiaZmumu	12.06.01	241k	161
5145_TW	PythiaZmumu	12.06.02	492k	329
5144	PythiaZee	12.06.01	360k	252
5144_TW	PythiaZee	12.06.02	192k	134
5144_TW	PythiaZee	12.06.04	493k	348

7.3 Detections of leptons and photons

The Z^0 bosons are reconstructed with a pair of oppositely charged leptons of the same type. Electrons are selected with the IsEM objects of category 0x7FF that match with inner detector particle tracks. Photons are also of the IsEM 0x7FF category without matching track. Muons are objects in muon_boy data bank. The Z^0 decay leptons are tagged with the MCtruth bank that contains the HEPEVT of generator particles and their four momentum. By matching reconstructed particle direction with those of MCtruth, the origin of the reconstructed particles is identified. Shown in Fig. 62 are the resolution

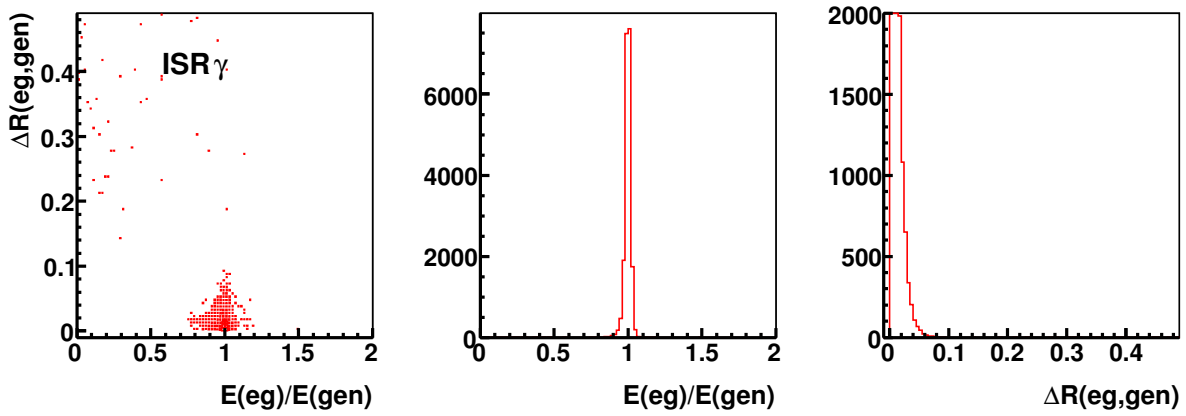

Figure 62: Plotted are the deviation in reconstructed energy and direction to the MCtruth parameters for ISR photons of $E_T(\gamma) > 25$ GeV.

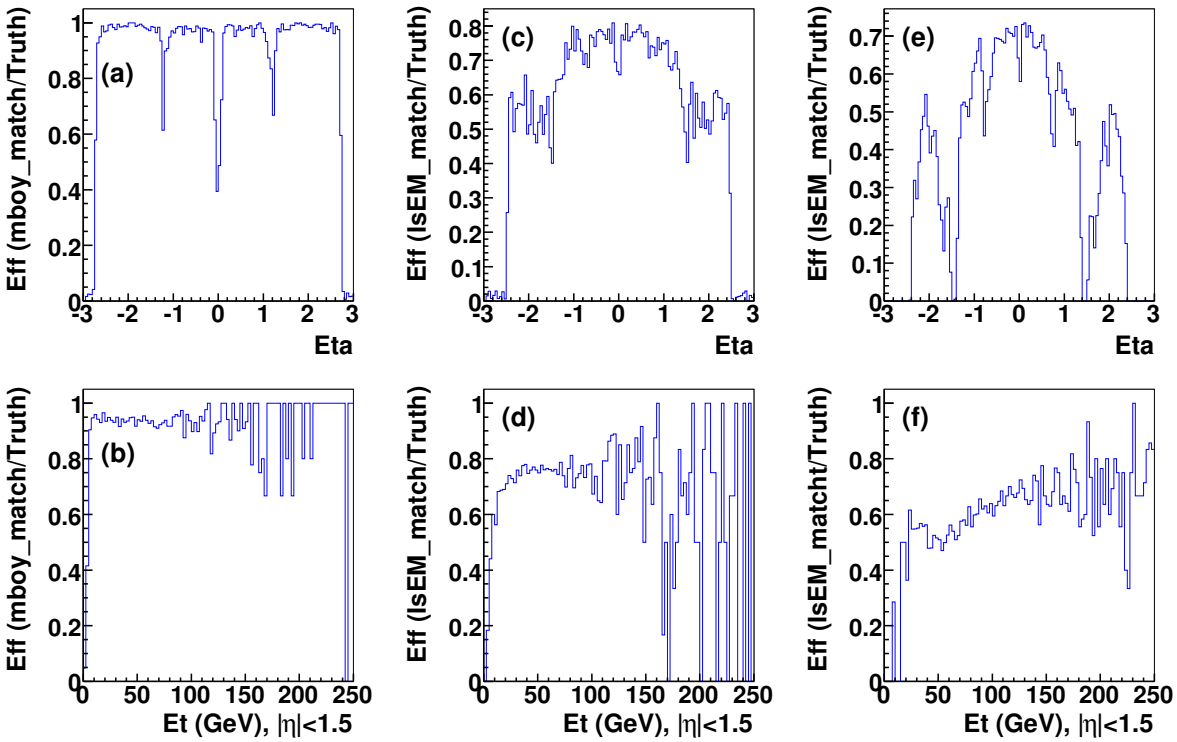

Figure 63: Reconstruction efficiencies of (a,b) muon_boy muon's, (c,d) lsEM 7xFF electrons of Z^0 decay, and (e,f) ISR photons of $E_T(\gamma) > 25$ GeV.

of reconstructed photon energy and direction to the MCtruth parameters. The photons were selected from ISR with $E_T(\gamma) > 25$ GeV. The energy resolution is 4 %, and the RMS of $\Delta R = (d\eta^2 + d\phi^2)^{1/2}$ is 0.018 Rad. Similar evaluations were also applied to Z^0 decay leptons. The muon energy resolution is 12 % and the ΔR RMS is 0.057 Rad. The electron energy resolution is 7 % and the ΔR RMS is 0.025 Rad.

The particle reconstruction efficiencies evaluated by matching to MCtruth are shown in Fig. 63. The muon_boy reconstruction (Fig. 63.a) has a uniform coverage up to $|\eta| < 2.7$. Loss is seen in the detector edges near $\eta = 0$ and ± 1.5. The distribution is approximately uniform in $p_T(\mu)$. The muon detection efficiency is 95 %. The detection of electrons and photons relies on the ECAL shower reconstruction algorithm with matching to tracks. The lsEM 0x7FF category has strong selection criteria imposed to prevent jet secondaries being wrongly recognized as a electron or photon. The reconstruction efficiencies reach a peak average of 80 % (70 %) in the barrel region ($|\eta| < 1.5$) for electrons (photons), respectively, In the forward region the ECAL reconstruction of shower cluster position is less precise due to the track matching quality that deteriorates by the tracking materials.

7.4 Topological distributions of $Z^0\gamma$ events

The observables of $Z^0\gamma$ events are the inclusive production of $e^+e^-\gamma$ and $\mu^+\mu^-\gamma$ particles, The datasets analyzed are the Pythia inclusive Z^0 production (CSC-ID 5144,5145) and the Z^0 with an ISR photon (CSC-ID 5899,5900). Events are selected the Z^0 reconstructed by the pair of the most energetic electrons or muons. The photon is the most energetic neutral lsEM particle. The photon type is tagged by MCtruth for "ISR photon" irradiated from the colliding quarks or gluons, and "FSR photon" from Z^0 decay

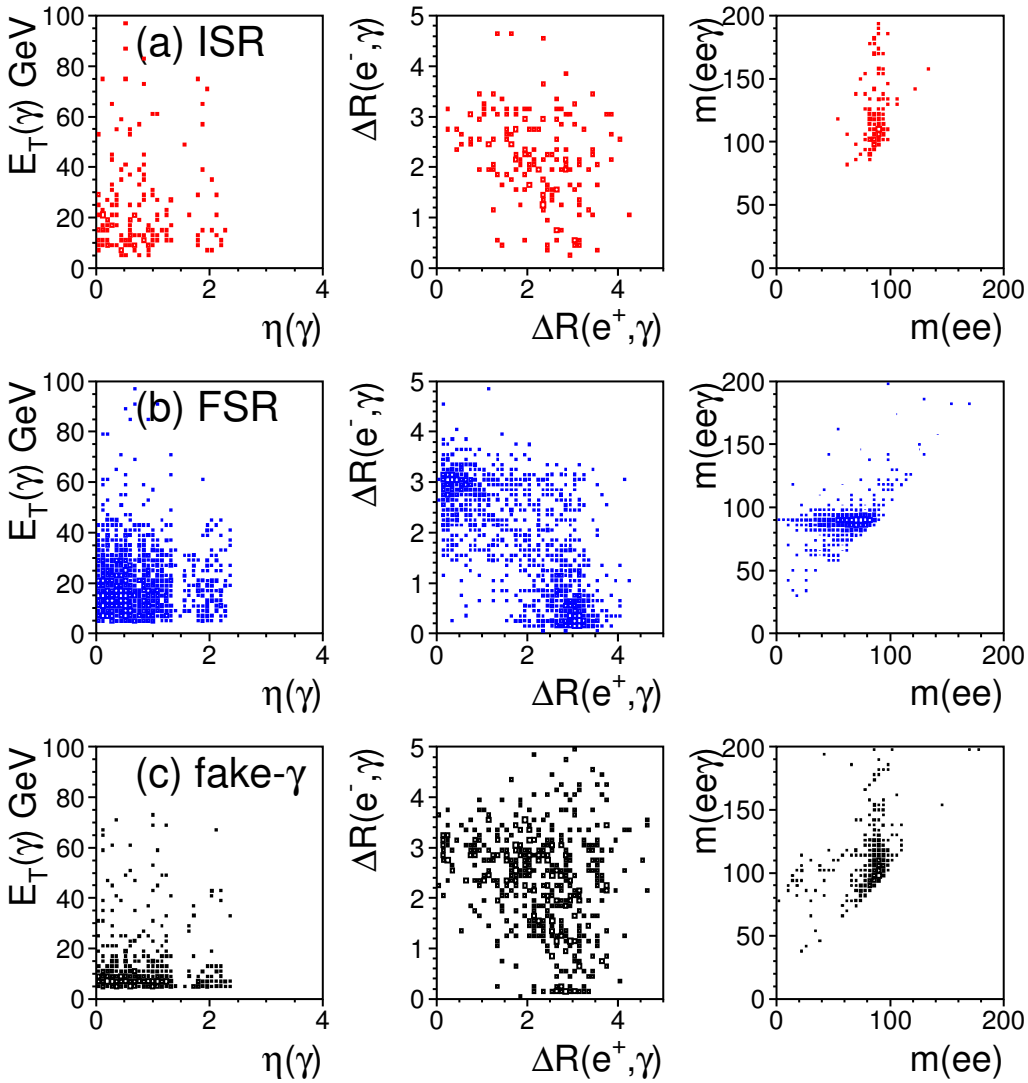

Figure 64: Distributions of $Z^0(ee)\gamma$ event variables with ISR, FSR and fake photons.

leptons. The event types with an ISR or FSR photon are distinguishable by invariant masses of lepton-pair and lepton-pair plus photon, and the photon direction to the leptons. Most FSR photons are very close to the Z^0 decay leptons and the invariant mass of m(l^+, l^-, γ) consistent with the Z^0 mass. Events with an ISR photon would have the invariant mass, $m(l^+, l^-)$, consistent with $m(Z)$, and the direction of the ISR photon separated from the Z^0 decay leptons.

Plotted in Fig. 64 are some of the most profound distributions of $Z^0\gamma$ events. Distributions of inclusive Z^0 events with a fake photon are also plotted. The fake photons were identified by matching to MCtruth and found to be mostly a neutral mesons (π^0, η, etc.) or charged mesons or electrons missing tracks. Fake photons are of jet secondaries or underlying event remnants, and the event topology is similar to events with an ISR photon. The most profound difference is seen for the $E_T(\gamma)$ of fake photons, that are distributed in less energetic region.

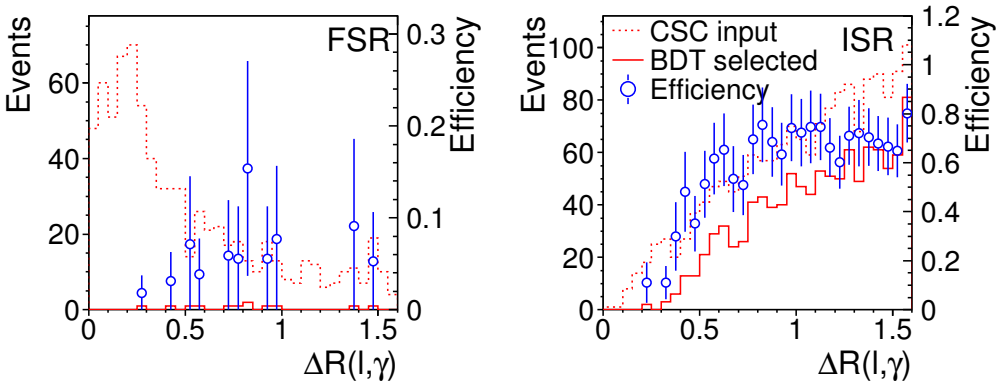

Figure 65: The opening angles in $\Delta R(l^{\pm},\gamma)$ of FSR and ISR photons to the nearest leptons (of $Z^0(\mu^+\mu^-)\gamma$ events), and the selection efficiencies with Boosted Decision Tree method.

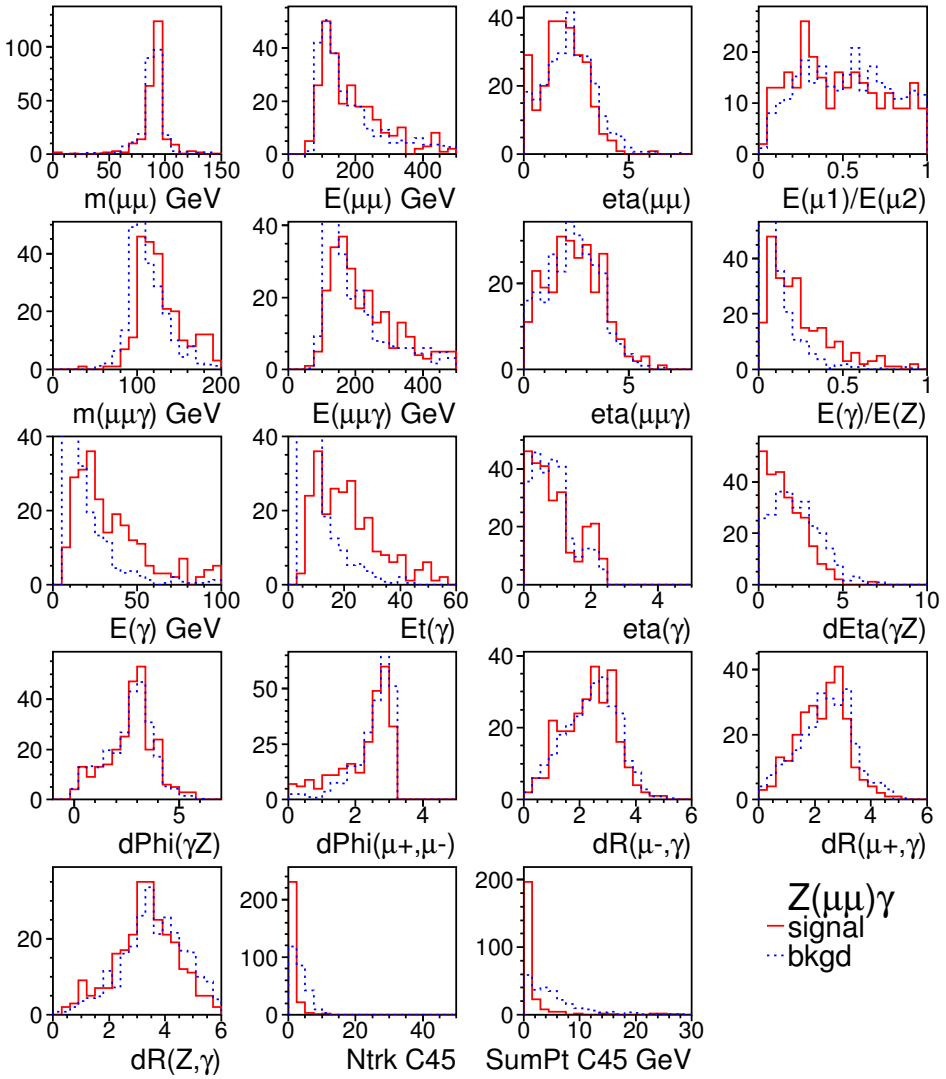

Figure 66: Distributions of variables used in Boosted decision tree for selection of $Z^0(\mu^+\mu^-)\gamma$ events with signal of ISR photons and background of fake photons.

7.5 $Z^0\gamma$ analysis based on Boosted Decision Trees

The physics interests in measuring $Z^0\gamma$ events are the cross section of Z^0 accompanied with an ISR photon and the $E_T(\gamma)$ distribution which may indicate new phenomenon beyond the Standard Model. The analysis emphasizing on the identification of "signal" events with ISR photon, discriminates "background" of 1) Z^0 with an FSR photon, 2) Z^0 with a fake photon, and 3) a small fraction of contamination from W production reconstructed as $l^+l^-\gamma$ final state.

The event selection was conducted with a Boosted Decision Tree method with training for separating $Z^0\gamma$ events of different photon types. Candidate $Z^0\gamma$ events are dominated with FSR photons that can by easily identified by the opening angle to the nearest lepton (Fig. 65). The training was in two stages: first separate the dominant FSR photon from the other, and second distinguish ISR photon against fake photon. The decision tree has 19 variables and the tests were conducted for a total 1000 tress. Distributions of event variables are illustrated in Fig. 66 for ISR photons and for background of fake photons. The characteristics in photon energy is profound. Fake photons originated from neutral mesons can not be distinguished by the limited ECAL segmentation for spacial resolution for decays into two photons. However, they are often accompanied with jet secondaries or underlying remnant particles. By counting the charged tracks in its neighborhood in a cone of 0.45 Rad, the multiplicities (Ntrk C45) and energy containment (SumPt C45) are useful parameters that differentiate background from ISR photons. Distributions of these variables are shown in Fig. 66.

7.6 $Z^0\gamma$ measurements of BDT selection

The event pre-selection of $E_T(\gamma) > 10$ GeV is chosen as low as reasonable above the Pythia generator threshold and is achievable by detector reconstruction. The expected FSR event rate is almost an order of magnitude higher than the ISR. The event rate with a fake photon is compatible to signal with an ISR photon. The number of reconstructed $Z^0\gamma$ candidates estimated for an integrated luminosity of 1 fb^{-1} are listed in Table. 44.

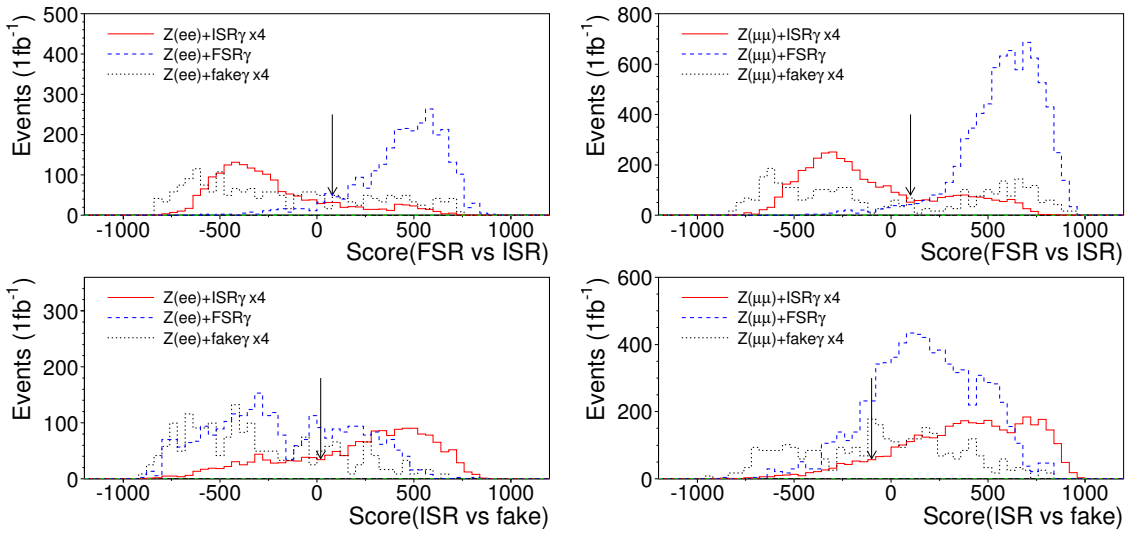

Figure 67: Test scores for the two trainings optimized for 1) FSR photons against the rest, and 2) ISR against fake photons. The arrows indicate the cuts chosen. The two columns show tests of Z^0 to e^+e^- (left) and $\mu^+\mu^-$ (right) separately.

The BDT training was conducted for Z^0 decays in electron and muon channels separately. Data samples were divided in half for training and test purposes. The test scores of the two decision trees trained for identification of FSR and ISR events are plotted in Fig. 67. The score of an event is the counting of correctness being recognized in the 1000 decision trees. The histograms shown are normalized to the expected number of events of 1 fb^{-1} (listed in Table 44). The arrows indicates the cuts chosen for selection of ISR events. The corresponding selection efficiency is 67 %, and the ISR Signal to Noise ratio is 2.0 (1.8), for Z^0 decays of electron (muon) channels, respectively.

Table 44: Number of Z^0 and $Z^0\gamma$ events of electron and muon decay channels for an integrated luminosity of 1 fb^{-1}. The photons are tagged for ISR, FSR, fake background, and contamination of W events. The ratio of ISR signal events to the rest are 1.8 (1.9) for electron and muon channels, respectively.

Pythia	Z inclusive $\sigma(Z \to e^+e^-) = 1675$ pb^{-1}				W inclusive	ZPhoton10
Detectable	e^+e^-	+ISRγ	+FSRγ	+fakeγ	$W(e\nu)\gamma$	e^+e^-,ISRγ
$E_T(\gamma) > 10$ GeV	376 k	430	2760	490	44	430
BDT cut ($\varepsilon = 67$ %)	–	–	70	74	–	288
NLO scaled	background (k=1.3)			187	–	(k=1.17) 337
Pythia	Z inclusive $\sigma(Z \to \mu^+\mu^-) = 1675$ pb^{-1}				W inclusive	ZPhoton10
Detectable	$\mu^+\mu^-$	+ISRγ	+FSRγ	+fakeγ	$W(\mu\nu)\gamma$	$\mu^+\mu^-$,ISRγ
$E_T(\gamma) > 10$ GeV	840 k	950	7500	790	930	950
BDT cut ($\varepsilon = 67$ %)	–	–	173	186	–	636
NLO scaled	background (k=1.3)			467	–	(k=1.17) 774

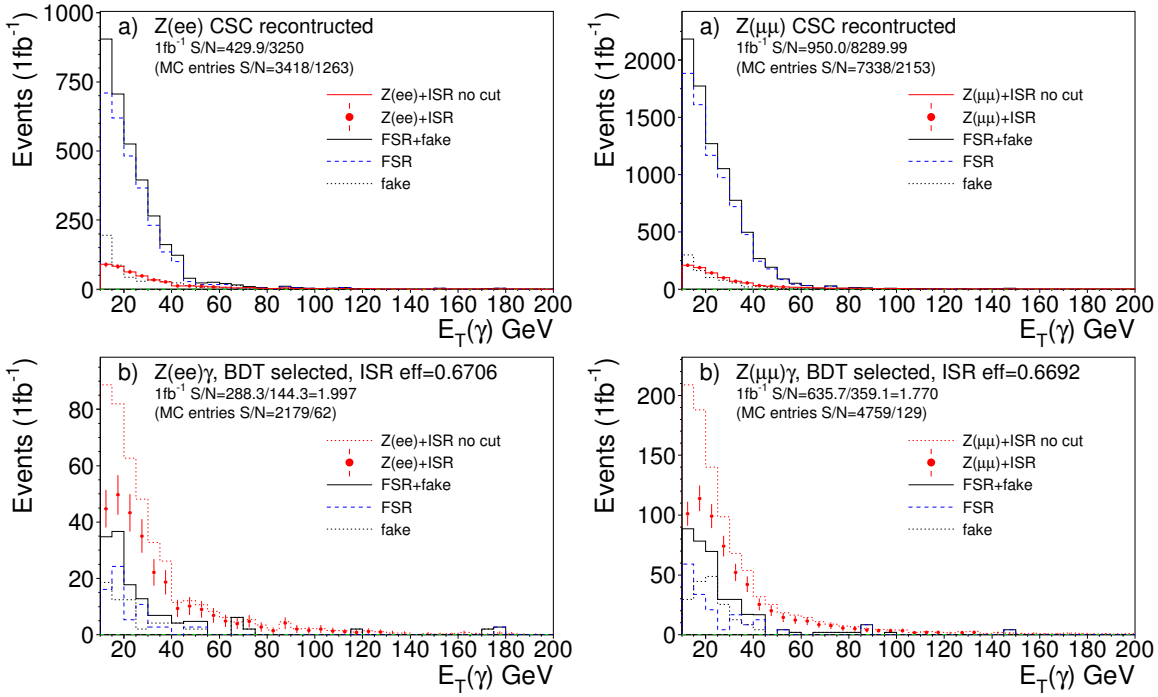

Figure 68: $E_T(\gamma)$ distributions of reconstructed $Z^0\gamma$ events (upper row) and after decision tress cuts (lower row), for Z^0 decays into electron (left) and muon pairs (right). The distributions are normalized (by about a factor three) to the 1 fb^{-1} expectation.

The ISR photon carries signatures of coupling to the colliding quarks. Event rate in the high $E_T(\gamma)$ is an important probe to new physics phenomenon. The Pythia CSC datasets are simulated for the leading order Standard Model predictions. With the decision tree selection cuts, the number of $Z^0\gamma$ events with an ISR photon for 1 fb^{-1} of data is estimated to be 290 events for the electron channel, and is about twice larger for the muon channel. The $E_T(\gamma)$ spectra before and after the decision tree cuts are shown in Fig. 68. The FSR photons, having similar $E_T(\gamma)$ distribution to ISR, attributes to about half of the background. The fake photons are populated in low $E_T(\gamma)$ region, and are distinguishable from the ISR in the $E_T(\gamma) \sim 20$ GeV region. The shape of E_T distribution in the low energy region is important for calibration and measurement of production cross section with ISR photons.

The Boosted Decision Tree variables include energy of detected photons and invariant masses of reconstructed Z^0 and so on. These variables carry discrimination power on background photons distributed mostly in the low E_T, low mass regions. Thus one see in Fig. 69 the increasing selection efficiency distributions versus $E_T(\gamma)$ and other other invariant mass and energy variables. Also plotted in Fig. 69 is the efficiency of number of charged tracks to the photon (N(trk) Corn45) in a angular cone of $\Delta R < 0.45$. ISR photons are isolated signals. The BDT selection is effective in keeping the track matching characteristics for discrimination from fake photons of underlying and jet remnants often accompanied with tracks.

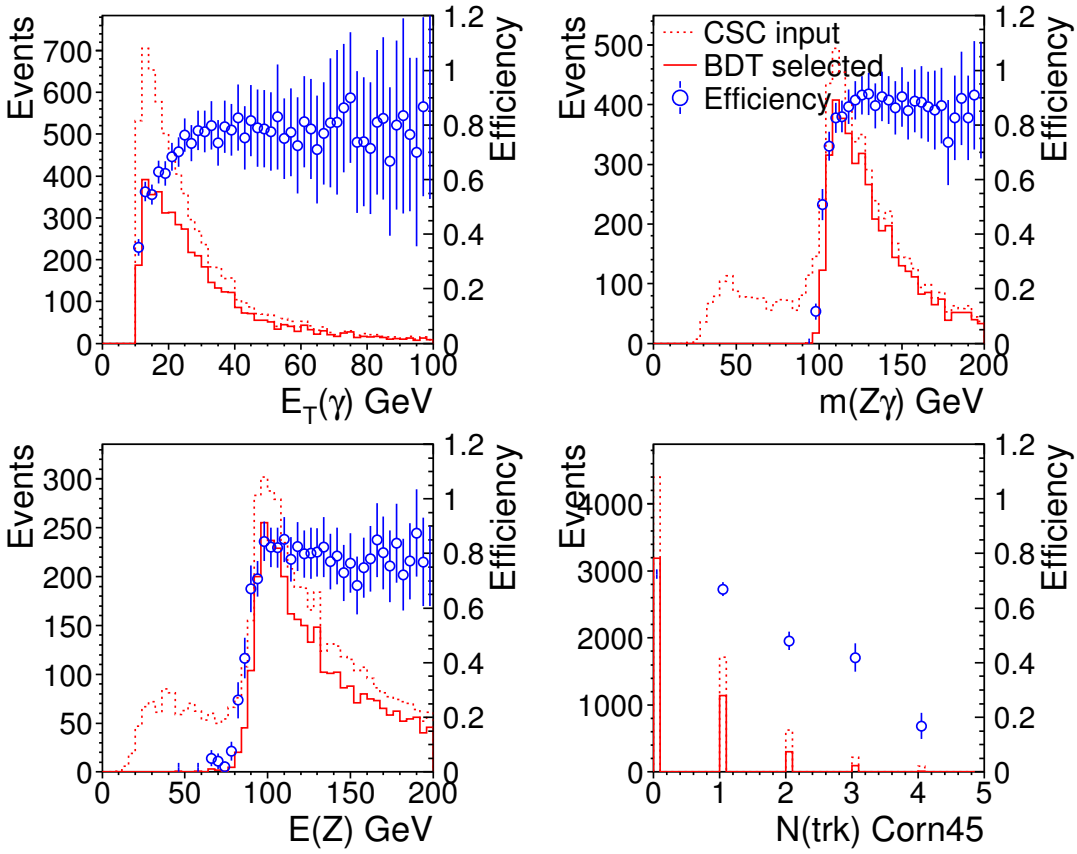

Figure 69: BDT selection efficiencies versus $Z^0\gamma$ event variables for signal events with ISR photons.

8 ZZ production and neutral triple gauge boson couplings

8.1 Introduction

The production of pairs of Z bosons at LHC is of great interest for two reasons. Firstly it provides a unique opportunity to test the Standard Model at the TeV energy scale, and secondly it is the irreducible background to the search for the Higgs boson in the $H \to ZZ$ decay channel. In the Standard Model, ZZ production proceeds through the t-channel $q\bar{q}$ scattering diagrams shown in Fig. 70(a) and (b). The ZZZ and $ZZ\gamma$ neutral triple gauge boson couplings are zero, hence there is no contribution from the diagram in Fig. 70(c) at tree level. At the one-loop level the contribution from this diagram is $\mathcal{O}(10^{-4})$ [28]. Measurements of the neutral triple gauge boson couplings provide a sensitive test of the gauge structure of Standard Model; non-zero values would indicate the presence of new physics beyond the Standard Model. Non-zero ZZZ and $ZZ\gamma$ couplings typically increase the ZZ cross section at high ZZ invariant mass and high p_T of the Z boson. The study of ZZ spin correlations can be used to discriminate $H \to ZZ$ from the effects of anomalous couplings, because the Z bosons from H decay tend to be longitudinally polarised whereas anomalous couplings lead to one transversely polarised and one longitudinally polarised Z boson.

ZZ production has been studied in e^+e^- annihilation at LEP [4], and first results from $p\bar{p}$ collisions at the Tevatron based on around 1fb^{-1} of data have been reported, as discussed in Section 3.1.1. The production cross section at LHC is predicted to be about 15–20 times larger than at the Tevatron. Predicted values at LHC at leading and next-to-leading order are shown in Table 45. The NLO value is around 15 pb; this does not include the contribution from gluon fusion, which is expected to be about 15% [39]. This contribution is not included in all studies in this section. As shown below, a measurement of the ZZ production cross section should be possible in the first year of LHC running, with as little as 1fb^{-1} of data.

We present studies of ZZ production using two decay channels. The $ZZ \to \ell\ell\ell\ell$ ($\ell = e, \mu$) channel has a clean, almost background-free, signature of four high p_T isolated leptons. The main backgrounds come from $t\bar{t}$ pair-production where both W bosons decay leptonically and the other two leptons come from the decay of the b quarks, and from Z boson production associated with jets, where the Z boson decays leptonically and is accompanied by leptons in heavy quark jets. The $ZZ \to \ell\ell\nu\nu$ channel is characterised by two high p_T isolated leptons with large missing transverse energy. It has a branching ratio about six times larger than $ZZ \to \ell\ell\ell\ell$, but suffers from much bigger backgrounds. These arise from $t\bar{t}$ and Z+jets events where one or more jets is not detected and gives a fake missing energy signature. In addition, this channel suffers an irreducible background from WZ events where the lepton from the decay of the W boson is undetected.

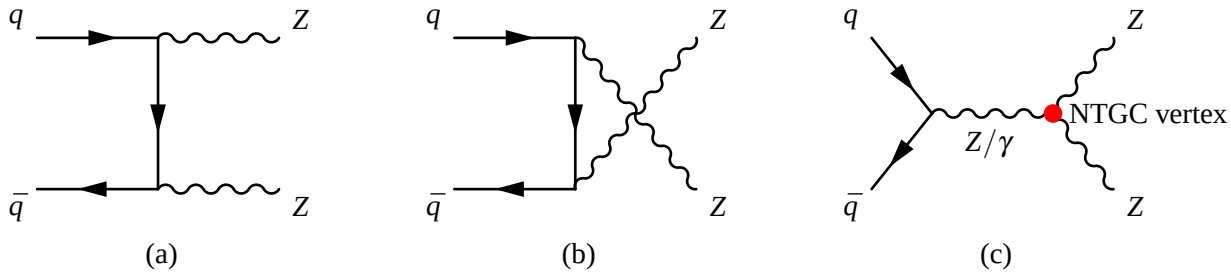

Figure 70: Feynman diagrams for ZZ production at leading order: (a) and (b) show the diagrams allowed in the Standard Model; (c) shows the diagram including the neutral gauge boson coupling which is forbidden in the Standard Model.

Table 45: Cross-section for $pp \to ZZ$ at $\sqrt{s}$ = 14 TeV. The first column shows the leading order value from Pythia for $pp \to (Z/\gamma^*)(Z/\gamma^*)$ with $m(Z/\gamma^*) > 12$ GeV. The second column shows the value from Pythia requiring $70 < m(Z/\gamma^*) < 110$ GeV. The third column shows the next-to-leading order value from MC@NLO, which is for pure on-shell ZZ production.

PDF set	Pythia σ [pb] $m(Z/\gamma^*) > 12$ GeV	Pythia σ [pb] $70 < m(Z/\gamma^*) < 110$ GeV	MC@NLO σ [pb]
CTEQ6L (LO)	11.15	9.55	–
CTEQ6M (NLO)	–	–	14.74
MRST01 (LO)	11.05	9.48	–
MRST02 (NLO)	(12.33)	(10.63)	15.32

The results of the ZZ production studies are used to investigate the expected sensitivity to anomalous neutral gauge boson couplings in early ATLAS data.

8.2 $Z^0Z^0 \to \ell^+\ell^-\ell^+\ell^-$ analysis

In this section we present a study on the Z^0Z^0 production channel via four lepton decay channels:

$$pp \to Z^0Z^0 \to e^+e^-e^+e^-, \;\; \mu^+\mu^-\mu^+\mu^-, \;\; e^+e^-\mu^+\mu^-.$$

The $pp \to Z^0Z^0$ total production cross section at $\sqrt{s} = 14TeV$ can be found in references [16, 15] by L.Dixon et al. and J.Campbell et al. respectivelly, for both MRST and the CTEQ(5) parton distribution functions. The total production cross sections at LO and NLO, without any cuts applied, are given in the two references are summarized in Table 46.

Table 46: Summary of cross section values given in references (see text) for the MSRT and CTEQ(5) PDFs . Values not in parentheses are taken from Campbell et al., whereas values in parentheses come from Dixon et al.

	σ_{LO}[pb]	σ_{NLO}[pb]	K_F
CTEQ(5)	12.9(11.8)	17.2(15.8)	1.33(1.34)
MRST	12.2(11.4)	16.3(15.2)	1.34(1.33)

The Z^0Z^0 Monte Carlo samples used in this analysis is for the $ZZ \to 4\ell, \;\; (\ell = e, \; \mu, \; \tau)$ process, which is generated by PYTHIA(v6.3) [20] (at LO) using the CTEQ(6) PDF. The Z/γ^* interference terms are included in the generator. With the mass cut on the dileptons decay from Z/γ^*, the cross section times the dilepton decay branching ratio, $\sigma \times BR$ is 159 fb. The next-to-leading-order (NLO) calculations give higher production cross sections. The k-factor (defined as $k = d\sigma(NLO)/d\sigma(LO)$) is about 1.35 when both Z^0's are on mass shell. However, when the Z^0/γ^* are off the Z^0 mass shell, the k-factor varies ranging from 1.15 to 1.52 for the $Z/\gamma^*Z/\gamma^*$ mass range from 115 GeV to 405 GeV, which is determined by using the MCFM MC calculations [15]. For this analysis, we will use a constant k-factor, 1.35, to normalize the $Z^0Z^0 \to 4\ell$ signal events.

The major background contributions to this channel come from the $t\bar{t} \to 4\ell + X$ and $Zb\bar{b} \to 4\ell + X$ processes. In our background studies, the $t\bar{t} \to 4\ell + X$ events are produced with MC@NLO [18] program, witch gives a total $t\bar{t}$ production cross section, of $\sigma = 833pb$ (NLO). The $Zb\bar{b} \to 4\ell + X$ events are produced with the AcerMC Monte Carlo [51] which gives the LO cross section, $\sigma = 52 \; pb$. PYTHIA program has been used for the hadronization process. The k-factor for this process is 1.42.

Table 47: Signal data samples summary table.

Process	Dataset	σ[fb]$\times$ BR	Filter	Filter eff.	K-factor	Events	L[fb^{-1}]
$ZZ \to 4\ell$	5980(v11.0.4)	159	$\mid \eta \mid < 2.7$, $p_T > 5$ GeV	0.219	1.35	154450	3284
$ZZ \to 4\ell$	5980(v12.0.6)	159	$\mid \eta \mid < 2.7$, $p_T > 5$ GeV	0.219	1.35	43000	913

Table 48: Background data samples summary table.

Process	Dataset	σ[pb]	k	Filter	Filter eff.	Events	L[fb^{-1}]
$Zb\bar{b} \to 4\ell$	5177(v12.0.6)	52	1.42	$Zb\bar{b} \to 4\ell$	0.00942	313689	451
$t\bar{t} \to 4\ell$	5211(v12.0.6)	833	–	$t\bar{t} \to 4\ell$	0.00728	152701	25.2

8.2.1 Signal and background MC Samples

Table 47 summarizes the basic properties of the signal samples used in this analysis. In these samples both $Z's$ are forced to decay to leptons (three flavors). Further 'filter' selection cuts are applied to generated MC events:

- Four leptons (e, μ) in final states. Those electrons and muons include from the Z/γ^* decays and from τ-lepton decays.
- $P_T^\ell > 5$ GeV.
- $|\eta_\ell| < 2.7$.

The overall filter efficiency is 21.9% as shown in Table 47. The format of all samples used is the Analysis Object Data (AOD) format [41]. Reconstruction was performed using both 11.0.4 and 12.0.6 releases of the Atlas Software framework, ATHENA.

The properties of the background samples studied for this channel are given in Table 48. The two main contributions are from $t\bar{t}$ and $Zb\bar{b}$ processes. Because of the large cross sections of the two channels, the number of events generated with ATHENA v11.0.4 correspond to very small luminosity, not allowing thus for a reliable background estimate. For this reason in ATHENA v12.0.6 filter cuts requiring 4 leptons in the final state were applied.

On the basis of the Z decay mode, signal events can be categorized as follows:

- both Z bosons decaying to muons ('4μ')
- both Z bosons decaying to electrons ('$4e$')
- one Z decaying to muons and the other to electrons ('$2\mu 2e$')

In Table 49 the five possible event configurations are given and their respective percentage contributions to the $ZZ \to 4\ell$ sample are shown. In case of taus present in the event with subsequent leptonic decays the contribution to the above categories is given in the same table. Note that the event topologies $3e1\mu$ and $3\mu 1e$ resulting from at least one Z decaying to τs, which accounts for the 3.32% of the $ZZ \to 4\ell$, are not studied here. The contribution of this decay to the other 3 event configurations is not taken into account in the calculation of the efficiencies, since these events do not survive the selection cuts for the Z mass as explained below.

In Fig. 71(a) the invariant mass distributions from PYTHIA of the four leptons for the three event topologies is shown, before any cut is applied. The two structures below 200 GeV correspond to events

Table 49: The composition of the $ZZ \to 4\ell$ sample according to the final state configuration and the contribution to the five possible event topologies from the τ leptonic decays of the Z's.

Channel	Fraction in $ZZ \to 4\ell$ [%]	Channel	$Z \to \tau \to \ell(\mu, e)$ contribution [%]
$ZZ \to 4\mu$	23.41	$ZZ \to 4\mu$	1.17
$ZZ \to 4e$	22.70	$ZZ \to 4e$	0.97
$ZZ \to 2\mu 2e$	46.56	$ZZ \to 2\mu 2e$	1.87
$ZZ \to 2\tau 2\ell(\mu, e, \tau)$	7.33	$ZZ \to 3\mu 1e$	1.76
		$ZZ \to 1\mu 3e$	1.56
Total	100.0	Total	7.33

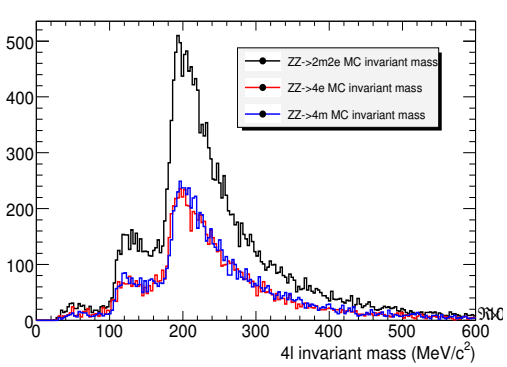

(a) The invariant mass distribution for $ZZ \to 4\ell$ PYTHIA events for the three event categories : 4μ, $4e$ and $2\mu 2e$.

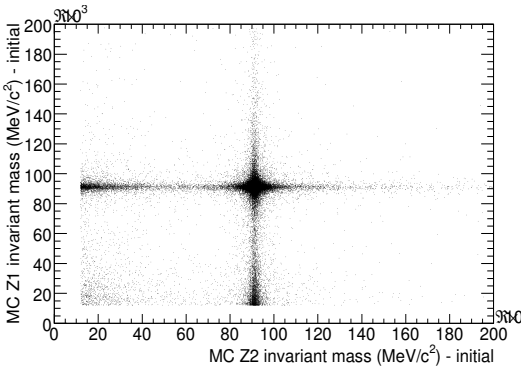

(b) Mass correlations of the two Z bosons in the PYTHIA sample. The three event types ZZ, ZZ^* and Z^*Z^* are clearly separated.

Figure 71: Four lepton invariant mass distributions (left figure) and correlation of the two Z bosons (right figure) in the signal sample.

Table 50: Fraction of events in the PYTHIA sample classified according to the two boson mass.

	$70 < m(Z) < 110$ [%]	$m(Z) \pm 5Z_{width}$ [%]	$m(ZZ) > 2M(Z)$ [%]
ZZ	72.9	69.1	80.0
ZZ^*	23.4	26.4	17.6
Z^*Z^*	3.7	4.5	2.4

with one or both Z bosons off-mass shell. This is clearly illustrated in Fig. 71(b), where the mass correlations of the two Z's are drawn.

In Table 50, the classification of PYTHIA events is done either using the ZZ invariant mass or the definition of the on-mass shell Z. In column 1, on-mass shell window lies between $70-110$ GeV, in column 2 the window is $M_Z \pm 5Z_{width}$, where $M_Z = 91.19$ GeV and $Z_{width} \simeq 2.5$ GeV [50]. In the third column the ZZ window opens above $2M_Z$ while the ZZ^* and Z^*Z^* lie in the regions $100-2M(Z)$ and < 100 GeV respectivelly.

In the current analysis, the cross section was measured using two different mass regions. The mass region characterized as tight requires both Z's to have reconstructed invariant mass between 70 and 110 GeV. This corresponds to Z's with generated mass $\pm 5\sigma$ around the mass value and therefore represents 70% of the PYTHIA sample. The second mass region characterized as loose requires one Z between 70 and 110 GeV and the other Z invariant mass > 20 GeV. This corresponds to 89% of the PYTHIA sample. It is important to define the mass region using the constrain on the Z mass (one or both) instead of the reconstructed 4-lepton invariant mass in order to eliminate combinatorials and background events.

Given that the p_T of the leptons is used in the analysis for the selection of the signal, the ordered lepton p_T distributions as generated by PYTHIA, are shown in Fig. 72 for each event topology and lepton flavour.

8.2.2 Physics objects and lepton pre-selection

The identification of leptons and information on their properties used in the analysis, in both signal and background samples, are provided by the official reconstruction algorithms of the ATLAS software. Muons identified by the STACO reconstruction algorithm and electrons identified by the Egamma or Egammasoft reconstruction algorithm [52] are retrieved from the corresponding AOD containers. A set of pre-selection cuts, which is described below, is applied to the muon and electron collections.

Muon pre-selection cuts

- $p_T > 6$ GeV/c , $|\eta| < 2.7$
- Muon tracks should be MuonSpectrometer-Inner Detector combined tracks or MuonSpectrometer standalone tracks in the rapidity region $2.5 < |\eta| < 2.7$, since this region is outside the Inner Detector's acceptance.
- $\chi^2/ndf < 15$ of the match between the MS and ID tracks
- $\chi^2/ndf < 15$ of the track fit

Electron pre-selection cuts

- $p_T > 6$ GeV/c , $|\eta| < 2.5$
- $0.5 < E/P < 3.0$

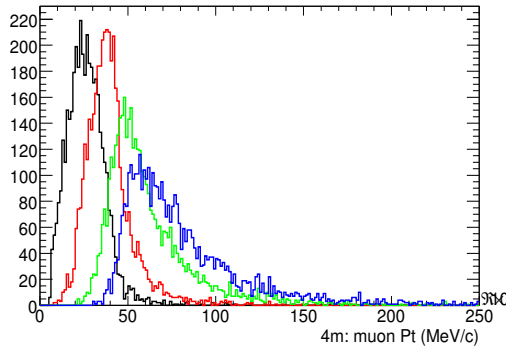

(a) Ordered p_T distributions of the 4 muons in 4μ events.

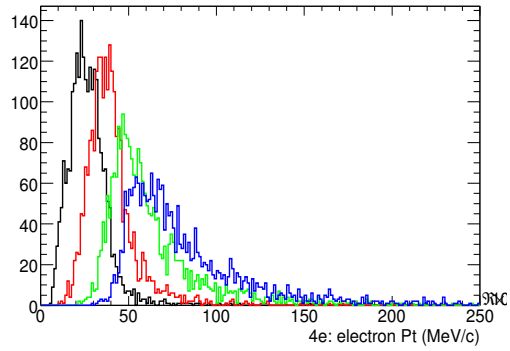

(b) Ordered p_T distributions of the 4 electrons in $4e$ events.

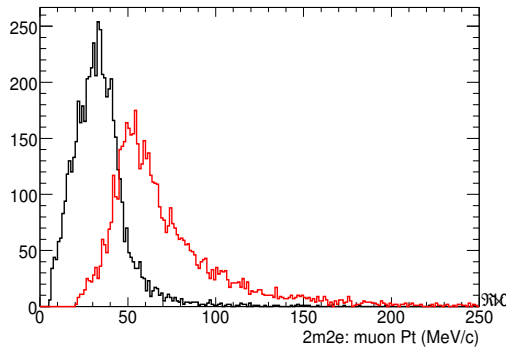

(c) Ordered p_T distributions of the 2 muons in $2\mu 2e$ events.

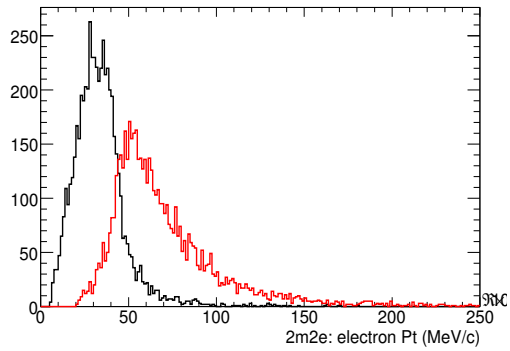

(d) Ordered p_T distributions of the 2 electrons in $2\mu 2e$ events.

Figure 72: Lepton p_T distributions, ordered for the 4μ, $4e$ and $2\mu 2e$ events.

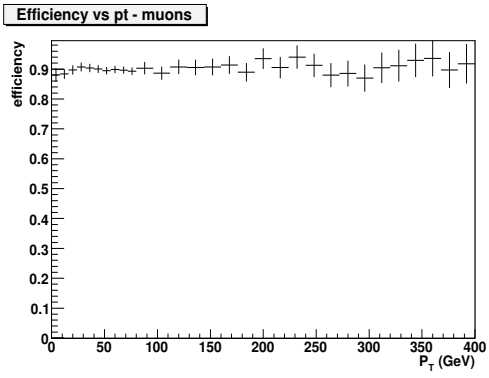

(a) p_T dependence of the muon reconstruction efficiency in ZZ events

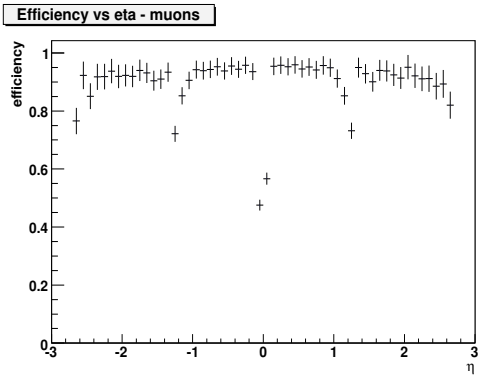

(b) η dependence of the muon reconstruction efficiency in ZZ events

Figure 73: Muon reconstruction efficiencies as a function of p_T and η.

Table 51: Reconstruction efficiency for muons and electrons.

	v11.0.4	v12.0.6
electrons	87.86%	81.39%
muons	93.31%	89.99%

8.2.3 Lepton reconstruction efficiency

The single muon reconstruction efficiency for muons coming from Z decays is shown in Fig. 73 and the single electron reconstruction efficiency for electrons coming from Z decays in Fig. 74, as a function of p_T and η.

The above efficiency plots are constructed by dividing, in each p_T or η bin, the number of muons/electrons reconstructed in this bin to the original number of generated 'true' leptons originating from Z decays in the same bin. The reconstructed leptons are required to 'match' in η and ϕ with the generated ones. A 'true' lepton is considered 'matched' to the reconstructed if the distance $dR = \sqrt{d\eta^2 + d\phi^2}$ is less than 0.1. Reconstructed leptons with no match to any of the generated ones in the event are characterized as fakes and they do not contribute to the efficiency calculation which is given in Table 51.

8.2.4 Event Selection

After applying the pre-selection criteria described in section 8.2.2, events are classified according to the number of same flavour leptons. Three categories are considered. Events with 4 or more muons, events with 4 or more electrons and events with 2 or more muons and 2 or more electrons. Lepton pairs of the same flavour and opposite charge are formed in each category and pairs with both leptons lying within a cone of radius $dR < 0.2$ are rejected. The remaining pairs are combined in doublets to form one 4 lepton candidate.

The two main criteria which are used to discriminate signal from background are the lepton's p_T and isolation. In all three event topologies the isolation criterion is applied to all four leptons and the two opposite sign pairs are required to have at least one lepton with $p_T > 20$ GeV$/c$.

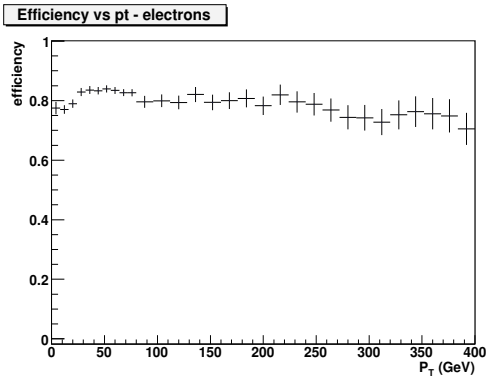

(a) p_T dependence of the electron reconstruction efficiency in ZZ events

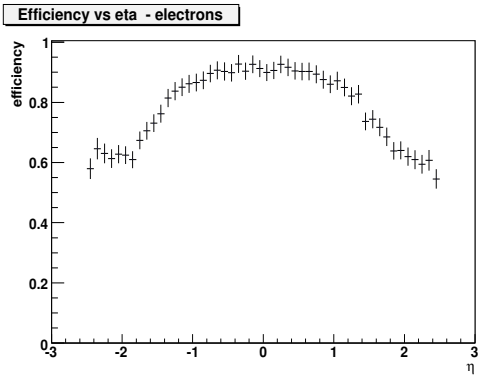

(b) η dependence of the electron reconstruction efficiency in ZZ events

Figure 74: Electron reconstruction efficiencies as a function of p_T and η.

Isolation cuts

For muon isolation the variable I is defined as,

$$I = \frac{E_T^{0.4}}{E_T^{\mu}} \tag{6}$$

where $E_T^{0.4}$ is the transverse energy in a cone around the muon track of radius $dR = 0.4$ and E_T^{μ} is the transverse energy of the muon. For electrons the *isEM* flag is used. Electron candidates have to pass a series of cuts based on the shower shape properties in different compartments of the calorimeter as well as variables combining Inner Detector and Calorimeter informations. If a cut is not passed, then a bit is set in the *isEM* flag. For more information on the physical meaning of each bit see reference for electron reconstruction [1].

A muon is considered isolated if $I < 0.2$ and an electron is considered isolated if the first four bits of the *isEM* flag are set, which implies that only calorimeter based related criteria are required. In Figure 75 the distribution of the muon isolation variable I is given for each of the four muons, for both signal and background. Distributions in each plot are normalized with respect to the same number of events.

Maximum p_T cut

The p_T distribution of the highest p_T lepton in each electron and muon pair is shown in Fig. 76. Fig. 76(a) and 76(b) are for the 4μ and $4e$ case respectively, while Fig. 76(c) and 76(d) for the muon and electron pair of the $2\mu 2e$ case. All pairs are required to have at least one lepton above 20 GeV.

Plots in Fig. 77 show the efficiency of the p_T^{max} and isolation cuts for the 4μ event topology, while plots in Fig. 78 show the p_T^{max} cut efficiency also for the $4e$ and $2\mu 2e$ final states.

Mass cut

In order to eliminate combinatorial background and background with leptons not originating from Z decays, a cut on the reconstructed Z invariant mass is applied. One or both Z's are required to have reconstructed invariant mass between $70 - 110$ GeV. Thus we define two cases(mass regions) in the

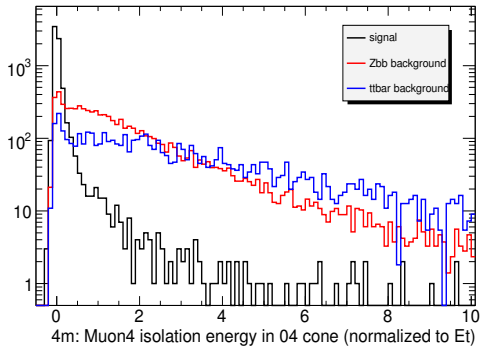

(a) Isolation variable I (see text) for the softest muon

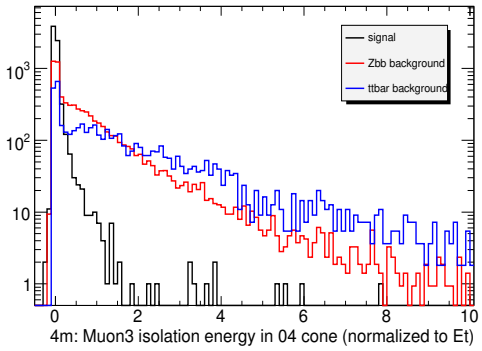

(b) Isolation variable I (see text) for the 3rd highest p_T muon

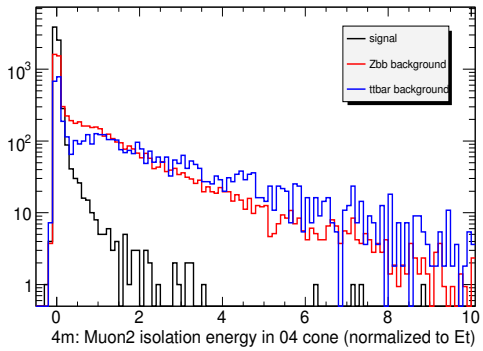

(c) Isolation variable I (see text) for the 2nd highest p_T muon

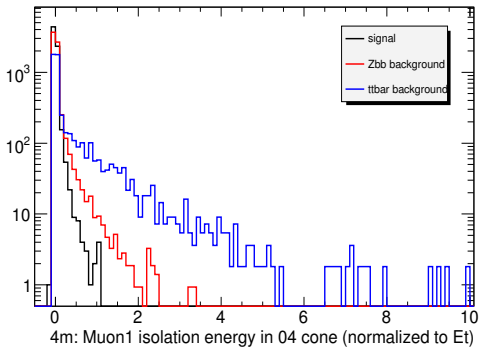

(d) Isolation variable I (see text) for the highest p_T muon

Figure 75: Muon isolation variable for signal and background in the 4 muon final state case.

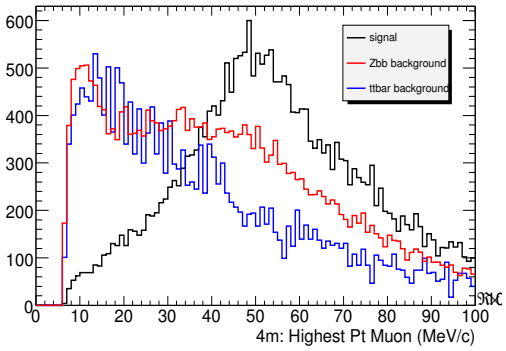

(a) p_T of the hardest muon in the 4μ case

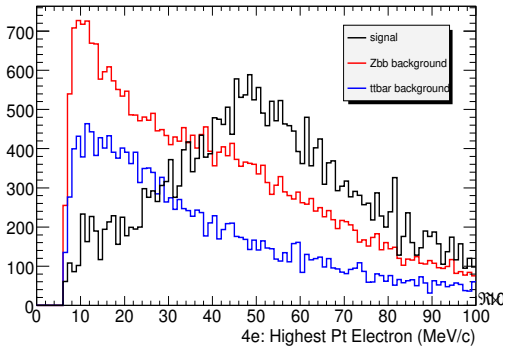

(b) p_T of the hardest electron in the $4e$ case

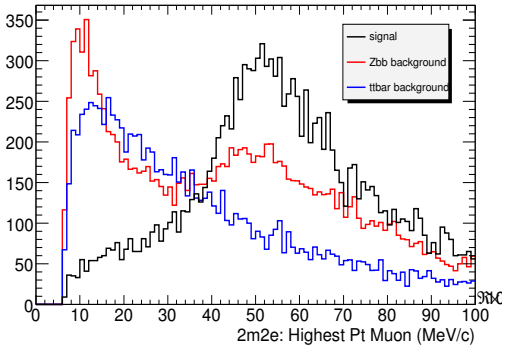

(c) p_T of the hardest muon in the $2\mu 2e$ case

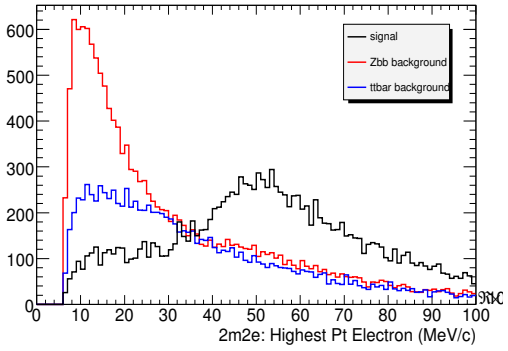

(d) p_T of the hardest electron in the $2\mu 2e$ case

Figure 76: Max P_t discriminating variable for signal and background.

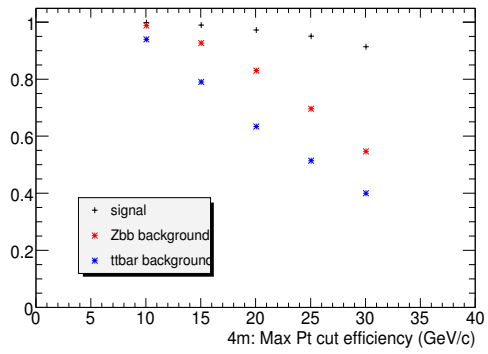

(a) Efficiency of the p_T cut

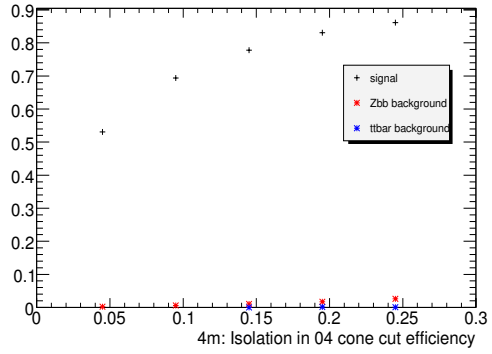

(b) Efficiency of the isolation cut

Figure 77: Efficiency of the p_T^{max} and the isolation cuts, for the 4μ case.

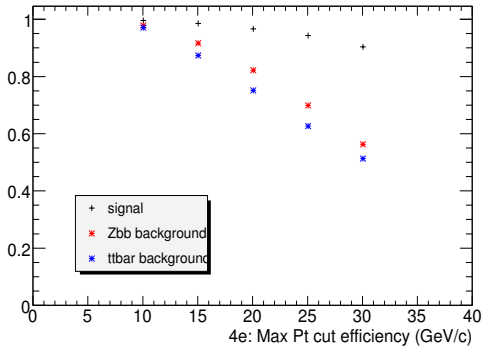

(a) Efficiency of the p_T cut for the $4e$ case

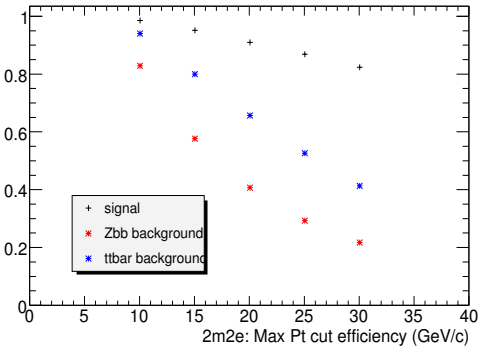

(b) Efficiency of the p_T cut for the $2\mu 2e$ case

Figure 78: Efficiency of the p_T^{max} cut, for the $4e$ and $2\mu 2e$ case.

Table 52: Signal selection cut efficiencies

	4μ [%]		$4e$ [%]		$2\mu 2e$ [%]	
Lepton Preselection	70.67		62.27		65.40	
Pair formation,dR	99.34		87.97		93.37	
Isolation,p_T^{max}	81.11		58.62		59.07	
Z Mass	Tight	Loose	Tight	Loose	Tight	Loose
	72.68	91.99	76.09	93.47	77.81	95.19
Total	41.39 ± 0.64	52.38 ± 0.72	24.43 ± 0.50	30.01 ± 0.56	28.07 ± 0.37	34.34 ± 0.41

analysis. In the first case, refered here as tight, both Z bosons should fulfill the invariant mass requirement. These events correspond to the on-mass shell ZZs (70% of the PYTHIA sample as shown in Table 50). The second mass region, refered here as loose, requires one Z on-mass shell and the second with an invariant mass > 20 GeV. The events of this category constitute the irreducible background of the $H \rightarrow ZZ^* \rightarrow 4\ell$ and it is therefore important to measure its shape and cross section.

8.2.5 Cut efficiency

The cut flow described in the previous section and their respective efficiencies for the signal three event topologies is given in Table 52. The lepton pre-selection efficiency is calculated with respect to the initial number of signal events while the efficiencies reported for each set of cuts are computed relatively to the previous one. The product of the relative efficiencies agrees with the ratio of the reconstructed events after all cuts to the generated ones.

Tables 53 and 54 summarize the efficiency of the same set of cuts for the two background processes $Zb\bar{b}$ and $t\bar{t}$ respectively. Again, each efficiency value refers to the previous one and the product of the relative efficiencies agrees with the one obtained from the ratio of the number of events after cuts to the original number of generated events.

Table 53: $Zb\bar{b}$ background cut efficiencies.

	4μ [%]		$4e$ [%]		$2\mu 2e$ [%]	
Lepton Preselection	6.33		10.70		18.36	
Pair formation,dR	77.29		59.08		48.49	
Isolation,p_T^{max}	1.28		4.27		0.65	
Z Mass	Tight	Loose	Tight	Loose	Tight	Loose
	2.03	24.87	2.24	25.59	8.79	69.76
Total($\times 10^{-3}$)	1.28 ± 0.64	15.62 ± 2.23	6.06 ± 1.39	69.16 ± 4.70	5.10 ± 1.28	40.48 ± 3.59

Table 54: $t\bar{t}$ background cut efficiencies.

	4μ [%]		$4e$ [%]		$2\mu 2e$ [%]	
Lepton Preselection	3.20		24.84		36.12	
Pair formation,dR	62.69		53.59		43.59	
Isolation,p_T^{max}	0.13		0.31		0.12	
Z Mass	Tight	Loose	Tight	Loose	Tight	Loose
	25.00	50.00	1.61	20.97	3.45	37.93
Total($\times 10^{-3}$)	0.66 ± 0.66	1.31 ± 0.93	0.66 ± 0.66	8.51 ± 2.36	0.66 ± 0.66	7.20 ± 2.17

8.2.6 Trigger efficiency

The trigger efficiencies are computed for all three final state topologies in the case of Level 1(L1) and Event Filter(EF) triggers. For the 4μ topology the efficiency to find at L1 a muon with $p_T >$ 20 GeV(Mu20) and at EF an isolated muon with $p_T > 20$ GeV(Mu20i) is given in Table 55.

For the $4e$ topology, the middle columns of Table 13 show the efficiency at L1 trigger to find an isolated electron with EM cluster energy > 25 GeV(e25i) which corresponds to an electron with $p_T >$ 18 GeV, or two electrons with EM cluster energy > 15 GeV(2e15) which corresponds to electrons with $p_T > 11$ GeV. Also in the $4e$ case at EF level the efficiency of one isolated electron with $E_T > 25$ GeV or two isolated electrons with $E_T > 15$ GeV(2e15i) is given in Table 13.

Finally, for the $2\mu 2e$ event topology the efficiency for a L1 muon with $p_T > 20$ together with an isolated electron with EM cluster energy > 25 GeV and the efficiency for an EF isolated muon with $p_T > 20$ GeV together with an EF isolated electron with $E_T > 25$ GeV is given also in Table 13. Note that the efficiencies shown are calculated with respect to the number of events left after all selection cuts are applied, including both cuts in the Z invariant mass, tight and loose.

Table 55: Trigger efficiencies

		4μ [%]			$4e$ [%]			$2\mu 2e$ [%]	
		Tight	Loose		Tight	Loose		Tight	Loose
L1	Mu20	99.81	99.70	2e15	100	100	Mu20+e25i	95.55	95.17
				e25i	99.96	99.97			
EF	Mu20i	99.23	99.96	e25i	99.71	99.76	Mu20i+e25i	88.25	86.93
				2e15i	98.79	98.44			

Table 56: Signal cut efficiency using v11.0.4

	4μ [%]		$4e$ [%]		$2\mu 2e$ [%]	
Lepton Preselection	77.00		67.39		72.42	
Pair formation,dR	99.44		91.08		95.28	
Isolation,p_T^{max}	81.56		66.81		64.90	
Z Mass	Tight	Loose	Tight	Loose	Tight	Loose
	73.47	91.68	73.94	92.70	76.36	94.80
Total	45.88 ± 0.36	57.25 ± 0.40	30.32 ± 0.29	38.02 ± 0.33	34.20 ± 0.22	42.45 ± 0.24

8.2.7 Comparison between v11.0.4 and v12.0.6

Initialy the analysis was performed using the signal sample generated and reconstructed with ATHENA v11.0.4. In Table 56 the cut efficiencies using v11.0.4 samples is given. When comparing this table with the one obtained from v12.0.6 data(Table 52) there is evident a decrease in efficiency by a factor of 1.1 for the 4μ and 1.2 for $4e$ and $2\mu 2e$ cases in v12.0.6. The discrepancies in the efficiencies between the two versions are mainly attributed to changes in the electron and muon reconstruction efficiencies.

8.2.8 Experience with analysis on the GRID

Part of this analysis was performed using GRID resources. This was achieved using Ganga v4.3.5 and v4.4.0 interface [49]. Due to Computing Element instabilities, sample shuffling and Ganga's limitations in re-submission of jobs, the success rate was pretty low, therefore the manageable samples (Pythia signal) were transferred and analysed with local cpu resources. The large $Zb\bar{b}$ and $t\bar{t}$ samples were still analyzed with Ganga at the ROMA1 site, where the successful jobs finished within a couple of days.

8.2.9 Expected signal and background

The invariant mass distributions of the four leptons for the 4μ,$4e$ and $2\mu 2e$ event topologies are shown in Figures 79, 80 and 81 respectivelly. In each figure the distributions for both mass regions –tight and loose– are given in (a) and (b) respectivelly. The expected contribution from $Zb\bar{b}$ background is superimposed in the plots. Both signal and expected background are normalized to $10\,fb^{-1}$. The contribution of the $Zb\bar{b}$ background is mainly affecting the low invariant mass region while the $t\bar{t}$ background cannot be superimposed in the plots because of the limited available statistics.

The expected number of signal and background events for each of the three final state configurations at $1\,fb^{-1}$ is given in Table 57 for the tight Z mass cut and in Table 58 for the loose Z mass cut. Errors shown are statistical only. It is evident that for reliable estimation of the $t\bar{t}$ background a larger sample is required.

Summarizing, with $1\,fb^{-1}$ of data we expect a total of ~ 10 and ~ 12 signal events respectivelly in the two mass regions, and 0.18 and 1.65 background events. Although the background error is large because of limited statistics a measurement of the $ZZ(ZZ^*)$ cross section if feasible even with $1\,fb^{-1}$. Note that the above results do not include the K_f.

8.2.10 Systematic uncertainties

The systematic uncertainties to the signal comprise: a)the uncertainty in the luminosity which is estimated to 6.5% after the first $0.3\,fb^{-1}$, b) the uncertainty from the PDF's used to $\sim 3\%$, c) the scaling

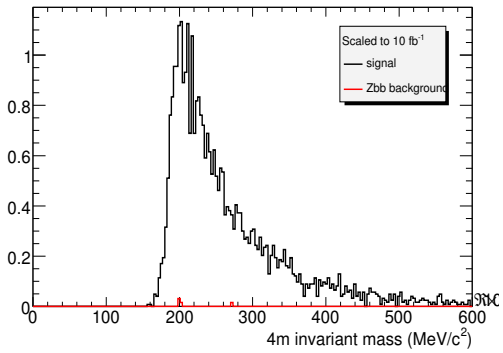

(a) Invariant mass of 4μ after all cuts, for signal and $Zb\bar{b}$ background using the tight mass cut region.

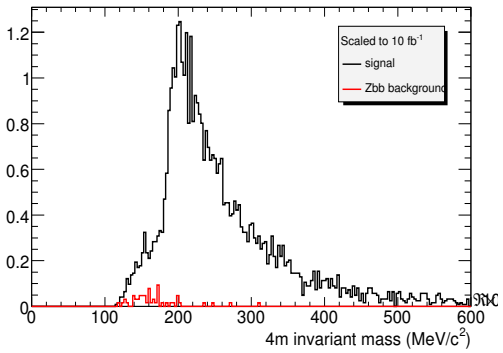

(b) Invariant mass of 4μ after all cuts, for signal and $Zb\bar{b}$ background using the loose mass cut region.

Figure 79: Invariant mass of 4μ after all cuts, for signal and $Zb\bar{b}$ background.

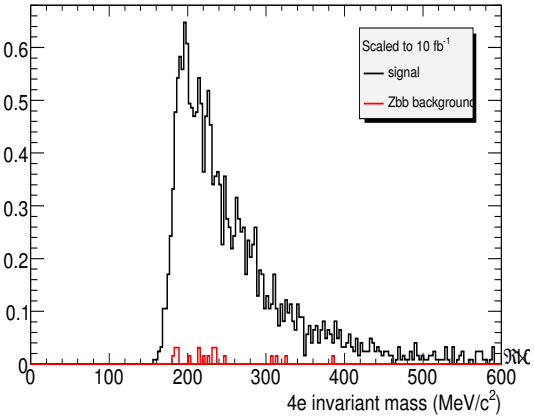

(a) Invariant mass of $4e$ after all cuts, for signal and Zbb background using the tight mass cut region.

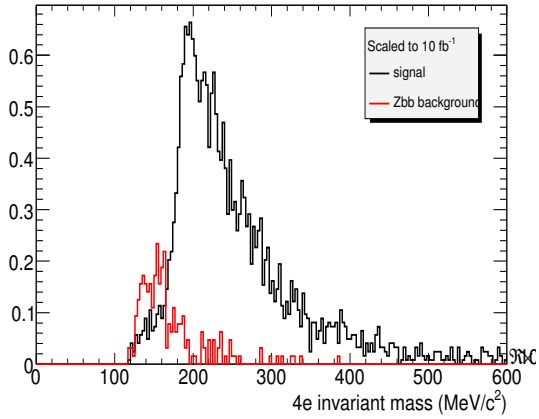

(b) Invariant mass of $4e$ after all cuts, for signal and Zbb background using the loose mass cut region.

Figure 80: Invariant mass of $4e$ after all cuts, for signal and $Zb\bar{b}$ background.

Table 57: Expected signal and background events at $L = 1 fb^{-1}$ using the tight Z mass cut.

	4μ events	$4e$ events	$2\mu 2e$ events	Total
Signal	4.52±0.05	2.59±0.04	6.18±0.06	13.3 ±0.09
$Zb\bar{b}$	0.009±0.003	0.042±0.007	0.035±0.006	0.076±0.010
$t\bar{t}$	0.04±0.04	0.04±0.04	0.04±0.04	0.12±0.07
Total bgr	0.049±0.040	0.082±0.040	0.075 ±0.040	0.20±0.07

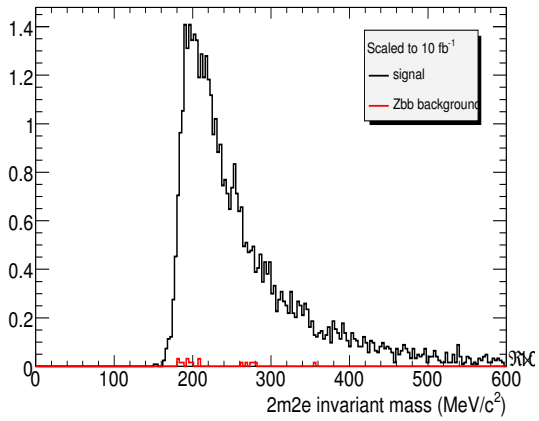

(a) Invariant mass of $2m2e$ after all cuts, for signal and $Zb\bar{b}$ background using the tight mass cut region.

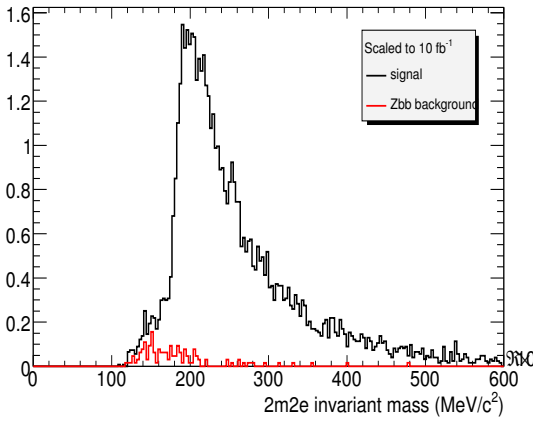

(b) Invariant mass of $2m2e$ after all cuts, for signal and $Zb\bar{b}$ background using the loose mass cut region.

Figure 81: Invariant mass of $2\mu 2e$ after all cuts, for signal and $Zb\bar{b}$ background.

Table 58: Expected signal and background events at $L = 1\,fb^{-1}$ using the loose Z mass cut.

	4μ events	$4e$ events	$2\mu 2e$ events	Total
Signal	5.72±0.06	3.17±0.04	7.56±0.07	16.5 ±0.10
$Zb\bar{b}$	0.11±0.01	0.48±0.02	0.28±0.02	0.87±0.03
$t\bar{t}$	0.08±0.06	0.52±0.14	0.44±0.13	1.03±0.20
Total bgr	0.19±0.06	1.00±0.14	0.72 ±0.13	1.90±0.20

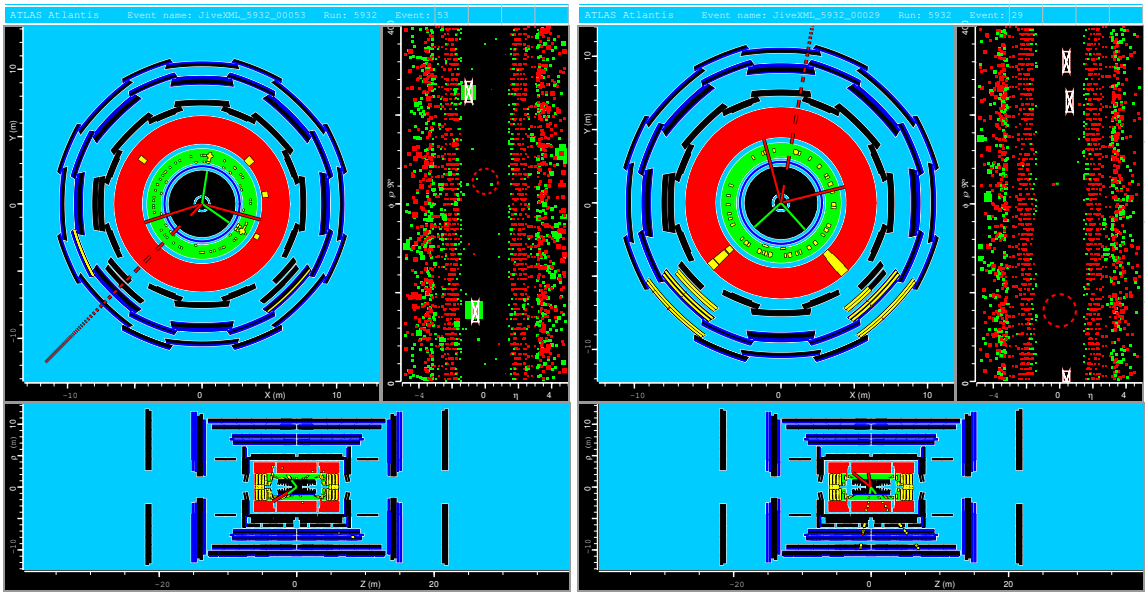

Figure 82: Monte Carlo $ZZ \to \ell\ell\nu\bar{\nu}$ events shown by the ATLAS event display, Atlantis. The left-hand diagram is an example of an electron event, while the right-hand diagram shows a corresponding muon example. Both diagrams show the $x-y$ plane (top-left panel), the $\eta-\phi$ plane (top-right panel) and the $x-z$ plane (lower panel). The inner detector is shown by the black central region, with the EM-calorimeter in green, the hadron calorimeter in red and the muon system in blue. The green lines depict reconstructed tracks, while red solid lines represent the true neutrino tracks. The red dashed line shows the direction of the missing transverse energy. Calorimeter deposits and muon chambers containing hits are highlighted in yellow.

uncertainty for the NLO calculations or equivalently to the K_f to $\sim 5\%$ and d) $\sim 3\%$ uncertainty to lepton identification assumed the same for electrons and muons. Assuming gaussian distributions for all the above uncertainties, the total systematic uncertainty to the signal amounts to 9.2%.

As seen from this analysis the measurement of the ZZ and ZZ^* cross section is essentially background free but at $L = 1\,fb^{-1}$ is dominated by statistical error. At $L = 10\,fb^{-1}$ the statistical error will drop to about 10% and systematic error will have a similar impact.

8.3 $ZZ \to llvv$ analysis

In this section, we focus on the ZZ neutral diboson channel where one of the Z bosons decays invisibly to a neutrino pair, the other to an electron or muon (lepton) pair. The signature for these events will be two high-p_T leptons with a large missing transverse energy ($\not\!\!E_T$) due to the neutrino pair leaving the detector. Event displays of two typical signal events are shown in figure 82.

Despite having a less distinct signature, and therefore larger background than the complementary $ZZ \to 4\ell$ diboson channel, the neutrino channel has the advantage of an enhanced cross section. All three neutrino generations contribute, making the cross section ~ 6.2 times larger for the missing energy channel. The main backgrounds will either come from channels with large cross sections, such as $t\bar{t}$ and $Z \to \ell^+\ell^-$, or those with a similar signature to the signal, such as the WZ diboson channel. To reduce these backgrounds, we define a set of simple cuts on discriminating parameters.

8.3.1 Monte Carlo events

The datasets used for signal and background in this analysis are shown in tables 59 and 60 for versions 11.0.42 and 12.0.6 of the simulation respectively. The tables show the physics process, the Monte Carlo dataset number, the Generator used, the production cross section, a summary of filters applied, the filter efficiency, K-factor, number of events and luminosity. The cross sections and filter efficiencies have been calculated by generating small samples ($\sim$ 10000 events) with the same input job options as the official samples.

The $ZZ \to \ell\ell\nu\bar{\nu}$ signal datasets are produced with two different Monte Carlo generators. The 11.0.4 data uses the PYTHIA [20] generator at leading order, while 12.0.6 uses MC@NLO to generate next-to-leading order hard scattering matrix elements, which are hadronised with Herwig and Jimmy. For the 11.0.4 signal, the PYTHIA cross section is scaled up using the K-factor quoted in table 59.

Similarly, different generators have been used to produce the various background samples. They are mostly a mixture of PYTHIA and MC@NLO events, with the exception of the Wt sample which is generated with the ACERMC [51].

Any data produced with MC@NLO will contain a mixture of events with positive ($+1$) and negative (-1) weights. To obtain an accurate distribution or event yield, negatively weighted events are subtracted from the positively weighted distributions.

8.3.2 EventView preselection

Preselection and overlap removal have been done in this analysis using the EventView set of analysis tools, which create Athena-Aware NTuples (AANs) from the Analysis Object Datafiles (AODs). Here electrons are inserted first, followed by photons, muons, τ-jets and finally particle jets, to ensure that no particles overlap within cone of size $\Delta R = 0.1$.

Electron identification Electrons are only inserted into the EventView if they pass the following cuts. First, electrons must be reconstructed with the *egamma* algorithm [1] using cuts based on the shower shape properties in the calorimeters as well as variables combining inner detector tracks with calorimeter deposits. For this analysis we apply the mask `(isEM & 0x7FF)==0`, which requires all cuts to be passed except for those involving the TRT.

Electron candidates are also required to be isolated in the calorimeter to ensure high p_T jets are not misidentified as electrons. Figure 83 shows the distribution of the transverse energy in a cone $\Delta R = 0.45$ around the electron track. To ensure the electrons are isolated, a cut is made requiring $E_T(\text{cone}) < 8$ GeV. With these criteria in place we can plot the selection efficiency of electrons by comparing the number of true electrons generated by the simulation to the subset that are successfully reconstructed. This is done by matching true to reconstructed electrons using a cone of size $\Delta R < 0.01$.

Figure 84 shows the reconstruction efficiency as a function of p_T and η for electrons present in both the `11.0.4` and `12.0.6` signal datasets respectively. The efficiency for electrons drops sharply below $p_T \sim 30$ GeV for both datasets due to poor reconstruction at low momentum. Crack regions in the detector are clearly seen as the efficiency drops at $|\eta| = 1.4$ and $\eta = 0$.

The electron efficiency is around 12% lower for 12.0.6 Monte Carlo compared to 11.0.4, with a uniform drop across the p_T range $0 - 200$ GeV.

For electrons to be pre-selected by the EventView algorithm, an initial set of kinematic cuts are applied requiring $p_T > 5$ GeV and $|\eta| < 2.5$. With these in place an overall efficiency of $75.0 \pm 0.5\%$ is achieved for 11.0.4 signal electrons, dropping to $62.6 \pm 0.6\%$ for 12.0.6.

In addition to the "good quality" electrons described above, we also define "loose" electrons, which are used to veto background events from the WZ channel. In this case, no `isEM` cut is required and electrons can also come from the *SoftE* algorithm [52]. As with the good quality case, we apply kinematic

Process	Dataset No.	Generator	σ/pb	Filter	Filter Eff.	K-factor	N	L/fb^{-1}
$ZZ \to \ell\ell\nu\bar{\nu}$	5981	PYTHIA	0.300	$2\ell\ p_T > 5$ GeV, $\|\eta\| < 2.7$	0.667	1.323	48700	184.1
$ZZ \to 4\ell$	5931	MC@NLO	0.0668		1.0	1.0	26681	267.86
$W^+W^- \to e\nu e\nu$	5921	MC@NLO	1.30		1.0	1.0	43100	22.54
$W^+W^- \to \mu\nu\mu\nu$	5924	MC@NLO	1.25		1.0	1.0	10950	5.96
$W^+W^- \to \tau\nu\tau\nu$	5927	MC@NLO	1.41		1.0	1.0	45850	22.08
$W^+Z \to \ell\nu\ell^+\ell^-$	5941	MC@NLO	0.427		1.0	1.0	18700	31.38
$W^-Z \to \ell\nu\ell^+\ell^-$	5971	MC@NLO	0.267		1.0	1.0	40900	110.67
$Z \to ee$ ($M_Z > 80$ GeV)	5152	MC@NLO	1874	$1\ell p_T > 10$ GeV, $\|\eta\| < 2.7$	0.858	1.0	69550	0.04
$Z \to \mu\mu$ ($M_Z > 80$ GeV)	5151	MC@NLO	1874	$1\ell p_T > 5$ GeV, $\|\eta\| < 2.8$	0.887	1.0	82600	0.04
$Z \to \tau\tau$ ($M_Z > 60$ GeV)	5146	PYTHIA	1656	$2\ell p_T > 5$ GeV, $\|\eta\| < 2.8$	0.047	1.0	12118	0.16
$Z \to ee$ ($p_T(Z) > 100$ GeV)	5185	PYTHIA	22.23	$1\ell p_T > 10$ GeV, $\|\eta\| < 2.7$	0.945	1.0	58700	2.79
$Z \to \mu\mu$ ($p_T(Z) > 100$ GeV)	5186	PYTHIA	22.23	$1\ell p_T > 5$ GeV, $\|\eta\| < 2.8$	0.960	1.0	95500	4.47
$Z \to \tau\tau$ ($p_T(Z) > 100$ GeV)	5187	PYTHIA	22.15	$2\ell p_T > 5$ GeV, $\|\eta\| < 2.8$	0.085	1.0	28000	14.87
$Z \to \nu\nu$	5183	PYTHIA	715	$p_T(Z) > 50$ GeV	1.0	1.0	47300	0.07
Wt	5500	ACERMC	26.7	One W$\to$e/μ/τ, other W $\to$jets	1.0	1.0	71250	2.67
$t\bar{t} \to \ell + X$	5200	MC@NLO	759	No all-hadronic channels.	0.555	1.0	428747	0.74

Table 59: Monte Carlo samples used in the analysis with Athena version 11.0.4. The table shows the physics process and dataset number, the generator, cross section, a description of any filters with the appropriate efficiency, the K-factor used to scale leading order samples, the number of events and the luminosity.

Process	Dataset No.	Generator	σ/pb	Filter	Filter Eff.	K-factor	N	L/fb^{-1}
$ZZ \to \ell\ell\nu\bar{\nu}$	5932	MC@NLO	0.397		1.0	1.0	118000	199.37
$ZZ \to 4\ell$	5931	MC@NLO	0.0668		1.0	1.0	49250	399.70
$W^+W^- \to e\nu e\nu$	5921	MC@NLO	1.30		1.0	1.0	19900	10.41
$W^+W^- \to e\nu\mu\nu$	5922	MC@NLO	1.27		1.0	1.0	19850	10.68
$W^+W^- \to e\nu\tau\nu$	5923	MC@NLO	1.35		1.0	1.0	19750	9.86
$W^+W^- \to \mu\nu\mu\nu$	5924	MC@NLO	1.25		1.0	1.0	10000	5.49
$W^+W^- \to \mu\nu e\nu$	5925	MC@NLO	1.27		1.0	1.0	20000	10.92
$W^+W^- \to \mu\nu\tau\nu$	5926	MC@NLO	1.33		1.0	1.0	20000	10.37
$W^+W^- \to \tau\nu\tau\nu$	5927	MC@NLO	1.41		1.0	1.0	19950	9.60
$W^+W^- \to \tau\nu e\nu$	5928	MC@NLO	1.35		1.0	1.0	13749	6.89
$W^+W^- \to \tau\nu\mu\nu$	5929	MC@NLO	1.33		1.0	1.0	20000	10.33
$W^+Z \to \ell\nu\ell^+\ell^-$	5941	MC@NLO	0.427		1.0	1.0	52078	80.45
$W^-Z \to \ell\nu\ell^+\ell^-$	5971	MC@NLO	0.267		1.0	1.0	52619	130.69
$Z \to ee$ ($M_Z > 80$ GeV)	5152	MC@NLO	1874	$1\ell p_T > 10$ GeV, $\lvert\eta\rvert < 2.7$	0.858	1.0	99950	0.05
$Z \to \mu\mu$ ($M_Z > 80$ GeV)	5151	MC@NLO	1874	$1\ell p_T > 5$ GeV, $\lvert\eta\rvert < 2.8$	0.887	1.0	99150	0.05
$Z \to \tau\tau$ ($M_Z > 60$ GeV)	5146	PYTHIA	1656	$2\ell p_T > 5$ GeV, $\lvert\eta\rvert < 2.8$	0.047	1.0	98950	1.27
$Z \to ee$ ($p_T(Z) > 100$ GeV)	5185	PYTHIA	22.23	$1\ell p_T > 10$ GeV, $\lvert\eta\rvert < 2.7$	0.945	1.0	191150	9.10
$Z \to \mu\mu$ ($p_T(Z) > 100$ GeV	5186	PYTHIA	22.23	$1\ell p_T > 5$ GeV, $\lvert\eta\rvert < 2.8$	0.960	1.0	198400	9.30
$t\bar{t}$	5200	MC@NLO	759	No all hadronic channels.	0.555	1.0	422450	0.73

Table 60: Monte Carlo samples used in the analysis with Athena version 12.0.6. The table shows the physics process and dataset number, the generator, cross section, a description of any filters with the appropriate efficiency, the K-factor used to scale leading order samples, the number of events and the luminosity.

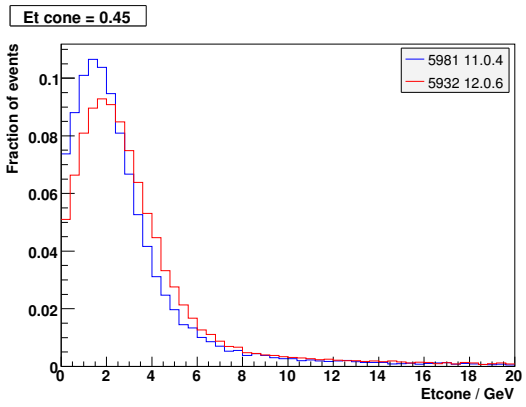

Figure 83: The distribution of transverse energy in a $\Delta R = 0.45$ cone around the electron track for electrons present in the signal $ZZ \to \ell\ell\nu\bar{\nu}$ events. Version 11 data are shown in blue while version 12 data are in red.

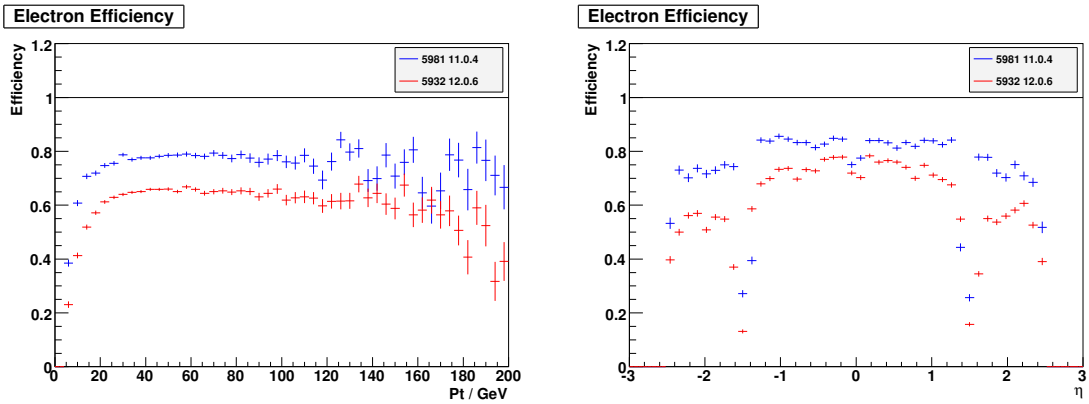

Figure 84: Electron efficiency in the signal as a function of p_T and η for version 11 (blue) and 12 (red) $ZZ \to \ell\ell\nu\bar{\nu}$ signal datasets.

cuts $p_T > 5$ GeV and $|\eta| < 2.5$, but no isolation is required. These loose electrons are not used in reconstruction of the Z boson.

Muon identification This analysis uses muons from the *MuID* [1] algorithm, which takes tracks in the muon system and attempts to match them with inner detector tracks, using a χ^2 with five degrees of freedom. To ensure good quality muons in this analysis, cuts are applied requiring the initial track match to have $\chi^2/N_{\text{dof}} < 10$ and a global fit quality $\chi^2/N_{\text{dof}} < 5$. As shown in figure 85, these cuts are fairly loose to keep the muon efficiency high. The slight discrepancy between the 11.0.4 and 12.0.6 match χ^2 distribution is thought to be due to a redefinition of the variable between the two versions.

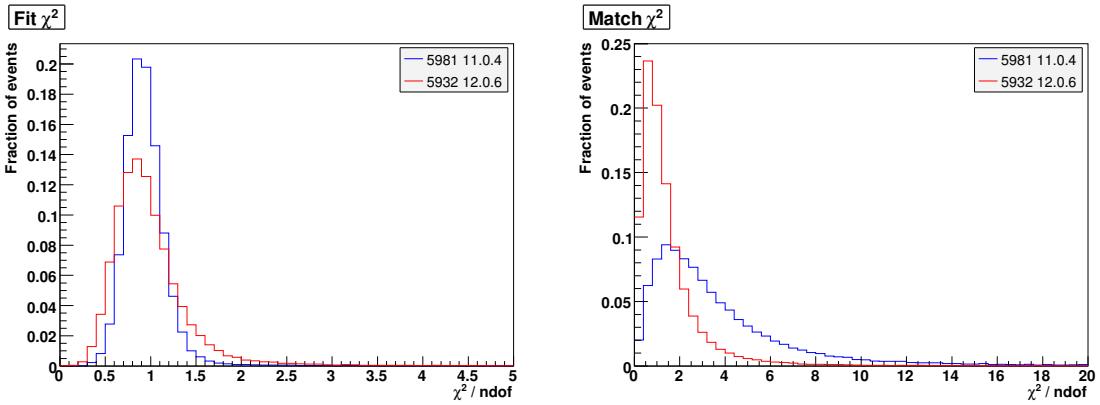

Figure 85: Muon algorithm quality distributions for version 11 (blue) and 12 (red) $ZZ \to \ell\ell\nu\bar{\nu}$ Monte Carlo. The left-hand plot shows the χ^2/N_{dof} distribution of the initial match between muon and inner detector tracks. The right-hand plot shows the χ^2/N_{dof} for the global fit.

Figure 86 shows the distribution of energy deposited within a $\Delta R = 0.45$ cone around the muon track. To be selected for analysis, we require muons to be isolated with $E_T(\text{cone}) < 5$ GeV.

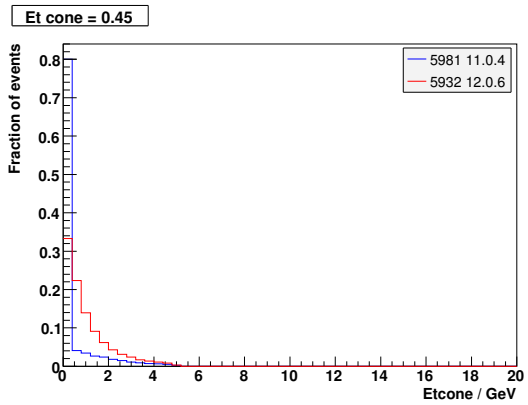

Figure 86: The distribution of transverse energy in a $\Delta R = 0.45$ cone around the muon track for version 11 (blue) and 12 (red) $ZZ \to \ell\ell\nu\bar{\nu}$ signal datasets.

The selection efficiency for muons present in the signal channel is shown in Figure 87. The efficiency for muons is higher than electrons, and is similar for both Monte Carlo datasets. The η distribution shows similar efficiency drops due to cracks in the detector, most notably at $\eta = 0$.

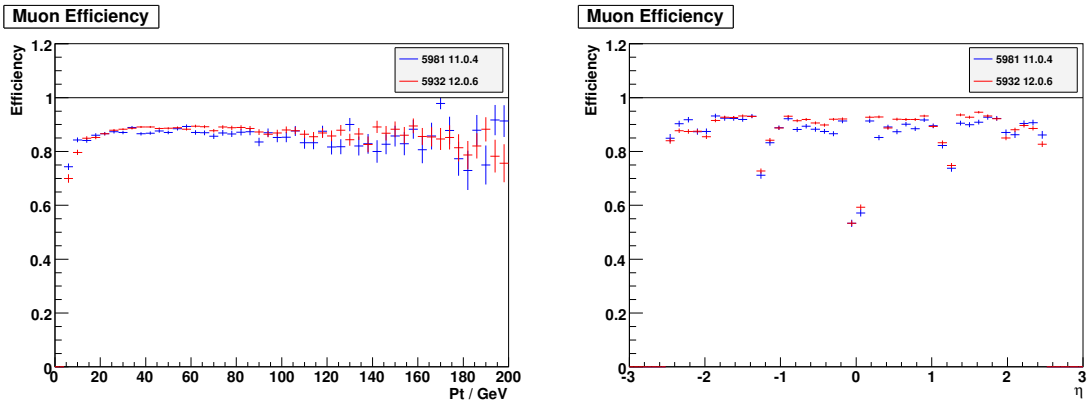

Figure 87: Muon efficiency as a function of p_T and η for version 11 (blue) and 12 (red) $ZZ \to \ell\ell\nu\bar{\nu}$ signal datasets.

Muon pre-selection cuts of $p_T > 5$ GeV and $|\eta| < 2.5$ give an overall efficiency of $86.3 \pm 0.3\%$ for the 11.0.4 sample and $87.7 \pm 0.4\%$ for 12.0.6.

As with electrons, we also define a set of "loose muons", which can come from the either the *MuID* or *LowPt* algorithms [1] and do not have any quality restrictions imposed. The same kinematic cuts are imposed, so that $p_T > 5$ GeV and $|\eta| < 2.5$, but no isolation cuts are applied. The muons from this loose selection are not used for Z boson reconstruction.

The lepton identification pre-selection cuts and efficiencies for electrons and muons are summarised in table 61. Both types of lepton exhibit similar kinematic distributions, and so are considered as "leptons" for the remainder of the analysis. As there is also a good agreement between 11.0.4 and 12.0.6 datasets, the plots below mostly show distributions from the 12.0.6 Monte Carlo only.

	Electron	Muons
Algorithm	egamma `(isEM & 0x7FF)==0`	MuID $\chi^2_{\text{match}}/N_{\text{dof}} < 10$ $\chi^2_{\text{fit}}/N_{\text{dof}} < 5$
Isolation	$E_T(\Delta R = 0.45) < 8$ GeV	$E_T(\Delta R = 0.45) < 5$
Kinematics	$p_T > 5$ GeV $\lvert\eta\rvert < 2.5$	$p_T > 5$ GeV $\lvert\eta\rvert < 2.5$
Efficiency		
`11.0.4`	$75.0 \pm 0.5\%$	$86.3 \pm 0.3\%$
`12.0.6`	$62.6 \pm 0.6\%$	$87.7 \pm 0.4\%$

Table 61: Summary of the lepton identification criteria and pre-selection cuts.

Jet identification Jets are also used in the analysis to distinguish between signal and background events. The pre-selection criteria are looser than for leptons as good quality reconstructed jets are not required. Tau jets can come from either the *TauRec* or *Tau1p3p* [1] algorithms with no limit placed on the number of tracks. QCD particle jets come from the *ConeTowerParticleJets* [1] container, with a cone size of $\Delta R = 0.7$. Both types of jet have a $p_T > 5$ GeV preselection cut applied. Both tau jets and particle jets will simply be referred to as "jets" in the rest of this analysis.

8.3.3 Analysis cuts

In this anslysis, we define simple cuts in an effort to reduce events from the background channels listed in tables 59 and 60. In general, each cut is used to suppress a particular background channel, as described below. We also investigate a number of different triggers that could potentially be used to pre-select events.

Lepton Kinematics We first select two oppositely charged good quality leptons with $p_T > 20$ GeV. Figure 88 (left) shows that this reduces much of the $t\bar{t}$ background which contains softer leptons than the signal. This cut also reduces the background from $Z \to \tau^+\tau^- \to \ell^+\ell^-\nu_l\bar{\nu_l}\nu_\tau\bar{\nu_\tau}$ as the electrons and muons are produced with reduced p_T. We also require the leptons to lie within the limits of the inner detector pseudorapidity range, so apply a cut $|\eta| < 2.5$.

Lepton pairs are also required to have an invariant mass close to the Z mass, specifically $|m_{\ell\ell} - 91.2\ \text{GeV}| < 10$ GeV. This is equivalent to $\sim 5\sigma$ of the signal width, and helps to reduce background combinatorics where the lepton pair does not come directly from a Z decay. These include $t\bar{t}$, $Z \to \tau^+\tau^-$ and $WW \to \ell\nu\ell\nu$ shown in figure 88 (right). It should be noted that the Z width is not included in the 12.0.6 MC@NLO sample. As a result, the width of the peak in figure 88 is due to detector resolution alone.

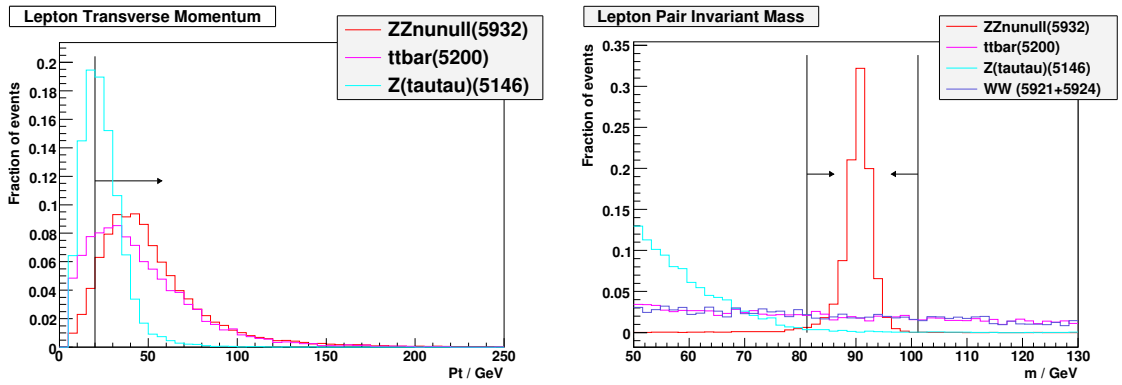

Figure 88: The lepton p_T distribution (left) and lepton pair invariant mass before cuts for the signal (red), with $t\bar{t}$ (magenta), $Z \to \tau^+\tau^-$ (cyan) and WW (purple) background using version 12 data. The plots are normalised to unit area for comparison of distribution shapes.

A lepton veto is also imposed by combining the good quality and loose lepton selection and removing any events with more than two leptons in total. This reduces background from the WZ channel, the Z from which has an almost identical signature to the signal, and the neutrino from W decay also appears as missing transverse energy, $\not{E}_T$. The third-lepton veto supresses the WZ background by $\sim 30\%$. If the lepton from the W is not reconstructed, however, this background channel becomes more problematic as it is almost indistinguishable from the signal.

Missing E_T cuts A main characteristic of the signal decay is a large missing transverse energy ($\not{E}_T$) from the $Z \to \nu\bar{\nu}$ decay. Here we use the $\not{E}_T$ variable calculted with the cell-based algorithm *RefMET* [1]. An important background, due to its large cross section, comes from the $Z \to \ell^+\ell^-$ Drell-Yan process, where jets are produced in addition to the leptons. If these jets are aligned with cracks in the detector, then they will fake $\not{E}_T$ as they will not be fully accounted for in the calorimeters. This background can be significantly reduced by applying a 50 GeV $\not{E}_T$ cut as shown in figure 89 (left). The background

from $ZZ \to 4\ell$ is also reduced, but this is less significant as it has a much smaller cross section. The WZ channel is also suppressed by this cut as only one neutrino is produced, and hence the $\not\!\!E_T$ distribution is slightly softer.

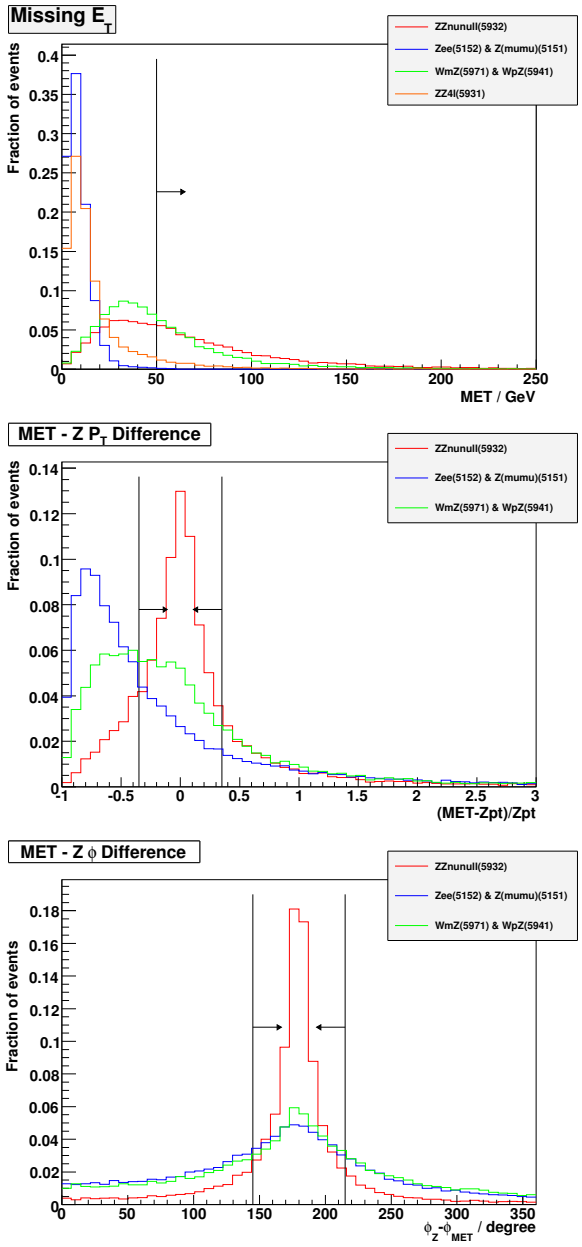

Figure 89: The $\not\!\!E_T$ and $\not\!\!E_T - p_T(Z)$ magnitude and angle matching distributions before cuts for the signal (red), $ZZ \to 4\ell$ (orange), $Z \to \ell^+\ell^-$ (blue) and WZ (green) using version 12 data. The plots are normalised to unit area for comparison of distribution shapes.

We also expect the signal to have a missing p_T that is equal and opposite to that of the reconstructed Z, assuming that the ZZ pair is produced with no initial p_T and that they decay back-to-back. Figure 89 (middle and right) shows a clear peak in the signal for both magnitude and angle matches. The WZ background shows a worse magnitude match as some of the W momentum is lost to either an electron or

muon on decay. This means that the missing p_T will not quite match up with that of the recoiling Z. The angle distribution shows a peak in both the WZ and $Z \to ll$ channels. In the case of WZ, this is because the W and Z are produced in approximately opposite directions. When the W decays, the neutrino will be deflected and so the peak has a wider distribution. In a similar way, in $Z \to ll$, the Z is likely to be produced with some quarks recoiling against it. These will manifest themselves as jets which can fake $\not\!\!E_T$. Cuts at

$$\frac{|\not\!\!E_T - p_T(Z)|}{p_T(Z)} < 0.35 \quad \text{and} \quad 145^\circ < \phi_Z - \phi_{MET} < 215^\circ, \tag{7}$$

equivalent to $\sim 2\sigma$ of the signal peaks help to reduce the WZ background.

Jet veto A jet veto is also useful to reduce backgrounds with large hadronic activity. For example, the predominant decay channel for the top quark in $t\bar{t}$ is the $t \to Wb$ final state, resulting in several high p_T jets. Figure 90 shows the reconstucted jet multiplicity to be much higher in the $t\bar{t}$ channel than in the signal. Jets from this background are also harder than those in the signal, so its contribution can be reduced by applying a veto on events containing any jets with

$$p_T(\text{jet}) > 30 \text{ GeV} \quad \text{and} \quad |\eta_{\text{jet}}| < 3.0 \tag{8}$$

Figure 90 also highlights a difference in jet multiplicity between the two signal datasets. The 12.0.6 data contains an average of 5.3 jets per event, whereas 11.0.4 only contains 1.8. This difference is because the 11.0.4 data used PYTHIA, a leading order generator and only includes soft jets that are approximately collinear with the two Z bosons. MC@NLO, on the other hand, includes additional Feynman diagrams with hard gluon radiation.

Zp_T cut The final cut to be applied is on the transverse momentum of the reconstructed Z boson. This is needed to reduce the background from the single Z channel, whose $p_T(Z)$ distribution drops much faster than the signal, as shown in figure 91. A cut of $p_T(Z) > 100$ GeV significantly reduces this background, without harming the sensitivity to anomalous couplings, which only manifest themselves at high p_T.

Cut flow Tables 62 and 63 give a summary of the cuts applied and present the expected number of events passing cuts for version 11.0.4 and 12.0.6 datasets respectively. If some Monte Carlo events remain after cuts, the final row in each column gives the statistical error. If no events pass cuts, the figure given is the number of expected events at the 90% confidence level. The $Z \to ll$ column shows results for the two high $p_T(Z)$ samples, 5185 and 5186 as samples 5151 and 5152 do not give enough statistics at high p_T .

Figure 92 shows the $\ell^+\ell^-$ invariant mass distribution of events passing all cuts except for the Z mass window for 12.0.6 data. The remaining backgrounds after cuts come partly from $Z \to ll$ and $t\bar{t}$, which due to their relatively large cross sections, still contain lepton pairs that pass the final p_T cut. The remaining WZ background is more difficult to remove, as it has almost identical properties to the signal if one lepton is not reconstructed.

8.3.4 Yields and trigger

The overall signal efficiency is $\varepsilon = 3.2\%$ for 11.0.4 data, with a signal to background ratio of $S/B = 2.2 \pm 0.2$, compared to $\varepsilon = 2.6\%$ and $S/B = 2.0 \pm 0.8$ for 12.0.6. The expected sensitivity of the $ZZ \to \ell\ell\nu\bar{\nu}$ channel is summarised in table 64.

Figure 93 shows the selection efficiency of the signal as a function of $p_T(Z)$, and will be used to estimate the anomalous coupling limits in section 8.4.1 The initial dip in efficiency at $p_T < 50$ GeV is

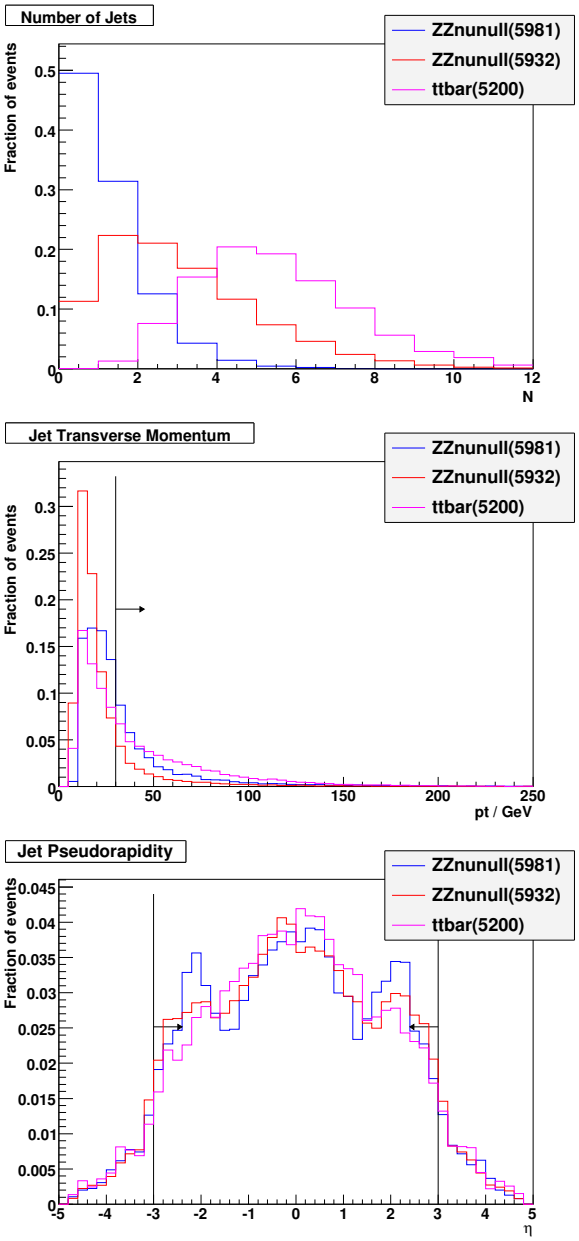

Figure 90: The jet multiplicity, p_T and η distributions for the version 11 signal (blue), version 12 signal (red) and $t\bar{t}$ background. The arrows indicate the region rejected by the jet veto. The distributions are shown without cuts and normalised to unit area to compare shapes.

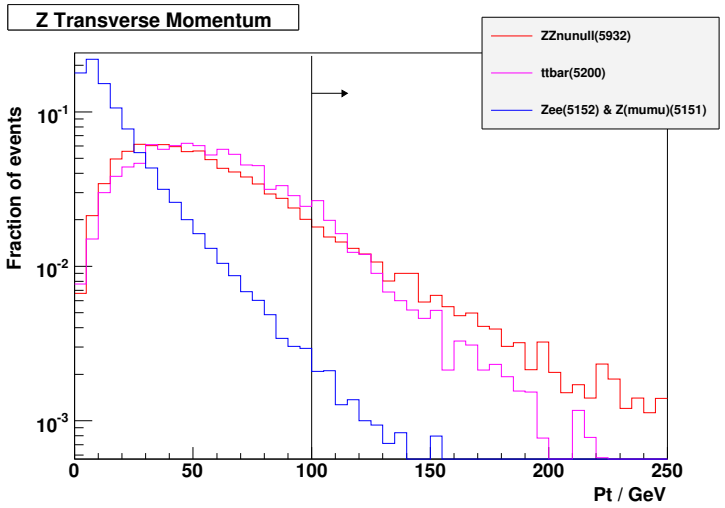

Figure 91: The $p_T(Z)$ distribution for the version 12 signal (red), $Z \to \ell^+\ell^-$ (blue) and $t\bar{t}$ (magenta). Plots are shown without applying cuts and are normalised to unit area.

Process	$ZZ \to \ell\ell\nu\bar{\nu}$	$ZZ \to 4l$	$Z \to ll$	$t\bar{t}$	WZ	Wt	WW	$Z \to \tau\tau$
$p_T^l > 20$ GeV, $\lvert\eta_l\rvert < 2.5$	120.4	61.1	14700	5110	304	2.3	499	2396
Third-lepton veto	89.6 (74.4%)	2.7 (4.4%)	2920 (19.9%)	413 (8.1%)	51.2 (16.8%)	0.8 (34.8%)	384 (77.0%)	1742 (72.7%)
$\lvert m_{ll^-} - 91.2$ GeV$\rvert < 10$ GeV	81.6 (91.1%)	2.4 (88.9%)	2710 (92.8%)	97.1 (23.5%)	43.6 (85.2%)	0.4 (50.0%)	86.1 (22.4%)	57.1 (3.3%)
$p_T^{\text{miss}} > 50$ GeV $\lvert p_T^{\text{miss}} - p_T^Z\rvert / p_T^Z < 0.35$ $\phi_{\text{miss}} - \phi_Z < 35^\circ$	31.4 (38.5%)	0.3 (12.5%)	29.3 (1.1%)	16.2 (16.7%)	10.0 (22.9%)	0 (0.0%)	19.2 (22.3%)	0 (0.0%)
Jet Veto ($p_t^{jet} > 30$ GeV and $\lvert\eta_{jet}\rvert < 3$)	29.1 (92.7%)	0.3 (100.0%)	1.6 (5.5%)	5.9 (36.4%)	8.3 (83.0%)	0 (0.0%)	17.9 (93.2%)	0 (0.0%)
$p_T(l^+l^-) > 100$ GeV	**8.6** (29.6%)	**0.09** (30.0%)	**1.6** (100.0%)	**0** (0.0%)	**2.0** (24.1%)	**0** (0.0%)	**0.14** (0.8%)	**0** (0.0%)
Statistical Error (90% CL):	0.2	0.02	0.6	(2.5)	0.2	(0.9)	0.08	(10.1)

Table 62: Cut flow table for signal and background after cuts for an integrated luminosity of 1 fb^{-1}, using 11.0.4 full simulation data. The values in brackets indicate the percentage of events passing each cut relative to the previous cut.

Process	$ZZ \to \ell\ell\nu\bar{\nu}$	$ZZ \to 4l$	$Z \to ll$	$t\bar{t}$	WZ	WW	$Z \to \tau\tau$
$p_T^l > 20$ GeV, $\lvert\eta_l\rvert < 2.5$	130.1	54.3	13100	4530	271.2	491.1	2170
Third-lepton veto	101.9 (78.3%)	3.1 (5.7%)	1900 (14.5%)	428.9 (9.5%)	52.9 (19.5%)	375.6 (76.5%)	1690 (77.9%)
$\lvert m_{l\bar{l}} - 91.2\text{ GeV}\rvert < 10$ GeV	100.2 (98.3%)	2.7 (87.1%)	1740 (91.6%)	110.2 (25.7%)	45.3 (85.6%)	83.8 (22.3%)	40.1 (3.4%)
$p_T^{\text{miss}} > 50$ GeV $\lvert p_T^{\text{miss}} - p_T^Z\rvert / p_T^Z < 0.35$ $\phi_{\text{miss}} - \phi_Z < 35^\circ$	38.0 (39.9%)	0.34 (12.6%)	3.8 (0.2%)	17.9 (16.2%)	9.4 (20.8%)	18.3 (21.8%)	0 (0.0%)
Jet Veto ($p_t^{jet} > 30$ GeV and $\lvert\eta_{jet}\rvert < 3$)	34.4 (90.5%)	0.30 (88.2%)	0.44 (11.6%)	6.0 (33.5%)	7.6 (80.9%)	16.7 (91.3%)	0 (0.0%)
$p_T(l^+l^-) > 100$ GeV	**10.2** (29.7%)	**0.08** (26.7%)	**0.4** (90.9%)	**3.0** (50.0%)	**1.7** (22.4%)	**0.02** (0.1%)	**0** (0.0%)
Statistical Error (90% CL):	0.2	0.01	0.2	2.1	0.1	0.22	(1.6)

Table 63: Cut flow table for signal and background after cuts for an integrated luminosity of 1 fb^{-1}, using 12.0.6 full simulation data. The values in brackets indicate the percentage of events passing each cut relative to the previous cut.

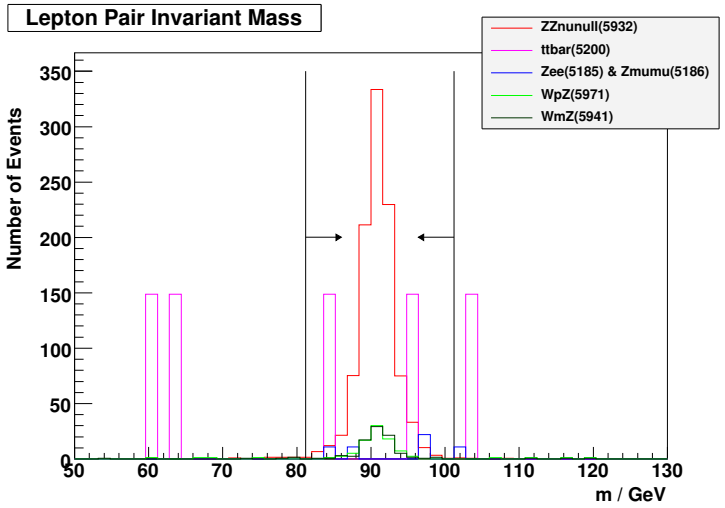

Figure 92: The lepton pair invariant mass distribution after all cuts except for the mass window restriction. The histograms have been scaled to represent the number of events expected in 100 fb^{-1} of data.

Dataset	11.0.4	12.0.6
$N_{\text{signal}}(1\text{ fb}^{-1})$	8.6 ± 0.2	10.2 ± 0.2
$N_{\text{background}}(1\text{ fb}^{-1})$	3.8 ± 0.9	5.2 ± 2.6
Efficiency	3.2%	2.6%
S/B	2.2 ± 0.2	2.0 ± 0.8
$S/\sqrt{B}(0.1\text{ fb}^{-1})$	1.4	1.4
$S/\sqrt{B}(1\text{ fb}^{-1})$	4.4	4.5
$S/\sqrt{B}(10\text{ fb}^{-1})$	14.0	14.1

Table 64: Expected signal yields and sensitivity for 0.1, 1 and 10 fb^{-1} . The errors shown are statistical only.

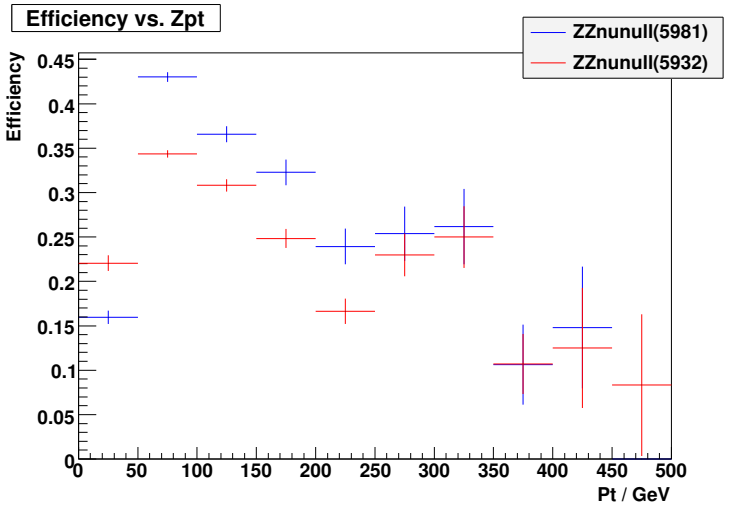

Figure 93: Signal selection efficiency against $p_T(Z)$ for 11.0.4 and 12.0.6 Monte Carlo. The efficiency is defined as the number of reconstructed events passing selection cuts over the number of true events with $p_T(l) > 20$ GeV, $|\eta_l| < 2.5$ and $\not{E}_T > 50$ GeV.

caused by the absolute $\not{E}_T$ cut. The drop in efficiency towards high p_T is caused by the jet veto, as signal events containing high p_T Z bosons are also likely to contain high p_T jets.

In order for events to be recorded by ATLAS, they must first pass the Level 1 (L1) hardware trigger and the High Level Trigger (HLT), which consists of the Level 2 trigger and a software-based Event-Filter (EF). Trigger information is included in the 12.0.6 datasets, and it essential to check that events passing selection cuts also pass appropriate triggers. Here we require events to pass either the `e25i` or `mu20i` triggers to be passed for electron or muon events respectively. The `2e15i`, `2mu6`, `met10` triggers are also considered.

Table 65 shows the efficiency of the trigger after all of the above cuts have been applied. If we require either `e25i` or `mu20i` to be passed, a trigger efficiency of 97.0% is acheived. If a more complex trigger menu is chosen, for example requiring `met10` to also be passed, this efficiency drops to 53.9%, due to muon events failing to trigger. Similarly, while the `2e15i` trigger is 84.5% efficient, the dimuon trigger `2mu06` admits virtaully no events. As the trigger definitions are constantly evolving, these efficiencies will also change. For early data it therefore seems sensible to choose a simple trigger, which in this case is `e25i` or `mu20i`.

Electrons		Muons		Total	
Trigger	Efficiency	Trigger	Efficiency	Trigger	Efficiency
L1E25I	99.8%	MU20	98.1%	L1E25I or MU20	98.6%
HLT e25i	98.4%	HLT mu20i	96.4%	HLT e25i or mu20i	97.0%
HLT e25i + met10	98.4%	HLT mu20i + met10	36.2%	HLT (e25i or mu20i) + met10	53.9%
HLT 2e15i	84.5%	HLT 2mu06	0.1%	HLT 2e15i or 2mu06	24.1%

Table 65: Trigger efficiencies for the signal after all cuts.

8.3.5 Discussion

As table 64 shows, the two different signal versions predict different yields by $\sim 8\ \sigma$. This is most likely to be due to differences in the generators used in the study. Despite this, the estimated significance shows a good agreement between versions, and a statistically significant measurement of the $ZZ \rightarrow \ell\ell\nu\bar{\nu}$ channel could be made after $\sim 1\text{fb}^{-1}$ of data.

The errors on the background estimates remain large in both cases due to the limited statistics available after cuts. For example, only two 12.0.6 events pass cuts in the $t\bar{t}$ channel, but this corresponds to over half of the total background. Larger full simulation samples are not currently practical, so this background will need to be estimated either using fast simulation samples, or by performing fits.

The expected number of events will also contain a theoretical uncertainty due to errors in the PDF libraries used to generate events. Comparison of the CTEQ6M and MRST(02) PDF sets give the ZZ production cross section in ATLAS as 14.74 pb and 15.32 pb respectively, corresponding to an additional uncertainty of $\sim 3\%$.

A previous study has been carried out with fast simulation (Atlfast) Monte Carlo [42] using a similar set of cuts. The two main differences are that no $\not{E}_T$matching cuts are applied, and the Zp_T cut is tightened to 150 GeV. With this analysis, 5.8 signal events are predicted in 1 fb^{-1} , with 0.4 background events, giving $S/B = 16$. Applying the same set of cuts to the 12.0.6 full simulation gives 3.4 signal and 4.4 background events, with $S/B = 0.78$. This difference is because the fast simulation only applies a simple smearing to measured parameters, instead of mimicking the entire detector readout. The Atlfast study also assumes lepton efficiency of 90% which will improve signal efficiency and will veto more background with three or more leptons.

8.4 Anomalous neutral gauge couplings

Measurements of the $pp \rightarrow ZZ$ differential cross section can be used to measure, or set limits on, ZZZ and $ZZ\gamma$ couplings. These couplings are zero at tree level in the Standard Model. Measurements of the couplings provide a sensitive test of the Standard Model, and non-zero values would indicate the presence of new physics beyond the Standard Model.

As discussed in Section 2, production of on-shell ZZ pairs is sensitive to two ZZZ and two $ZZ\gamma$ anomalous couplings, f_i^V, $i = 4,5$, V=Z,γ. The f_4^V couplings are CP-violating; therefore the associated helicity amplitudes do not interfere with the Standard Model amplitudes, and cross sections are independent of the sign of the coupling. The f_5^V couplings violate P. The f_5^V couplings contribute to the Standard Model cross section at one-loop level, but these contributions are $\mathcal{O}(10^{-4})$ [28]. To avoid violation of unitarity, we use a generalized dipole form factor:

$$f_i^V(\hat{s}) = \frac{f_{i0}^V}{(1+\hat{s}/\Lambda_{FF}^2)^n}$$

where $\hat{s}$ is the square of the parton c.m. energy and Λ_{FF} is a form factor scale which is related to the scale of the new physics generating the anomalous ZZV coupling. The results below use n = 3 and Λ_{FF} = 2 TeV.

In this analysis we have used the leading-order Monte Carlo generator of Baur and Rainwater [43] (henceforth referred to as BR), with the CTEQ6L PDF set, to study the effects of anomalous couplings. This program generates the hard scattering process and Z boson decays only. Figure 94 compares the Standard Model prediction from the BR program with those from PYTHIA and MC@NLO for the p_T distribution of the visibly-decaying Z boson in $ZZ \rightarrow \ell\ell\nu\nu$ events. To correspond to the kinematic cuts applied in the $ZZ \rightarrow \ell\ell\nu\nu$ event selection, we require both generated leptons to satisfy $p_T(\ell) > 20$ GeV and $|\eta(\ell)| < 2.5$ and the invisibly decaying Z to satisfy $p_T(\nu\nu) > 50$ GeV. The BR prediction contains no initial-state radiation or underlying event; the p_T of the visibly-decaying Z boson is therefore identical

to that of the invisibly-decaying Z boson, hence the distribution is zero below 50 GeV. In PYTHIA and MC@NLO, parton showering and hard gluon radiation result in different p_T values for the two Z bosons, so the distribution extends below 50 GeV. Parton showering in PYTHIA results in a harder p_T distribution than in the purely leading-order BR prediction, with the hard gluon radiation in MC@NLO hardening the spectrum further. It has been verified that good agreement is observed between the BR generator and PYTHIA if parton showering in PYTHIA is turned off.

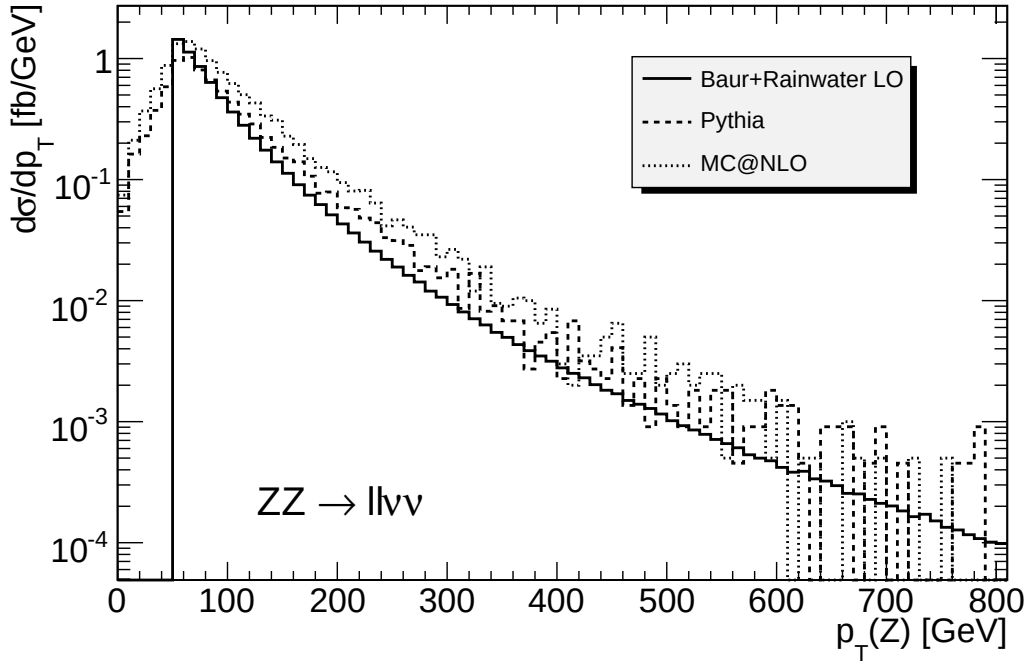

Figure 94: Generator-level differential cross section for $pp \to ZZ \to \ell\ell\nu\nu$ ($\ell = e, \mu$) at $\sqrt{s}$ = 14 TeV from different event generators. Distributions are shown for events satisfying $p_T(\nu\nu) > 50$ GeV, $p_T(\ell) > 20$ GeV and $|\eta(\ell)| < 2.5$, where $p_T(\nu\nu)$ is the p_T of the Z which decays to neutrinos.

Non-zero ZZZ and $ZZ\gamma$ couplings typically increase the ZZ cross section at high ZZ invariant mass and high p_T of the Z boson. Figure 95 shows the p_T distribution of the Z boson in $ZZ \to \ell\ell\nu\nu$ events satisfying the above cuts for various values of the coupling f_4^Z, calculated using the BR program. We see an enhancement in the cross section which increases with p_T and with coupling.

8.4.1 Fit procedure

In order to estimate limits on anomalous couplings which may be obtained from measurements of ZZ production in early ATLAS data, we consider the p_T distribution of the Z boson. In the $ZZ \to \ell\ell\nu\nu$ channel we use the visible Z boson reconstructed from the charged leptons. In the $ZZ \to \ell\ell\ell\ell$ channel we choose one of the two reconstructed Z bosons in each event at random. Simulated 'fake data' distributions are fitted with the sum of expected signal and background distributions, where the signal distribution depends on the anomalous couplings. A binned maximum likelihood fit is employed, with systematic errors included by convolution with the predictions. Fits are performed to each channel separately, and a combined fit is performed by multiplying together the likelihoods from the two channels assuming no correlated errors. Results are presented below for each coupling assuming that only one coupling is

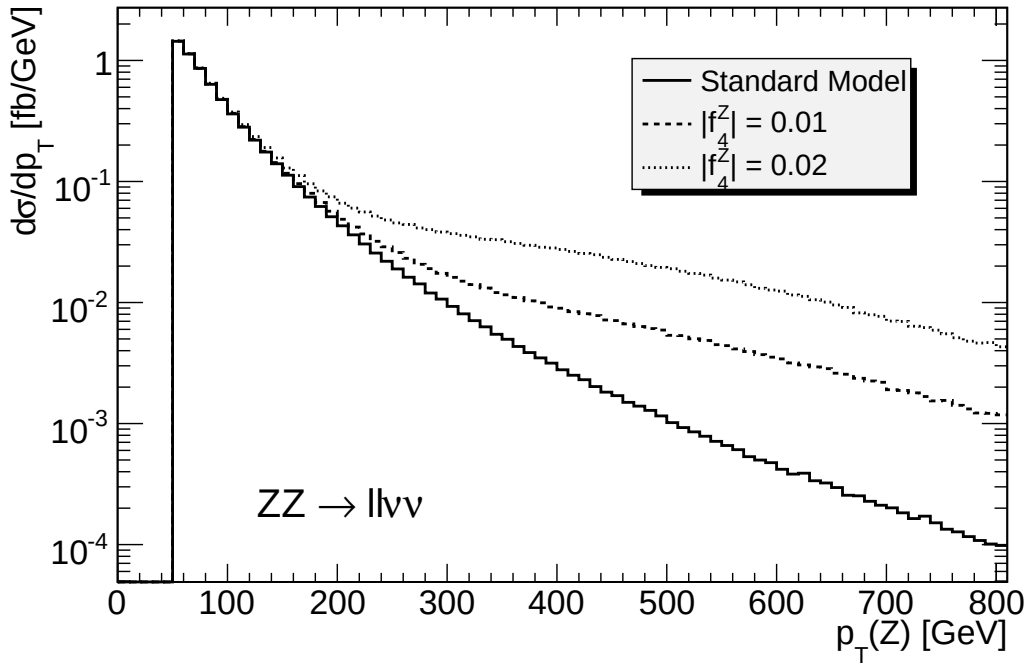

Figure 95: Differential cross section for $pp \to ZZ \to \ell\ell\nu\nu$ ($\ell = e, \mu$) at $\sqrt{s}$ = 14 TeV for different values of the anomalous coupling f_4^Z. The cross sections are calculated using the LO Monte Carlo program of Baur and Rainwater, with $\Lambda_{FF} = 2$ TeV and n = 3. All couplings except f_4^Z are assumed to be zero. Distributions are shown for events satisfying $p_T(\nu\nu) > 50$ GeV, $p_T(\ell) > 20$ GeV and $|\eta(\ell)| < 2.5$.

non-zero, and that it is real.

Signal prediction. The signal distribution is obtained by combining the predictions of the BR program with the MC@NLO full-simulation studies described in the previous two sections. In each p_T bin, the leading order signal cross section is calculated for several values of coupling using the Baur and Rainwater Monte Carlo program [43]. This calculation includes the kinematic cuts described above for the $\ell\ell\nu\nu$ channel; no kinematic cuts are applied in the case of the $\ell\ell\ell\ell$ channel. The points are fitted to a quadratic function in the coupling, and this fit is used to obtain the cross section at an arbitrary coupling value. The leading-order predictions are multiplied by the ratio of the MC@NLO prediction (with the same kinematic cuts) to the BR Standard Model prediction to account for next-to-leading-order effects. The expected number of signal events is calculated using the NLO-corrected cross section, the efficiency of the selection cuts and the integrated luminosity. The efficiency of the selection cuts is determined from the fully-simulated MC@NLO signal sample as described in Sections 8.2 and 8.3. The efficiencies for each channel are shown in Fig. 96. For the $\ell\ell\ell\ell$ channel the efficiency, which is relative to all generated events, tends to increase with p_T . For the $\ell\ell\nu\nu$ channel the efficiency is with respect to events generated with $p_T(\nu\nu) > 50$ GeV, $p_T(\ell) > 20$ GeV and $|\eta(\ell)| < 2.5$, and drops with increasing p_T . The increase in cross section from anomalous couplings rises with p_T . Therefore the signal predictions for are somewhat dependent on the p_T binning chosen, particularly for the $\ell\ell\nu\nu$ channel. For example, for $f_4^Z = 0.01$ (roughly the expected 95% C.L. for 10 fb^{-1} of data) the total number of $\ell\ell\nu\nu$ events predicted using the average efficiency is 7% higher than the prediction using the binning in Fig. 96. This leads to uncertainties of around 15% on the expected limits.

Background prediction. The expected background distribution in the $\ell\ell\ell\ell$ channel is calculated from the fully-simulated Monte Carlo events. *Currenly this is Zbb only.* The background is small, and the large errors on the expected background resulting from Monte Carlo statistics have a negligible effect on the limits. In the $\ell\ell\nu\nu$ channel the expected background is large, and there are insufficient fully-simulated Monte Carlo events to make a good estimate of the shape of the expected background distribution. The p_T distributions of the various backgrounds have been compared with signal before applying event-selection cuts. While many backgrounds (particularly single Z events) have a steeply-falling p_T spectrum below 100 GeV, at higher p_T values the spectra are fairly similar to that of the signal events. Therefore the background distribution is taken to be a constant fraction of the Standard Model signal expectation. The signal:background ratio of 1.96 observed in Section 8.3 gives a background:signal ratio of 0.51 ± 0.21, where the error is from Monte Carlo statistics. The effect of varying this background fraction has been studied.

Fake 'data' samples. Fake 'data' distributions are generated from the expected numbers of Standard Model signal and background events. A systematic error on the signal correlated across p_T bins is included by multiplying the expected distribution by a random number selected from a Gaussian distribution with mean one and standard deviation equal to the fractional systematic error discussed below. The signal expectation is further fluctuated according to the error on the efficiency arising from Monte Carlo statistics in each p_T bin. The background is treated in a similar manner; signal and background systematic errors are assumed uncorrelated. Finally, a Poisson fluctuation is applied to the total numbers of events in each bin.

Likelihood fit. At each value of integrated luminosity, 1000 fake data distributions are generated. Each distribution is fitted to the sum of expected signal and background using a binned maximum likelihood fit with a single free parameter. Systematic errors are included in the fit by convolving the expected signal

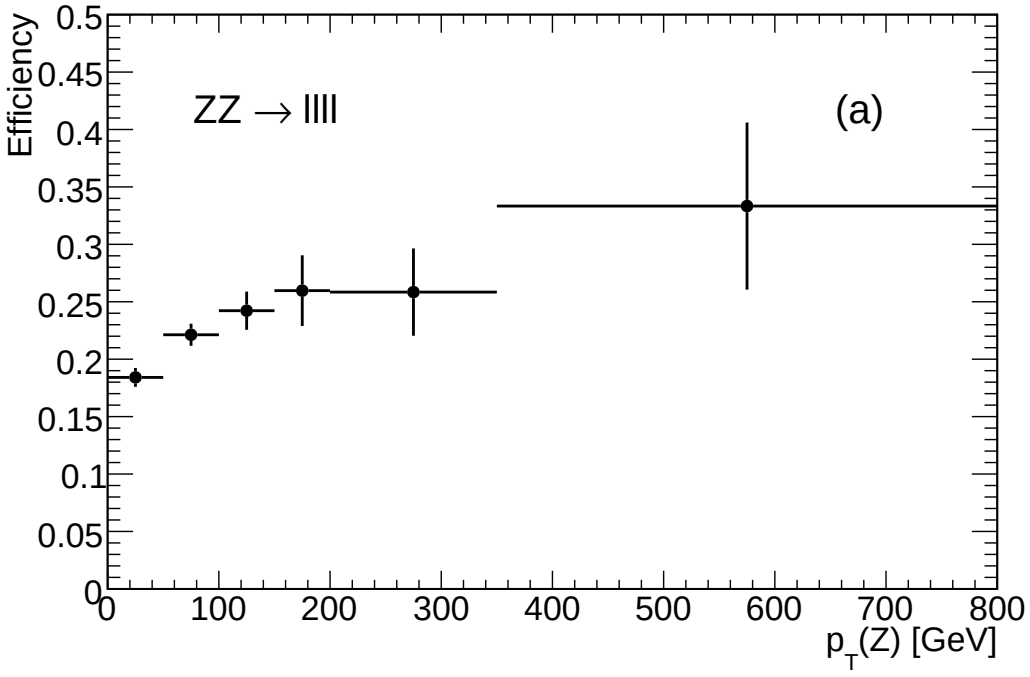

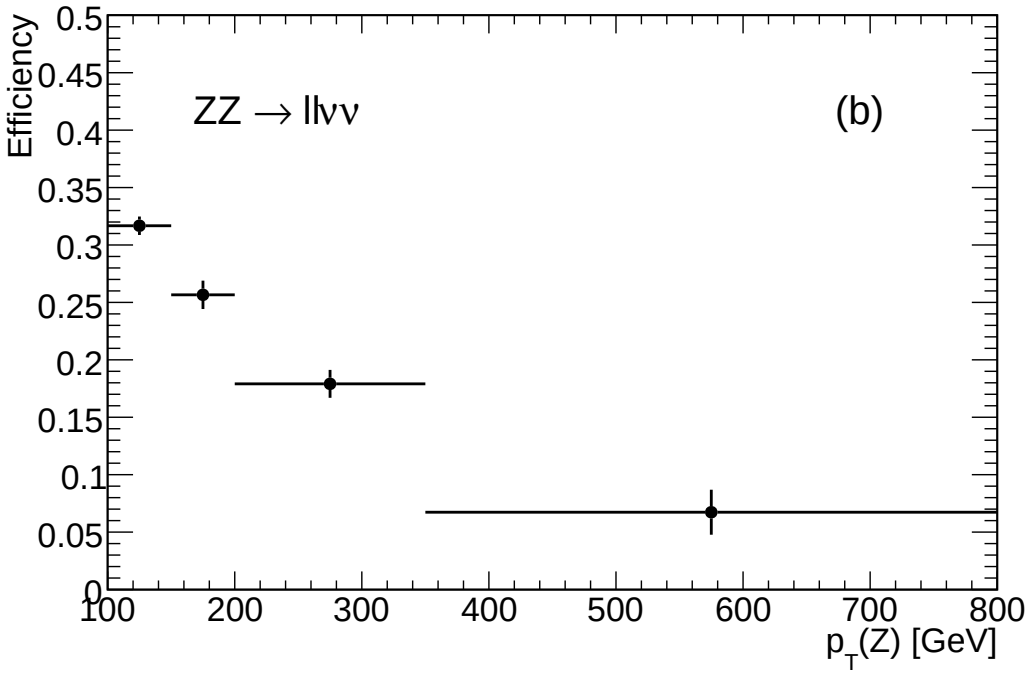

Figure 96: (a) Efficiency of selection cuts as a function of p_T in the $ZZ \to \ell\ell\ell\ell$ channel. Efficiency is defined as the number of events passing the selection cuts described in Section 8.2 with the reconstructed p_T of a randomly selected Z boson in a given bin divided by the total number of generated events with true Z boson p_T in that bin. (b) Efficiency of selection cuts as a function of p_T in the $ZZ \to \ell\ell\nu\nu$ channel. In this case, efficiency is defined as the number of events passing the selection cuts described in Section 8.3 with reconstructed Z boson p_T in a given bin divided by the number of events generated with true Z boson p_T in that bin which also satisfy $p_T(\nu\nu) > 50$ GeV, $p_T(\ell) > 20$ GeV and $|\eta(\ell)| < 2.5$.

and background numbers with Gaussians. The likelihood function for a single p_T bin j takes the form:

$$\mathscr{L}_j = \int_{1-3\sigma_s}^{1+3\sigma_s} \int_{1-3\sigma_b}^{1+3\sigma_b} G(r_s;1,\sigma_s)\, G(r_b;1,\sigma_b)\, P(n;r_s\nu_s(f_i^V)+r_b\nu_b) dr_s dr_b$$

where $P(n;r_s\nu_s(f_i^V)+r_b\nu_b)$ is the Poisson probability of observing n events from a distribution with mean $(r_s\nu_s(f_i^V)+r_b\nu_b)$; ν_s and ν_b are the expected numbers of signal and background events respectively, with ν_s being a function of the anomalous coupling parameter f_i^V. $G(r_s;1,\sigma_s)$ is a Gaussian function with mean one and standard deviation σ_s, where σ_s is the fractional systematic error on the signal prediction; $G(r_b;1,\sigma_b)$ is a similar Gaussian function with standard deviation σ_b equal to the fractional background systematic error. The likelihood function for each channel is formed by multiplying together the likelihoods for each p_T bin:

$$\mathscr{L} = \prod_j \mathscr{L}_j,$$

and when fitting to the combined channels the likelihoods for each channel are multiplied together. The negative log likelihood is miminized.

In the case of the signal, the total systematic error in each bin is the sum in quadrature of the error on efficiency from Monte Carlo statistics and a systematic error of 7.2%, comprising 6.5% from luminosity and 3% from lepton identification. With the above formulation of the likelihood function, this systematic error is effectively uncorrelated between p_T bins (and between channels). The likelihood function can be adapted to include the correlations by introducing another integral over the correlated part of the systematic error separate from that over the uncorrelated part. However, for low integrated luminosities it is found that the effect of correlations is small, and for simplicity the above formulation has been used for the results presented below. The background systematic errors arise from Monte Carlo statistics of the background samples which dominate other expected contributions. For the $\ell\ell\ell\ell$ channel the values are p_T -bin dependent; for the $\ell\ell\nu\nu$ channel a value of 41% is used for all bins.

The 95% C.L. interval on f_i^V is determined from the values at which the negative log likelihood is 1.92 above the minimum. In a small number of cases (at most $\sim$3%, depending integrated luminosity) the fit in the $\ell\ell\nu\nu$ does not converge: these fits are discarded when calculating the average limits. In some fits the negative log likelihood has two minima (equivalent in the case of the symmetric f_4^V couplings) separated by a local maximum which is more than 1.92 above the minimum. In this case, the limits are taken from the extreme points at which the negative log likelihood reaches 1.92 above the minimum.

8.4.2 Results and discussion

An example fit for each channel is shown in Fig. 97. The results presented here use four p_T bins for the $\ell\ell\nu\nu$ channel and six p_T bins for the 4-lepton channel, as shown in Fig. 97. Reasonable modifications to the number or position of p_T bins change the expected limits by up to 15% (12%) in the $\ell\ell\nu\nu$ ($\ell\ell\ell\ell$) channel. Removing the first two p_T bins for the $\ell\ell\ell\ell$ channel, and fitting only the region $p_T > 100$ GeV has a negligible effect on the limits.

Table 66 shows the mean expected limits from each channel separately, and from combining the channels, for various values of integrated luminosity. With an integrated luminosity of 1 fb^{-1} the sensitivities of the two channels are very similar. At higher luminosities, the $\ell\ell\ell\ell$ channel becomes somewhat more sensitive, because it has lower background and hence a lower associated systematic error. With as little as 1 fb^{-1} of data it should be possible to improve the LEP limits [4] on f_4^Z, f_5^Z and f_5^γ by an order of magnitude using a single channel, while a similar improvement on f_4^γ will require both channels.

At an integrated luminosity of 10 fb^{-1} , the expected limits have only a low sensitivity to the background level and to the systematic errors. With the same signal efficiency but no background, the limits

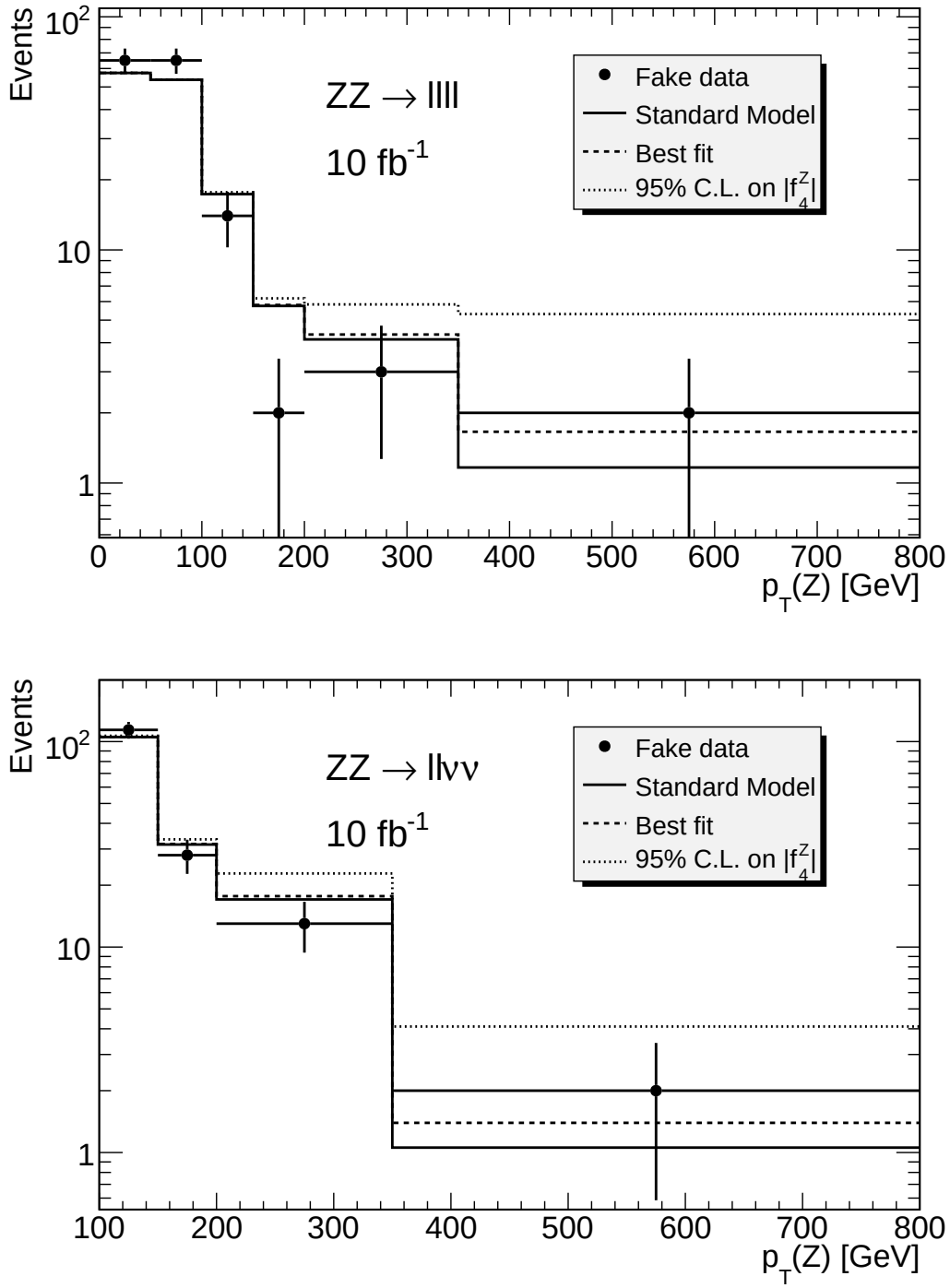

Figure 97: Example of a fit to one fake data sample in each channel. The points show the total number of 'data' events in each bin (not number per unit p_T). The histograms show the Standard Model prediction (solid), the best fit (dashed) and the 95% C.L. limit on $|f_4^Z|$ (dotted).

Table 66: Expected 95% C.L. intervals on anomalous couplings from fits to the $ZZ \to \ell\ell\ell\ell$ channel, the $ZZ \to \ell\ell\nu\nu$ channel and both channels together for various values of integrated luminosity. In each case, other anomalous couplings are assumed to be zero.

$ZZ \to \ell\ell\ell\ell$				
L / fb^{-1}	f_4^Z	f_5^Z	f_4^γ	f_5^γ
1	[–0.023, 0.023]	[–0.024, 0.024]	[–0.028, 0.028]	[–0.029, 0.028]
10	[–0.010, 0.010]	[–0.010, 0.010]	[–0.012, 0.012]	[–0.013, 0.012]
30	[–0.008, 0.008]	[–0.008, 0.008]	[–0.009, 0.009]	[–0.009, 0.009]
$ZZ \to \ell\ell\nu\nu$				
L / fb^{-1}	f_4^Z	f_5^Z	f_4^γ	f_5^γ
1	[–0.024, 0.024]	[–0.024, 0.025]	[–0.029, 0.029]	[–0.030, 0.029]
10	[–0.012, 0.012]	[–0.012, 0.012]	[–0.014, 0.014]	[–0.015, 0.014]
30	[–0.009, 0.009]	[–0.009, 0.009]	[–0.011, 0.011]	[–0.011, 0.011]
Combined				
L / fb^{-1}	f_4^Z	f_5^Z	f_4^γ	f_5^γ
1	[–0.018, 0.018]	[–0.018, 0.019]	[–0.022, 0.022]	[–0.022, 0.022]
10	[–0.009, 0.009]	[–0.009, 0.009]	[–0.010, 0.010]	[–0.011, 0.010]
30	[–0.006, 0.006]	[–0.006, 0.007]	[–0.008, 0.008]	[–0.008, 0.008]

from the $\ell\ell\nu\nu$ channel improve by 10%, while those from the $\ell\ell\ell\ell$ channel change by only $\sim$0.2%; in the latter case, doubling the background has an effect of only $\sim$0.4%. Reducing all systematic errors to zero improves the limits by 7% (6%) in the $\ell\ell\nu\nu$ ($\ell\ell\ell\ell$) channel. Thus, the background level and systematic errors are unlikely to be important factors in obtaining limits from early data.

As discussed above, the expected limits are affected by the choice of p_T bins. The number of bins is currently limited by the statistics of the fully-simulated Monte Carlo events. Future studies would benefit from increased signal Monte Carlo statistics, particularly in the high p_T region. In addition, samples of fully-simulated events with anomalous couplings should be used to investigate the dependence of the efficiency at a particular p_T value on the production diagram.

9 Summary

In this note, we have presented the analysis of W^+W^-, $W^\pm Z^0$, Z^0Z^0, $W^\pm\gamma$ and $Z^0\gamma$ diboson final states with leptonic decays of $W^\pm$ and Z^0 bosons in the ATLAS detector with the release 12 software. We concluded that the Standard Model signals of W^+W^-, $W^\pm Z^0$, $W^\pm\gamma$ and $Z^0\gamma$ can be established with statistical significance better than 5 for the first 0.1 fb^{-1} integrated luminosity and the Z^0Z^0 signals both with four-lepton final states and with dilepton plus neutrino-pair decay channels can be established with 1 fb^{-1}. Table 67 lists the expected numbers of signal and background events and statistical significance of observing the Standard Model signals, after taking into account the known background contributions.

Table 67: Summary of signal and background of all diboson final states for 1 fb^{-1} integrated luminosity. The last column indicates type of analysis and the overall signal selection efficiencies.

Diboson mode	Signal	Background	S/$\sqrt{B}$	Analysis (signal eff.)
$W^+W^- \to e^\pm\nu\mu\mp\nu$	419.9 ± 3.5	80.8 ± 8.0	47	BDT (eff=15.2%)
$W^+W^- \to \mu+\nu\mu^-\nu$	90.3 ± 1.6	20.2 ± 2.8	20	BDT (eff=6.6%)
$W^+W^- \to e^+\nu e^-\nu$	78.0 ± 1.6	35.4 ± 3.6	13	BDT (eff=4.1%)
$W^+W^- \to \ell^+\nu\ell^-\nu$	103.1 ± 2.6	16.6 ± 2.0	25	Cut based (eff=1.3%)
$W^\pm Z \to \ell^\pm\nu\ell^+\ell^-$	152.6 ± 1.7	16.1 ± 2.5	38	BDT (eff=17.9%)
	53.4 ± 1.6	8.0 ± 1.1	19	cut based (6.3%)
$ZZ \to 4\ell$	16.5 ± 0.1	1.9 ± 0.2	12	cut based (eff=7.7%)
$ZZ \to \ell^+\ell^-\nu\bar{\nu}$	10.2 ± 0.2	5.2 ± 2.0	4.5	cut based (eff=2.6%)
$W\gamma \to e\nu\gamma$	1901 ± 77	1474 ± 147	50	BDT (eff=6.7%)
$W\gamma \to \mu\nu\gamma$	2976 ± 121	2318 ± 232	62	BDT (eff=10.5%)
$Z\gamma \to e^+e^-\gamma$	337.4 ± 12	187.2 ± 19	25	BDT (eff=5.5%)
$Z\gamma \to \mu^+\mu^-\gamma$	774.8 ± 25	466.7 ± 47	36	BDT (eff=12%)

In all the analysis, the L1 and HLT trigger efficiencies for the final states are studied. The triggers of $1e25i$ and $lmu20$ are sufficiently efficient for leptons from boson decays(see Table 13, 55, 65). Therefore in the early LHC running at low luminosities, for multi-lepton final states, we expect the overall event trigger efficiency to be high (over 95% for all of the channels relative to offline event selection) when the single electron and muon triggers are not prescaled. When the luminosity is sufficiently high such that single electron and muon trigger will be prescaled, it is necessary to rely on the two lepton triggers, such as 2e15i and 2mu6. In such case, the signal with only one lepton in final state will suffer a loss of trigger efficiency, while the final state with at least two leptons can still be triggered efficiently.

As discussed in Section 2 in general, and in Sections 4-8 specifically for each diboson final state, the deviation from the Standard Model prediction for these final states can lead to indications of physics beyond the standard model. The sensitivities are expressed in terms of constraints on the anomalous triple gauge boson couplings in the effective Lagrangian. The W^+W^-, $W^\pm Z^0$, $W^\pm\gamma$ final states are sensitive to the charged anomalous TGC's through the $W^+W^-Z^0$ and $W^+W^-\gamma$ vertex. Table 68 compares the 95% confidence level sensitivity interval for charged anomalous TGC's using observables from different diboson final states with 10 fb^{-1} integrated luminosity. More complete lists of the sensitivities with different cutoff Λ, luminosities and observables are given in corresponding sections in the note.

The neutral anomalous TGC's can be explored by the $Z^0\gamma$ and Z^0Z^0 final states. Both $Z^0Z^0 \to \ell^+\ell^-\ell^+\ell^-$ and $Z^0Z^0 \to \ell^+\ell^-\nu\bar{\nu}$ are used to constrain the neutral anomalous TGC parameters (f_4^Z, f_5^Z, f_4^γ, f_5^γ). The 95% C.L. intervals on the anomalous couplings for 10 fb^{-1} luminosity are list in Table 69.

Table 68: 95% C.L. interval of the anomalous coupling sensitivities from W^+W^-, $W^\pm Z^0$, $W^\pm\gamma$ final states with 10.0 fb^{-1} integrated luminosity and the cutoff $\Lambda = 2$TeV. The table also indicates the variables used in the fit to set the AC sensitivity interval. For comparison, some recently published limits from Tevatron and LEP are also listed.

Diboson, (fit spectra)	λ_Z	$\Delta\kappa_Z$	Δg_1^Z	$\Delta\kappa_\gamma$	λ_γ
WW, (M_T)	[-0.040, 0.038]	[-0.035, 0.073]	[-0.149, 0.309]	[-0.088, 0.089]	[-0.074, 0.165]
WZ, (M_T)	[-0.015, 0.013]	[-0.095, 0.222]	[-0.011, 0.035]		
$W(e\nu)\gamma$, ($P_T(\gamma)$)				[-0.34, 0.12]	[-0.07, 0.03]
$W(\mu\nu)\gamma$, ($P_T(\gamma)$)				[-0.30, 0.09]	[-0.05, 0.02]
$W^\pm\gamma$ (D0), L = 0.16fb^{-1}				[-0.88,0.96]	[-0.2,0.2]
WZ, (D0) L = 1.0fb^{-1}	[-0.17, 0.21]	[-0.12, 0.29] ($\Delta g_1^Z = \Delta\kappa_Z$)			
WW, (LEP)	($\lambda_\gamma = \lambda_Z$,$\Delta\kappa_Z = \Delta g_1^Z - \Delta\kappa_\gamma \tan^2\theta_W$)		[-0.051,0.034]	[-0.105,0.069]	[-0.059,0.026]

The ATLAS diboson physics studies for the CSC note are a collective effort by nine ATLAS groups. While each individual analysis is done independently, a few common analysis techniques and tools are shared. For event selection, the Boosted Decision Trees technique is used in the analysis of W^+W^-, $W^\pm Z^0$, $W^\pm\gamma$ and $Z^0\gamma$ final state. This method is described in detail in Appendix A. In general, the multivariate method improves the signal to background ratio, especially for events with less well defined kinematics, such as final states involving W. The input variables are chosen to differentiate the signal events from the background events, such as particle identification variables, lepton isolation energy, additional jet activities in the event, and significance of the missing transverse energy, as well as the kinematic relations between the leptons. The *BDT*-output spectrum is used as a discriminator to separate the signal from the background. The sensitivity to the signal events can be optimized by varying the cut on the *BDT*-output.

The presence of the anomalous TGC's modifies the diboson production mechanism, in terms of total production rate as well as phase space distributions. The binned likelihood method with event weighting is the most effective way to detect the presence of the anomalous TGC's. It is practically impossible to simulate the events with every different non-standard model coupling, but it is also not necessary, because the SM events can be re-weighted according the additional contributions from the anomalous couplings on an event by event basis. The re-weighting process requires that for each event, according to the kinematics, the ratio of matrix element squared of the SM process to that of process including and SM and non-SM contributions be known. This is equivalent to simulate the events with all different anomalous couplings. In practice, because of the limitation of the generators, the *re-weighting* is parametrized with only a limited number of variables.

The current status of the MC generators for diboson is less than satisfactory. *MC@LNO* is integrated with parton shower (Herwig), but it does not have matrix elements for the effective Lagrangian beyond the Standard Model with the anomalous couplings. The *BHO* MC program can generate at the LO and NLO the diboson events with anomalous couplings, but it can not be correctly integrated with the parton shower programs. In our current analysis, *MC@LNO* is used to simulate the SM events. Then the *BHO* MC with anomalous TGCs is used to re-weight the events so that the fully simulated events can effectively have the anomalous TGC's, or the fast simulation of *BHO* MC events are corrected by

Table 69: Expected 95% C.L. intervals on anomalous couplings from fits to the $ZZ \to \ell\ell\ell\ell$ channel, the $ZZ \to \ell\ell\nu\nu$ channel and both channels together for 10 fb^{-1} integrated luminosity. In each case, other anomalous couplings are assumed to be zero. 95% C.L. NTGC limits from LEP ZZ detection are also listed.

f_4^Z	f_5^Z	f_4^γ	f_5^γ
$ZZ \to \ell\ell\ell\ell$			
[–0.010, 0.010]	[–0.010, 0.010]	[–0.012, 0.012]	[–0.013, 0.012]
$ZZ \to \ell\ell\nu\nu$			
[–0.012, 0.012]	[–0.012, 0.012]	[–0.014, 0.014]	[–0.015, 0.014]
Combined			
[–0.009, 0.009]	[–0.009, 0.009]	[–0.010, 0.010]	[–0.011, 0.010]
LEP Limit			
[–0.30, 0.30]	[–0.34, 0.38]	[–0.17, 0.19]	[–0.32, 0.36]

the full simulation for acceptance and efficiency, and used directly to compare with the MC mock data. A third approach is under the investigation. The approach intends to include the LO *BHO* MC events into the parton shower MC programs (Pythia or Herwig), thus allowing the full simulation of events with anomalous TGC's. The NLO effects are then taken into account by P_t dependent k-factors, derived at generator level.

As discussed in Section 3, from the Tevatron experience, it is essential that the detector performance, such as lepton and photon identification efficiencies and the fake rates should be studied and determined with real data. We have presented in the $W^\pm Z^0$ section in this note a study of the muon detection efficiency determined by the so called $tag - probe$ method developed in D0 experiment, and compared the results to the efficiencies determined by using the MC truth information. Very good agreement between two methods has achieved. The most challenge work will be understanding the QCD background from data and estimating the systematic uncertainties from data, different MC generators and PDF's. Our continued efforts will focus on those issues and the development of the tools and procedures for LHC diboson physics studies.

References

[1] https://twiki.cern.ch/twiki/bin/view/Atlas/CSCNotesList
https://twiki.cern.ch/twiki/bin/view/Atlas/CSCDistributedProduction
http://atlas-computing.web.cern.ch/atlas-computing/packages/athenaCore/athenaCore.php
https://twiki.cern.ch/twiki/bin/view/Atlas/HighPtView
https://twiki.cern.ch/twiki/bin/view/Atlas/ElectronReconstruction
https://twiki.cern.ch/twiki/bin/view/Atlas/MoreMuidInfo
http://atlas-samusog.web.cern.ch/atlas-samusog/muonboy/Muonboy.htm
https://twiki.cern.ch/twiki/bin/view/Atlas/JetS
https://twiki.cern.ch/twiki/bin/view/Atlas/EtMiss
https://twiki.cern.ch/twiki/bin/view/Atlas/TriggerUserPage
https://twiki.cern.ch/twiki/bin/view/Atlas/CBNTVariblelist
https://twiki.cern.ch/twiki/bin/view/Atlas/MuonRecoPedia
https://twiki.cern.ch/twiki/bin/view/Atlas/TauRec
https://twiki.cern.ch/twiki/bin/view/Atlas/Tau1P3PIntegrated

[2] L. Breiman, J.H. Friedman, R.A. Olshen, and C.J. Stone, *Classification and Regression Trees*, Wadsworth International Group, Belmont, California (1984).

Y. Freund and R.E. Schapire (1996), *Experiments with a new boosting algorithm*, Proc COLT, 209–217. ACM Press, New York (1996).

J. Friedman, *Greedy function approximation: a gradient boosting machine*, Annals of Statistics, 29(5), 1189-1232(2001).

J. Friedman, T. Hastie, R. Tibshirani, *Additive Logistic Regression: a Statistical View of Boosting*, Annals of Statistics, 28(2), 337-407(2000).

[3] E. Church *et al.*, BooNE Proposal, FERMILAB-P-0898(1997).

Byron P. Roe, Hai-Jun Yang, Ji Zhu, Yong Liu, Ion Stancu, Gordon McGregor, *Boosted decision trees as an alternative to artificial neural networks for particle identification*, Nucl. Instrum. & Meth. A **543** (2005) 577-584, [physics/0408124];

Hai-Jun Yang, Byron P. Roe, Ji Zhu, *Studies of boosted decision trees for MiniBooNE particle identification*, Nucl. Instrum. & Meth. A **555** (2005) 370-385,[physics/0508045];

Hai-Jun Yang, Byron P. Roe, Ji Zhu, *Studies of Stability and Robustness for Artificial Neural Networks and Boosted Decision Trees*, NIM A **574** (2007) 342-349, [physics/0610276];

Hai-Jun Yang, Tiesheng Dai, Alan Wilson, Zhengguo Zhao, Bing Zhou *A Multivariate Training Technique with Event Reweighting*. [arXiv:0704.3706];

The MiniBooNE Collaboration, A.A. Aguilar-Arevalo et.al., *A Search for electron neutrino appearance at the* $\Delta m^2 \sim 1\ eV^2$ *scale*, [hep-ex/0704.1500], Physical Review Letter (in press);

The BABAR Collaboration, B. Aubert et.al., *Measurement of CP-violating asymmetries in the* $B^0 \to K^+K^-K^0$ *Dalitz plot*,[hep-ex/0607112];

The D0 Collaboration, V.M. Abazov et.al., *Evidence for Production of Single Top Quarks and First Direct Measurement of* $|V_{tb}|$, Phys. Rev. Lett. **98** , 181802 (2007);

J. Bastos, *Tagging heavy flavours with boosted decision trees*, Physics, 0702041.

[4] D. Abbaneo *et al.*, ALEPH, DELPHI, L3, OPAL Collaborations and LEP Electroweak Working Group and SLD Heavy Flavor and Electroweak Group, CERN-EP-2001-098 [hep-ex/0112021];

Review of Particle Physics (PDG), p1098 (2004);

The LEP collaborations ALEPH, DELPHI, L3, OPAL and the LEP electroweak working group, *A Combination of Preliminary Electroweak Measurements and Constraints on the Standard Model*: CERN-PH-EP-2006-042, hep-ex/0612034, November 2006.

[5] The CDF Collaboration, Phys. Rev. Lett. **94**, 041803 (2005).

[6] The DØ Collaboration, Phys. Rev. D **71**, 091108 (2005).

[7] The CDF Collaboration, hep-ex 0605066(2006).

[8] The DØ Collaboration, Phys. Rev. Lett. **94**, 151801 (2005).

[9] The CDF Collaboration, Fermilab Seminar August 2007.

[10] The DØ Collaboration, hep-ex 0709.2917 (2007).

[11] The CDF Collaboration, Phys. Rev. Lett. **94**, 041803 (2005).

[12] The DØ Collaboration, Phys. Lett. B**653**, 378(2007).

[13] The CDF Collaboration, Winter Conference Note Jan. 2006.

[14] The DØ Collaboration, Summer Conference Note, March 2007.

[15] J.M. Campbell and R.K. Ellis, 'Update on vector paor production at hadron collider', Phys. Rev. D60, 113006(1999).

[16] L. Dixon, Z. Kunszt, A. Signer, 'Vector boson pair production in hadronic couplings at $O(\alpha_s)$: Lepton correction and anomalious couplings', Phys. Rev. D**60**, 114037(1999).

[17] J. Ohnemus, Order-α_s calculation of hadronic $W^{\pm}\gamma$ and $Z\gamma$ production', Phys. Rev. D**47**, 940(1993); V. Barger, T. Han, D. Zeppenfeld, J. Ohnemus, 'Pair production of $W^{\pm}$, γ and Z in association with jets', Phys. Rev. D**41**, 2782(1990).

[18] Stefano Frixione and Bryan Webber,

http://www.hep.phy.cam.ac.uk/theory/webber/MCatNLO/.

[19] http://projects.hepforge.org/lhapdf/pubs
J. Pumplin, D.R. Stump, J. Huston, H.L. Lai, P. Nadolsky, W.K. Tung, 'New Generation of Parton Distributions with Uncertainties from Global QCD Analysis', hep-ph/0201195

[20] Sjostrand, T., et al., Comput. Phys. Commun., **135**, 238259 (2001).

[21] Baur, U., Han, T., and Ohnemus, J., Phys. Rev., D50, 1917 (1994) (WGamma calculation);
Baur, U., Han, T., and Ohnemus, J., Phys. Rev., D51, 3381 (1995) (WZ Calculation);
Baur, U., Han, T., and Ohnemus, J., Phys. Rev., D53, 1098 (1996) (WW Calculation);
Baur, U., Han, T., and Ohnemus, J., Phys. Rev., D57, 2823 (1998) (ZGamma calculation).

[22] M. Dobbs, 'Probing the Three Gauge-boson Couplings in 14 TeV Proton-Proton Collisions', Ph. D. Thesis (2002), University of Victoria.

[23] T. Binoth, M. Ciccolini, N. Kauer and M. Kraemer, 'Glue-induced W-boson pair production at LHC', JHEP12, 046(2006)

[24] F. Larios, M. A. Perez, G. Tavares-Velasco, J. J. Toscano, 'Triliear neutral gauge boson couplings in effective theories', Phys. Rev. D**63**, 113014(2001);

U. Baur and D. Zeppenfeld, 'Unitarity constraints on the electroweak three vector boson vertices', Phys. Lett. B**201**, 383(1988);

Hagiwara K, P. Peccei, D. Zeppenfeld, ' Probling the weak boson sector in $e^+e^- \to W^+W^-$', Nucl. Physics B**282**, 253(1987).

[25] Bilenky at el., Nucl. Phys. B268 (1986).

[26] K. Hagiwara, S. Ishihara, R. Szalapski, and D. Zeppenfeld, 'Low energy effects of new interaction in the electroweak boson sector', Phys. Rev. 48, 2182(1993).

[27] U. Baur, T. Han and J. Ohnemus, 'QCD corrections and anomalous couplings in $Z\gamma$ production at hadron colliders', Phys. Rev. D**57**, 2823(1998).

G. J. Gounaris, J. Layssac, F. M. Rennard, 'New and standard physics contributions to anomalous Z and γ self-couplings', Phys. Rev. D**62**, 073013(2000).

U. Baur, D. Rainwater, 'Probing neutral gauge boson self-interactions in ZZ production at hadron collider', Phys. Rev. D**62**, 113011(2000).

M. A. Perez and F. Ramirez-Zavaleta, 'CP violation effects in the decay $Z \to \mu^+\mu^-\gamma$ induced by $ZZ\gamma$ and $Z\gamma\gamma$ couplings', hep-ph/0410212v4, 11 Jan. 2005.

[28] G. J. Gounaris, J. Layssac and F. M. Renard, Phys. Rev. **D62** 073013 (2000).

[29] http://hepwww.rl.ac.uk/theory/seymour/herwig/hw65_manual.htm

[30] Atlas Fast Simulation: http://www.hep.ucl.ac.uk/atlas/atlfast/

[31] S. Weinberg, Phys. Rev. Lett. 19, 1264 (1967);
A. Salam, p. 367 of Elementary Particle Theory, ed. N. Svartholm (Almquist and Wiksells, Stockholm, 1969);
S.L. Glashow, J. Iliopoulos, and L. Maiani, Phys. Rev. D2, 1285 (1970).

[32] A. Wilson, et.al., 'Study of ZW, WW and ZZ Production Using ATLAS Full Simulation Data', ATL-COM-PHYS-2006-033.

[33] S. Hassani, ATLAS-COM-PHYS-2002-013.

[34] M. Dobbs, com-phys-2002-019.

[35] M. Dobbs, proceedings, Hadron Collider Physics, 2004.

[36] The Electroweak Working Group of the LEP Collaborations, Aleph, Delphi, L3, OPAL; hep-ex/0103048, March 2001.

[37] J. Ellison and J Wudka, hep-ph/9804322, UCRHEP-T227

[38] Baur, U., Han, T., and Ohnemus, J., Phys. Rev., D**48**, 5140 (1993).
Baur, U., Han, T., and Ohnemus, J., Phys. Rev., D**51**, 3381 (1995).

[39] E. W. N. Glover and J. J. van der Bij, ' Z Boson Pair Production Via Gluon Fusion', Nucl. Phys. **B321** 561 (1989).
C.Zecher, T.Matsuura, J.J. van der Bij, 'Leptonic Signals from off-shell Z Boson Pairs at Hadron Colliders', Z. Phys. C **64** 219 (1994).

[40] S. Haywood et al. Electroweak Physics, hep-ph/0003275 v1 28 Mar 2000

[41] Ketevi A. Assamagan et al. Final report of the ATLAS AOD/ESD Definition Task Force, ATLAS-SOFT-2004-006, 14 December 2004.

[42] S. Hassani, 'Prospects for measuring neutral gauge boson couplings in ZZ production with the ATLAS detector', ATL-COM-PHYS-2002-012.

[43] U. Baur and D. Rainwater, Phys. Rev. **D62** 113011 (2000).

[44] S. Frixione, P. Nason, G. Ridolfi, Nucl. Phys.**B282** (1987) 253.

[45] R. Bonciani *et al.*, Nucl. Phys.**B529** (1998) 424.

[46] H. Aihara *et al. Electroweak Symmetry Breaking and New Physics at the TeV Scale,* edited by T. Barklow, S. Dawson, H. Haber and J. Siegrist, World Scientific, Singapore.

[47] R.K. Elis, W.J. Stirling, B.R. Webber, "QCD and Collider Physics", Cambridge Monographs in Particle Physics, Nuclear Physics and Cosmology **8** (1996) 1.

[48] Lj. Simić *et al* ATLAS Notes, ATL-PHYS-2006-011, CERN 2006.

[49] Distributed Analysis Using Ganga: https://twiki.cern.ch/twiki/bin/view/Atlas/DistributedAnalysisUsingGanga

[50] Particle Data Group: W.-M. Yao *et al.*, Journal of Physics, G **33**, 1 (2006)

[51] AcerMC: http://borut.web.cern.ch/borut/

[52] ATLAS Detector and Physics Performance, Technical Design Report. ATLAS TDR 15, CERN/LHCC 99-15

Appendices

A Boosted decision trees

In this note, we used an advanced data analysis technique - Boosted Decision Trees(BDT) for diboson analysis to improve the physics potential. BDT [2] has been firstly reported for the data analysis in MiniBooNE experiment, it works better than Artificial Neural Networks(ANN). The BDT has been used in HEP data analysis in recent years [3]. The detail technique of the BDT can be found in the references [2].

The motivation for the boosting algorithm is to design a procedure that combines many "weak" classifiers(eg. decision trees to achieve a powerful classifier(eg. boosted decision trees).

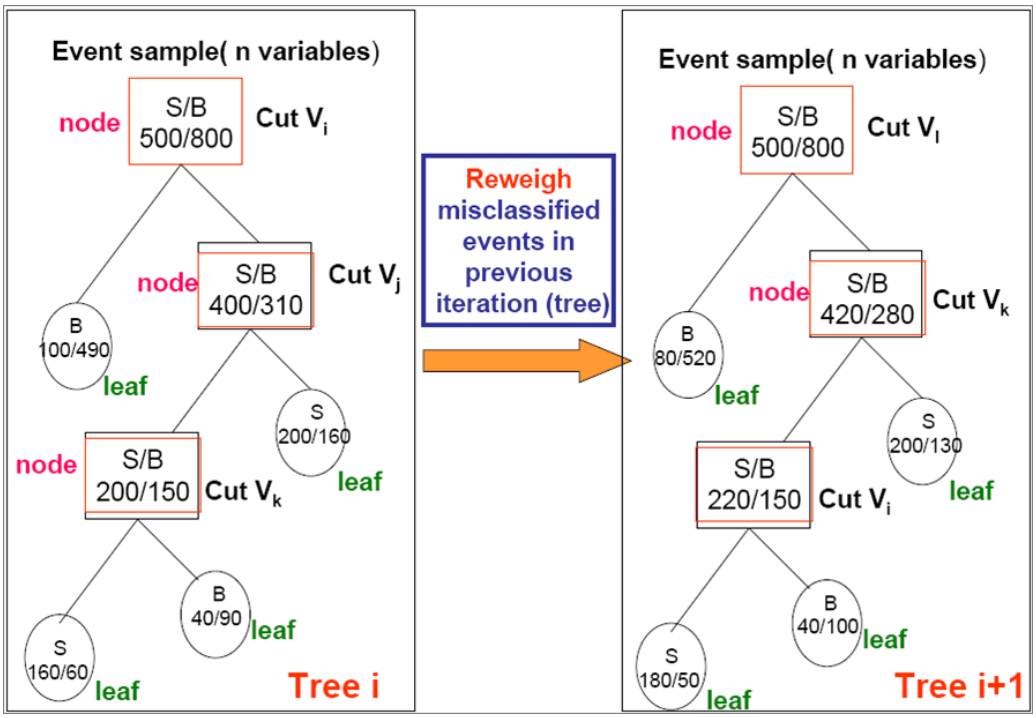

Figure 98: Diagrams for Boosted decision-trees. From $Tree(i)$ to $Tree(i+1)$ the mis-classified events are increased weights based on *boosting* argurithm. The 'note' (box) in the diagram is the variable to be split to separate signal and background in the 'decision-tree' structure. S and B denote signal and background, respectively. The 'circles' are tree leaves, depending on the signal to background ratio, those leaves are defined as signal ot background leaves.

We only give a very brief description in this note. As illustrated in Figure 98, the BDT program works with a set of data including both *signal* and *background*. Data are presented by a set of physics variable distributions. A *decision-tree* will split data recursively based on 'cuts' on the input variables until a stopping criterion is reached (e.g. purity, too few events, number of nodes). Every event ends up in a *signal* or a *background* 'leaf' of the decision tree. Misclassified events will be given larger weights in the next tree (boosting). Such procedure is repeated several hundreds to thousand times until the performance reaches optimal. For a given event, if it lands on the *signal* leaf in one tree, it is given a score of 1, otherwise, -1. The sum of the *weighted* scores from all trees is the final score (BDT output) of the event. The procedure described above is the BDT *training* procedure. The measure of

the *BDT* performance to separate the signal from the background is done with statistically independent *test* sample. For a given *test* event, it is followed through each tree in turn. The high score for a given test event means this event is most likely a *signal* event, and low score, a *background* event. The major advantages of boosted decision trees are their stability, their ability to handle large number of input variables, and their use of boosted weights for misclassified events to give these events a better chance to be correctly classified in succeeding trees.

A.1 Decision Trees

What criterion is used to define the quality of separation between signal and background in the split? Imagine the events are weighted with each event having weight W_i. Define the purity of the sample in a branch by

$$P = \frac{\sum_s W_s}{\sum_s W_s + \sum_b W_b},$$

where $\sum_s$ is the sum over signal events and $\sum_b$ is the sum over background events. Note that $P(1-P)$ is 0 if the sample is pure signal or pure background. For a given branch let

$$Gini = (\sum_{i=1}^{n} W_i) P(1-P),$$

where n is the number of events on that branch. The criterion chosen is to minimize

$$Gini_{left\ son} + Gini_{right\ son}.$$

To determine the increase in quality when a node is split into two branches, one maximizes

$$Criterion = Gini_{father} - Gini_{left\ son} - Gini_{right\ son}.$$

At the end, if a leaf has purity greater than 1/2, then it is called a signal leaf and if the purity is less than 1/2, it is a background leaf. Events are classified signal if they land on a signal leaf and background if they land on a background leaf. The resulting tree is a *decision tree*.

A.2 Boosting Algorithms

If there are N total events in the sample, the weight of each event is initially taken as $1/N$. Suppose that there are N_{tree} trees and m is the index of an individual tree. Let

- $x_i =$ the set of PID variables for the ith event.
- $y_i = 1$ if the ith event is a signal event and $y_i = -1$ if the event is a background event.
- $w_i =$ the weight of the ith event.
- $T_m(x_i) = 1$ if the set of variables for the ith event lands that event on a signal leaf and $T_m(x_i) = -1$ if the set of variables for that event lands it on a background leaf.
- $I(y_i \neq T_m(x_i)) = 1$ if $y_i \neq T_m(x_i)$ and 0 if $y_i = T_m(x_i)$.

There are at least two commonly used methods for boosting the weights of the misclassified events in the training sample. For diboson analysis, we only used ε-Boost, briefly described in the following.

For ε-Boost [2], after the mth tree, change the weight of each event i, $i = 1,...,N$:

$$w_i \rightarrow w_i e^{2\varepsilon I(y_i \neq T_m(x_i))},$$

where ε is a constant of the order of 0.01. Renormalize the weights, $w_i \rightarrow w_i / \sum_{i=1}^{N} w_i$. The score for a given event is $T(x) = \sum_{m=1}^{N_{tree}} T_m(x)$, which is the sum of the scores over individual trees.

Typically, one may build several hundred or 1000 trees this way until the BDT preformance is optimal. In the diboson analysis, we built 1000 decision trees using ε-boost algorithm with $\varepsilon = 0.01$. Each tree has 20 leaves, the minimum events in each leaf is 50. A score is now assigned to an event as follows. The event is followed through each tree in turn. If it lands on a signal leaf it is given a score of 1 and if it lands on a background leaf it is given a score of -1. The sum of all the scores is the final score of the event. High scores mean the event is most likely signal and low scores that it is most likely background. By choosing a particular value of the score on which to cut, one can select a desired fraction of the signal or a desired ratio of signal to background.

A.3 How to Select Input Variables

One of the major advantages of the boosted decision tree algorithm is that it can handle large numbers of input variables. Generally speaking, more input variables cover more information which may help to improve signal and background event separation. Often one can reconstruct several dozens variables which have some discriminant power to separate signal and background events. Some of them are superior to others, and some variables may have correlations with others. Too many variables, some of which are "noise" variables, won't improve but may degrade the boosting performance. It is useful to select the most useful variables for boosting training to maximize the performance. The effectiveness of the input variables was rated based on two criterion;
1) how often each variable was used as a tree splitter,
2) the gini index contribution of each variable.

A.4 Event Reweighting Training Technique

The recent development we made for LHC physics analysis is the event reweighting technique incorporated in the original ANN and BDT programs. For the standard ANN and BDT techniques, the weights for training events are equal. It works fine if training MC samples from different physics processes are generated based on their cross sections. For hadron colliders such as LHC, however, it is unrealistic and inefficient to generate MC data for all the physics processes with full detector simulation based on their production rates. This is simply because of limited CPU time and data storage capacity. If we treat these MC events from different sources equally using the standard training technique, ANN and BDT will pay more attention to the more numerous MC events which will introduce a large training bias and degrade the overall background rejection. To avoid the training prejudice and to improve the PID performance, I presented a multivariate training technique using event reweighting for ATLAS data analysis which enable us to build single powerful PID by properly combining all backgrounds together using event reweighting for PID training. The ANN and BDT with event reweighting training has significantly better performance than those with the standard training technique.

B Binned maximum likelihood

To build the confidence intervals we used *binned maximum likelihood caculations*. Expected and 'observed' (from MC experiments) events are binned by one or more observable. Observables such as $M_T(VV)$ and $p_T(V)$ are choosen because we find in MC experiments their distribution is especially sensitive to anomalous TGCs. The most dramatic effect is an increase in the high M_T or p_T cross section, so it is important to also include the overflow bin in our likelihood calculation.

For each bin expected signal and background are compared to the the 'observation' with a likelihood. At it's core, the likelihood is based on Poisson statistics

$$p(n;\nu) = \frac{\nu^n\, e^{-\nu}}{n!}, \quad \text{with } \nu = \nu_S + \nu_B,$$

where ν the predicted mean value of the expected number of events, which is determined by both the signal, ν_S, and the background, ν_B. The predicted signal is determined from the standard equation, $\nu_S = \mathscr{L}\varepsilon\sigma$. Here $\mathscr{L}$ is the total integrated luminosity, ε is the overall acceptance, and σ is the cross section which is a function of the coupling parameters. For background process, the cross sections are taken from the SM predictions. We assume the systematic errors of the signal and background are Gaussian and uncorrelated for each bin. Thus, we convolve two Gaussian distributions with the Poisson distribution to form the likelihood

$$L = \int_{1-3\sigma_b}^{1+3\sigma_b} \int_{1-3\sigma_s}^{1+3\sigma_s} g_s\, g_b\, \frac{(f_s\nu_s + f_b\nu_b)^n\, e^{-(f_s\nu_s+f_b\nu_b)}}{n!}\, d f_s\, d f_b$$

where

$$g_i = \frac{e^{(1-f_i)^2/2\sigma_i^2}}{\int_0^\infty e^{(1-f_i)^2/2\sigma_i^2}}, \quad i = s, b.$$

Here the total systematic uncertainty of signal and background appear as σ_s and σ_b, respectively.

From these likelihoods a total log-likelihood is formed from all the bin likelihoods. Some processes may also be separated into multiple channels (such as the three decay combinations of $WW \to ee, e\mu, \mu\mu$). Also, we will include a factor of -2 which makes this test statistic comparable to a chi-squared distribution. Thus, the log likelihood is

$$LL = -2 \sum_{k=\text{channels}} \sum_{i=\text{bins}} \log(L_i^k).$$

For this test statistics the 95% confidence-level interval is taken to be at the minimum+1.92 when fitting one anomalous coupling, and at the minimum+2.99 for a fit in a 2-dimensional space of anomalous couplings.

C W^+W^- event selection based on straight cut analysis (with CBNT)

A complementary study on $W^+W^- \to \ell^+\nu\ell^-\nu$ event selection and analysis has been performed using the CBNT datasets. Comparing to the analysis based on the *AOD* datasets, much more background events have been included in the studies. The strategy of this study is make sure to establish the W^+W^- signal with enough statistical significance for the first integrated luminosity of 0.1 fb^{-1}. This analysis also served as a stepping stone to develop the advanced analysis tool, the Boosted-Decision-Trees, for diboson physics studies.

C.1 WW event selection with straight cuts

Event Selection for WW leptonic decays with straight cuts are described below.

- Two isolated leptons with transverse momentum, p_T, greater than 20 GeV, and at least one with p_T greater than 25 GeV.
- Missing transverse energy, $\not\!\!E_T$, greater than 30 GeV.
- Invariant mass of two leptons, $M_{\ell\ell}$, greater than 30 GeV; veto the events with M_{ee} or $M_{\mu\mu}$ within the Z-mass window: 70 GeV $< M_{\ell\ell} <$ 120 GeV.
- Vector sum $E_T^{had} = |\sum(\vec{E}_T^{\ell}) + missing\vec{E}_T| <$ 60 GeV.
- Sum of total jet transverse energy to be less than 120 GeV.
- Maximum number of hadronic jets with energy greater than 30 GeV = 1.
- Transverse momentum of the dilepton $p_T(\vec{\ell}_1 + \vec{\ell}_2) >$ 30 GeV.
- Vertex difference between two leptons in beam direction, $\Delta Z < 0.8mm$, and in transverse plane (impact parameter), $\Delta A < 0.1mm$.

Overall detection acceptance for $WW \to e\nu\mu\nu$ is about 6.5%, which includes geomatric and kinematic acceptance ($\sim$ 38.5%), and lepton ID and event selection efficiencies ($\sim$ 16.8%).

The background for $e^+\nu e^-\nu$ and $\mu^+\nu\mu^-\nu$ channels are much higher compared to the $e\mu + \not\!\!E_T$ channel. We have to apply additional cuts to reject the dilepton events from Drell-Yan and $Z + jet$ processes. For $\mu^+\mu^-$ final state we further required the event must satisfy the following additional cuts:

$$\Delta\phi(\mu, \not\!\!E_T) > 1\ rad,\ \ and\ \ E_T^{had} < 40\ \text{GeV}.$$

For e^+e^- final state, we applied following additional cuts:

- $0.9 < E/P < 2.0$;
- $N_{jet} < 1$;
- $0.5 < \Delta\phi(e^+, e^-) < 2.5$;
- $H_t <$ 400 GeV, where H_t is the total visible transverse energy in an event;
- $\not\!\!E_T/\sqrt{H_t} > 90$.

C.2 Results

The signal and background events pass the selection cuts are summarized in Table 70. Number of events are normalized to 1 fb^{-1} integrated luminosity. From this Table, it is clear that the most sensitive channel for WW detection is the $e\mu + \not{E}_T$ final state. We expect to observe 267 $e\mu + \not{E}_T$ events with 1 fb^{-1} integrated luminosity. 2/3 of the events should be the $WW \to e\nu\mu\nu$ signal. The signal statistical significance, $\sigma = S/\sqrt{B}$, is 18.9. Even for 0.1 fb^{-1} integrated luminosity, we should be able to establish the $WW \to e\nu\mu\nu$ signal with significance better than 5.

Process	N_{signal}	$N_{\text{background}}$	S/B
$WW \to e^{\pm}\nu\mu^{\mp}\nu$	178.1 ± 2.1	88.8 ± 14	2.01
$WW \to e^{+}\nu e^{-}\nu$	21.6 ± 1.1	22.4 ± 3.4	0.96
$WW \to \mu^{\pm}\nu\mu^{\mp}\nu$	31.5 ± 1.6	113.2 ± 16.5	0.28

Table 70: Expected signal and background events for $WW \to \ell^{+}\nu\ell^{-}\nu$ detection using cut-based analysis. Events are normalized to 1 fb^{-1} integrated luminosity.

Background breakdown for $WW \to e\nu\mu\nu$ analysis is listed in Table 71. From our analysis we found that the major background contributions come from the $t\bar{t}$ and the $Z + jets$ events.

Process	N_{selected}	Percentage
$WW \to e^{+}\nu e^{-}\nu$	178	100%
Total background	88.8	100%
$t\bar{t}$	25.1	28.3%
$Z + jets$	24.7	27.8%
$W^{\pm}Z$	14.0	15.8%
Drell-Yan$(\ell^{+}\ell^{-})$	12.57	14.2%
$W \to \mu\nu$	11.0	12.4%
$Z\gamma$	1.2	1.4%
$ZZ \to \ell\ell\ell\ell$	0.5	0.5%

Table 71: Expected signal and breakdown of the background events from different sources for $WW \to e\nu\mu\nu$ detection based on cut-based analysis. Events are normalized to 1 fb^{-1} integrated luminosity.

D Study of the $W\gamma$ background for W^+W^- detection

A significant background to $W(W \to e\nu)$ production is $W\gamma$ production, where the photon converts asymmetrically in the tracker material to produce a single high-momentum electron. We have investigated methods of $W\gamma$ background reduction, and find both conversion removal and hit requirements in the inner pixel layers to be effective.

MC Samples

To study $W\gamma$ production at ATLAS, we use CBNT ntuples produced in ATLAS reconstruction version 11 from a $W\gamma$ PYTHIA-generated event sample. The sample was generated with initial-state photon radiation (ISR) and a leading-order cross section of 11.7 pb. We expect higher-order QCD corrections to be of a similar size to those at the Tevatron, O(60%). Final-state radiation (FSR) contributes twice the cross section of ISR at low photon momentum, but drops significantly with increasing photon energy. We anticipate FSR corrections to be smaller than QCD corrections for the final event sample.

Prior to detector simulation, events are filtered with a requirement of photon $E_T > 25$ GeV, with a resulting efficiency of 63.7%. We expect a filter with a lower E_T threshold would increase the background by no more than a few percent. A total of 95550 events are used for our background studies.

Background Estimate

We obtain a rough estimate of the number of background events expected in the $(W \to e\nu)(W \to e\nu)$ sample by selecting events with two electron candidates with $E_T > 25$ GeV and $\not\!\!E_T > 25$ GeV. The candidates are required to have $E/p < 3$, hadronic to electromagnetic energy ratio (Had/EM) < 0.02, isolation energy < 0.2, and an associated track with $p_T > 10$ GeV. We estimate the background using a cross section of $11.7 \times 0.673 \times 1.6 = 12.6$ pb, which accounts for the filter efficiency and the NLO QCD correction. We find an acceptance of $1305/95550 = 0.01366$ for the kinematic and electron identification selection, resulting in 172 events per fb^{-1} in the $ee\nu\nu$ sample. At this level, $W\gamma$ production would be the dominant background in this sample, so we next investigate methods of background reduction.

Since the $W\gamma$ background results from a conversion in the tracker material, we expect a conversion removal algorithm to significantly reduce this background. We developed an algorithm searching for opposite-sign tracks to the identified electron track, with the two tracks having a mass consistent with zero ($|m| < 0.2$ GeV), similar polar angle ($\Delta\cot\theta < 0.008$), and a common vertex (minimum two-track $r\phi$ separation between -1 cm and 0.1 cm). The conversion radius of such track pairs is shown in Fig. 99.

We additionally study the conversion variable `eg_convTrkMatch` in the CBNT. This variable has complementary conversion rejection to our simple algorithm. Rejecting events passing our simple algorithm, we would expect 110 $W\gamma$ events per fb^{-1}; rejecting events passing the `eg_convTrkMatch` variable would result in 97 events per fb^{-1}. Rejecting events passing either algorithm gives only 42 events per fb^{-1}.

If the conversion is highly asymmetric, there may be only one reconstructed track from the conversion. In this case, a track-based conversion removal will not be effective. However, since the conversion occurs in the tracking material, requiring the electron track to have a hit in an inner layer of the tracking material will significantly reduce the amount of material in which the photon can convert. We find that requiring at least 1 B-layer hit cuts the background in half (after conversion rejection), to 21 events per fb^{-1}.

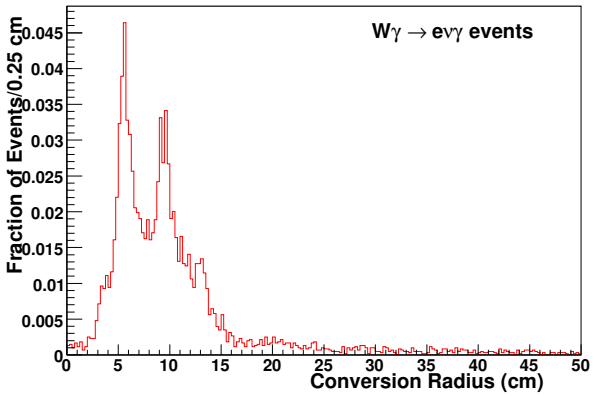

Figure 99: The radius of conversion of track pairs satisfying requirements on the two-track mass, difference in polar angle, and minimum $r\phi$ separation.

Summary

We have estimated the $W\gamma$ background to the $(W \to e\nu)(W \to e\nu)$ sample. Without selection targeting conversions, the signal to background ratio is on the order of 1 to 1. Applying conversion rejection and a B-layer hit requirement reduces the background by a factor of ≈ 8. Further studies are necessary to investigate the efficiency of these requirements for electrons from WW decay.

E Anomalous TGC sensitivity study using fast simulations

This section describes the anomalous TGC sensitivity studies in W^+W^- production using fast simulations to the MC events produced with non-SM anomalous couplings.

The most stringent direct limits on the anomalous TGC parameters have been achieved by the LEP experiments using the $e^+e^- \to W^+W^-$ events at LEP II program. The 95% C.L. intervals [4] obtained by combining the results from the four LEP experiments (until the end of 1999, at center-of-mass energies up to 202 GeV) are:

$$-0.051 < \Delta g_1^Z < +0.034$$

$$-0.105 < \Delta\kappa_\gamma < +0.069$$

$$-0.059 < \lambda_\gamma < +0.026.$$

The TGC parameters are related by $\lambda_\gamma = \lambda_Z$ and $\Delta\kappa_Z = \Delta g_1^Z - \Delta\kappa_\gamma \tan^2\theta_W$. In each case, the parameter listed was varied while the remaining are fixed to their SM value. Both statistical and systematic uncertainties are included.

E.1 BHO MC generator

For the study of anomalous TGC the NLO MC generator of Baur, Han and Ohnemus [21] (henceforth referred to as BHO) is used. This program generates WW production, with W decaying to leptons. The most general C and P conserving anomalous WWZ and $WW\gamma$ couplings are included. In this generator the diagrams contributing to $\mathcal{O}(\alpha_s)$ are the squared Born (LO) graphs, the interference of the Born with the virtual one-loop graphs, and the squared real emission graphs. The BHO generator employs the phase space slicing method and the calculation is performed in the narrow width approximation for the leptonically decaying gauge bosons. The program generates the n-body final state events, for the Born and virtual contributions, and the n+1-body final state events for the real emission contributions. The spin correlations in the leptonic decays are included everywhere except in the virtual contributions. The BHO generator is interfaced to PYTHIA for the fragmentation of partons and hadronization, and ATLfast for the fast simulation of the ATLAS detector. The events produced by the BHO generator contain the leptonic decay products of WW bosons (the n-body final state), and at most one colored parton in the final state (the n+1-body final state). For the events with a colored parton in the final state, the method of independent fragmentation [47] is used to produce the color-singlet particles which form the input for detector simulation. The standard parton shower approach cannot be applied to the events produced by the BHO generator, since this would double count regions of phase space. The CTEQ5M PDF and factor scale $Q^2 = M_W^2$ is used.

After fast simulations of ATLAS detector, the set of kinematic cuts "B", described in section 4.4.1, is applied. This set of cuts optimizes sensitivity to anomalous TGC measurements. Since MC@NLO generator is more realistic, shape and cross section of BHO distributions (used for TGC study) are corrected to MC@NLO distributions (with same kinematic cuts). Comparison of BHO and MC@NLO p_T distributions obtained after fast and full simulations of ATLAS detector and selection cuts B is shown in Fig. 100.

E.2 Fast simulation and fitting method

Anomalous TGC affect both the total production cross section and the differential cross section. Since the anomalous couplings contribute only in the $s-$ channel, their effects are concentrated particularly in central rapidity region and at large transverse momenta of W bosons and W^+W^- pairs. Since in the

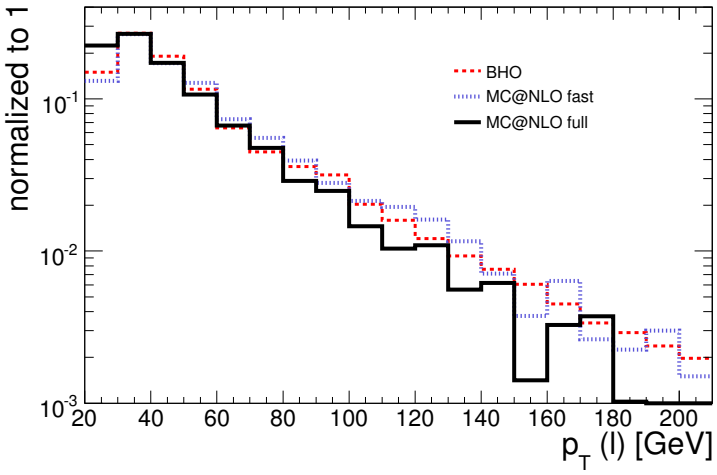

Figure 100: BHO and MC@NLO predictions for lepton p_T distribution after fast and simulations of ATLAS detector and "B" selection (section 4.4.1).

dilepton channels the W and W^+W^- transverse momenta cannot be unambiguously reconstructed, as an option the transverse momentum distribution of leptons or lepton pairs can be studied.

In this note, the limits of the anomalous TGC couplings are evaluated by using a binned maximum likelihood fit to compare the p_T distributions of "mock" ATLAS data to the Monte Carlo reference distributions (theoretical expectations) which are a function of the TGC parameters. The p_T distribution of "mock" data which correspond to an ATLAS experiment is simulated with SM TGC parameters using BHO generators interfaced with PYTHIA. The shape of BHO distribution and corresponding cross section obtained after fast simulation of ATLAS detector, and kinematical cuts (selection "B") are corrected to MC@NLO distribution obtained after full simulation of ATLAS detector (with same kinematic cuts).The "mock" data distribution is constructed by sampling each bin according to a Poisson distribution with the mean given by the relevant bin content of the SM reference histogram. Afterwords, contribution of all background processes is added.

Monte Carlo reference distributions (theoretical expectations) as a function of the TGC parameters. are obtained by expressing differential cross section in each p_T bin by a quadratic function of two coupling parameters i.e.:

$$\frac{d\sigma(\Delta\kappa,\lambda)}{dp_T} = \alpha_0 \frac{d\sigma_{SM}}{dp_T} + \alpha_1\Delta\kappa + \alpha_2\lambda + \alpha_3\Delta\kappa^3 + \alpha_4\lambda^2 + \alpha_5\Delta\kappa\lambda\,. \tag{9}$$

The six α_i coefficients are determined for each p_T bin by fitting the function Eq. (9) to nine BHO Monte Carlo samples for the following combinations of two TGC parameter values: $(-\Delta\kappa,\lambda)$, $(0,\lambda)$, $(\Delta\kappa,\lambda)$, $(-\Delta\kappa,0)$, $(0,0)$, $(\Delta\kappa,0)$, $(-\Delta\kappa,-\lambda)$, $(0,-\lambda)$, $(\Delta\kappa,-\lambda)$. These values form 3×3 grid centered on the SM values of $(\Delta\kappa,\lambda)$=(0,0). The size of the grid is chosen to be slightly larger than the expected 95% C.L. for the corresponding pair of couplings. With extracted coefficients α_i and β_i, we are able to predict the cross section in a given p_T bin for any pair $(\Delta\kappa,\lambda)$. The error of such a parametrization is evaluated by calculating the cross sections with the BHO generator at random points inside the grid and then comparing them with the the approximation Eq. (9). The largest error of the approximation is found to be less than 2%. MC reference distributions are obtained after fast simulation of ATLAS detector, and after kinematical cuts (selection "B"). Each bin of MC reference distributions is multiplied by the corresponding factor obtained from the ratio of MC@NLO and BHO distribution with SM values of TGC parameters. Finally, contribution of all background processes is added. The details of the binned likeliyhood fit are described in section 8.4.

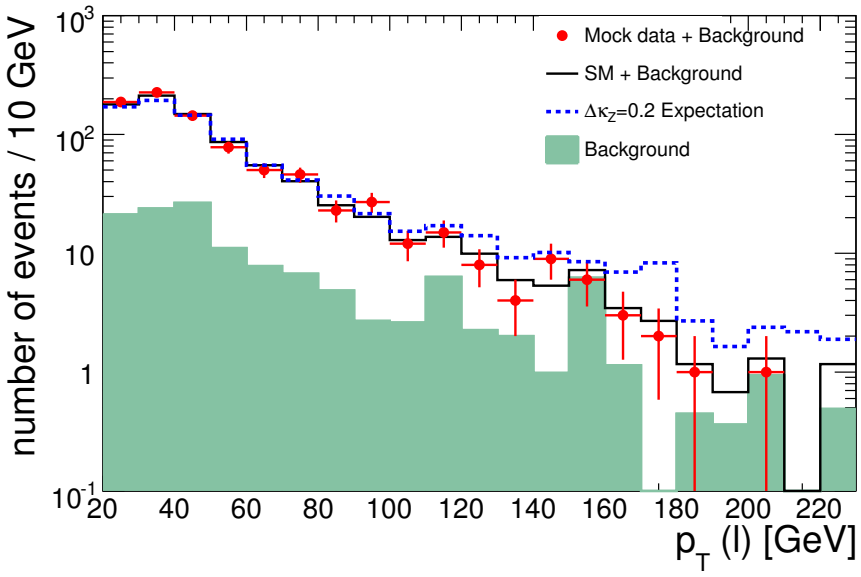

Figure 101: The transverse momentum distribution of leptons after applying the kinematic cuts. The points with error bars represent "mock" data with integrated luminosity of 10 fb^{-1} . The lines are SM MC distribution and $\Delta\kappa_Z = 0.2$ theoretical expectation. The contribution of all backgrounds to reference distributions is shown as a shaded histogram.

An example of a maximum likelihood fit to the transverse momentum distribution of leptons is shown in Figure 101. The points with error bars represent "mock" data with integrated luminosity of 10 fb^{-1} . The lines are SM MC distribution and $\Delta\kappa_Z = 0.2$ theoretical expectation. The contribution of backgrounds to reference distributions is shown as a shaded histogram.

E.3 Anomalous TGC limits

The limits for anomalous TGC are derived when one or two parameters of the of WWV couplings are varied from their SM values. By varying the parameters of WWZ or $WW\gamma$ couplings separately it is possible to compare sensitivity limits for TGC parameters in WW, WZ and $W\gamma$ production.

The 95% C.L. limits obtained when only one parameter of the WWZ and $WW\gamma$ couplings is varied are summarized in Table 72. In order to obtain the best estimate of the limits that will be achieved at ATLAS, they are averaged over 1000 simulated ATLAS experiments. The limits are shown for various integrated luminosity (1, 10 and 30 fb^{-1}) and for form factor scale, Λ =2 TeV. The systematic uncertainties associated with the sensitivity limits of the TGC parameters are included. The following systematic effects are estimated: background rate systematics, parton density function systematics, systematics arising from neglected higher order corrections, and systematics arising from size of the grid and p.d.f.'s used for the MC reference distributions. It is found that at integrated luminosities up to 30 fb^{-1} the TGC limits have only a low sensitivity to the systematic errors. From the Table 72 we can see that with increasing integrated luminosity from 1 to 30 fb^{-1} limits will be improved and precise investigation of TGC will be possible with the first 10fb^{-1} of LHC data. However, these results should be taken with caution, because they have been derived simply by scaling the histograms obtained for low luminosity, and effects such as the pile-up have not been accounted for. Nevertheless, the results provide information on how an increase in luminosity will improve the sensitivity limits of TGC parameters. For integrated luminosity of 30 fb^{-1} and form factor scale Λ =2 TeV, WWZ couplings $\Delta\kappa_Z$ and λ_Z can be measured with an accuracy of 0.05 to 0.08 with 95% C.L. Increase of form factor scale from 2 to 5 TeV, improves sensitivity

Table 72: 95% Confidence Limits for WWZ and $WW\gamma$ coupling parameters for various integrated luminosity and for formfactor scale Λ =2 TeV.

	1 fb^{-1}	10 fb^{-1}	30 fb^{-1}
WWZ couplings			
$\Delta\kappa_Z$	(-0.16, +0.24)	(-0.077, 0.11)	(-0.055, 0.083)
λ_Z	(-0.17, 0.12)	(-0.085, 0.064)	(-0.061, 0.058)
Δg_Z^1	(-0.56, 0.66)	(-0.30, 0.45)	(-0.22, 0.33)
$WW\gamma$ couplings			
$\Delta\kappa_\gamma$	(-0.36, 0.52)	(-0.18, 0.27)	(-0.091, 0.15)
λ_γ	(-0.32, 0.30)	(-0.19, 0.16)	(-0.14 0.12)
Equal couplings: $\Delta\kappa_Z$=$\Delta\kappa_\gamma$, λ_Z=λ_γ			
$\Delta\kappa$	(-0.12, 0.19)	(-0.060, 0.097)	(-0.041, 0.072)
λ	(-0.14, 0.10)	(-0.071, 0.052)	(-0.052 0.039)

limits by $\approx 40-50\%$. Because of the larger coupling of the Z boson to quarks and to the W bosons, the W^+W^- production is more sensitive to WWZ couplings than to $WW\gamma$ couplings. Consequently, the limits for $\Delta\kappa_\gamma$ and λ_γ are ≈ 2 times larger compared to the limits of WWZ couplings. Comparison with limits obtained from WZ and $W\gamma$ production shows that in spite of limited information available for the final state, the WW production can provide stringent limits for the $\Delta\kappa_Z$ parameter, compared with the sensitivities expected in other channels at LHC. This TGC limits are in fair agreement with a previous study [48] carried out completely with fast simulation of ATLAS detector and "B" selection cuts.